



THE UNIVERSITY *of* EDINBURGH

This thesis has been submitted in fulfilment of the requirements for a postgraduate degree (e.g. PhD, MPhil, DClinPsychol) at the University of Edinburgh. Please note the following terms and conditions of use:

This work is protected by copyright and other intellectual property rights, which are retained by the thesis author, unless otherwise stated.

A copy can be downloaded for personal non-commercial research or study, without prior permission or charge.

This thesis cannot be reproduced or quoted extensively from without first obtaining permission in writing from the author.

The content must not be changed in any way or sold commercially in any format or medium without the formal permission of the author.

When referring to this work, full bibliographic details including the author, title, awarding institution and date of the thesis must be given.

Processing of Thick Section Epoxy Powder Composite Structures

James M. Maguire

Thesis submitted to The University of Edinburgh in partial fulfilment of the
requirements for the degree of Doctor of Philosophy

February 2019



THE UNIVERSITY *of* EDINBURGH
School of Engineering

Declaration

I declare that this thesis is an original report of my research, has been written by me and has not been submitted for any previous degree. The experimental work is almost entirely my own work; the collaborative contributions have been indicated clearly and acknowledged. Due references have been provided on all supporting literatures and resources.

James M. Maguire

February 2019

Abstract

The use of epoxy powder as the primary matrix in thick fibre-reinforced composite parts is investigated.

The characteristics of three epoxy powders are assessed using several experimental techniques, focusing on their curing behaviour. At least one epoxy powder is shown to have advantageous characteristics for manufacturing thick-section composites.

Material models are developed which can describe the processing behaviour (cure kinetics, viscosity change, etc.) of an epoxy powder. The cure kinetics model makes use of an additional rate constant to better describe the rate of cure at both high and low temperatures. The chemorheological model is based on an existing model for toughened epoxies.

A one-dimensional simulation tool for manufacturing thick-section composite laminates is developed in MATLAB. The simulation tool employs a resin flow model for vacuum-bag-only prepregs to describe the infusion process and subsequent thickness change. This thickness change is coupled to a model for through-thickness heat transfer which can be solved numerically for various thermal boundary conditions. The model is used to explore the suitability of epoxy powders for the manufacturing thick-section composite structures.

The aforementioned simulation tool is validated against experimental results for thick-section composite laminates. The experiments are carried out using a modified heated tool and test apparatus which apply known thermal boundary conditions. A linear variable differential transformer is used to measure the thickness change of each laminate during testing, while thermocouples are used to measure the temperatures at various positions within each laminate. The results of the tests show good agreement with the one-dimensional simulation tool. Additional simulations are performed to investigate the influence of material format, thickness change, and heating methods. Methods for reducing thermal and cure gradients are explored also.

A method is outlined for implementing the process models within commercial finite element software, Abaqus FEA. User subroutines for heat transfer and thermal expansion are used to define the various process models. One-dimensional simulations are validated, and a convergence study is performed on time step size and element size. Simulations show the effect of in-plane heating for glass-fibre and carbon-fibre laminates, and the processing of a wind turbine blade root section is investigated.

Overall, it is shown that thick-section composite structures can be manufactured using a low-cost commodity epoxy powder from the coating industry, and that these structures do not suffer from the risk of uncontrollable thermal events.

Lay Summary

Fibre-reinforced polymer composites are well known for their high strength/stiffness-to-weight ratio, which has made them a popular choice in lightweighting high performance structures such as aircraft, sports cars, and wind turbine blades. In the latter case, glass-fibre reinforced epoxy is the dominant material system due to cost-performance considerations in the wind energy industry, however, manufacturing challenges still exist when upscaling existing technologies. As turbine blades continue to increase in length, the thicknesses of the root and spar of the blade also tend to increase. During the manufacture of these huge blades, heat can build up in the thick sections due to the chemical curing reaction of the epoxy. This problem is exacerbated by the insulating properties of the constituent materials i.e. epoxy and a reinforcing fabric (usually glass-fibre based). The manufacturing cycle must be carefully controlled to ensure that the build-up of heat does not damage the blade. This often leads to extended cycle times and cost accrued by the manufacturer. One alternative to using conventional, highly exothermic, epoxies is to use low-cost epoxy powders from the coating industry. These powders generate much less heat when curing, thus offering a possibility to control temperatures within thick sections in a safer manner.

In this thesis, the characteristics of three epoxy powders were investigated using experimental techniques. One epoxy powder was chosen for further study based on its suitability for manufacturing thick composite parts. Mathematical material models were developed which can describe the characteristics of the epoxy powder for a given temperature cycle. Additional mathematical process models were developed which can describe the processing of a thick composite part using an epoxy powder. The process models and material models were combined to create a one-dimensional simulation tool which can predict processing conditions within a thick composite part for a given temperature cycle. This simulation methodology was adapted further for a commercial software which could perform 1D, 2D, and 3D simulations. The accuracy of these simulation tools was confirmed by comparing the results against experimental tests under controlled conditions. The simulations showed that epoxy powders can be used to reduce the build up of heat in thick composite parts during manufacturing, and

that there is potential for further development of the technology. Additionally, it was shown that the simulation tools can be used to investigate various aspects of processing thick composite parts and reduce the need for expensive and time-consuming trial and error experiments.

Acknowledgements

Firstly, I must thank my PhD supervisor, Prof. Conchúr M. Ó Brádaigh. It has been an incredible journey, and I'm still amazed by the opportunities I have received because of you. I will be forever grateful for your continuous support, guidance, and positivity. Thank you also to my secondary supervisor Prof. Khellil Sefiane for your support and encouragement since my arrival in Edinburgh.

Thank you to the College of Science and Engineering at the University of Edinburgh, ÉireComposites Teo., and Johns Manville for funding my PhD research. Thank you also to the MaREI Centre, NUI Galway, and UCC for their previous funding.

Thank you to all the members of the composites research group (and Jake!) at the University of Edinburgh for reminding me that there is more to this field than epoxy powder and thick sections. Thank you to all the technical staff who have helped me over the last few years, especially Mr Eddie Monteith. A big thank you to my IMP colleagues for keeping me sane and giving me a reason to have a social life. In particular, thanks to all the people I've lived with while in Edinburgh; Murve, Leonardo, Anne and Anthony, Davide and Chiara (I feel like we've lived together!), and now Jinyu and Shūji. You're wonderful people, and I've been incredibly lucky to have had your company these last few years.

Thank you to Prof. R. Byron Pipes for hosting and supervising me at CMSC in Purdue University, and thank you to the Royal Society of Edinburgh for funding my trip under the John Moyes Lessells Travel Scholarship. Thank you to Dr. Nathan Sharp for his technical guidance and all the other researchers and staff in CMSC for being so welcoming. Thanks to David for being open-hearted and hilarious.

Thank you to the staff in SE Blade Technology B.V. for hosting me on a MARINCOMP secondment (a Marie Curie FP7 project funded under the IAPP call: Grant No. 612531). In particular, thank you to Dr. Kapileswar Nayak for the supervision, collaboration and wonderful hospitality (the latter also extends to Manju, Arun, and Kumaran).

Thank you to the staff at the Center for Composite Materials in the University of Delaware, particularly Prof. Suresh G. Advani and Dr. Pavel Simacek who hosted and supervised me. Thank you to Dr. John Tierney for being a great source of knowledge and entertainment. Thank you also to Lutz and Rodrigo for being my adopted brothers.

Thank you to the past and present staff at ÉireComposites Teo. for all the advice and assistance, and for hosting me on my first MARINCOMP secondment. Thanks to Bryan, Cormac, Mark, and the Mikes for all the help, craic, and car lifts.

Thank you to the staff at NIACE for their assistance and access to facilities, particularly Dr. Alistair McIlhagger and Dr. Edward Archer. Similarly, thank you to Dr. Terry McGrail and Mr. Ananda Roy at ICOMP in the University of Limerick.

Thank you to my old UCC colleagues, and to the wonderful Serena O'Neill and Helen Lynch; artists, fashionistas, and general all-round legends.

Thank you to my friends at NUI Galway, who hosted me as recently as last November. Thank you to Myles, Elaine, Donnacha, and (sort of) Tom... my voice is still hoarse from the late-night COD.

Finally, thank you to my family, I was going to say that you have been the one true constant in this crazy adventure, but we seem to have increased in number and age since I started... I could write a thesis on you lot alone, and maybe some day I will. I love you all so much.

To my mother, Patricia, I dedicate this work to you.

After studying engineering (mainly of the mechanical variety) for 10+ years, I have reached some philosophical conclusions about the profession. To summarise this, I have adapted a poem by my fellow Monaghan man, Patrick Kavanagh, entitled, 'Sanctity'. I have renamed it, 'Sagacity':

*To be a mechanic but not know the trade,
To be married and never have a wife,
Twin ironies by which engineers are made,
The agonising pincer-jaws of life.*

Table of Contents

Abstract	i
Lay Summary	iii
Acknowledgements	v
Table of Contents	vii
List of Publications	xii
List of Tables.....	xiv
List of Figures	xvi
Nomenclature	xxvii
1. Introduction	1
1.1 Project Motivation	1
1.2 Manufacturing Methods for Large Composite Structures.....	4
1.3 Processing Thick-section Structures	7
1.4 Thermosetting Powders	9
1.5 Technology Background	10
1.6 Objectives	13
1.7 Thesis Outline.....	14
2. Literature Review	17
2.1 Polymer Powder Technology	17
2.1.1 General Information on Powder Coatings.....	17
2.1.1 Powder Towpregging	19
2.1.2 Powder Binders	21
2.2 Material Characterisation and Modelling.....	22
2.2.1 Characterisation of Thermosetting Powders	22

2.2.2	Curing of Thermosets	27
2.2.3	Chemorheology of Thermosets	31
2.2.4	Thermal Degradation.....	34
2.2.5	Water Vapour Sorption	36
2.3	Process Modelling and Simulation	40
2.3.1	Resin Flow.....	40
2.3.2	Heat Transfer and Consolidation.....	49
2.3.3	Experimental Validation	60
3.	Experimental Characterisation of Epoxy Powder	65
3.1	Chapter Introduction and Overview	65
3.2	Materials and Methodology.....	66
3.2.1	Epoxy Powder Selection	66
3.2.2	Thermogravimetric Analysis.....	66
3.2.3	Differential Scanning Calorimetry	67
3.2.4	Parallel-plate Rheometry	69
3.2.5	Dynamic Mechanical Thermal Analysis	71
3.2.6	Dynamic Vapour Sorption	74
3.3	Results and Discussion	76
3.3.1	Downselection of Powders.....	76
3.3.2	Thermal Stability.....	76
3.3.3	Curing.....	77
3.3.4	Chemorheology	81
3.3.5	Crosslink Density	84
3.3.6	Water Vapour Sorption	85

3.4	Conclusions	90
4.	Material Modelling of Epoxy Powder	93
4.1	Chapter Introduction and Overview	93
4.2	Methodology	93
4.2.1	Differential Scanning Calorimetry.....	93
4.2.2	Parallel-plate Rheometry.....	94
4.2.3	Cure Kinetics Modelling.....	95
4.2.4	Chemorheological Modelling.....	98
4.2.5	Modelling of Powder Melting and Sintering	101
4.3	Results and Discussion.....	103
4.3.1	Cure Kinetics.....	103
4.3.2	Chemorheology.....	107
4.3.3	Powder Melting and Sintering	112
4.4	Conclusions	115
5.	One-dimensional Process Simulations.....	117
5.1	Chapter Introduction and Overview	117
5.2	Methodology	118
5.2.1	Resin Flow Model.....	118
5.2.2	Heat Transfer Model	125
5.2.3	Thermal Boundary Conditions.....	127
5.2.4	Material Properties	128
5.2.5	Initial Conditions.....	133
5.2.6	Numerical Computation.....	134
5.3	Results and Discussion.....	137

5.3.1	Case Study – Oven Processing of a 100-ply Laminate	137
5.3.2	Temperature Profiles	138
5.3.3	Cure Profile	140
5.3.4	Thickness Change	143
5.4	Conclusions	147
6.	Experimental Validation of Process Simulations	149
6.1	Chapter Introduction and Overview	149
6.2	Materials and Methodology	149
6.2.1	Material Format	149
6.2.2	Experimental Apparatus Design	150
6.2.3	Instrumentation and Signal Analysis	153
6.2.4	Laminate Manufacturing	155
6.2.5	Simulation of Test Laminate Processing	158
6.3	Results and Discussion	161
6.3.1	Uni-directional Laminates with Epoxy Powder	161
6.3.2	Partially Impregnated Triaxial Laminate	170
6.3.3	Investigation of VBO Prepreg Format	175
6.3.4	Investigation of Thickness Effects	177
6.3.5	Investigation of Heating Methods	178
6.3.6	Methods for Reducing Thermal Gradients and Cure Gradients	181
6.4	Conclusions	188
7.	Two-dimensional and Three-dimensional Process Simulations	193
7.1	Chapter Introduction and Overview	193
7.2	Methodology	194

7.2.1	Numerical Computation	194
7.2.2	Virtual Composite Part Development	196
7.2.3	Verification of the Numerical Methods	200
7.2.4	Convergence Study	202
7.3	Results and Discussion	205
7.3.1	In-plane Heat Transfer	205
7.3.2	Simulations of Turbine Blade Manufacturing.....	214
7.4	Conclusions	220
8.	Conclusions and Recommendations	223
8.1	Conclusions	223
8.2	Recommendations	225
	Appendices	229
	Bibliography.....	282

List of Publications

Journal Papers

1. Maguire, J. M., Nayak, K., Ó Brádaigh, C. M., ‘Characterisation of epoxy powders for processing thick-section composites structures’, *Materials and Design*, 139, p. 112-121, 2018, DOI: <https://doi.org/10.1016/J.MATDES.2017.10.068>
2. Maguire, J. M., Nayak, K., Simacek, P., Advani, S. G., Ó Brádaigh, C. M., ‘Novel epoxy powder for manufacturing thick-section composite parts under vacuum-bag-only conditions’, *Composites: Part A*, In preparation.
3. Maguire, J. M., Sharp, N. D., Pipes, R. B., Ó Brádaigh, C. M., ‘Advanced process simulations for thick-section epoxy powder composite structures’, *Composites: Part A*, In preparation.

Conference Papers

1. Maguire, J. M., Nayak, K., Glennon, C., Robert, C., Ó Brádaigh, C. M., ‘Experimental validation of process simulations for vacuum-bag-only prepreps in thick-section structures’, *14th International Conference on Flow Processes in Composite Materials*, Luleå, Sweden, 31st May, 2018.
2. Maguire, J. M., Sharp, N. D., Pipes, R. B., Ó Brádaigh, C. M., ‘Process simulations for manufacturing thick-section parts with low-cost fibre reinforced polymers’, *SAMPE Europe Conference*, Stuttgart, Germany, 16th November, 2017.
3. Maguire, J. M., Doyle, A., Ó Brádaigh, C. M., ‘Process modelling of thick-section tidal turbine blades using low-cost fibre reinforced polymers’, *12th European Wave and Tidal Energy Conference*, Cork, Ireland, 31st August, 2017.

4. Maguire, J. M., Ó Brádaigh, C. M., Simacek, P., Advani, S. G., ‘Through thickness resin flow and heat transfer modelling of partially impregnated composite materials for thick-section parts’, *13th International Conference on Flow Processes in Composite Materials*, Kyoto, Japan, 8th July, 2016. Available at: <https://www.fose1.plymouth.ac.uk/sme/fpcm/fpcm13/FPCM13.htm>
5. Maguire, J. M., Roy, A. S., Doyle, D. A., Logan, M. G., Ó Brádaigh, C. M., ‘Resin characterisation for numerical modelling of through-thickness resin flow during OOA processing of thick-section wind or tidal turbine blades’, *20th International Conference on Composite Materials*, Copenhagen, Denmark, 23rd July 2015. Available at: <http://www.iccm-central.org/Proceedings/ICCM20proceedings/>

List of Tables

Table 1.1. Comparison of epoxy powders with conventional epoxy systems.	10
Table 1.2. Mechanical properties for straightened CF/epoxy-powder.....	12
Table 2.1. Comparison of minimum viscosities for powder coatings and VBO prepreg resin.....	32
Table 2.2. Categorisation of hygroscopic materials as per the European Pharmacopoeia method.....	36
Table 2.3. List of inter-tow and intra-tow permeabilities for biaxial textiles.....	47
Table 2.4. Coefficients for the generalised boundary condition formulation.....	52
Table 3.1. Max total enthalpy of reaction for each of the epoxy powders.....	80
Table 3.2. DSC results for conditioned and unconditioned GRN 918 epoxy powder samples.....	81
Table 4.1. Fitted cure kinetics parameters for GRN 918 epoxy powder.....	97
Table 4.2. Parameters for the DiBenedetto model.....	98
Table 4.3. Chemorheological model parameters for GRN 918 epoxy powder.....	100
Table 4.4. Parameters for powder melting model.....	101
Table 4.5. Parameters for the sintering model.....	102
Table 5.1. Thermal properties used to model heat transfer in GRN 918.....	130
Table 5.2. Properties and parameters used for glass fibre fabric.....	132
Table 5.3. Properties used for bagging and tooling materials.....	133
Table 5.4. Initial conditions used for the process simulations.....	134
Table 6.1. Initial conditions for the simulation of Test Laminate 1.....	159
Table 6.2. Initial conditions for the simulation of Test Laminate 2.....	159
Table 6.3. Initial conditions for the simulation of Test Laminate 3.....	160

Table 6.4. Material properties used for the insulation and silicone rubber heating mat.	161
Table 6.5. First approximation of cure kinetics parameters for HZH01R.	184
Table 7.1. Initial conditions used for the tapered root section simulations.....	199
Table 7.2. Material properties/parameters used for carbon-fibre (CF) fabric.....	210
Table 7.3. Ratio of anisotropy for the various laminates that were simulated.....	212
Table A.1. Total enthalpy of reaction for each DSC used in the cure kinetics modelling.	235

List of Figures

Figure 1.1. A 6.0 MW floating wind turbine with a rotor diameter of 154 m being installed in 2017 as part of the 30 MW Hywind Scotland project	2
Figure 1.2. The SeaGen 1.2 MW tidal stream generator in Strangford Lough, Northern Ireland.	3
Figure 1.3. Rendered illustration of a wind turbine blade being manufactured via VARTM.	5
Figure 1.4. (A) Illustration and scanning electron microscope (SEM) micrograph of a VBO prepreg microstructure; (B) Rendered illustration of a VBO prepreg laminate lay-up	6
Figure 1.5. The root section of a 60 m wind turbine blade made from glass-fibre/epoxy composite (approximately 80 mm thick).	7
Figure 1.6. Temperature data for the processing of a tapered wind turbine root section.....	8
Figure 1.7. 12.6 m long wind turbine blades made using epoxy powder.....	11
Figure 2.1. Schematic diagram of the powder deposition and reclamation process used in the automotive industry	18
Figure 2.2. Schematic of the towpregging apparatus developed by Edie <i>et al.</i> (1989).	20
Figure 2.3. SEM images of an epoxy powder binder that has been melted onto glass-fibre (GF) fabric	22
Figure 2.4. Results of DSC, DL-TMA, and parallel-plate rheometry for a thermoset powder.....	24
Figure 2.5. Schematic illustration of polymer powder being heated from one side. .	25
Figure 2.6. A plot of DSC data and the results of the DiBenedetto equation.	30
Figure 2.7. Parallel-plate geometry for a rotational rheometer	31

Figure 2.8. Bismaleimide samples that have been exposed to 400°C, resulting in discolouration due to surface oxidation	35
Figure 2.9. Micrographs of laminates which have been manufactured using conditioned VBO prepreg samples.	37
Figure 2.10. Polymer powder samples stored at different RH values (values are shown to the bottom-right of each sample).....	38
Figure 2.11. Model predictions for moisture desorption with varying spherical particle diameters	39
Figure 2.12. Schematic of resin flow in a VBO prepreg.....	42
Figure 2.13. Thickness change in VBO prepregs due to air evacuation (0 - 250 min) and resin impregnation of the fibre-bed	44
Figure 2.14. A comparison of the resin flow model developed by (Cender <i>et al.</i> , (2013) and their experimental data for the degree of impregnation (filled area of fabric divided by the total fabric area).	46
Figure 2.15. Micrographs of tow impregnation in VBO prepregs which were exposed to ambient conditions for different lengths of time (i.e. out-time; shown in the top left corner of each image).	46
Figure 2.16. Flowchart showing how Joshi <i>et al.</i> (1999) implemented user programs/subroutines for cure kinetics within the heat transfer analysis of a commercial finite element software.	54
Figure 2.17. The thermal lag between the centre of the laminate and its surface increases dramatically as the thickness is increased.	56
Figure 2.18. Illustration of three types of curing evolution in thick-section composite laminates	57
Figure 2.19. Simulated residual stress profiles for three GF/polyester laminates of varying thickness.....	58

Figure 2.20. Schematic of an experimental apparatus for in-situ validation of a VBO prepreg resin flow model.....	61
Figure 2.21. Rendered image of an experimental apparatus for measuring laminate thickness change under controlled pressure conditions	62
Figure 2.22. Experimental and simulated thickness data for a prepreg laminate as it is processed in a heated press.....	63
Figure 2.23. Experimental set up for validating a heat transfer and cure kinetics model.....	64
Figure 3.1. Schematic of a TGA test cell	66
Figure 3.2. Schematic of a heat-flux DSC (left) and a power-compensation DSC (right).....	68
Figure 3.3. Photo of an AR 2000 rheometer with a temperature-controlled chamber for testing polymer melts at elevated temperatures.....	69
Figure 3.4. Rendered image of the picture-frame mould and flat backing plate that were used to manufacture neat resin specimens for DMTA	72
Figure 3.5. Schematic of DMTA flexural test fixtures for a clamped specimen (dual cantilever) (left), and a simply supported specimen (right)	73
Figure 3.6. A schematic diagram of a DVS analyser.....	75
Figure 3.7. Mass change of the epoxy powders w.r.t. temperature.....	77
Figure 3.8. DSC heat flow data for two epoxy powders during temperature scan tests at 10°C/min.....	78
Figure 3.9. DSC heat flow data for two samples of GRN 918.....	79
Figure 3.10. Comparison of the viscosity profiles for GRN 918 and HZH01R during a temperature scan at 5°C/min in a parallel-plate rheometer.	82
Figure 3.11. Comparison of viscosity profiles for conditioned and unconditioned GRN 918 samples tested at 5°C/min.....	83

Figure 3.12. Comparison of crosslink densities for GRN 918 and Ampreg 22.	84
Figure 3.13. DVS of GRN 918 under isothermal conditions (23°C).	86
Figure 3.14. Mass change for GRN 918 at three different temperatures.	87
Figure 3.15. Mass change for GRN 918 at 45°C and 50°C using smaller increments of RH.	88
Figure 3.16. Mass change for flakes of sintered epoxy at 35°C.	90
Figure 4.1. Illustration of a resin sample tested with a parallel-plate geometry	95
Figure 4.2. The log of each rate constant varied linearly as a function of temperature.	97
Figure 4.3. The initial viscosity of GRN 918 epoxy powder.	99
Figure 4.4. The gel point of the epoxy was assumed to occur at the crossover in storage and loss moduli.	100
Figure 4.5. Comparison of the isothermal DoC data and cure kinetics model for GRN 918.	103
Figure 4.6. Comparison of the temperature scan data and cure kinetics model for GRN 918.	104
Figure 4.7. Cure kinetics simulation of a typical temperature cycle for processing epoxy powder composites.	105
Figure 4.8. Plot of the DSC test results showing the non-linear relationship between <i>T_g</i> and DoC.	106
Figure 4.9. Comparison of the isothermal viscosity data and the chemorheological model for GRN 918.	107
Figure 4.10. Comparison of viscosity data for a temperature scan and the chemorheological model data for GRN 918.	108
Figure 4.11. DoC and viscosity profiles (top and bottom plots, respectively) for GRN 918.	109

Figure 4.12. The “flow time” as a function of temperature for GRN 918, and minimum viscosity at each temperature.....	110
Figure 4.13. Comparison of experimental viscosity data and the chemorheological model data for the temperature cycle described in Section 4.3.1.....	111
Figure 4.14. Comparison of the experimental data for GRN 918 and the model used to describe the powder melting process	113
Figure 4.15. Results of the sintering model and experimental data for GRN 918. ..	114
Figure 5.1. (Top) A thick laminate lay-up of glass-fibre/epoxy-powder VBO prepreg plies.	118
Figure 5.2. Schematic of the flow pattern in VBO prepregs.....	119
Figure 5.3. Physical representation of the 1D resin flow model at nodal position j and time step i	121
Figure 5.4. Illustration of the segmented layers in the 1D resin flow model.	123
Figure 5.5. Schematic of the forward time, centred space scheme used for the heat transfer model.....	125
Figure 5.6. Comparison of the results from RAVEN and from the finite difference code developed in MATLAB.	136
Figure 5.7. Plot of simulated ply temperatures within a 100-ply laminate.	138
Figure 5.8. Plot of the maximum temperature difference within the laminate vs time.	139
Figure 5.9. Plot of the simulated DoC evolution within the laminate.....	140
Figure 5.10. Plot of the maximum DoC difference within the laminate for each point in time.....	141
Figure 5.11. Simulation results at approx. 23.3 hr into the temperature cycle.	142
Figure 5.12. The thickness change plot of the GF/Epoxy-powder laminate during the temperature cycle.	144

Figure 5.13. Plot of the degree of impregnation during the simulated temperature cycle.	145
Figure 5.14. Plot of the resin viscosity during the impregnation and cure stages of the temperature cycle (note the time span on the horizontal axis).....	146
Figure 6.1. Conceptual design for the experimental validation apparatus.	151
Figure 6.2. Photo of the modified heated tool and tool frame.	152
Figure 6.3. Half-section of the apparatus design, rendered in Autodesk Inventor...	153
Figure 6.4. Schematic of an AC LVDT assembly	154
Figure 6.5. Lay-up of the thick-section laminates on the heated tool	155
Figure 6.6. Rendered image showing the position of the thermocouples within Test Laminate 2.....	156
Figure 6.7. Photo of the laminate preform under vacuum pressure.	157
Figure 6.8. Photo of the apparatus (outlined in yellow) during an experiment.	158
Figure 6.9. Comparison of simulated temperatures and thermocouple data for Test Laminate 1.....	162
Figure 6.10. Comparison of the simulated thickness change and LVDT measurements for Test Laminate 1.	163
Figure 6.11. Plot of the temperature difference between the centre of Ply 60 and 150 mm towards the edge, in the x and y directions.	164
Figure 6.12. Plot of LVDT data for a reheat cycle on Test Laminate 1.....	166
Figure 6.13. Cut-section of Test Laminate 1 showing the non-uniformity of thickness.....	166
Figure 6.14. USB microscope image of the upper third of Test Laminate 1 (X1 magnification).	167
Figure 6.15. Optical microscope image of Test Laminate 1 (X5 magnification). ...	167

Figure 6.16. Thermocouple data for Test Laminate 3 compared with results of a simulation.....	168
Figure 6.17. LVDT data for Test Laminate 3 compared with simulation results.	169
Figure 6.18. A plot of thermocouple data and simulated temperatures for Test Laminate 2.....	171
Figure 6.19. A plot of LVDT data and simulated thickness change for Test Laminate 2.....	172
Figure 6.20. Plot of the in-plane temperature difference between (0,0,44) and (0,150,44) in Test Laminate 2.....	173
Figure 6.21. Cut-section of Test Laminate 2.....	174
Figure 6.22. Micrographs of Test Laminate 2 at two locations.	174
Figure 6.23. Plot of the temperature at Ply 50 for varying levels of initial powder void fraction.	176
Figure 6.24. Comparison of simulations for a consolidated (C) laminate and an unconsolidated (UC) laminate.....	177
Figure 6.25. Simulated consolidation of three 100-ply laminates manufactured using different thermal boundary conditions.	179
Figure 6.26. Comparison of the maximum temperature difference in two 100-ply laminates.....	180
Figure 6.27. Comparison of the maximum degree of cure difference in two 100-ply laminates.....	181
Figure 6.28. Simulated DoC evolution for the 100-ply laminate of UD GF/GRN 918.	182
Figure 6.29. Plot of the maximum DoC difference and the maximum temperature difference.....	183
Figure 6.30. Plot of simulated temperatures for modified laminate and temperature cycle.	185

Figure 6.31. Plot of the DoC evolution for the modified laminate and temperature cycle.....	186
Figure 6.32. Plot of maximum DoC difference and maximum temperature difference for the modified laminate and temperature cycle.....	187
Figure 7.1. The simplified ply microstructure used in UMATHT.....	195
Figure 7.2. Three types of geometry were created for analysis in Abaqus FEA	196
Figure 7.3. The 3D geometry after being meshed using hexahedral elements.	198
Figure 7.4. Comparison of the temperature distribution from a 1D simulation in Abaqus FEA and the thermocouple data for Test Laminate 3.....	200
Figure 7.5. Comparison of the laminate thickness change from a 1D simulation in Abaqus FEA and the LVDT data for Test Laminate 3.	201
Figure 7.6. Simulated temperatures for a 3D 100-ply laminate.....	202
Figure 7.7. Simulated thickness change for a 3D 100-ply laminate.	203
Figure 7.8. The influence of element size and time step size on the overall simulation run time.	204
Figure 7.9. Contour plot of the 100-ply UD GF/epoxy laminate during the drying stage (i.e. 4 hrs into the cycle).....	206
Figure 7.10. Contour plot of the 100-ply UD GF/epoxy laminate during the impregnation stage (i.e. 18.67 hr into the cycle).....	207
Figure 7.11. Contour plot of the 100-ply UD GF/epoxy laminate during the cure stage (i.e. 23 hr into the cycle)	207
Figure 7.12. The time at which each contour was plotted w.r.t. the temperature cycle.	208
Figure 7.13. Comparison of 1D and 3D temperature predictions in a 100-ply UD glass-fibre laminate.	209
Figure 7.14. Contour plot of the 100-ply CF/epoxy laminate during the cure stage (i.e. 23 hr into the cycle).	211

Figure 7.15. Comparison of 1D and 3D temperature predictions in a 100-ply UD CF laminate.	212
Figure 7.16. Simulated thickness change for the 100-ply UD CF laminate using the standard temperature cycle and the modified temperature cycle from Chapter 6, Section 6.3.6.	213
Figure 7.17. Half-section of a tapered wind turbine blade root, designed by SE Blade Technology B.V.	214
Figure 7.18. Temperature distribution along the XZ plane of a tapered root section during the cure stage of a standard temperature cycle (i.e. 23 hr into the cycle).	215
Figure 7.19. Degree of cure distribution along the XZ plane of a tapered root section during the cure stage of a standard temperature cycle (i.e. 23 hr into the cycle).	215
Figure 7.20. Comparison of temperature results for the 1D and 2D simulations. ...	216
Figure 7.21. The temperature difference and DoC difference between the outside of the section (Ply 1) and the centre (Ply 34) for the new temperature cycle.	217
Figure 7.22. The tapered blade root geometry with yellow boxes marking where the specified temperature boundary conditions were applied.	218
Figure 7.23. 2D simulation of the tapered root section with the temperature distribution represented by colour contours.	219
Figure 7.24. 2D simulation of the tapered root section with the DoC distribution represented by colour contours.	219
Figure 7.25. The temperature difference and DoC difference between the outside of the blade root (Ply 1) and the centre (Ply 34) when triaxial CF fabric was used.	220
Figure A.1. Rheometer data for a strain sweep at 70°C.	229
Figure A.2. Rheometer data for a strain sweep at 90°C.	230

Figure A.3. Rheometer data for a strain sweep at 120°C.....	230
Figure A.4. Mass change for isothermal TGA tests of GRN 918 and A-S-SET 02 epoxy powders.	231
Figure A.5. DSC heat flow for A-S-SET 02 during a temperature scan at 1.5°C/min.	232
Figure A.6. Viscosity curve for a temperature scan of A-S-SET 02 epoxy powder	233
Figure A.7. Viscosity curves for isothermal tests of A-S-SET 02 epoxy powder ...	233
Figure A.8. Images of DMTA test specimens	234
Figure A.9. Isothermal DSC heat flow data for GRN 918 at three test temperatures.	234
Figure A.10. DSC heat flow for temperature scans of GRN 918 epoxy powder at three temperature ramp rates.	235
Figure D.1. The maximum allowable time step to achieve a stable solution for a GF/Epoxy-powder ply.....	272
Figure D.2. Test of simulation accuracy for two time step sizes: 0.5 s, and 2.5 s ...	273
Figure D.3. Plot of the specific heat capacity variation during the temperature cycle.	273
Figure D.4. Plot of the density variation of the plies during the temperature cycle.	274
Figure D.5. Plot of the effective thermal conductivity variation during the temperature cycle.	274
Figure D.6. Plot of the effective thermal diffusivity variation during the temperature cycle.	275
Figure D.7. Plot of the heat flow to/from the resin during the temperature cycle. ..	275
Figure D.8. Powder melting and sintering during the drying stage.	276
Figure D.9. Simulated temperatures in a 100-ply laminate manufactured using a heated steel tool, and 200 mm insulation at the top boundary.	276

Figure D.10. Simulated temperatures in a 100-ply laminate manufactured using a heated steel tool, and a silicone rubber heating mat at the top boundary.....	277
Figure D.11. Simulated temperatures for a 100-ply laminate processed using a modified cycle.....	277
Figure D.12. Simulated DoC evolution for the modified temperature cycle.	278
Figure D.13. Maximum temperature difference and maximum DoC difference for the modified temperature cycle.....	278
Figure D.14. Comparison of the simulated temperature distribution from Abaqus FEA and the thermocouple data for Test Laminate 1.	279
Figure D.15. Comparison of the simulated laminate thickness change from Abaqus FEA and the LVDT data for Test Laminate 1.....	279
Figure D.16. Comparison of the simulated temperature distribution from Abaqus FEA and the thermocouple data for Test Laminate 2.	280
Figure D.17. Comparison of the simulated laminate thickness change from Abaqus FEA and the LVDT data for Test Laminate 2.....	280
Figure D.18. 1D simulation results for the tapered root section, taken at the thickest point in the section i.e. 67 plies thick.....	281

Nomenclature

Latin symbols [units]

a	Boundary condition coefficient
A	Fitting constant
A_{ell}	Area of an ellipse [m ²]
A_{rec}	Area of a rectangle [m ²]
A_{α}	Pre-exponential cure constant [s ⁻¹]
A_{η}	Pre-exponential viscosity constant [Pa.s]
b	Boundary condition coefficient
B	Fitting constant
c	Boundary condition coefficient
c_P	Specific heat capacity [J/kg.K]
$c_{P,c}$	Specific heat capacity of the composite [J/kg.K]
$c_{P,f}$	Specific heat capacity of the fibre [J/kg.K]
$c_{P,r}$	Specific heat capacity of the resin [J/kg.K]
C	Diffusion constant
$C_{\eta 1}$	Fitting constant for chemorheological model
$C_{\eta 2}$	Fitting constant for chemorheological model
$C_{\chi 1}$	Fitting constant for sintering model
$C_{\chi 2}$	Fitting constant for sintering model
d	Shape factor
E_s	Flexural storage modulus [Pa]
E_{α}	Cure activation energy [J/mol]

E_η	Viscosity activation energy [J/mol]
E_χ	Powder sintering activation energy [J/mol]
G'	Shear storage modulus [Pa]
G''	Shear loss modulus [Pa]
h	Heat transfer coefficient [W/m ² K]
h_{ply}	Thickness of a fully impregnated ply (cured ply thickness) [m]
h_f	Thickness of fibre layer [m]
h_{fab}	Thickness of the fabric layer [m]
h_{pow}	Thickness of the powder layer [m]
h_r	Thickness of resin layer [m]
H	Enthalpy of reaction [J/g]
H_T	Total enthalpy of reaction [J/g]
H_U	Total enthalpy of relaxation [J/g]
i	Time step for finite difference code
j	Through-thickness nodal position for finite difference code
K	Permeability [m ²]
K_1	Inter-tow permeability [m ²]
K_2 or K_{tow}	Intra-tow (or tow) permeability [m ²]
$K_{\perp hex}$	Transverse tow permeability for hexagonal fibre packing [m ²]
$K_{\perp quad}$	Transverse tow permeability for quadratic fibre packing [m ²]
k_c	Chemically-controlled cure rate constant [s ⁻¹]
k_d	Diffusion-controlled cure rate constant [s ⁻¹]
k_e	Overall effective cure rate constant [s ⁻¹]

k_m	Intensity factor [K^{-1}]
k_α	Temperature-dependent cure rate constant [s^{-1}]
k_χ	Kinetic constant for sintering [s^{-1}]
L	Thickness of sintered powder samples [m]
L_1	Characteristic length of the inter-tow porous medium [m]
L_i	Initial thickness of the powder sintering samples [m]
l	Resin flow front distance from the inlet [m]
l_{bot}	Resin flow front distance from the bottom of the fabric layer [m]
l_{top}	Resin flow front distance from the top of the fabric layer [m]
l_{tot}	Total impregnation depth [m]
m	Reaction order
m_r	Resin mass fraction
n	Reaction order
P	Pressure [Pa]
P_{app}	Applied pressure [Pa]
P_f	Pressure at the flow front [Pa]
\mathbf{q}	Heat flow vector per unit area [W/m^2]
R	Gas constant [J/mol.K]
\mathbf{R}	Transformation matrix
R_{fib}	Fibre radius [m]
$R_{j,j-1}$	Thermal resistance of material between nodes i and j [m^2K/W]
R_{tow}	Hydraulic tow radius [m]
R_f	Radial flow front position [m]

T	Temperature [°C or K]
T_g	Glass transition temperature [°C or K]
T_{g0}	Initial glass transition temperature of uncured resin [°C or K]
$T_{g\infty}$	Glass transition temperature of the fully cured resin [°C or K]
$T_{i,s}$	Surface temperature at time step i [°C or K]
T_m	Peak temperature for enthalpy of melting [°C or K]
$T_P(i)$	Programmed temperature at time step i [°C or K]
T_θ	Onset temperature for melting [°C or K]
t	Time [s]
Δt	Time step size for finite difference code [s]
t_1	Time required to fill the inter-tow porous medium [s]
u	1D flow velocity [m/s]
\bar{u}	Flow velocity vector [m/s]
V_f	Fibre volume fraction
$V_{f,tow}$	Fibre volume fraction of the fibre tow
\mathbf{x}	Spatial vector [m]
z_r	Variable resin layer thickness [m]
Δz_{avg}	Average spatial difference [m]

Greek Symbols [units]

α	Degree of cure
α_c	Temperature-dependent critical degree of cure
α_g	Degree of cure at gelation

β	Degree of impregnation
γ	Thermal diffusivity [m^2/s]
$\dot{\gamma}$	Shear rate [s^{-1}]
η	Dynamic viscosity [Pa.s]
η_{g0}	Viscosity of uncured resin at T_{g0} [Pa.s]
η_0	Temperature-dependent viscosity at zero degree of cure [Pa.s]
η_∞	Theoretical viscosity at an infinitely high temperature [Pa.s]
η^*	Complex viscosity [Pa.s]
θ	Degree of melting
Θ	Ply angle [$^\circ$]
κ	Thermal conductivity [W/m.K]
$\kappa_{c,T}$	Transverse thermal conductivity of the composite [W/m.K]
κ_f	Thermal conductivity of the fibre [W/m.K]
κ_r	Thermal conductivity of the resin [W/m.K]
$\kappa_{r,liq}$	Thermal conductivity of the liquid resin [W/m.K]
$\kappa_{r,pow}$	Thermal conductivity of the powder [W/m.K]
κ_{xx}	Thermal conductivity in the x direction [W/m.K]
κ_{yy}	Thermal conductivity in the y direction [W/m.K]
κ_{zz}	Thermal conductivity in the z direction [W/m.K]
$\mathbf{\kappa}_{UD}$	Thermal conductivity matrix for a unidirectional ply [W/m.K]
$\mathbf{\kappa}_\Theta$	Thermal conductivity matrix for an angled ply [W/m.K]
λ	Fitting constant
ν_c	Crosslink density [mol/m^3]

ρ	Density [kg/m ³]
ρ_0	Initial density of the powder [kg/m ³]
ρ_c	Composite density [kg/m ³]
ρ_f	Fibre density [kg/m ³]
ρ_P	Bulk polymer density [kg/m ³]
ρ_r	Resin density [kg/m ³]
τ	Shear stress [Pa]
φ	Total porosity/resin volume fraction
φ_1	Inter-tow porosity
φ_2 or φ_{tow}	Intra-tow porosity
φ_{fab}	Porosity of the fabric layer
χ	Powder void fraction during sintering
χ_0	Pre-exponential rate constant for sintering
χ_∞	Final powder void fraction during sintering
ω	Angular velocity [s ⁻¹]

Acronyms and Abbreviations

ATL	Automated tape laying
BC	Boundary condition
CCD	Charge-coupled device
CF	Carbon fibre
CRTM	Compression resin transfer moulding
DDA	Dicyandiamide
DEA	Dielectric analysis

DL-TMA	Dynamic load thermal mechanical analysis
DMTA	Dynamic mechanical thermal analysis
DoC	Degree of cure
DoI	Degree of impregnation
DoM	Degree of melting
DSC	Differential Scanning Calorimetry
FBE	Fusion bonded epoxy
FEA	Finite element analysis
FRP	Fibre-reinforced polymers
GF	Glass fibre
HTC	Heat transfer coefficient
LCM	Liquid composite moulding
LCoE	Levelised cost of energy
LVDT	Linear variable differential transformer
Micro-CT	(or μ -CT) X-ray microtomography
ODE	Ordinary differential equation
OoA	Out-of-autoclave
PDE	Partial differential equation
PPR	Parallel-plate rheometry
RFI	Resin film infusion
RH	Relative humidity
RTM	Resin transfer moulding
SCRIMP	Seemann's composite resin infusion moulding process
SEM	Scanning electron microscope

TGA	Thermogravimetric analysis
TMA	Thermal mechanical analysis
UD	Uni-directional
VARTM	Vacuum assisted resin transfer moulding
VBO	Vacuum-bag-only
VOC	Volatile organic compound
WLF	Williams-Landel-Ferry
1D	One-dimensional
3D	Three-dimensional

1. Introduction

1.1 Project Motivation

Since the Kyoto Protocol was initiated in 1997, national governments have become increasingly active in promoting energy reforms. The adoption of renewable energy and sustainable systems has become a global priority, with many governments subsidising the capital costs of introducing and developing new technologies. Without entering the debate on whether subsidies are sustainable, or even beneficial (Kalkuhl, Edenhofer and Lessmann, 2013; Nicolini and Tavoni, 2017), there is an onus on manufacturers and developers of renewable energy devices to reduce the levelised cost of energy (LCoE).

After decades of development, the drive towards more cost-competitive wind energy is beginning to take effect; increasing rotor diameters and developments in off-shore wind (see Figure 1.1) offer economies of scale (Hollaway, 2013a). At the same time, these advances still pose several engineering challenges for turbine blade designers and manufacturers including the introduction of hybrid glass-carbon designs, accounting for fatigue damage, and performing on-site maintenance and repair in adverse weather conditions (Hollaway, 2013b).



Figure 1.1. A 6.0 MW floating wind turbine with a rotor diameter of 154 m being installed in 2017 as part of the 30 MW Hywind Scotland project (Equinor, 2018).

It is even more challenging for burgeoning tidal turbine developers as they try to achieve commercialisation of their new technology (Flaig, 2017). Oceans and seas are harsh, corrosive environments in general, but often tidal turbines are deployed in locations which exhibit extreme conditions (see Figure 1.2). The tidal turbine blades must withstand large cyclic loading from waves and underwater turbulence, erosion from sand particles, seawater ingress, bio-fouling, and ‘50 year’ storm wave events (Harper *et al.*, 2016). Furthermore, water is approximately 800 times denser than air, which means tidal streams contain significantly more kinetic energy than the air streams experienced by wind turbines. As a result, blades are typically much shorter in length e.g. 9 m. This is challenging from a manufacturing point of view because it means that changes in the hydrofoil geometry, laminate thickness, and blade twist must all occur over a smaller span than in wind turbines.

Regardless of these challenges, pressure is being put on the tidal energy industry to bridge the 15-year gap in development to wind energy. Strategic plans have been put forth to identify the main areas of priority (The European Technology and Innovation Platform for Ocean Energy, 2016). Amongst the major technology barriers of cost and reliability, “improving materials to survive the sea environment” was outlined as one of the three main research, design & innovation categories.

The manufacturing process is key to the performance of materials for both wind and tidal turbine blades. For example, Hardis *et al.* (2013) noted that, when manufacturing thick-section spar caps, the build-up of heat can create waves (warpage) that significantly impacts the fatigue life of blades. As such, leading tidal turbine blade manufacturers, such as Aviation Enterprises Ltd. (AEL, part of Airborne International), prioritise the investigation of laminate thickness effects for the final blade design (Harper *et al.*, 2016).

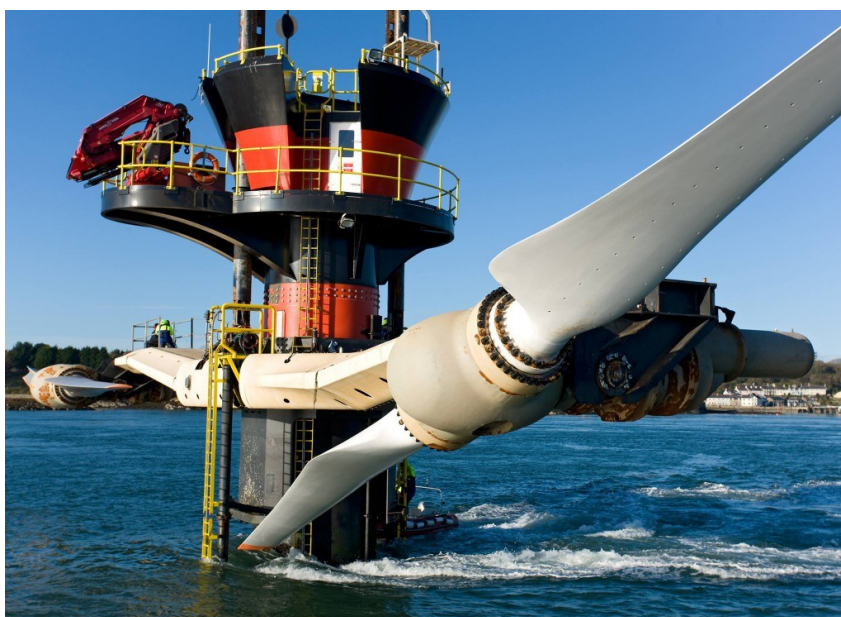


Figure 1.2. The SeaGen 1.2 MW tidal stream generator in Strangford Lough, Northern Ireland. The wake of the stationary tower indicates the speed and power of the water flow. Corrosion (rust) of the metallic nacelle is noticeable on the raised turbine (Siemens, 2012).

In summary, the primary motivation of this thesis is the need to reduce the cost of manufacturing thick-section structures for wind and tidal energy, while at the same time improving the quality and reliability of these large composite structures.

1.2 Manufacturing Methods for Large Composite Structures

Advanced composite materials have become popular for manufacturing large structures due to their high stiffness/strength to weight ratio and the need for increased energy efficiency in many transport sectors. For example, commercial aircraft such as the Boeing 787 Dreamliner contain 50% composite materials by weight, while today's wind turbines have composite blades are greater than 88.4 metres in length (Renewable Energy World, 2016).

In general, advanced composite materials are comprised of reinforcing fibres (carbon, glass, basalt, etc.) infused with a polymer matrix (thermoset or thermoplastic). The choice of fibres is driven by cost and performance; carbon fibres are significantly more expensive than glass fibres, but they offer higher specific strength and stiffness. The choice of polymer matrix is largely dictated by the ease of manufacturing: low viscosity thermosets (0.1 – 100 Pa.s) are preferred over thermoplastics (> 100 Pa.s) because they allow large components to be infused in a cost-effective manner. Within the thermoset family, epoxy systems are more commonly used for turbine blade manufacture due to their superior mechanical performance and chemical resistance compared to other cheaper thermosetting resins (i.e. polyester, vinyl ester, etc.) (Fiore and Valenza, 2013).

Many methods exist for manufacturing thermosetting composite materials, however, traditional benchmarks such as autoclave processing are limited by size and cost (Schlimbach and Ogale, 2012). Consequently, efforts are being made to develop new and existing out-of-autoclave (OoA) processes which can achieve similar quality for large structures at a reduced cost.

In the case of the marine and wind energy markets, cost is a major driver. This is reflected by the industry's initial use of hand lay-up/lamination with thermosetting resins; an inexpensive open-mould manufacturing technique (Summerscales, 2016). More recently, however, vacuum assisted resin transfer moulding (VARTM) has been widely adopted for manufacturing very large structures, such as boat hulls or blade skins (see Figure 1.3). This is due to more stringent quality controls and the general

environmental and health concerns associated with the hand lay-up process (Calabrese, Di Bella and Fiore, 2016).

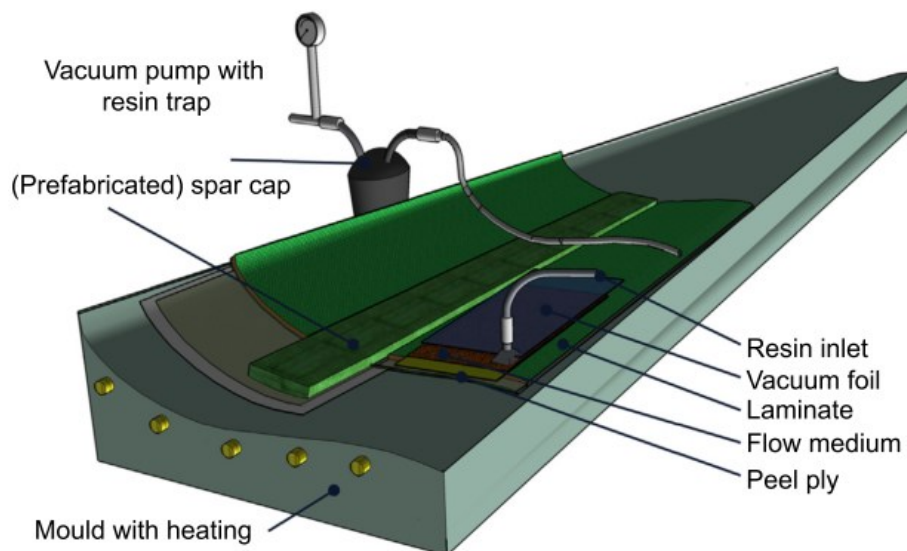


Figure 1.3. Rendered illustration of a wind turbine blade being manufactured via VARTM. A prefabricated spar cap is added to the VARTM assembly (Nijssen and de Winkel, 2016).

VARTM is a cost effective manufacturing method but requires significant expertise in designing appropriate flow strategies so that defects, such as dry spots, do not form e.g. the strategy must include locations of vacuum ports/injection gates/distribution media, timing for the opening and closing of gates and vents, etc. (Hsiao and Heider, 2012). To reduce complexity, manufacturing of these thicker sections is often carried out separately in a prefabrication process. At a later stage, the prefabricated part is introduced to the whole assembly during infusion of the skins (see Figure 1.3).

For the prefabrication of thick-section parts, OoA preregs, also known as vacuum-bag-only (VBO) preregs, are an alternative to VARTM. The development of VBO preregs has gained considerable attention in the aerospace industry due to the potential for achieving autoclave quality parts at greatly reduced costs (Centea, Grunenfelder and Nutt, 2015). These materials include partially impregnated preregs (a.k.a. ‘semi-pregs’), as shown in Figure 1.4, and fully impregnated preregs with some additional microstructure to allow for air evacuation.

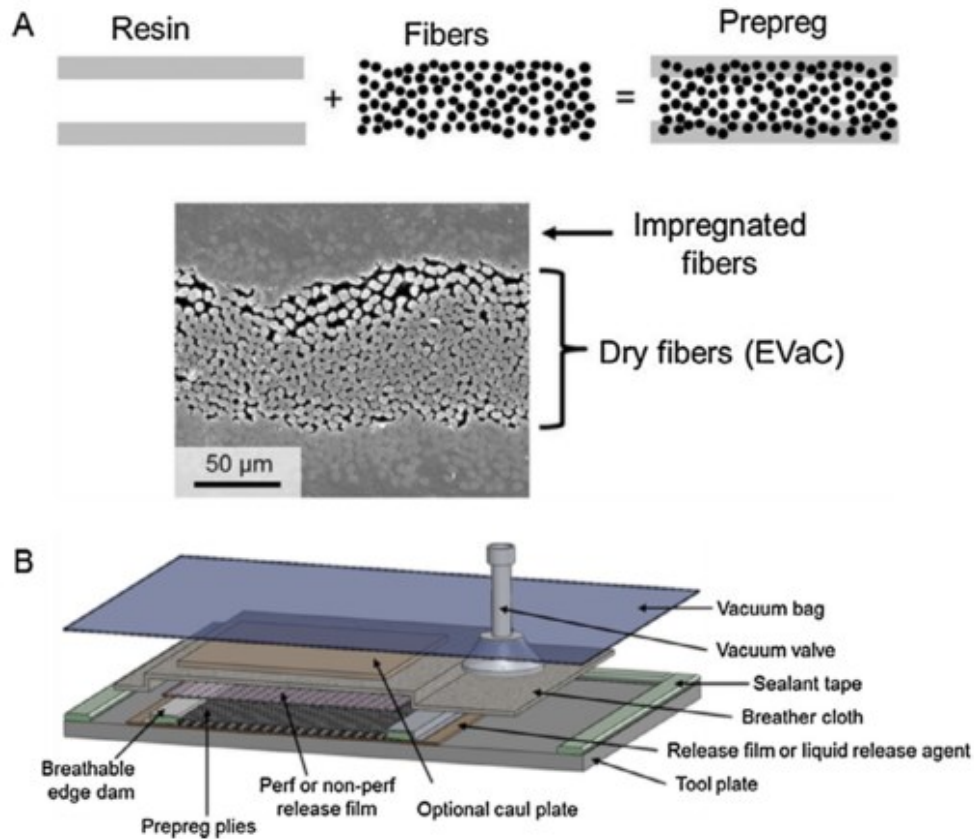


Figure 1.4. (A) Illustration and scanning electron microscope (SEM) micrograph of a VBO prepreg microstructure; (B) Rendered illustration of a VBO prepreg laminate lay-up (Centea, Grunenfelder and Nutt, 2015).

Compared to VARTM, the resin infusion process is less complex because the resin is only required to flow through-thickness into the adjacent dry fibre tows. Nevertheless, the majority of these materials have been developed by the aerospace industry and are usually expensive. A few exceptions that have been developed for the marine and wind energy sector include Gurit's SparPregTM, Hexcel's Hexply M9.6 series and M79 prepreg, and Cytec's (formerly ACG) VTM 260 series (Hollaway, 2014). These material systems are aimed at the manufacture of thick-section structures, such as the blade's spar and/or root. In the case of Hexcel's M79 system, they developed a 'low-exotherm' epoxy resin to address one of the main challenges in manufacturing thick-section structures with thermosetting resins: control of the exothermic curing reaction.

1.3 Processing Thick-section Structures

Thick composite sections are found in applications where structures experience extremely high loads. A good example is the root section of a wind turbine blade or a tidal turbine blade. In both cases, the transfer of power through the blades and into the rotor hub cause extremely high bending and twisting moments to occur in the root of the blade. To resist these loads, composite laminates up to 100 mm thick are required, as shown in Figure 1.5.

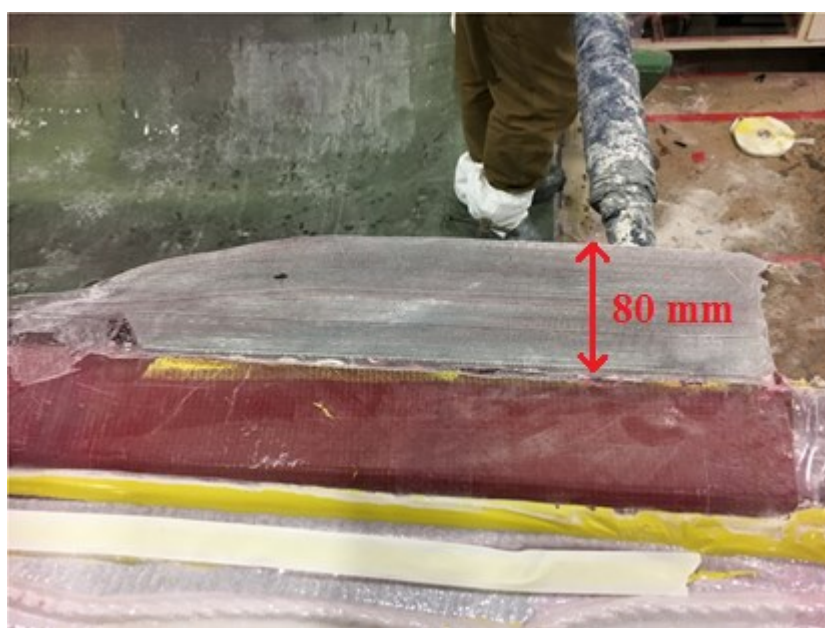


Figure 1.5. The root section of a 60 m wind turbine blade made from glass-fibre/epoxy composite (approximately 80 mm thick).

The processing of these thick-section structures with thermosetting resins is a challenge due to the exothermic heat produced by the curing reaction and the insulating properties of the materials involved i.e. polymers and reinforcing fabric. Even in the case of carbon fibres (CF), which have a relatively high longitudinal thermal conductivity (10 - 20 W/m.K for Polyacrylonitrile-based fibres), the through-thickness thermal conductivities of CF fabrics are two orders of magnitude lower (circa 0.1 - 0.2 W/m.K) (El-Hage, Hind and Robitaille, 2018). As a result, heat is slow to transfer out

of the thick laminate; this increases the temperature of the resin within, promotes further curing, and releases more heat until the reaction ceases. This auto-accelerative curing phenomena is also known as ‘thermal spiking’ or ‘thermal runaway’ (see Figure 1.6). It can cause thermal degradation of the polymer matrix and bagging materials, and/or component warpage (Bogetti and Gillespie, 1992; Wieland and Ropte, 2017). In either case, the manufacturer would incur significant financial repercussions from having to scrap components, so careful development is required.

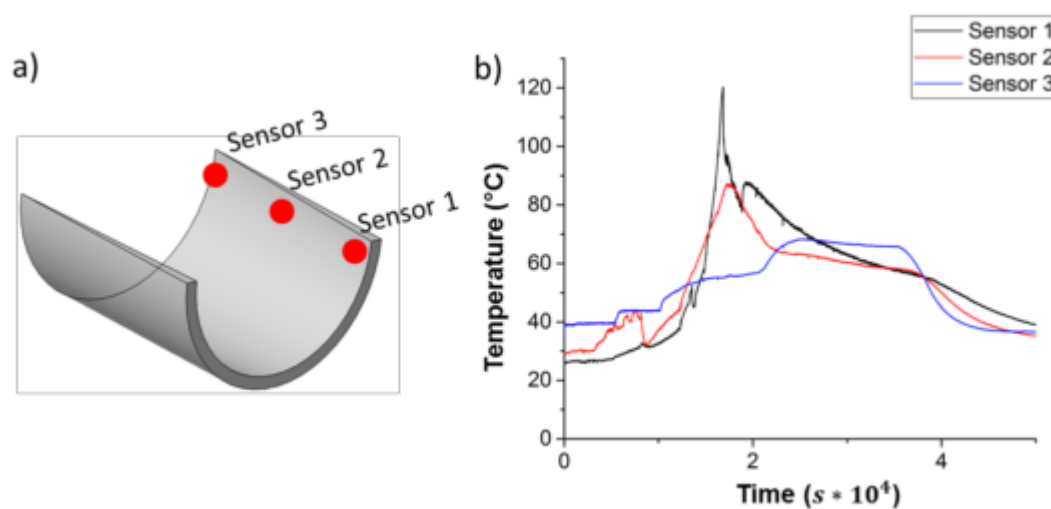


Figure 1.6. Temperature data for the processing of a tapered wind turbine root section: (a) Thermocouple locations on the top surface of the root laminate; (b) Sensor 1, at the thicker end of the root, exhibits a significant thermal spike due to the exothermic curing reaction. This effect diminishes as the part tapers down in thickness, with the temperature at sensor 3 being close to the prescribed temperature cycle temperature (Wieland and Ropte, 2017).

Purely heuristic approaches to controlling the exothermic curing reaction have been identified as being overly costly and often ineffective due to the need to use slower heating rates and extend the processing time. For this reason, significant research has gone into the modelling and simulation of this problem (Loos and Springer, 1983; Bogetti and Gillespie, 1991; Yi, Hilton and Ahmad, 1997; Shin and Hahn, 2004; Zimmermann and Van Den Broucke, 2012; Wieland and Ropte, 2017). In addition to this, numerous process optimisation schemes have been suggested for thick laminates

(Martinez, 1990; White and Kim, 1996; Ruiz and Trochu, 2006; Struzziero and Skordos, 2017).

Coupled heat transfer and cure kinetics models were the basis for most of the simulation tools developed, but the studies were often extended to include phenomena such as void growth, residual stresses, compaction due to through-thickness resin flow, etc. (discussed further in Chapter 2, Section 2.3). In most cases, the simulations and optimisations were effective in reducing thermal spiking and thermal gradients, and in some cases they helped to reduce the processing times. Nevertheless, Antonucci *et al.* (2002) alluded to there being one other variable which can be controlled in this situation; the cure chemistry of the thermosetting resin.

Low-exotherm thermosetting formulations offer a significant processing advantage in manufacturing thick-section structures, however, the literature on this subject is sparse. Hexcel is one of the few companies to release any technical publications on the development of these systems for thick-section composites. They showed that it was possible to manufacture “ultra thick” laminates using low-exotherm VBO prepregs (Radanitsch, 2014).

1.4 Thermosetting Powders

One type of resin system which has the potential to be used for low-exotherm VBO prepregs is thermosetting powder. Table 1.1 shows that the heat of curing generated by epoxy coating systems is significantly lower than that of conventional epoxy systems.

Thermosetting powders are not commonly used in industry as the primary polymer matrix for fibre-reinforced composites. In the late 1980s and early 1990s, NASA investigated the use of epoxy powders in prepreg tape (or ‘towpreg’) production for automated tape laying (ATL) (Baucom and Marchello, 1990; Bayha *et al.*, 1993). More recently, relevant applications are mostly limited to preform binders (Brody and Gillespie, 2005a, 2005b; Lionetto, Moscatello and Maffezzoli, 2016). This literature is discussed further in Chapter 2, Section 2.1.

Table 1.1. Comparison of epoxy powders with conventional epoxy systems.

Resin system type	Total enthalpy of reaction [J/g]	Source
Powder coating	78.0 – 137.7*	(Osterhold and Niggemann, 1998)
Powder coating	135.3	(Allred, Wesson and Babow, 2004)
Resin transfer moulding (RTM)	441.0 – 469.0	(Lionetto, Moscatello and Maffezzoli, 2016)
Resin film infusion (RFI)	435.4	(Garschke <i>et al.</i> , 2012)
VARTM	425.3	(Hardis <i>et al.</i> , 2013)
Prepreg	560.0	(Kenny and Opalicki, 1993)

* The range of values is due to some of the blends including non-reactive additives

Despite their relative obscurity in the composites field, thermosetting powders are a commodity product in the coating industry, which makes them a relatively low-cost material that is widely available in bulk quantities from a range of suppliers (e.g. DSM, AkzoNobel, 3M, etc.). Combined with powder deposition technologies, such as electrostatic spray (Misev and van der Linde, 1998), there is ample opportunity to create a variety of VBO prepreg materials using thermosetting powders.

1.5 Technology Background

VBO prepreps are well suited to low volume production of large parts due to ease of use and lower capital investment for equipment (Juska *et al.*, 2009; Schlimbach and Ogale, 2012). This has made them attractive to tidal turbine developers who are still at the design iteration stage (Sloan, 2012; Hollaway, 2013b).

In addition to the VBO prepreps already mentioned, ÉireComposites Teo. have developed a low-exotherm VBO prepreg system based on epoxy powder technology

from the powder coating industry. As shown in Figure 1.7, ÉireComposites Teo. were able to manufacture 12.6 m wind turbine blades using the epoxy powder semi-preg in combination with their patented integrally-heated ceramic tooling (Gardiner, 2012).



Figure 1.7. 12.6 m long wind turbine blades made using epoxy powder.

From these initial developments with the technology, it was evident that epoxy powders could provide advantages including being low-cost and generating a smaller exotherm than conventional epoxy systems. Nevertheless, it was deemed that more in-depth research was required to continue development for manufacturing longer, thicker wind turbine blades and tidal turbine blades.

ÉireComposites Teo., in collaboration with the University of Edinburgh, SE Blade Technology B.V., and several other project partners, secured European Commission funding for two research projects which investigated the epoxy powder technology further. The first project was MARINCOMP, Novel Composite Materials & Processes for Marine Renewable Energy, a Marie Curie FP7 Project funded under the IAPP call: Grant No. 612531. This was followed by POWDERBLADE, Commercialisation of Advanced Composite Material Technology: Carbon-Glass Hybrid in Powder Epoxy for Large Wind Turbine Blades, funded under Horizon 2020, Fast Track to Innovation Pilot: Project Reference 730747.

The main goal of the MARINCOMP project was “to reduce the cost and increase the reliability of offshore wind and tidal turbine blades and enable the drive toward lower cost per kilowatt renewable energy for both industries”. A preliminary investigation was carried out on the mechanical properties of epoxy powder based composites for various processing conditions (i.e. drying cycle vs. no drying cycle, increasing/decreasing cure temperature, and increasing/decreasing cure time) (Flanagan *et al.*, 2015). Transverse flexure testing of stitched uni-directional (UD) coupons showed the adverse effect of incomplete cure and incomplete drying. Mamalis *et al.*, (2018) investigated the effect of fibre straightness and fibre sizing on the mechanical properties of CF reinforced epoxy powder composites. They showed that pre-tensioning the CF improved the mechanical performance of the composite material due to increased fibre straightness, and they downselected a suitable sizing for the epoxy powder. Murray *et al.* (2018) confirmed the superior mechanical properties of pre-tensioned CF when compared to non-crimp stitched unidirectional CF fabric. Some of the mechanical properties for straightened CF/epoxy-powder are given in Table 1.2. In an attempt to automate fibre straightening, Robert *et al.* (2018) developed a towpregging system which could produce fully impregnated prepreg tape using the epoxy powder.

Table 1.2. Mechanical properties for straightened CF/epoxy-powder.

Property [units]	Value	Source
Tensile Modulus 0° [GPa]	120	(Mamalis <i>et al.</i> , 2018)
Tensile Strength 0° [MPa]	2650	(Mamalis <i>et al.</i> , 2018)
Tensile Modulus 90° [GPa]	7.1	(Murray <i>et al.</i> , 2018)
Tensile Strength 90° [MPa]	54.8	(Murray <i>et al.</i> , 2018)
Interlaminar shear strength [MPa]	77	(Mamalis <i>et al.</i> , 2018)

The main goal of the POWDERBLADE was to “bring to the market an innovative materials technology of carbon-glass fibre hybrid in powder epoxy to be commercialised initially in the production of larger wind turbine blades (60m+) at reduced cost and increased reliability/performance”. The project has largely focussed on the creation of three technical demonstrators for wind turbine blade manufacturing using the epoxy powder technology; the root section of the blade with novel bolt inserts, a carbon fibre spar, and a 6.0 m torsion box with a carbon-glass transition. Manufacturing of the root section is discussed further in Chapter 7.

1.6 Objectives

Given the aims and objectives of the project partners and collaborators, the overall aim of this thesis was to assist in the development of the epoxy powder technology in terms of material processing i.e. how best to process epoxy powder-based composites, particularly for thick-section parts.

As such, the main objectives for this thesis are:

- To experimentally characterise the key processing properties of epoxy powders and determine their suitability for manufacturing thick-section composite structures.
- To develop material models that can predict the behaviour of the epoxy powders over a range of processing conditions.
- To develop process models for manufacturing thick-section composites structures using powder-based VBO preregs.
- To implement the process models in commercial software so that manufacturing can be simulated.
- To validate the process simulations experimentally.

Preliminary investigations into the epoxy powder found that the absence of a drying cycle significantly increased the void content of the composite laminate (Flanagan *et al.*, 2015). Consequently, the secondary objectives of this thesis were the following:

- To investigate the water vapour sorption properties of epoxy powder in relation to storage conditions and drying.
- To determine if sub-optimal storage conditions had any permanent effects on cure kinetics or viscosity after being dried under vacuum.

1.7 Thesis Outline

Chapter 2 is an extensive review of the literature that is relevant to this thesis. It begins by bringing together information on polymer powder technologies from a wide range of research areas. This is followed by a review of material characterisation techniques and semi-empirical material modelling. The last section of the review goes into significant detail on resin flow modelling of VBO prepregs, heat transfer modelling of thick-section composites, and experimental validation of process models for thick-section composites.

Chapter 3 outlines the material characterisation techniques and the results for three epoxy powders. The results of the tests are discussed in relation to processing thick-section composites and they are used to identify a suitable epoxy powder for further investigation.

Chapter 4 describes the cure kinetics and chemorheological modelling of epoxy powders. The models are presented along with the fitting parameters for the chosen epoxy powder. The results of the models are compared with the experimental data to confirm their accuracy.

Chapter 5 outlines the development of a finite difference code for simulating thick-section composite manufacturing using VBO prepregs. A resin flow model for VBO prepregs is described, along with a basic through-thickness (1D) heat transfer model for composite materials. These constitutive models are coupled together with the cure kinetics and chemorheological models to form the basis of the code. The numerical computation of the code is discussed, and the results of a case study are presented.

Chapter 6 provides information on experimental validation of the process models. A full description of the apparatus is given, along with information on the signal analysis and the lay-up of the thick-section test laminates. The results for temperature and thickness change are compared with the numerical simulations to validate the models. Additional simulations are presented which investigate various processing effects.

Chapter 7 details the implementation of the process models in a commercial finite element analysis (FEA) software. A convergence study is carried out and the model is verified against experimental results. The influence of in-plane heating is investigated and simulation results for 3D geometries are presented.

Chapter 8 summarises the main findings of this thesis and presents recommendations on future work within this area of research.

2. Literature Review

2.1 Polymer Powder Technology

2.1.1 General Information on Powder Coatings

Powdered thermosets have been developed for the coating industry since the 1950s, and were widely adopted in the subsequent decades due to being a cost-effective, environmentally friendly alternative to liquid coating systems (Misev and van der Linde, 1998). Some of the major economic and environmental advantages identified by the coating industry were the ability to apply the powder without the need for solvents containing volatile organic compounds (VOCs) and the option of recovering excess powder during deposition for reuse (Conesa *et al.*, 2004). A schematic diagram of the latter process is shown in Figure 2.1.

Much of the initial research in this field was subject to intellectual property, however, in the 1990s, companies began to release more technical publications on the development of powder coating technology. Examples include DSM Resins (Misev and van der Linde, 1998), Eastman Chemical Company (Witzeman, 1996), Akzo Nobel (Gherlone, Rossini and Stula, 1998), Herberts GmbH (Osterhold and Niggemann, 1998), and Dow Chemical Company (Rouw, 1998).

Many thermoset powder coating blends were reported, using various curing agents/crosslinkers and other additives (e.g. TiO_2 , a white pigment) to achieve specific properties for different applications. Typically, the backbone of these formulations was either an epoxy resin, a polyester resin or a hybrid mixture of the two (Gherlone, Rossini and Stula, 1998).

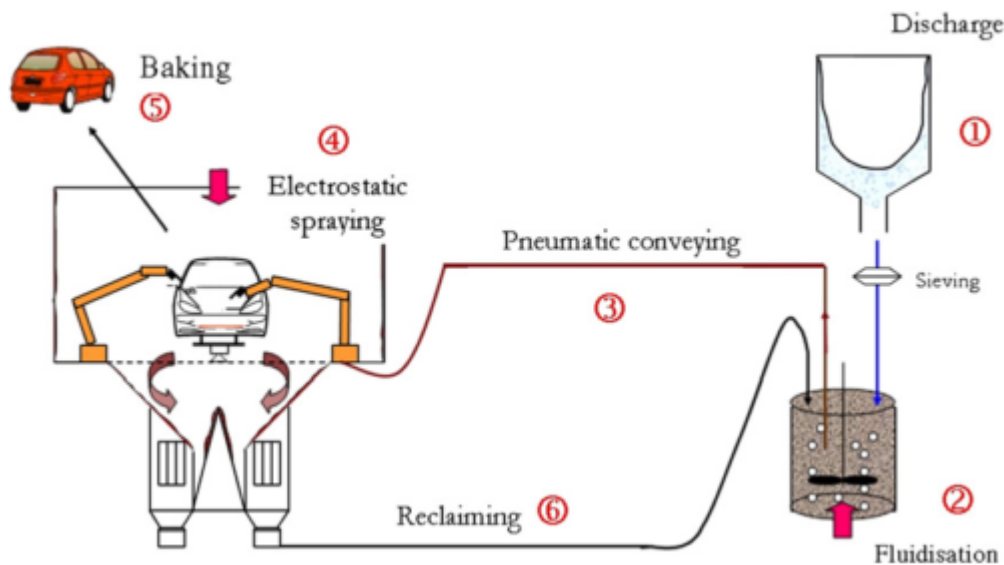


Figure 2.1. Schematic diagram of the powder deposition and reclamation process used in the automotive industry (Thomas *et al.*, 2008).

An interesting feature of many powders was the latency of their curing agents. Gherlone *et al.* (1998) showed that, for good storage stability, the powder mixture must have a glass transition temperature (T_g) above ambient conditions, however, they also showed that latency above the T_g allowed sufficient time for the powder to melt and form a uniform coat (a.k.a film levelling). This is analogous to composite processing, where latent curing agents can be used to extend the time available for infusion (Summerscales, 2016). Summerscales (2016) compiled a short list of latent curing systems which included epoxy resin and dicyandiamide (DDA); a formulation that has been used for composite structures in the aerospace and automotive industries (Sharma and Luzinov, 2011), and also commonly used for epoxy powder coatings (Osterhold and Niggemann, 1998; Parra *et al.*, 2002; Saliba *et al.*, 2015).

Relevant to the production of powder prepreg materials, Misev and van der Linde (1998) outlined a variety of deposition methods for applying powder coatings to a substrate material, including the use of fluidised beds for smaller objects and the use of spraying for larger objects. In many instances, the deposition methods were designed to electrostatically charge the powder particles, either by friction (tribo-charging) or by direct application of a charge in a corona bell, so that the powder would be attracted to the earthed substrate.

2.1.1 Powder Towpregging

The concept of using polymer powders to impregnate fibre tows has been explored since the 1970s (Price, 1973). It was of particular interest for thermoplastic composites due to the difficulty of infusing fibre tows with highly viscous thermoplastic polymers. By interspersing fine powder particles throughout a spread tow, the flow distance was minimised.

In the late 1980s and early 1990s, NASA and supporting academics conducted several investigations into powder towpregging with both thermoplastics and thermosets (Edie *et al.*, 1989; Baucom and Marchello, 1990; Bayha *et al.*, 1993; Stone and Springer, 1995). Edie *et al.* (1989) gave in-depth detail on the development of a towpregging apparatus (shown in Figure 2.2) for NASA's high-temperature thermoplastic polyimide. The apparatus pneumatically spread tensioned carbon fibre tows and passed them through a fluidised bed of polymer powder. With the powder deposited, the towpreg was preheated by a small convection oven and then fully melted by passing it between two electrically conductive rollers (i.e. electrical resistance heating). With this system, they achieved line speeds of 1.6 – 3.8 m/min, however, further development of the technology improved line speeds to 15-20 m/min (Bayha *et al.*, 1993; Stone and Springer, 1995).

Basic cost analyses were carried out to investigate the potential for scaling of the process (Baucom and Marchello, 1990) and to compare its environmental impact to other prepreg production processes such as hot melt prepregging and solution prepregging (Stone and Springer, 1995). Stone and Springer (1995) found the use of

powder to be more economical and environmentally friendly in much the same way as the coating industry did i.e. little or no VOCs and little waste disposal due to reuse of powder.

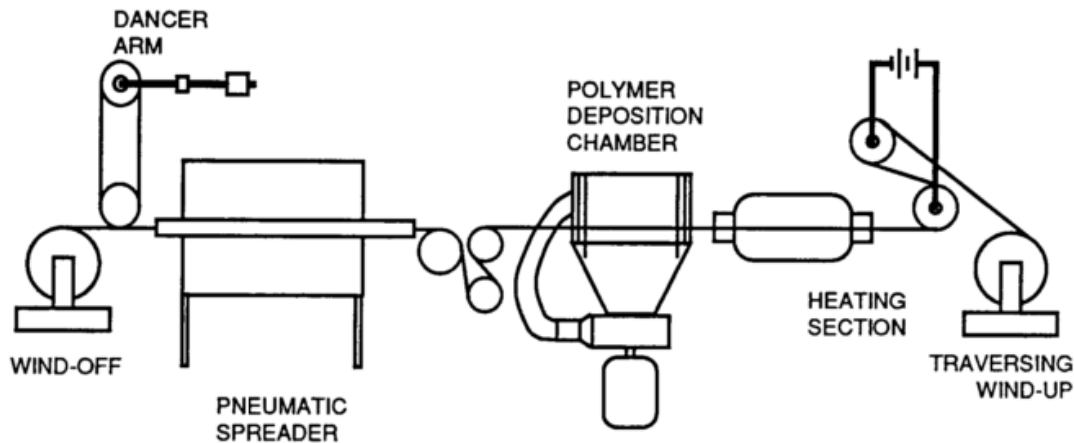


Figure 2.2. Schematic of the towpregging apparatus developed by Edie *et al.* (1989).

Over the last three decades, thermoplastic towpregging was investigated by numerous other researchers who were interested in such topics as process modelling (Woolard and Ramani, 1995; Miller, Wei and Gibson, 1996; Padaki and Drzal, 1999), and the utilisation of towpreg for pultrusion or for textile fabrication processes such as weaving, and braiding (Ramasamy, Wang and Muzzy, 1996; Novo *et al.*, 2016).

In contrast to thermoplastic towpregs, little research has been published on the development of thermosetting towpreg, particularly in cases where powder has been used to produce the towpreg. Yang *et al.* (1991) investigated three commercial epoxy powder coatings and three high temperature thermoset powders (an epoxy, a bismaleimide and a pre-imidised polyimide) for towpregging. They found that both the high-temperature epoxy and the bismaleimide performed well mechanically, despite the former having a significant void content and having been stored at ambient conditions for over 3 months prior to towpreg production. They expressed surprise at this and stated that “clearly, the ‘out-time’ for this epoxy is very good”. The term ‘out-time’ was in reference to the fact that liquid prepregs/towpregs needed to be

refrigerated to slow the cure reaction rate and that, when thawed, they had a finite time at ambient conditions before being adversely affected by cure advancement (Kim, Centea and Nutt, 2014).

The enthalpy of reaction was not reported by Yang *et al.* (1991). Nevertheless, Adherent Technologies Inc. reported the enthalpy of reaction for a low-exotherm epoxy powder (143 J/g) which they used for low-cost towpreg production (Allred, Wesson and Babow, 2004).

2.1.2 Powder Binders

In addition to coatings, polymer powders have been widely used as binders, or “tackifiers”, to produce composite preforms for infusion (via RTM, VARTM, etc). It was found that preforms could be produced by depositing a nominal amount of powder onto dry fibre mat or fabric (usually 3 – 9 weight % w.r.t. dry fabric, as shown in Figure 2.3) and then applying heat and pressure to sinter/melt the powder and form the mat or fabric. It has been shown that the binder can have a significant effect on several mechanical properties of the composite material (Tanoglu and Tugrul Seyhan, 2003; Brody and Gillespie, 2005a; Wu, Klunker, *et al.*, 2013; Daelemans *et al.*, 2015), as well as additional effects on processing properties (Brody and Gillespie, 2005b; Wu, Xie, *et al.*, 2013; Lionetto, Moscatello and Maffezzoli, 2016).

In general, it was found that the compatibility of the binder and the infusing resin system was key in tailoring the properties of the laminate. For example, Brody and Gillespie (2005a) found that a thermoset binder significantly improved the interlaminar fracture toughness of a thermoset composite laminates due to its chemical reactivity, while a thermoplastic polyester binder had a detrimental effect.

In regard to processing, the binders were found to increase the resin viscosity to the detriment of the infusion process (in addition to reducing the fabric permeability prior to dissolution) and often influenced the kinetics of the cure reaction (Brody and Gillespie, 2005b; Lionetto, Moscatello and Maffezzoli, 2016).

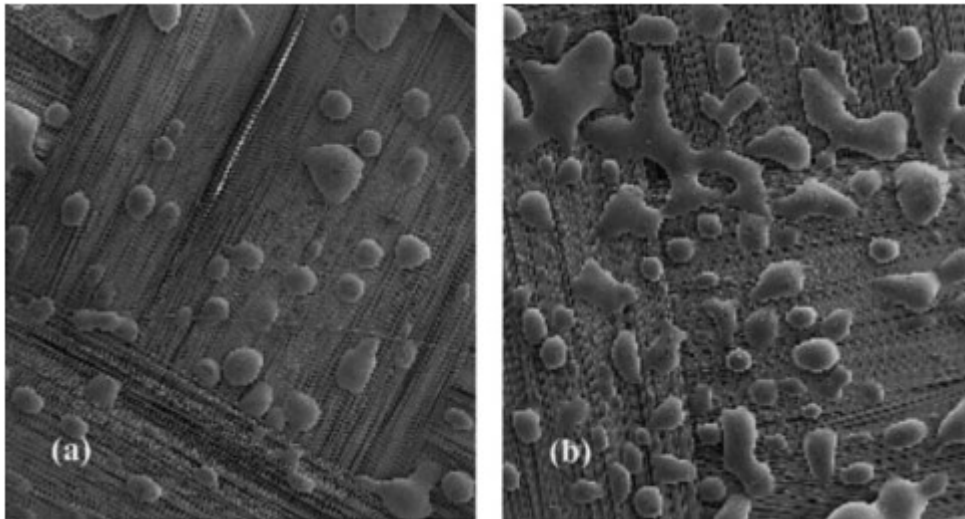


Figure 2.3. SEM images of an epoxy powder binder that has been melted onto glass-fibre (GF) fabric: (a) 3 wt% binder; (b) 9 wt% binder (Brody and Gillespie, 2005a).

One example where an epoxy powder binder was used as the sole polymer matrix was presented by Luchoo *et al.* (2010). In their work, an epoxy powder was sprayed with chopped carbon-fibre (CF) bundles through a propane burner onto a mould to form a net-shape charge for compression moulding. The epoxy powder was supplied by Hexcel and likened to a commercial toughened epoxy prepreg system. They reported the total enthalpy of reaction of the epoxy powder as being 290.4 J/g, which is relatively high compared to other reported epoxy powder systems.

2.2 Material Characterisation and Modelling

2.2.1 Characterisation of Thermosetting Powders

Since the 1990s, a significant amount of the powder coatings research was focused on experimental characterisation. Differential scanning calorimetry (DSC) was commonly used due to its ability to capture important processing behaviour over a wide range of temperatures (Gherlone, Rossini and Stula, 1998; Belder, Rutten and Perera, 2001; Ramis *et al.*, 2003; Barletta *et al.*, 2007; Saad and Serag Eldin, 2012; Saliba *et al.*, 2015). DSC can provide information on the different chemical and thermodynamic events based on measuring the heat flow to (endothermic) or from

(exothermic) a sample for a given temperature change. Gherlone *et al.* (1998) showed that it was possible to use DSC to determine the initial T_g of the powder, the total enthalpy of the curing reaction, and the cured T_g . They outlined how the powder storage stability was limited by its initial T_g , above which the powder softened to form a viscous liquid and became impossible to handle and disperse using powder deposition methods.

Belder *et al.* (2001) supplemented DSC testing with additional characterisation techniques (i.e. rheometry and a modified dynamic load thermal mechanical analysis (DL-TMA)) that probed the powder mechanically as well as thermally to gain a more robust understanding of the processing behaviour. As shown in Figure 2.4, they confirmed the transition from loose powder to a highly viscous liquid above the initial T_g , and found that elevated temperatures were required to achieve low processing viscosities.

The overlapping endothermic peak and step change in heat flow were common features of thermosetting powders, and the step change was generally attributed to the T_g of the powder as previously mentioned. The endothermic peak, however, was an indirect result of enthalpic relaxation. Enthalpic relaxation occurs in amorphous polymers (or in the amorphous region of semi-crystalline polymers) due to the polymer chains relaxing towards thermodynamic equilibrium over a period of time at near isothermal and isobaric conditions below the T_g (Aref-Azar *et al.*, 1996). This results in a loss of energy from the polymer chains. If the temperature is increased back above the T_g , the polymer chains take in heat to return to their previous energy state, resulting in the endothermic peak which is seen in the DSC data. In this way, enthalpic relaxation occurs during material storage, and the endothermic peak signals the return to a higher energy state. The enthalpic relaxation should not be misconstrued as the sintering of powder at temperatures above the T_g when the powder particles melt and the polymer begins to flow due to increased molecular mobility. This topic is discussed further in Chapter 3, Section 3.3.3.

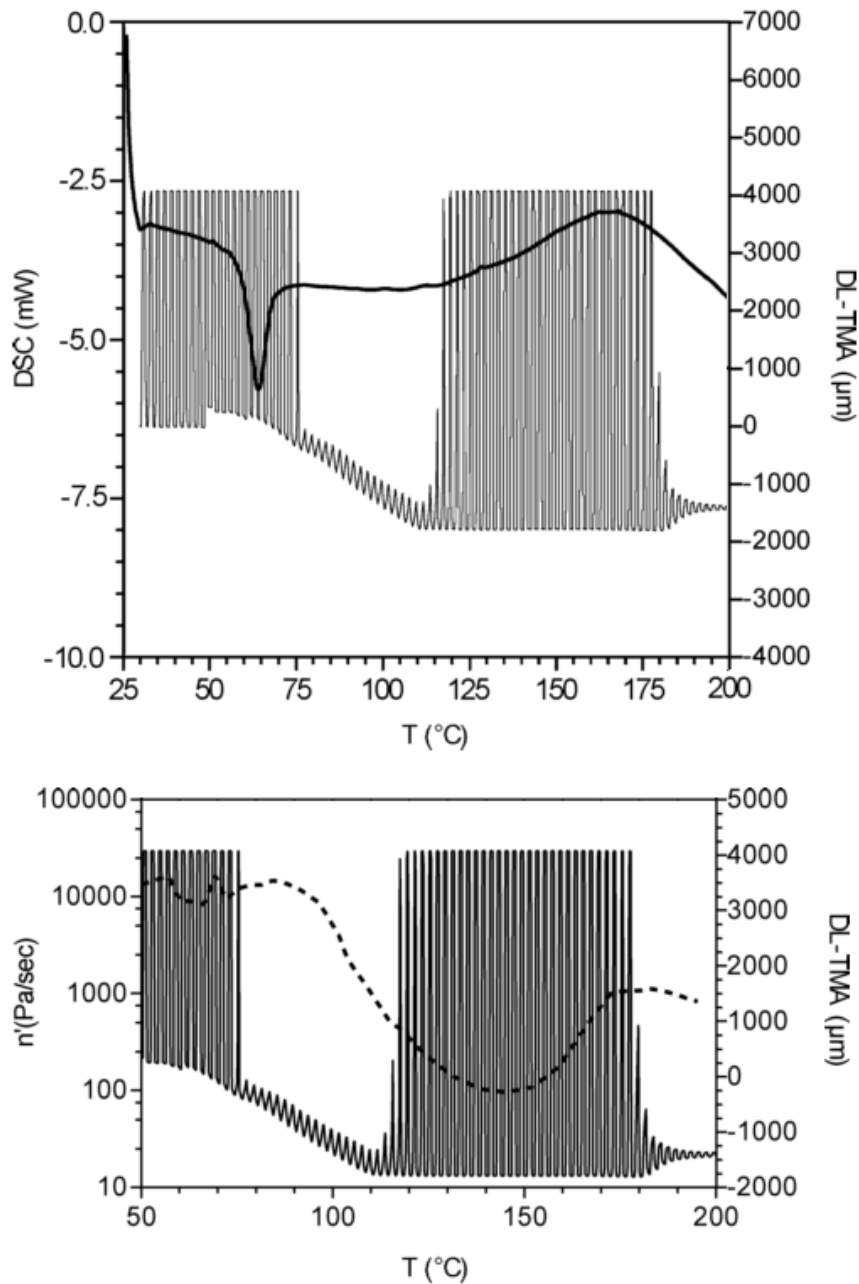


Figure 2.4. Results of DSC, DL-TMA, and parallel-plate rheometry for a thermoset powder. (Top) Powder melting is characterised by a step change in the DSC heat flow data (due to the initial T_g) and an overlapping endothermic peak (due to enthalpic relaxation). Curing of the resin generates an exothermic peak. (Bottom) The DL-TMA probe is initially free to move in the loose powder, but is restricted then as the powder sinters and becomes highly viscous. Freedom of movement is regained at higher temperatures due to a reduction in viscosity, and then diminishes again as the epoxy reaches the gel point (Belder, Rutten and Perera, 2001).

Figure 2.4 also shows the typical chemorheological behaviour of a thermosetting powder; very high viscosity just above the glass transition temperature, a reduction in viscosity due to temperature increase, and a subsequent rise in viscosity as gelation occurs. For powder coatings, rheometry was also used to investigate the relationship of viscosity and film levelling of the resin (i.e. the sintering of the resin and wetting of the substrate to form a uniform film, see Figure 2.5). This was due to the latter's importance for surface appearance and forming a uniform protective barrier. Film formation required that the epoxy powders be capable of achieving low viscosities; minimum viscosities of 5.54 – 626.0 Pa.s were reported, depending on the heating rate used (Osterhold and Niggemann, 1998; Barletta *et al.*, 2007; Wuzella *et al.*, 2014).

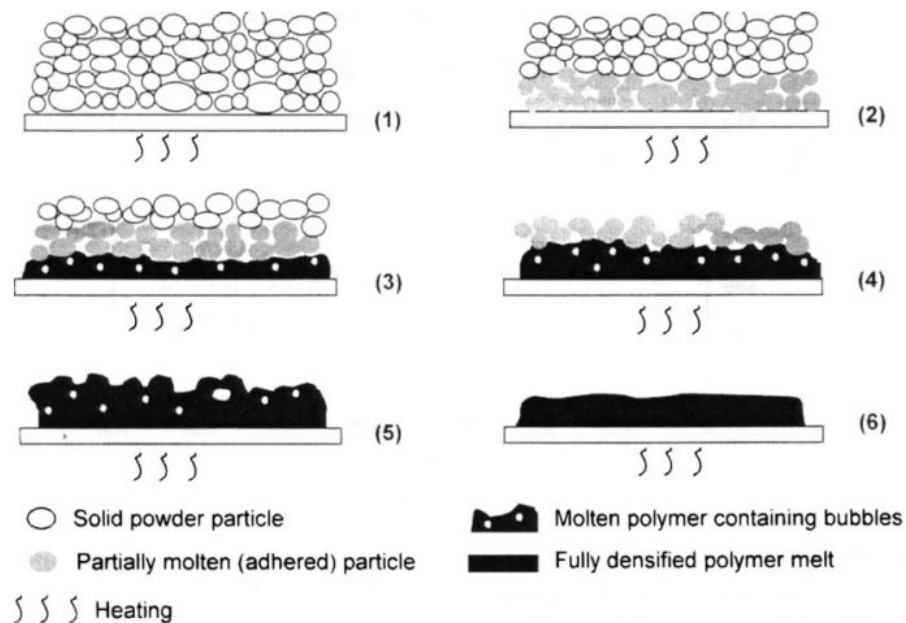


Figure 2.5. Schematic illustration of polymer powder being heated from one side. The polymer melts and then, when a low enough viscosity is achieved, it sinters together to form a fully densified polymer melt (Kontopoulou and Vlachopoulos, 2001).

Greco and Maffezzoli (2003) presented models to describe the melting and sintering of polymer powder. For a polyethylene powder, they measured the enthalpy of melting using a DSC and assumed it to be dependent on the cumulative distribution of lamellar

crystal thicknesses in the semi-crystalline polymer. As such, they fitted the data to the following S-shaped Richard's function:

$$\frac{d\theta}{dT} = k_m e^{(-k_m(T-T_m))} [1 + (d-1)e^{(-k_m(T-T_m))}]^{d/(1-d)} \quad (2.1)$$

Where θ is the degree of melting (DoM), k_m is the intensity factor [K^{-1}], T is temperature [K], T_m is the temperature at the enthalpic peak [K], and d is the shape factor. Note: throughout the thesis, units for equations are given in square brackets e.g. [units].

Equation 2.1 assumes that, at a given temperature, a specific amount of melting occurs instantaneously; however densification of the powder due to sintering is dependent on viscosity reduction and surface tension (Frenkel, 1945). Kandis and Bergman (1997) developed an Arrhenius-type semi-empirical relation to describe the kinetics of the sintering process:

$$\frac{d\chi}{dt} = -k_\chi e^{\left(-\frac{E_\chi}{R(T-T_\theta)}\right)} (\chi - \chi_\infty) \quad (2.2)$$

Where k_χ is the kinetic constant [s^{-1}], E_χ is the activation energy for the sintering process [J/mol], R is the universal gas constant [J/mol.K], T_θ is the onset temperature for melting [K], χ_∞ is the final powder void fraction, and the powder void fraction χ at any time t [s] is described by,

$$\chi = 1 - \frac{\rho_r}{\rho_p} \quad (2.3)$$

Where ρ_p is the bulk density of the polymer [kg/m^3], and the density ρ_r [kg/m^3] at any time t is determined using,

$$\rho_r = \rho_0 \frac{L_0}{L} \quad (2.4)$$

Where ρ_0 is the initial density of the powder [kg/m^3], L_0 is the initial thickness of the powder samples [m], and L is the thickness [m] at any time t .

Greco and Maffezzoli (2003) fit the sintering model (Equation 2.2) to thickness measurements from thermal mechanical analysis (TMA) and showed that it better

described the densification of the powder than the melting model (Equation 2.1). It should be noted that Greco and Maffezzoli (2003) wrote an incorrect version of Equation 2.4, with the thickness ratio inverted.

2.2.2 Curing of Thermosets

The curing process is a fundamental aspect of thermoset composite manufacturing that dictates many of the material properties of a finished composite part. It is governed by complex chemical reactions involving the polymerisation and crosslinking of molecular chains to form a rigid network. This crosslinked network binds the reinforcing fibres together to form the finished composite part. For this reason, characterisation of thermoset resins and modelling of their cure kinetics have been the subject of numerous studies.

Cure kinetics modelling may be accomplished mechanistically if the reactants and their quantities are known, however, this information is unavailable in many instances. A simpler approach is to use rate equations to form a phenomenological model for the process and then fit the model parameters to empirical data (Yousefi, Lafleur and Gauvin, 1997). Generally, the parameters for these semi-empirical models are determined using data from DSC tests.

As previously mentioned, DSC can be used to measure the enthalpy of the reaction w.r.t. temperature and time. It is assumed that the rate of change of the enthalpic heat flow, dH/dt , is proportional to the reaction rate, $d\alpha/dt$:

$$\frac{d\alpha}{dt} = \frac{1}{H_T} \frac{dH}{dt} \quad (2.5)$$

where H_T is the total enthalpy of reaction [J/g]. The degree of cure (DoC), α , is determined then by integrating Equation 2.5 with respect to time as follows:

$$\alpha = \frac{1}{H_T} \int_0^t \left(\frac{dH}{dt} \right) dt \quad (2.6)$$

The autocatalytic models developed by Kamal *et al.* (1973, 1974), given by Equations 2.7 and 2.8, have gained widespread usage for a variety of thermosetting systems,

$$\frac{d\alpha}{dt} = k_{\alpha}\alpha^m(1 - \alpha)^n \quad (2.7)$$

$$\frac{d\alpha}{dt} = (k_{\alpha 1} + k_{\alpha 2}\alpha^m)(1 - \alpha)^n \quad (2.8)$$

Where m and n are the reaction orders, and k_{α} is a cure rate constant [s^{-1}] which has a temperature dependency described by the following Arrhenius expression:

$$k_{\alpha i} = A_{\alpha i} \exp\left(\frac{-E_{\alpha i}}{RT}\right), \quad i = 1, 2 \quad (2.9)$$

Where A_{α} is the pre-exponential cure constant [s^{-1}], and E_{α} is the cure activation energy [J/mol].

Chern and Poehlein (1987) developed an improved cure rate constant, k_d , by accounting for the transition to a diffusion-controlled reaction at a critical DoC, α_c i.e. the mobility of the polymer chains in the crosslinked network is reduced to the point where further conversion is dependent on diffusion of the reactants.

$$k_d = k_c \exp[-C(\alpha - \alpha_c)] \quad (2.10)$$

Where k_c is the chemically-controlled cure rate constant [s^{-1}], C is a diffusion constant, and α_c is the critical DoC, which often has a temperature dependence due to improved molecular mobility with increasing temperatures (Garschke *et al.*, 2013).

Cole *et al.* (1991) highlighted that Equation 2.10 would lead to an abrupt transition to diffusion and suggested the following diffusion factor, $f(\alpha)$, which allowed for a more gradual transition:

$$f(\alpha) = \frac{k_e}{k_c} = \frac{1}{1 + \exp[C(\alpha - \alpha_c)]} \quad (2.11)$$

Where k_e is the overall effective cure rate constant [s^{-1}] given by:

$$\frac{1}{k_e} = \frac{1}{k_d} + \frac{1}{k_c} \quad (2.12)$$

More recently, cure kinetics models have been developed for vacuum-bag-only (VBO) prepreg resin systems based on the above equations (Kratz *et al.*, 2012; Kim, Centea

and Nutt, 2014). Kim *et al.* (2014) were able to model the effect of out-time on the cure kinetics of a VBO prepreg, however, the models required more than 20 parameters to be fitted to DSC data. As previously mentioned, the concept of out-time comes from the fact that prepreg resins typically have a T_g below ambient conditions. Once the prepreps are removed from refrigerated storage, the resin will undergo significant curing until it vitrifies. Vitrification occurs because the T_g is a function of the DoC, and as the DoC increases the T_g will approach ambient conditions.

Grunenfelder and Nutt (2012) showed that DSC could be used to determine the relationship between out-time, DoC, and T_g . They modelled the T_g and DoC as being linearly related, however, such a relationship only holds true at low DoCs. The DiBenedetto equation (DiBenedetto, 1987) is much more commonly used to describe the relationship between the T_g and DoC (Ramis *et al.*, 2003; Khoun, Centea and Hubert, 2009; Kratz *et al.*, 2012; Hardis *et al.*, 2013):

$$\frac{T_g - T_{g0}}{T_{g\infty} - T_{g0}} = \frac{\lambda\alpha}{1 - (1 - \lambda)\alpha} \quad (2.13)$$

Where T_{g0} is the initial glass transition temperature of the uncured resin [$^{\circ}\text{C}$ or K], $T_{g\infty}$ is the glass transition temperature of the fully cured resin [$^{\circ}\text{C}$ or K], and λ is a fitting constant. As can be seen in Figure 2.6, the relationship typically becomes non-linear above the gel point of the resin.

It should be noted that characterisation of curing is not solely restricted to DSC, other techniques can be used to generate useful data and inform cure models. Ramis *et al.* (2003) used dynamic mechanical thermal analysis (DMTA) and TMA, in addition to DSC, to characterise a thermoset powder coating in terms of mechanical curing and chemical curing. They used data from all three techniques to describe the cure kinetics (implementing an isoconversional analysis method) and $T_g - \text{DoC}$ relationship for the powder coating. From the compiled data they were able to construct a time-temperature-transition diagram. Others have even implemented in-situ measurement techniques such as dielectric analysis (DEA) to characterise cure (Hardis *et al.*, 2013; Kim, Centea and Nutt, 2014).

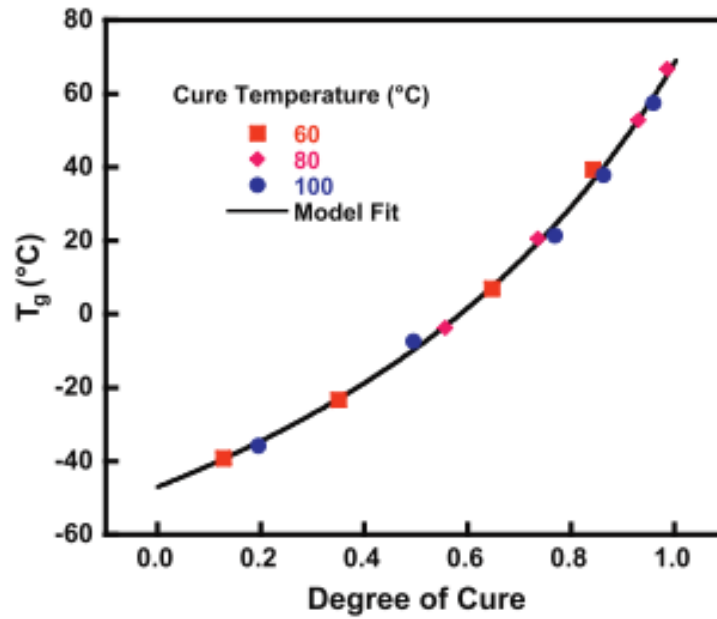


Figure 2.6. A plot of DSC data and the results of the DiBenedetto equation. It shows that the T_g -DoC relationship becomes non-linear above the gel point circa 0.6 (60% conversion)(Hardis *et al.*, 2013).

Alternative techniques also offer their own unique advantages in terms of the cure related phenomena that they can characterise. For example, DMTA has been used to quantify the crosslink density of cured resins, ν_c , based on the following simple relationship (Hill, 1997; Liu *et al.*, 2009):

$$\nu_c = \frac{E_s}{3RT} \quad (2.14)$$

Where E_s is the flexural storage modulus [Pa] at a temperature, T , measured well above the T_g [K].

DMTA has also been used to characterise the relationship of DoC, temperature, and elastic modulus development for residual stress analyses involving cure shrinkage (Kravchenko, Kravchenko and Pipes, 2016).

2.2.3 Chemorheology of Thermosets

Another fundamental process in composite manufacturing is the impregnation of the reinforcing fibre-bed. This process is largely dictated by the permeability of the reinforcement, the viscosity of the polymer matrix, and the pressure applied to drive the polymer into the fabric (see Darcy's Law in Section 2.3.1). The viscosity, η , describes the relationship of shear stress, τ [Pa], to shear strain rate, $\dot{\gamma}$ [s^{-1}], for a polymer melt (see Equation 2.15), and may vary with numerous parameters including temperature, time, and shear rate,

$$\eta = \frac{\tau}{\dot{\gamma}} \quad (2.15)$$

For thermosetting resins, or any other system that chemically reacts, the study of their viscoelastic behaviour is referred to as chemorheology (Halley and Mackay, 1996). Halley and Mackay (1996) listed out the numerous types of rheometer with which thermosets can be tested, however, rotational rheometers with a parallel-plate arrangement (shown in Figure 2.7) are the most commonly used.

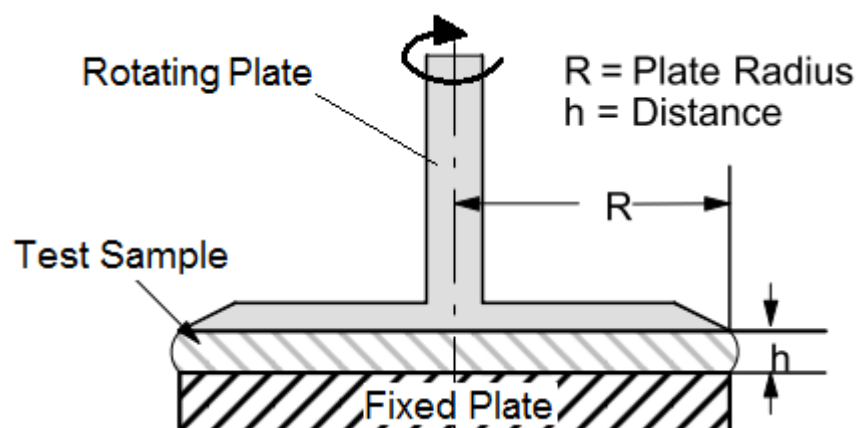


Figure 2.7. Parallel-plate geometry for a rotational rheometer (Schramm, 1994).

Parallel-plate rheometry (henceforth referred to as PPR) can be carried out in steady shear (continuous rotation of one plate) or dynamic shear (oscillation of one plate). Oscillation tests are preferred for chemorheology because they do not interfere with

the crosslinking network of the polymer during cure, and therefore gelation effects can be measured (Schramm, 1994). In this respect, the gel point of resins can be determined in several ways. One of the most common methods is to identify the gel point as being the time at which the shear storage modulus (G') and shear loss modulus (G'') intersect (Khoun, Centea and Hubert, 2009; Wuzella *et al.*, 2014; Lionetto, Moscatello and Maffezzoli, 2016). A more accurate method was developed by Winter (1987) in which the gel point was defined as being the point at which the loss tangent becomes independent of frequency.

In using the oscillation mode, Schramm (1994) noted that it is important to determine the linear viscoelastic region of a polymer before proceeding with further tests. The linear viscoelastic region of a polymer represents the stress-strain conditions under which a rheometer can measure accurate, reproducible viscosity data. It can be determined by performing a stress/strain amplitude sweep at a given frequency or, alternatively, by performing a frequency sweep at a given stress/strain amplitude.

Table 2.1. Comparison of minimum viscosities for powder coatings and VBO prepreg resin.

Resin system type	Minimum viscosity [Pa.s]*	Source
Epoxy coating	22.4 – 626.0	(Osterhold and Niggemann, 1998)
Polyester coating	32.7 – 85.0	(Belder, Rutten and Perera, 2001)
Hybrid coating	5.54 – 18.97	(Barletta <i>et al.</i> , 2007)
Epoxy coating	9.0	(Wuzella <i>et al.</i> , 2014)
VBO prepreg	1.0 – 100.0**	(Centea <i>et al.</i> , 2015)

* *The minimum viscosity is dependent on the temperature conditions (e.g. heating rate) and the resin formulation.*

** *This range of values is representative of multiple VBO resins systems.*

The minimum viscosity of different polymer systems can vary greatly. Summerscales (2016) compiled a list of dynamic viscosities which were indicative of different composite systems, ranging from thermoplastic monomer (< 0.02 Pa.s) to high performance thermoplastics such as polyether ether ketone (300 Pa.s). With respect to VBO prepreg resins, Kratz *et al.* (2012) described the resin ‘flow time’ as being the time at which the resin viscosity was below 100 Pa.s i.e. the time at which any significant fabric impregnation would occur. Based on this description, thermoset powders have been reported to achieve minimum viscosities which are suitable for VBO prepreg processing, as shown in Table 2.1.

Similar to cure kinetics modelling, numerous semi-empirical models have been developed to describe the chemorheological behaviour of thermoset resins with respect to time and temperature. The model developed by Castro and Macosko (1980) for reactive polyurethane systems is among the most popular for general use with thermosetting systems.

$$\eta = \eta_0 \exp\left(\frac{\alpha_g}{\alpha_g - \alpha}\right)^{A+B\alpha} \quad (2.16)$$

Where α_g is the DoC at gelation, A and B are fitting parameters, and η_0 is the temperature dependent viscosity [Pa.s] at zero DoC as described by the following Arrhenius expression:

$$\eta_0 = A_\eta \exp\left(\frac{E_\eta}{RT}\right) \quad (2.17)$$

Where A_η is the pre-exponential viscosity constant [Pa.s], and E_η is the viscosity activation energy [J/mol]. Given that Equation 2.16 contains a term for the DoC, it can be coupled a cure kinetics model, however, it should be noted that the model tends to infinity as α approaches α_g .

Although the author has been unable to find literature on chemorheological modelling of powder coatings, Lionetto *et al.* (2016) managed to model the effects of an epoxy powder binder on the chemorheology of a RTM-grade epoxy resin using a model developed by Kenny and Opalicki (1993) for toughened epoxies. Kenny and Opalicki

(1993) found that the Arrhenius-type temperature dependency gave a poor fit for their toughened epoxy system and instead employed a Williams-Landel-Ferry (WLF) type equation as follows:

$$\eta = \eta_{g0} \exp\left(\frac{-C_{\eta1}[T - T_g(\alpha)]}{C_{\eta2} + T - T_g(\alpha)}\right) \left(\frac{\alpha_g}{\alpha_g - \alpha}\right)^A \quad (2.18)$$

Where η_{g0} is the viscosity of the uncured resin [Pa.s] at the initial glass transition temperature, T_{g0} , and $C_{\eta1}$ and $C_{\eta2}$, and are fitting constants.

This model accounts for the change in the T_g as a function of the DoC, which can be described using Equation 2.13. As such, Equation 2.18 can also account for vitrification of the resin i.e. significant rise in viscosity due to the T_g of the resin approaching the cure temperature.

As with the Castro-Macosko model (Equation 2.16), the Kenny-Opalicki model (Equation 2.18) tends towards infinity as α approaches α_g , however, this model also tends to infinity if the temperature, T , drops sufficiently below the T_g to cancel with C_2 .

In relation to VBO prepreg resin systems, a modified version of the Castro-Macosko model (Equation 2.16) has been used to achieve relatively accurate results (Kratz *et al.*, 2012). The modification involved additional fitting parameters and the use of an extra Arrhenius term to better model the zero DoC viscosity.

2.2.4 Thermal Degradation

In addition to the resin flow and curing processes, another key aspect of manufacturing a composite structure is that it should not be exposed to high enough temperatures to cause degradation of the polymer matrix and/or fibre sizing. This can be challenging for highly exothermic reactive systems. As indicated by Hsiao and Heider (2012), the cure reaction rate increases exponentially with temperature (see Equations 2.7 - 2.9) meaning that temperatures within thick sections can severely overshoot the prescribed temperature cycle. In this sense, determining the thermal degradation characteristics

of the material can act as an upper limit for the process window (Khoun, Centea and Hubert, 2009).

Thermogravimetric analysis (TGA) has been used widely to investigate thermal degradation and the emission of gases (VOCs and/or moisture) by measuring the mass change of a sample as a function of temperature and time. The emission of vaporised moisture or solvents can occur at relatively low temperatures e.g. the boiling point of water. Saliba *et al.* (2015) noted a small mass loss (0.3 ± 0.1 %) due to the removal of adsorbed moisture from an epoxy powder coating, however, this was common for conventional epoxy systems also (Chatterjee, 2009; Grunenfelder and Nutt, 2010). The onset of significant chemical decomposition depends on the chemical structure of the polymer as varying degrees of energy are required to cause chain scission and other chemical transformations. In the case of thermosetting systems, typically this onset of chemical decomposition was reported as being in the range of 300°C to 400°C (Parra *et al.*, 2002; Chatterjee, 2009; Saliba *et al.*, 2015).

Chatterjee (2009) used additional characterisation techniques (DMTA and dielectric measurements) to demonstrate the effect of thermal degradation on the thermo-mechanical properties of three thermosetting resin systems. All three resins showed marked reductions in storage modulus and T_g for increasing exposure time at elevated temperatures, as well as severe discolouration due to surface oxidation (see Figure 2.8).

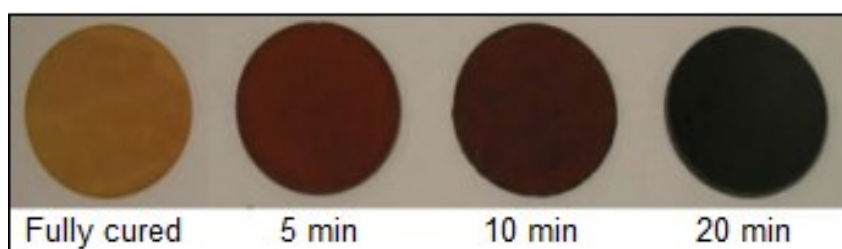


Figure 2.8. Bismaleimide samples that have been exposed to 400°C, resulting in discolouration due to surface oxidation (Chatterjee, 2009).

2.2.5 Water Vapour Sorption

Water vapour sorption involves the adsorption and desorption of air-bound moisture to and from a solid or liquid phase. Adsorption is a surface phenomenon where the gaseous molecules physically adhere or chemically bond to the surface of the solid or liquid phase, and desorption is the reverse process.

Surface area is an important aspect for adsorption, this is reflected in the use of zeolites as adsorbents; their microporous crystalline structure results in extremely high surface area and the ability to adsorb large quantities of water i.e. they are very hygroscopic (Goldsworthy, 2014). Polymers, however, are either amorphous or semi-crystalline. For amorphous polymer powders, water molecules can adsorb to the outer surface of the powder particles and then diffuse through the polymer chains to bond to the functional groups which act as adsorption sites (Toribio *et al.*, 2004). As such, many polymers exhibit hygroscopic behaviour. The amount of moisture uptake varies as a function of numerous parameters such as time, temperature, relative humidity (RH), chemical structure, etc. As shown in Table 2.2, the moisture content of the epoxies mentioned in the previous section (circa 0.3%) suggests that they can be categorised as slightly hygroscopic (Allada *et al.*, 2016).

Table 2.2. Categorisation of hygroscopic materials as per the European Pharmacopoeia method.

Category	Moisture uptake* [% w/w]
Non-hygroscopic	-
Slightly hygroscopic	0.2 – 2.0
Moderately hygroscopic	2.0 – 15.0
Very hygroscopic	> 15.0

* Weight increase due to moisture sorption at 25°C and 80% RH.


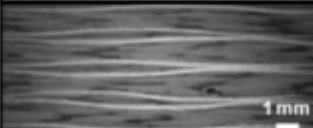
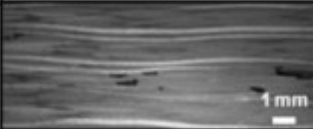
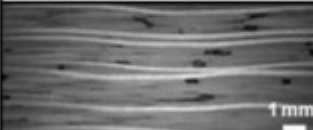
VBO Laminates		Void Content (Vol %)	Thickness (mm)
As Received		<<.1	5.08 ± .01
70% RH		.08 ± .08	5.13 ± .01
80% RH		1.00 ± .29	5.31 ± .05
90% RH		2.62 ± .48	5.48 ± .02

Figure 2.9. Micrographs of laminates which have been manufactured using conditioned VBO prepreg samples. Thresholding shows the voids in high contrast. The void content increases with RH (Grunenfelder and Nutt, 2010).

Despite the relatively small amount of moisture present in uncured epoxy systems, it can have significant effects on the processing of fibre-reinforced composite laminates. Grunenfelder and Nutt (2010) conditioned VBO prepreg samples at 35°C for three different RH values (70%, 80%, and 90%) and measured the resulting moisture contents using both TGA and Fischer titration. They found that, although autoclave pressures (e.g. 6 atm) easily suppressed void growth, the vapour pressure of entrapped moisture was sufficient to overcome the VBO pressure (i.e. 1 atm) at elevated

temperatures. Consequently, the void content of the VBO prepreg increased with moisture content, as shown in Figure 2.9.

Mohan *et al.* (2013) conditioned prepreg fabric using saturated salt solutions in order to determine the effect of storage humidity on the performance of a co-cured composite joint. They measured moisture sorption during storage of the prepreg by measuring the mass change with a microbalance and then measured desorption using TGA for a typical processing temperature cycle. They found that increasing levels of RH decreased the mixed-mode fracture toughness of the joint and decreased the T_g of the epoxy adhesive layer due to plasticisation. Sharp *et al.* (2017) also found that the T_g of the cured resin decreased with increasing moisture content in the uncured resin.

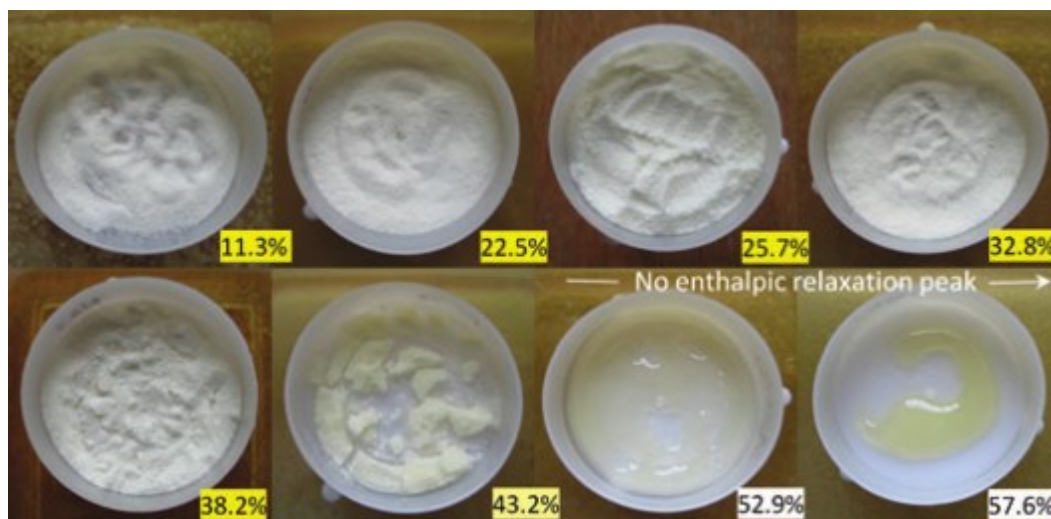


Figure 2.10. Polymer powder samples stored at different RH values (values are shown to the bottom-right of each sample). As the RH increases, the T_g approaches the storage temperature and the polymer undergoes ‘caking’ (43.2%) and then sinters (52.9%) (Yuan, Carter and Schmidt, 2011).

This relationship between the T_g and RH has an important consequence for thermoset powders; a decrease in the T_g can result in a significant change in the storage stability of the powder. It has been shown that, at temperatures close to T_g , increases in the RH caused polymer powders to ‘cake’ and then fully sinter as the T_g approached the

storage temperature; see Figure 2.10 (Yuan, Carter and Schmidt, 2011). Even in the ‘caked’ state, the powder would no longer be suitable for normal powder handling as the powder particles have already begun to melt and adhere together. Furthermore, the sintering of powder would result in entrapment of moisture.

Research has shown that an effective means of removing entrapped gases in VBO preregs is to include gas pathways in the prepreg architecture (Kratz and Hubert, 2013; Cender *et al.*, 2016), however, lengthy vacuum holds are often required depending on the air permeability of the prepreg (up to 16 hr for large parts (Centea, Grunenfelder and Nutt, 2015)). Centea *et al.* (2015) reviewed the development of VBO preregs, and while much has been done on studying their air permeability and void growth due to entrapped gases, there has been little research on the characterisation or modelling of the desorption properties of the materials.

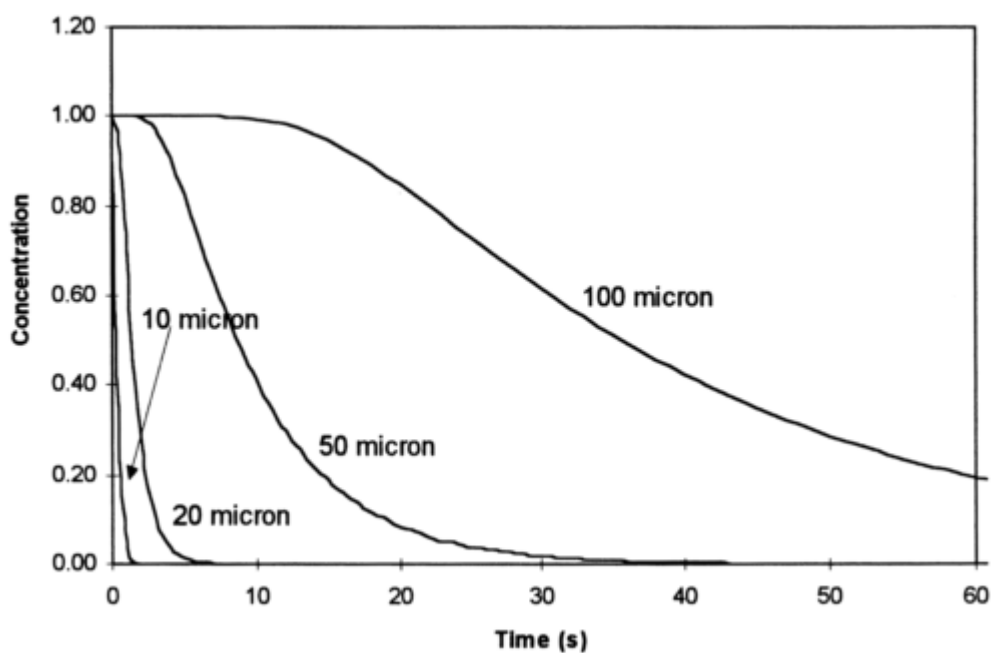


Figure 2.11. Model predictions for moisture desorption with varying spherical particle diameters (Padaki and Drzal, 1999).

Interestingly, Padaki and Drzal (1999) considered this aspect when developing powder impregnated tape and modelled the diffusion of moisture from powder particles,

showing that diffusion time increased with increasing particle size, as shown in Figure 2.11. Although they did not consider adsorption phenomena, it is likely that the higher surface area to volume ratio of smaller particles meant that moisture removal was predominantly via adsorption from the outer surface of the particles. As the particle size increased, diffusion of moisture through the bulk polymer would have become the more dominant process w.r.t time. Temperature would also play a significant role in the rate of desorption but their model did not account for this dependency.

2.3 Process Modelling and Simulation

2.3.1 Resin Flow

The modelling and simulation of flow processes in composite materials has undergone a great deal of development in the last three decades, owing largely to the advent of liquid composite moulding (LCM) processes (Advani and Hsiao, 2012). These processes typically involve using a pressure difference to drive low viscosity liquid resin into a dry fibre preform in a closed mould (e.g. RTM) or a vacuum-bagged open mould (e.g. VARTM). Due to the high risk of flow-induced defects (e.g. dry spots, entrapped air bubbles, race tracking, etc.), modelling and simulation have been effective tools for the design and optimisation of flow strategies (Sozer, Simacek and Advani, 2012). There are several commercially available software packages for simulating LCM processes, such as PAM-RTM (ESI Group), Moldex3D, and LIMS (Liquid Injection Molding Simulation, University of Delaware).

In most cases, thermoset resin flow through a fibre-bed has been modelled using Darcy's Law (i.e. flow through a porous media) as a governing equation (Darcy, 1856). The flow velocity, \bar{u} , is solved for a given pressure gradient, ∇P [Pa], within the porous media as follows:

$$\bar{u} = -\frac{K}{\eta} \cdot \nabla P \quad (2.19)$$

Where K is the permeability of the porous media [m^2], and η is the viscosity of the fluid [Pa.s].

As can be seen from Equation 2.19, flow velocity is dependent on viscosity, permeability, and the pressure gradient. Due to the proportional relationship with the pressure gradient, the flow velocity decreases as the flow distance increases. Consequently, reducing the distance that the resin must flow results in a significant reduction of the flow time. The importance of this relationship is demonstrated by the use of distribution media for infusing structures with large in-plane dimensions (e.g. wind turbine skins). The distribution media allow resin to flow rapidly over the fabric preform and then flow through the thickness of the laminate, which is typically much smaller than the in-plane dimensions.

In prepregs, resin flow can occur through-thickness also, usually as a result of high compaction pressures squeezing excess resin from the fibre-bed so that vapour bubbles can be suppressed and a higher fibre volume fraction (FVF) can be achieved. Squeeze flow models have been developed to simulate this process; the models accounted for in-plane and/or out-of-plane (i.e. through-thickness) resin flow, as well as the resultant thickness change due to compaction (Loos and Springer, 1983; Dave, Kardos and Duduković, 1987; Gutowski *et al.*, 1987; Hubert, 1996; Shin and Hahn, 2004). COMPRO (Convergent Manufacturing Technologies Inc.) is one commercial simulation software which can model this type of compaction due to resin flow (Hubert, 1996).

VBO prepregs also experience through-thickness resin flow, but on a smaller length scale; the resin is distributed onto one or both sides of reinforcement and generally flows out-of-plane into the adjacent dry fibre tows. Centea and Hubert (2012) used Darcy's Law to model the process as one-dimensional (1D) resin flow into the fibre tows, using an equivalent hydraulic radius R_t for the elliptical geometry of the tows.

$$\frac{d\beta}{dt} = -\frac{K_{tow}}{\varphi_{tow}\eta R_{tow}^2} \left(\frac{P_{app} - P_f}{(1 - \beta) \ln(1/(1 - \beta))} \right) \quad (2.20)$$

Where K_{tow} is the tow permeability [m^2], φ_{tow} is the tow porosity, P_{app} is the applied pressure [Pa], P_f was assumed to be the vacuum pressure (i.e. 0 Pa) minus the capillary pressure, and β is the degree of impregnation (DoI) described as,

$$\beta = 1 - \frac{R_f}{R_{tow}} \quad (2.21)$$

Where R_f is the radial flow front position [m].

Alternatively, the resin flow in VBO prepregs can be considered dual-scale in nature (Cender, Simacek and Advani, 2013); macroscopic flow around the fibre tows (inter-tow flow), and microscopic flow within the fibre tows (intra-tow flow), as shown in Figure 2.12. In this regard, it has been shown that the inter-tow permeability can be up to four orders of magnitude higher than the intra-tow flow (Kuentzer *et al.*, 2006; Zhou *et al.*, 2006).

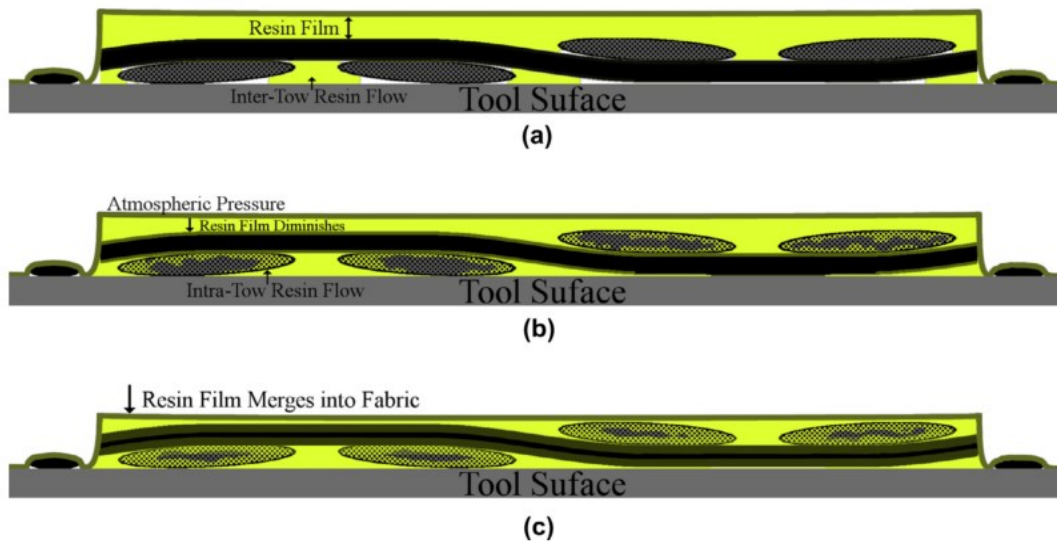


Figure 2.12. Schematic of resin flow in a VBO prepreg: (a) 1 atmosphere of pressure forces the resin film to flow into the inter-tow space of the adjacent reinforcing fabric; (b) having filled the higher permeability inter-tow space, the resin begins to fill the intra-tow spaces; (c) the resin film diminishes and the tows reach full impregnation (Cender, Simacek and Advani, 2013).

Cender *et al.* (2013) modelled the dual-scale flow phenomena as 1D resin flow through two porous media in series; assuming that the resin would fill the inter-tow region entirely before beginning to impregnate the intra-tow region due to the difference in permeabilities. They derived the following analytical solutions for inter-tow flow (Equation 2.22) and intra-tow flow (Equation 2.23) by combining Darcy's Law with

mass conservation and integrating for time and pressure boundary conditions $P|_{x=0} = P_{app}$ and $P|_{x=l} = 0$:

$$l = \sqrt{\frac{2K_1 P_{app}}{\varphi_1 \eta} t} \quad , \quad l < L_1 \quad (2.22)$$

Where l is the flow front position [m] at any time t [s], K_1 is the inter-tow permeability [m^2], φ_1 is the inter-tow porosity, and L_1 is the characteristic length of the inter-tow region [m].

$$l = L_1 - \frac{K_2 L_1}{2K_1} + \sqrt{\left(\frac{K_2 L_1}{2K_1}\right)^2 + \frac{2K_2 P_{app}}{\varphi_2 \eta} (t - t_1)} \quad , \quad l \geq L_1 \quad (2.23)$$

Where K_2 is the intra-tow permeability [m^2] (equivalent to K_{tow}), φ_2 is the intra-tow porosity, and t_1 is the time [s] at which the resin flow transitions from the inter-tow region to the intra-tow region. Note that an incorrectly derived version of Equation 2.23 was presented by Cender *et al.* (2013). As such, the derivation of the above version is given in the Appendices: B. Process Models.

While the model developed by Centea and Hubert (2012) is perhaps more accurate in modelling the porous media as an ellipse, it assumes that the initial DoI has been advanced to the point that the inter-tow region is completely filled. This is not always the case as a lower DoI can increase the air permeability of the VBO prepreg (Cender *et al.*, 2016), leading to improved gas evacuation and low porosity (Centea, Grunenfelder and Nutt, 2015).

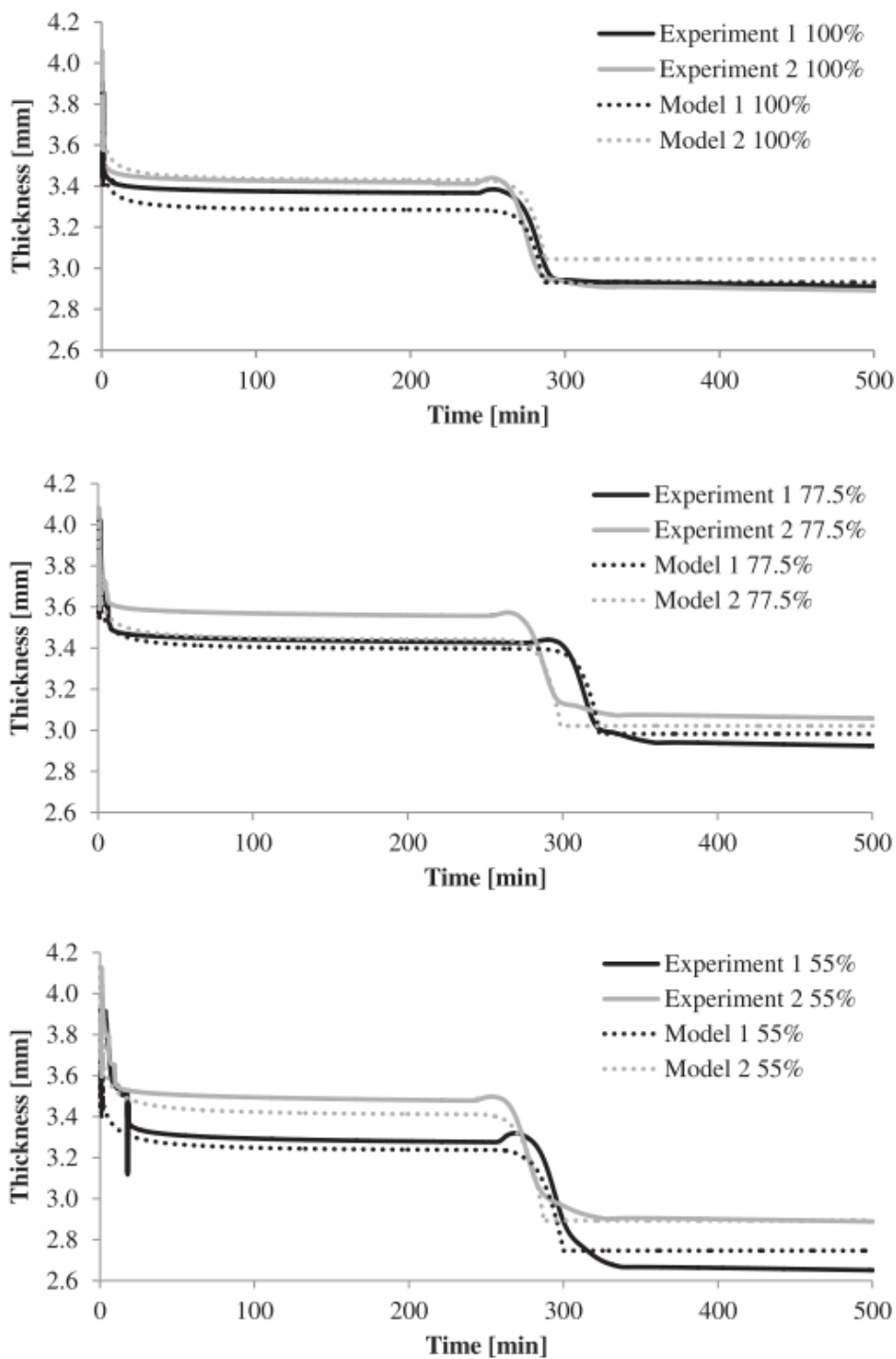


Figure 2.13. Thickness change in VBO prepreps due to air evacuation (0 - 250 min) and resin impregnation of the fibre-bed (Helmus *et al.*, 2016). The graphs are shown in order of decreasing vacuum pressure i.e. top - 100% vacuum, middle - 77.5% vacuum, bottom - 55% vacuum. The experiments show that, at high DoI, the impregnation becomes slower with deficient pressure conditions.

More recently, efforts have been made to develop a coupled air evacuation and resin impregnation model for VBO prepregs. Helmus *et al.* (2016) used an existing model for air evacuation (Arafath, Fernlund and Poursartip, 2009) to determine the evolution of the pressure gradient in the resin flow model (based on Darcy's Law). In contrast to the previous models for resin flow in VBO prepregs, Helmus *et al.* (2016) did not assume incompressibility for the fibre-bed, but instead used governing equations which were developed for thermoplastic resin flow in compressible fibre mats (Michaud and Manson, 2001). Interestingly, they showed that the laminate underwent thickness change (approx. 30% total reduction) during both air evacuation and fibre-bed impregnation, as shown in Figure 2.13. Modelling thickness change due to resin flow and the importance of laminate thickness for heat transfer is discussed further in Section 2.3.2.

One existing limitation of resin flow models for VBO prepregs is that they can overestimate the impregnation rate at high DoI. This may be as a result of deficient pressure (due to poor vacuum and/or entrapped gas) and/or fibre-resin pressure sharing i.e. pressure applied by the vacuum bag is shared by the fibre-bed as the resin film diminishes. Figure 2.13 shows that the final thickness reduction due to resin flow became more gradual as the vacuum pressure was reduced. Cender *et al.* (2013) showed similar discrepancies for > 65% impregnation using in-situ monitoring of the resin flow progression (see Figure 2.14) and attributed it to fibre-resin pressure sharing. The ex-situ micro-CT scans used by Centea and Hubert (2012) did not have the temporal resolution to capture any effects that may or may not have occurred due to deficient pressure conditions or fibre-resin pressure sharing.

As alluded to in Section 2.2, it has also been shown that the cure kinetics and viscosity of VBO resins can be greatly affected by the out-time and exposure to sub-optimal storage conditions (Kim, Centea and Nutt, 2014, 2017). These factors have significant consequences for the tow impregnation and porosity in the cured laminate (Grunenfelder and Nutt, 2010; Grunenfelder *et al.*, 2013). In particular, Grunenfelder *et al.* (2013) showed that tow impregnation was inhibited by a significant increase in resin viscosity (two orders of magnitude) for 56 days out-time as shown in Figure 2.15.

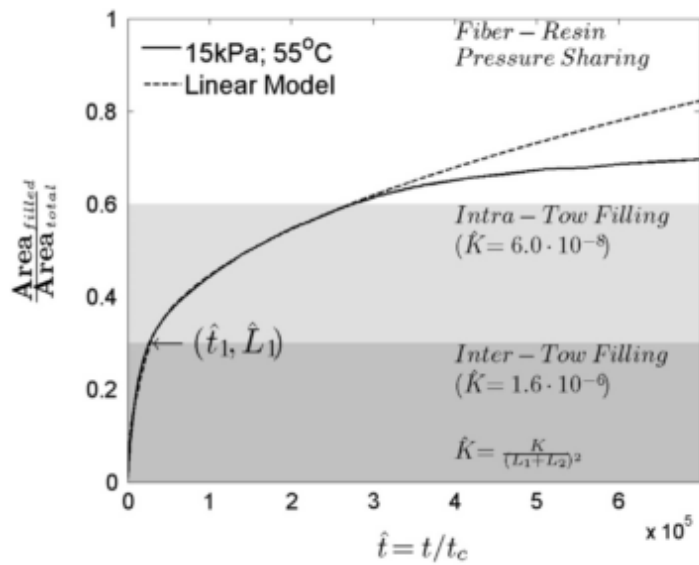


Figure 2.14. A comparison of the resin flow model developed by (Cender *et al.*, (2013) and their experimental data for the degree of impregnation (filled area of fabric divided by the total fabric area). Above 0.65 the experimental data diverges due to fibre-resin pressure sharing.

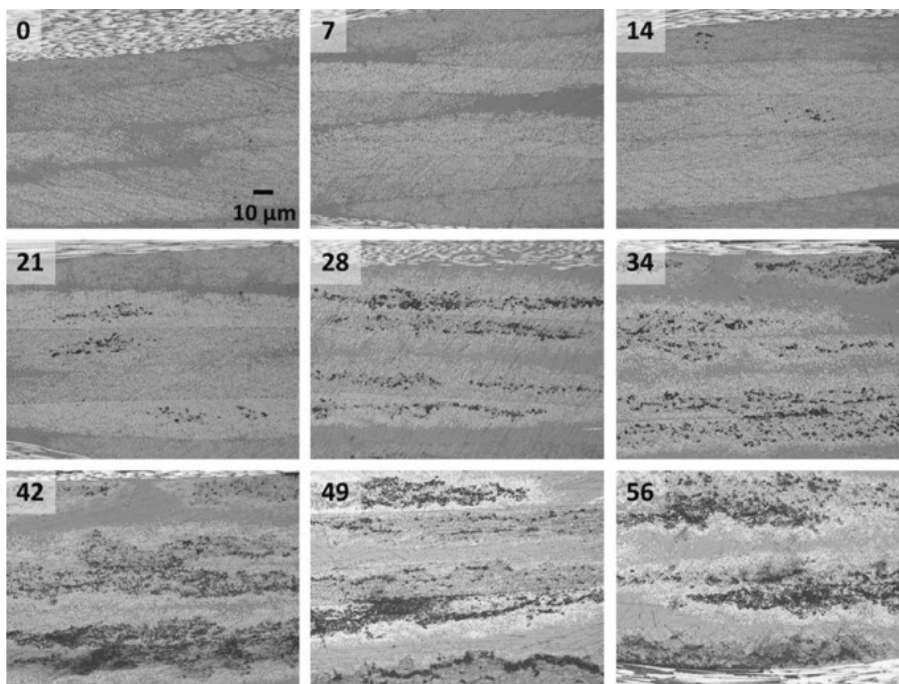


Figure 2.15. Micrographs of tow impregnation in VBO prepregs which were exposed to ambient conditions for different lengths of time (i.e. out-time; shown in the top left corner of each image).

Tow impregnation reduced with increasing out-time. (Grunenfelder *et al.* 2013).

Given the importance of the viscosity and permeability for the resin flow model, care must be taken to assign realistic values for these two properties. While chemorheology has been discussed in Section 2.2.3, characterisation of fibre reinforcement permeability is a sizable area of research in its own right, and the correct methodology is still the topic of debate (Vernet *et al.*, 2014). Separating this into inter-tow and intra-tow permeability is even more challenging; a list of experimentally determined dual-scale permeabilities from the literature has been compiled in Table 2.3.

Table 2.3. List of inter-tow and intra-tow permeabilities for biaxial textiles.

Textile type	Inter-tow permeability [m ²]	Intra-tow permeability [m ²]	Source
Woven GF*	11.65×10^{-10}	3.0×10^{-14}	(Kuentzer <i>et al.</i> , 2006)
Woven CF*	8.45×10^{-10}	1.8×10^{-14}	(Kuentzer <i>et al.</i> , 2006)
Stitched GF*	17.4×10^{-10}	12.05×10^{-14}	(Kuentzer <i>et al.</i> , 2006)
Stitched GF*	9.95×10^{-10}	2.55×10^{-14}	(Kuentzer <i>et al.</i> , 2006)
Woven GF*	11.85×10^{-10}	3.36×10^{-14}	(Zhou <i>et al.</i> , 2006)
Woven CF*	8.55×10^{-10}	2.26×10^{-14}	(Zhou <i>et al.</i> , 2006)
Stitched GF*	17.95×10^{-10}	12.8×10^{-14}	(Zhou <i>et al.</i> , 2006)
Stitched GF*	10.2×10^{-10}	2.54×10^{-14}	(Zhou <i>et al.</i> , 2006)
Woven CF**	0.25×10^{-10}	1.5×10^{-14}	(Cender <i>et al.</i> , 2013)
Woven CF**	0.15×10^{-10}	1.5×10^{-14}	(Cender <i>et al.</i> , 2013)
Woven CF***	-	2.5×10^{-15}	(Centea and Hubert, 2012)
Woven CF***	-	1.5×10^{-15}	(Centea and Hubert, 2012)
Woven CF***	-	1.5×10^{-15}	(Centea and Hubert, 2012)

* Average values of two experiments

** Values at 55 kPa

*** Values at 101.3 kPa

In all cases, the permeability values in Table 2.3 were back-calculated from experiments using flow models. It should be noted that Kuentzer *et al.* (2006) and Zhou *et al.* (2006) used two different methods to back-calculate values from the same experimental data. As can be seen, there are orders of magnitude difference in the values reported, however, it is not unusual to see such a difference in experimentally measured textile permeabilities when various methodologies are employed on slightly different material systems. Centea and Hubert (2012) supplemented their experimental approach by using analytical models to calculate the theoretical transverse tow permeability for quadratic ($K_{\perp quad}$) and hexagonal ($K_{\perp hex}$) packed tows (Gebart, 1992):

$$K_{\perp quad} = \frac{16}{9\pi\sqrt{2}} \left[\sqrt{\frac{\pi}{4V_{f,tow}}} - 1 \right]^{5/2} R_{fib}^2 \quad (2.24)$$

$$K_{\perp hex} = \frac{16}{9\pi\sqrt{6}} \left[\sqrt{\frac{\pi}{2\sqrt{3}V_{f,tow}}} - 1 \right]^{5/2} R_{fib}^2 \quad (2.25)$$

Where $V_{f,tow}$ is the fibre volume fraction of the tow, and R_{fib} is the radius of the fibre [m]. Although Gebart's models assume an ideal packing structure for the fibres within the tows, Centea and Hubert (2012) achieved relatively good agreement with the experimentally determined permeabilities. It should be noted, however, that these models are incorrectly written in (Centea and Hubert, 2012) as they have included the -1 within the square root.

In relation to the VBO prepreg resin flow models that have been discussed, it should be pointed out that all the models were used to simulate processing of thin laminates only (< 4 mm thick), with simplified assumptions made for the temperature conditions. For example, Cender *et al.* (2013) assumed isothermal conditions for their experiments and were able to solve the resin flow problem analytically, while Centea and Hubert (2012) and Helmus *et al.* (2016) input the time-temperature data directly into the model and assumed uniform temperature throughout the laminate.

For thick-section composites, a uniform temperature distribution cannot be assumed as large temperature gradients are known to develop; more of which is discussed in the next section. It should also be noted that the following section continues with further discussion of consolidation/thickness change due to resin flow, focusing more on how it is incorporated into process simulations along with heat transfer models.

2.3.2 Heat Transfer and Consolidation

As discussed in Chapter 1, Section 1.3, processing thick-section composites is difficult due to the inherent insulating properties of the fibres and polymer matrix. This challenge is compounded by using highly exothermic thermosetting resin systems which can cause “thermal runaway” of the composite part during manufacture; leading to part warpage or even decomposition of the polymer matrix and bagging materials.

For the above reasons, a considerable amount of research has been carried out on heat transfer modelling of thick-section composite parts manufactured using thermosetting resins. Several heat transfer models for thick-section composites were developed in the 1980s and early 1990s (Loos and Springer, 1983; Lee and Springer, 1990; Martinez, 1990; Bogetti and Gillespie, 1991; Twardowski, Lin and Geil, 1993), which built on previous work modelling heat transfer and exothermic reactions for neat polymer mouldings (Pusatcioglu *et al.*, 1980). In cases where the heat transfer model was coupled with a resin flow model, it was assumed that convective heat transfer due to resin flow was negligible. Instead, heat was assumed to transfer via conduction through the resin and fibres, with the curing reacting acting as an additional heat source (Loos and Springer, 1983; Twardowski, Lin and Geil, 1993; Young, 1995; Oh and Lee, 2002). As such, the heat transfer within the laminate was modelled using the well-known *heat equation* with an additional term for heat generation from the exothermic curing reaction. The *heat equation* includes both the second spatial derivative of temperature and the time derivative of temperature, making it a partial differential equation (PDE) which can be written as:

$$\rho_c c_{P,c} \frac{\partial T}{\partial t} = \kappa \nabla^2 T + (1 - V_f) \rho_r H_T \frac{\partial \alpha}{\partial t} \quad (2.26)$$

Where ρ_c is the composite density [kg/m^3], $c_{P,c}$ is the specific heat capacity of the composite [J/kg.K], T is temperature [K], κ is anisotropic thermal conductivity [W/m.K], V_f is the fibre volume fraction, ρ_r is the resin density [kg/m^3], H_T is the total enthalpy of the curing reaction [J/g], and α is the DoC.

The assumption of negligible convective heat transfer due to resin flow was later justified for resin film infusion by Loos and MacRae (1996). This was confirmed also for autoclaved prepregs by Costa and Sousa (2003) who used the *convection-diffusion equation* for the problem and found that the diffusion term was sufficiently dominant to neglect convection.

A rule of mixtures approach was implemented by several authors for describing the composite density and specific heat capacity in Equation 2.26 (Loos and Springer, 1983; Martinez, 1990; Joshi, Liu and Lam, 1999; Ruiz and Trochu, 2005; Zimmermann and Van Den Broucke, 2012; Wieland and Ropte, 2017):

$$\rho_c = \rho_f V_f + \rho_r (1 - V_f) \quad (2.27)$$

$$c_{P,c} = \frac{c_{P,f} \rho_f V_f + c_{P,r} \rho_r (1 - V_f)}{\rho_f V_f + \rho_r (1 - V_f)} \quad (2.28)$$

Where subscripts f and r denote fibre and resin, respectively.

With the assumption that the thermal conductivity of a composite lamina was transversely isotropic, the following model (Springer and Tsai, 1967) was widely applied for describing the through-thickness thermal conductivity $\kappa_{c,T}$ (Loos and Springer, 1983; Martinez, 1990; Twardowski, Lin and Geil, 1993; Young, 1995; Oh and Lee, 2002; Costa and Sousa, 2003; Sorrentino, Polini and Bellini, 2014):

$$\frac{\kappa_{c,T}}{\kappa_r} = \left(1 - 2 \sqrt{\frac{V_f}{\pi}} \right) + \frac{1}{D} \left[\pi - \frac{4}{\sqrt{1 - (D^2 V_f / \pi)}} \tan^{-1} \frac{\sqrt{1 - (D^2 V_f / \pi)}}{1 + D \sqrt{V_f / \pi}} \right] \quad (2.29)$$

Where κ_r is the thermal conductivity of the resin [W/m.K], and the parameter D is described by,

$$D = 2 \left(\frac{\kappa_r}{\kappa_f} - 1 \right) \quad (2.30)$$

Where κ_f was the thermal conductivity of the fibre [W/m.K]. Note that Equation 2.29 is a corrected version presented by Twardowski *et al.* (1993).

Early development of thick-section process simulations focused on 1D heat transfer assuming that for sufficiently large in-plane dimensions, through-thickness heat transfer would dominate (Loos and Springer, 1983; Martinez, 1990; Twardowski, Lin and Geil, 1993; Young, 1995). Typically, these studies assumed that the temperature and cure dependency of the resin and fibre properties were negligible. Moreover, Twardowski *et al.* (1993) attempted to show that such dependencies had little effect on the overall temperature predictions for thick-section laminates. Much of the early research also neglected modelling detailed boundary conditions (BCs) e.g. conduction through the tool and bagging, forced convection, radiation, etc. Instead, a specified temperature BC was commonly used at the laminate surface (Loos and Springer, 1983; Lee and Springer, 1990; Martinez, 1990; Twardowski, Lin and Geil, 1993). For initialising the heat transfer model, most of these studies assumed a uniform temperature and DoC (α) throughout the thick laminate; generally, it was assumed that initially $\alpha = 0$.

Later studies developed 2D and 3D models to investigate in-plane heating and more complex geometries, such as right angle bends and tapered sections, (Bogetti and Gillespie, 1991; Yi, Hilton and Ahmad, 1997; Joshi, Liu and Lam, 1999; Oh and Lee, 2002; Costa and Sousa, 2003; Yan, 2008; Wieland and Ropte, 2017). Bogetti and Gillespie (1991) implemented a generalised temperature BC formulation which was used to prescribe either insulated, specified temperature, or convective BCs.

$$a \frac{\partial T_s}{\partial \hat{n}} + bT_s + cT(t) = 0 \quad (2.31)$$

Where T_s is the surface boundary temperature [K], \hat{n} is the outward unit normal to the domain surface, $T(t)$ is the programmed temperature [K] (e.g. autoclave temperature), and a , b , and c are the coefficients which define the prescribed BC (given in Table

2.4). This generalised formulation was implemented, subsequently, by other authors also (Young, 1994; Yi, Hilton and Ahmad, 1997). Additionally, authors of later studies used cure/temperature-dependent properties in their simulations and achieved good accuracy when compared to experimental data (Shin and Hahn, 2004; Ruiz and Trochu, 2005).

Table 2.4. Coefficients for the generalised boundary condition formulation.

Boundary condition type	a	b	c
Specified temperature	0	1	-1
Insulated	1	0	0
Convective*	1	$(h/k)_{eff}$	$-(h/k)_{eff}$

* $(h/k)_{eff}$ is the effective heat transfer coefficient (HTC) which quantifies the heat flow to/from the part surface.

In regard to solving the heat transfer equation, for simplified cases, some analytical solutions were developed to describe the temperature distribution in thick-section composites, and the critical laminate thickness which could be safely processed using a given resin system (Shi, 2016). In most cases, however, a numerical approach was required to solve the heat transfer models due to the highly transient nature of manufacturing thick-section composites.

In the literature, finite difference methods were most commonly used by the early developers to discretise and solve the *heat equation* (Equation 2.26) (Loos and Springer, 1983; Martinez, 1990; Bogetti and Gillespie, 1991, 1992; Twardowski, Lin and Geil, 1993). These finite difference methods approximated the thermal gradient term using a central space scheme or similar scheme,

$$\frac{\partial^2 T}{\partial z^2} \approx \frac{T_{j-1} - 2T_j + T_{j+1}}{\Delta z^2} \quad (2.32)$$

Where z is the spatial increment in the through-thickness direction [m], and the subscript j denotes the nodal position.

This simplification of the thermal gradient term allowed Equation 2.26 to be solved as a system of ordinary differential equations (ODEs). Numerous numerical methods have been developed for solving ODEs and PDEs (Kreyszig, Kreyszig and Norminton, 2011); Twardowski *et al.* (1993) employed the above approximation and solved their heat transfer model using a fourth order Runge-Kutta method, while others used the Crank-Nicolson method due to its stability for solving Equation 2.26 (Martinez, 1990; Shin and Hahn, 2004).

Later work began to focus more closely on implementing finite element schemes to numerically solve the process models. Yi *et al.* (1997) developed a 3D finite element model where the *heat equation* (Equation 2.26) was rewritten over an element of volume v , in Cartesian coordinates, as,

$$\int_v \rho_c c_{p,c} \frac{\partial T(\mathbf{x}, t)}{\partial t} dv = \int_v \left[-\text{div } \mathbf{q} + \rho_c H_T \frac{\partial \alpha(T, t)}{\partial t} \right] dv \quad (2.33)$$

Where \mathbf{x} is the spatial vector [m], and \mathbf{q} is the heat flow vector per unit area [W/m^2] due to conduction;

$$\mathbf{q} = -\boldsymbol{\kappa} \nabla T \quad (2.34)$$

$$\boldsymbol{\kappa}(T, \alpha) = \begin{bmatrix} \kappa_{xx} & \kappa_{xy} & \kappa_{xz} \\ \kappa_{yx} & \kappa_{yy} & \kappa_{yz} \\ \kappa_{zx} & \kappa_{zy} & \kappa_{zz} \end{bmatrix} \quad (2.35)$$

Using these equations, along with the initial condition of uniform temperature distribution at $t = 0$ and the generalised boundary condition formula developed by Bogetti and Gillespie (1991), they derived finite element equations for the problem. Furthermore, they could express temperature dependencies within the elements by using shape functions to interpolate. Having discretised the finite element equations w.r.t time, they implemented an iterative Newton-Raphson method to solve the temperature increment implicitly for each time step and a fourth order Runge-Kutta scheme to solve the cure kinetics equations. Park *et al.* (2003) developed a similar 3D finite element program in FORTRAN, but used the trapezoidal rule to solve the finite

element equations. In both cases, the authors found that the solution converged for a time step size of 0.5 - 0.6 seconds, which was relatively small given that the temperature cycles require several hours to complete.

As commercial finite element software became more advanced, some authors identified the potential for performing composite processing simulations in a more efficient and effective manner than trying to develop their own finite element codes.

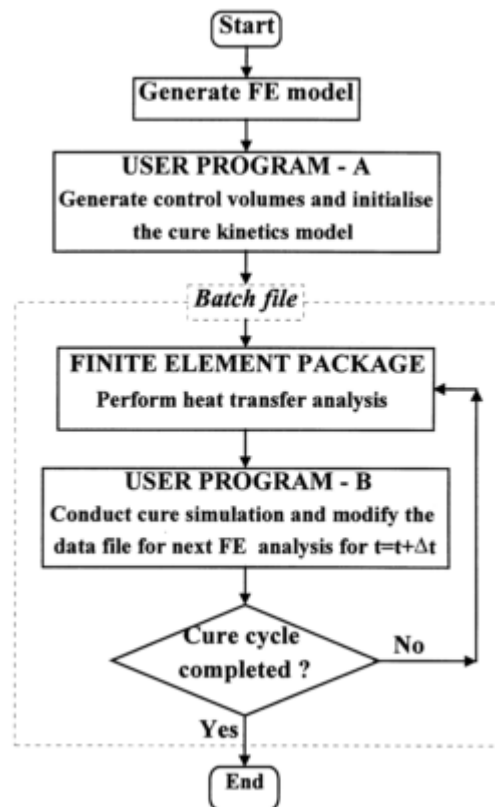


Figure 2.16. Flowchart showing how Joshi *et al.* (1999) implemented user programs/subroutines for cure kinetics within the heat transfer analysis of a commercial finite element software.

Joshi *et al.* (1999) developed user programs/subroutines which could introduce cure kinetics as a heat source term within the transient heat transfer analysis of a finite element software called LUSAS (see the flowchart in Figure 2.16). This allowed them to simulate the processing of three geometries in an autoclave using a time step size of 30 seconds. The geometries included a 23 mm thick flat laminate in 1D and 3D, a honeycomb sandwich panel in 1D, and an I-beam in 2D. Similarly, Oh and Lee (2002)

used ANSYS® to perform 3D heat transfer simulations of a 20 mm thick GF/epoxy laminate processed in an autoclave (again, with 30 second time steps). Similar to Yi *et al.* (1997), they implemented a fourth order Runge-Kutta scheme to compute the cure kinetics. Furthermore, they were able to compute a resin flow model (based on the model developed by Gutowski *et al.* (1987)) as a nonlinear transient heat transfer analysis within ANSYS® due to the forms of the equation being the same. As a result, they could determine the resin pressures and thickness change during consolidation. Lastly, they used an in-built optimisation capability in ANSYS® to generate a temperature cycle which reduced both the thermal overshoot and the cycle time.

Commercial software packages were used by several other authors also: Zimmermann and Van Den Broucke (2012) used MSC Marc/Mentat to perform a thermomechanical finite element analysis of 80 mm thick composite sections infused with RTM 6 resin; Sorrentino *et al.* (2014) used PAM-RTM to simulate heat transfer and cure kinetics in a 20 mm thick laminate made from prepreg; Shi (2016) used the heat transfer module of COMSOL Multiphysics along with MATLAB to perform 3D curing simulations of a 40 mm thick section.

While most available literature was focused on autoclave prepregs, Kratz *et al.* (2012) published one of the few papers involving the manufacture of thick laminates (12 mm and 20 mm) using VBO prepregs. They used a 1D simulation software, called RAVEN, to perform a coupled heat transfer and cure kinetics analysis of two CF/Epoxy VBO prepregs. The simulations were used to validate cure kinetics models that they had developed, but did not account for consolidation (i.e. thickness change) due to resin flow, which seemed to introduce some error into the analysis.

In general, process simulations for thick-section composites varied in terms of whether or not they accounted for consolidation of the laminate. While Loos and Springer (1983) modelled squeeze flow in thick prepreg laminates, they did not explicitly investigate the effects of consolidation on heat transfer. Bogetti and Gillespie (1991) opted not to model consolidation, due to the added complexity of modelling in 2D, however, they acknowledged that thickness effects would strongly influence the processing of thick sections. With simulations, they demonstrated that increasing

laminates created a thermal lag between the prescribed temperature cycle and the centre of the laminate. Building on this, Twardowski *et al.* (1993) implemented approximations for consolidation (based on either uniform linear or exponential change in FVF over a set period of time) and found that it had a significant effect on heat transfer in the laminate during processing. They also demonstrated the worsening thermal mismatch between the prescribed temperature cycle and the centre of the laminate as the thickness increased (see Figure 2.17). This trend was corroborated by Shi (2016) via analytical models, numerical simulations, and experiments.

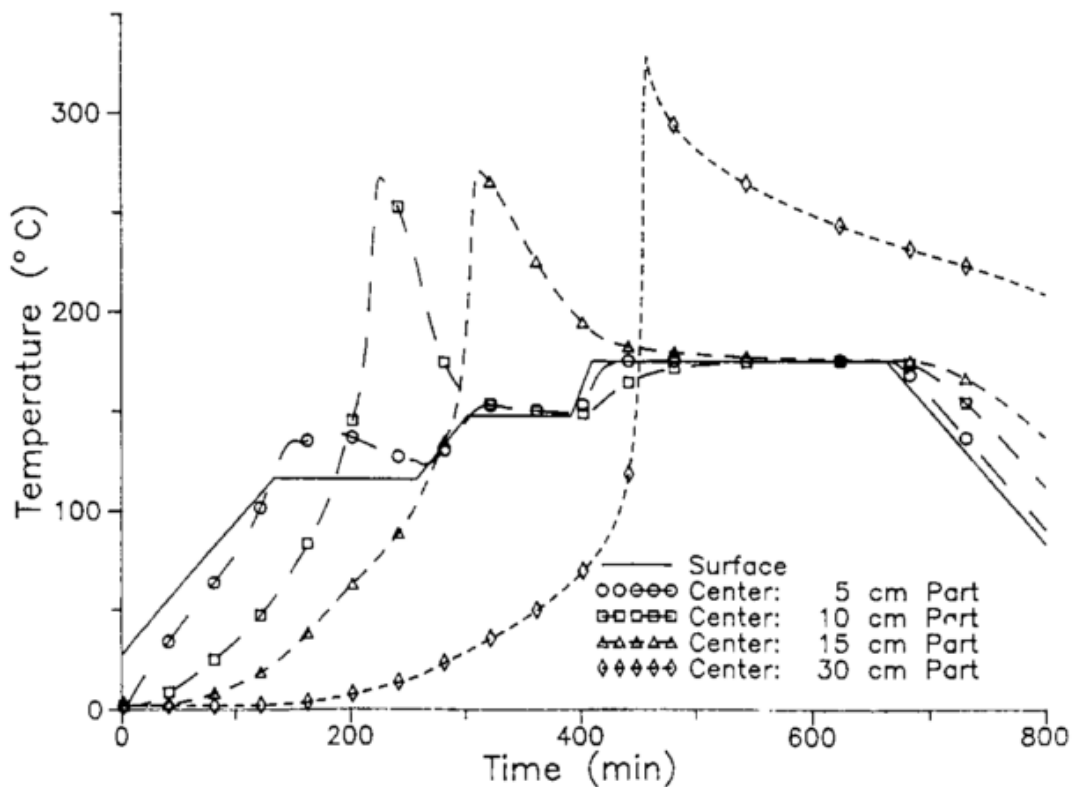


Figure 2.17. The thermal lag between the centre of the laminate and its surface increases dramatically as the thickness is increased. This leads to high temperature peaks and large gradients in temperature (Twardowski, Lin and Geil, 1993).

Oh and Lee (2002) modelled both heat transfer and consolidation, however, the simulations were performed separately so that the models were not fully coupled i.e. data from the heat transfer model was input into the consolidation model, but not vice

versa. Shin and Hahn (2004), on the other hand, developed a finite difference code which fully coupled resin flow and heat transfer of a thick prepreg laminate processed in a heated press. They used Darcy's Law to express the change in laminate thickness,

$$\Delta h = h_o - h = \int_0^h \left[\frac{K}{\eta} \frac{\partial P}{\partial z} \right] dt \quad (2.36)$$

Where h_o is the initial laminate thickness [m].

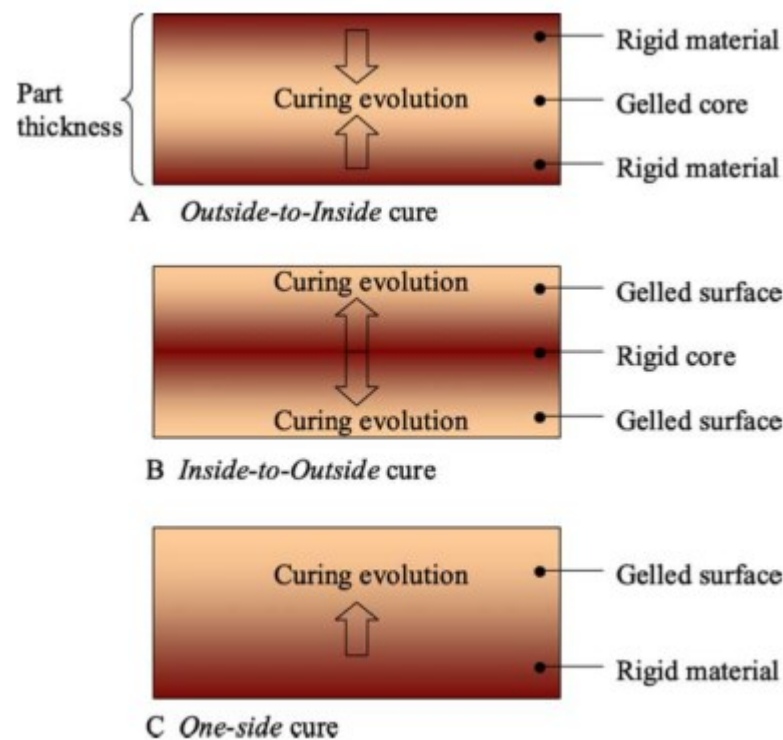


Figure 2.18. Illustration of three types of curing evolution in thick-section composite laminates:

- (A) Outside-to-inside curing results in a final stress state where the outer surfaces are in compression while the centre is under tension; (B) Inside-to-outside curing results in a final stress state where the outer surfaces are in tension while the centre is under compression; (C) One-sided curing where the stress state is asymmetric (Ruiz and Trochu, 2005).

Bogetti and Gillespie (1992) revisited thickness effects with a 1D simulation tool for process-induced residual stress and deformation (GF/polyester and GF/Epoxy). They showed that different curing profiles occurred depending on the thickness of the

laminates and how heat was applied. In thinner laminates, curing progressed from the centre of the laminate towards the surface (inside-to-outside curing). At a critical thickness, however, the cure evolution inverted so that curing progressed from the exterior surface of the laminate towards the centre (outside-to-inside curing) due to the lag in heat transfer (see Figure 2.18 for the different types of curing evolution).

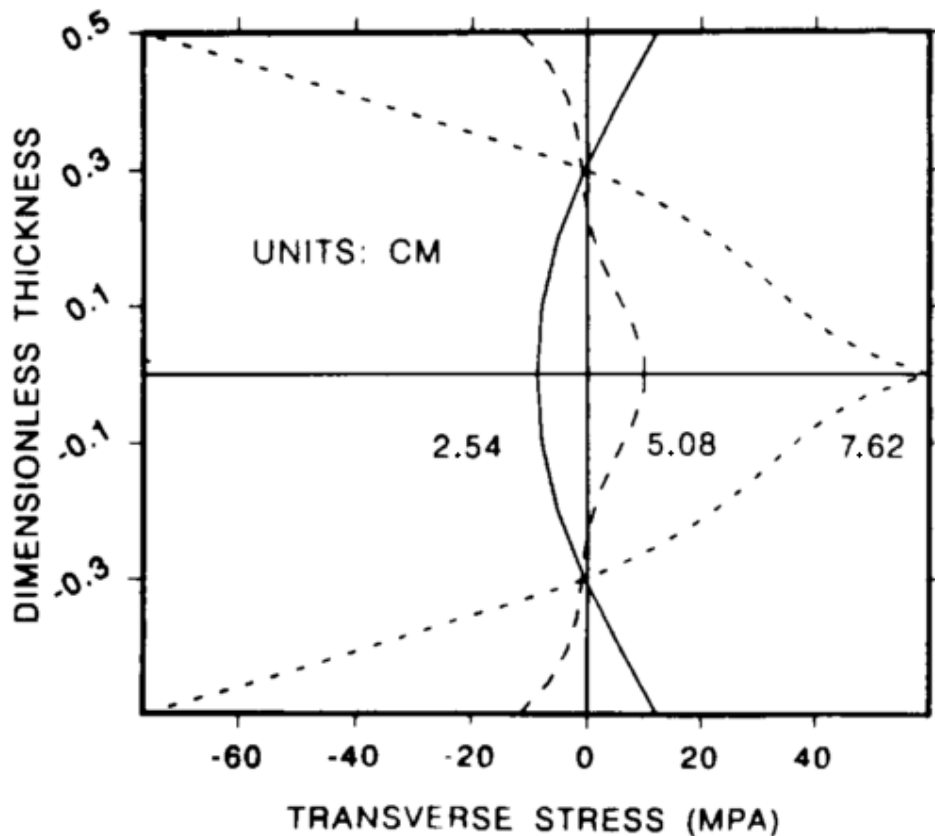


Figure 2.19. Simulated residual stress profiles for three GF/polyester laminates of varying thickness. The centre of each laminate is at a dimensionless thickness of 0.0, and the exterior surfaces of the laminate are at ± 0.5 . Above a thickness of 2.54 cm the stress profile inverts due to a corresponding inversion of the cure profile (Bogetti and Gillespie, 1992).

Bogetti and Gillespie (1992) argued that the outside-to-inside scenario was undesirable due to the severe stresses that resulted from cure shrinkage and thermal expansion (see Figure 2.19). They claimed that the residual stresses induced in the GF/polyester laminates were severe enough to cause transverse matrix cracking and delamination.

It should be noted, however, that the polyester was shown to have much higher cure shrinkage (4 – 6%) than the epoxy (1 – 3%). A parametric analysis showed that for some cases of lower cure shrinkage, the shrinkage cancelled out with the thermal expansion strains so that the laminate achieved a near stress-free state. It was also shown that asymmetric heating (e.g. one-sided heating) resulted in an asymmetric stress profile which would consequently lead to warpage.

A later study by Ruiz and Trochu (2005) investigated the curing and residual stress evolution of 15 mm thick GF/polyester laminates. Their results showed that outside-to-inside curing and inside-to-outside curing resulted in similar stress gradients in the final laminates, however, for outside-to-inside curing, the stress gradient evolved earlier while the resin was at a low DOC. This meant that the elastic modulus of the resin was low enough that the residual stresses could cause matrix cracking and/or generate voids.

In an attempt to optimise the curing cycle, many authors investigated the effect of changing heating ramp rates and introducing cooling stages without considering the effects of process-induced residual stresses (Loos and Springer, 1983; Martinez, 1990). Bogetti and Gillespie (1991, 1992) subsequently showed that increasing the heating rates had a similar effect to increasing the laminate thickness i.e. inverting the curing profile and potentially increasing the residual stresses to the point of matrix cracking and delamination. White and Kim (1996) suggested manufacturing thick parts by partially processing the laminate in thinner sections so as to reduce the overall exotherm and allow for faster heat transfer. They showed that the interlaminar properties were not reduced by this process, instead, interlaminar shear strength improved due to a significant reduction in void content. Despite this, they did not consider the obvious financial drawbacks of this process i.e. increased cycle time and demand on resources (labour and consumables). Pillai *et al.* (1997) combined the models of Bogetti and Gillespie (1991, 1992) with a heuristic approach to develop another optimisation tool which focused on the dual importance of uniform curing and cycle time reduction. Additional considerations they acknowledged were the avoidance of thermal degradation due to exotherm, achieving full consolidation and

minimising void content. More recently, researchers have implemented more advanced technologies, such as genetic algorithms, to develop powerful optimisation tools for the curing of thick laminates (Ruiz and Trochu, 2006; Struzziero and Skordos, 2017).

It should be noted that modelling process-induced residual stresses and implementing optimisation algorithms were outside the scope of this project. Nevertheless, they are important considerations for manufacturing thick-section composite structures and should be considered for future development (see Chapter 8, Section 8.2).

2.3.3 Experimental Validation

An important aspect of simulating composites processing is being able to experimentally validate the process models that are used. This section focuses on experiments which were developed for resin flow and heat transfer model validation.

In Section 2.3.1, the resin flow models presented for VBO prepregs were developed for thin laminates with which a uniform temperature could be assumed in the through-thickness direction. As such, heat transfer analysis of the laminate was not necessary and resin flow could be measured either in-situ or ex-situ for a given test temperature. Centea and Hubert (2011, 2012) were able to freeze thin laminates (4 plies thick) in a partially impregnated state by rapidly cooling them at various stages during a standard temperature cycle. Subsequently, they performed X-ray microtomography (micro-CT or μ -CT) to measure the resin flow front position within a tow for the given time and temperature profile. While this method was very intuitive for studying the progression of resin flow within a tow, the data resolution was relatively poor (i.e. several data points for an entire temperature cycle). This was because an individual laminate had to be manufactured and micro-CT scanned to collect each data point (micro-CT includes 2 hours scanning and 5 hours reconstruction for each sample). In addition, the samples had to be small (< 15 mm by 15 mm) to capture flow front position, as the image resolution was dependent on sample size.

In contrast, Cender *et al.* (2013) experimentally validated their resin flow model using an in-situ method. Under isothermal conditions, a charge-coupled device (CCD) camera was used to track flow front progression through a transparent tool, as shown in Figure 2.20. This method provided much greater data resolution for validating the resin flow model, however, it was limited to single ply tests as the camera could only track resin flow on the dry side of one ply. It was also questionable whether resin impregnation at the centre of the tow was well represented by these tests.

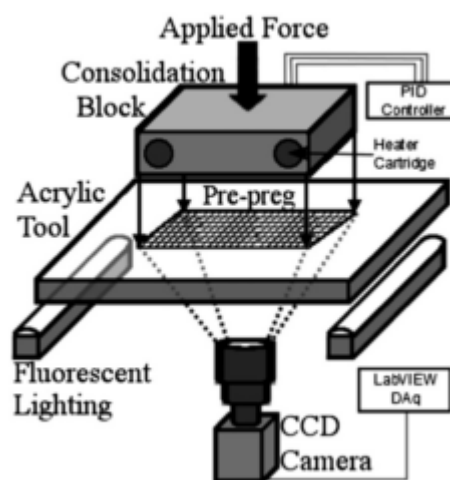


Figure 2.20. Schematic of an experimental apparatus for in-situ validation of a VBO prepreg resin flow model (Cender, Simacek and Advani, 2013).

A later study by Centea and Hubert (2013) examined the consolidation of VBO prepreps under deficient pressure conditions. They developed an experimental apparatus, shown in Figure 2.21, which could measure the thickness change of a thin laminate using a non-contact sensor. Although, this method did not give a direct visualisation of the flow progression, they were able to analyse the final state of the cured laminates using optical microscopy. They found that the laminate thickness reduced during air evacuation and resin flow, and that the rate of thickness change was affected by pressure conditions. This latter effect was due to entrapped gases resisting resin flow, resulting in macroscopic and microscopic voids. Helmus *et al.* (2016) used

these experiments to validate their models for air evacuation and resin flow, previously discussed in Section 2.3.1, and achieved good accuracy.

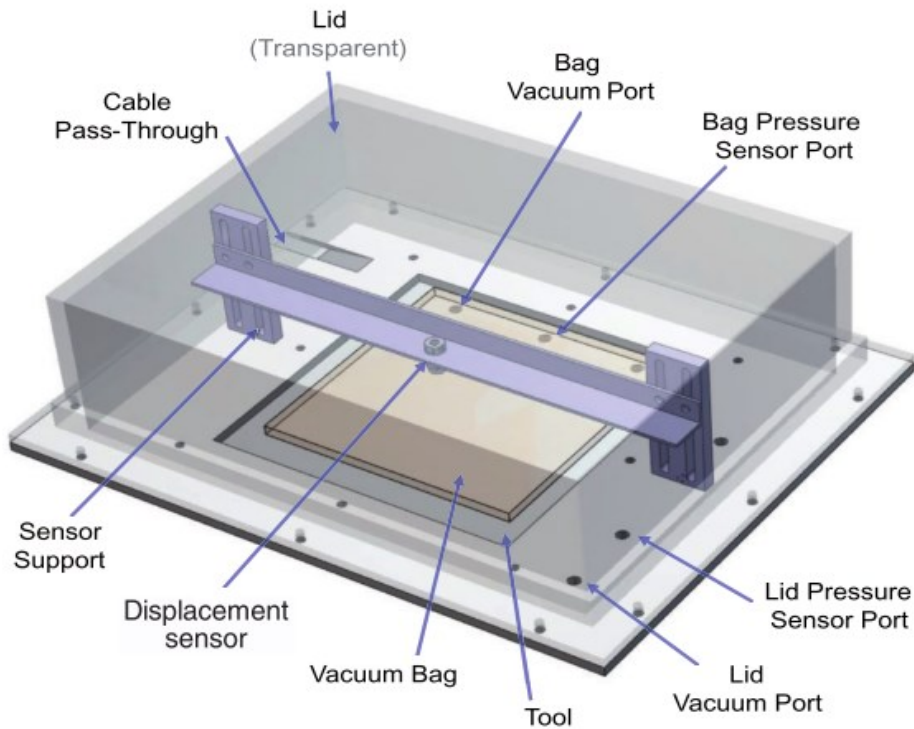


Figure 2.21. Rendered image of an experimental apparatus for measuring laminate thickness change under controlled pressure conditions (Centea and Hubert, 2013; Helmus *et al.*, 2016).

Monitoring laminate thickness change was an effective means of validating resin flow/consolidation models for thick-section laminates also. Gutowski *et al.* (1987) developed a specialised compression die which could measure the resin pressure in a laminate and the thickness change as a controlled load was applied. To apply a controlled load, the fixture was mounted in an Instron Test Machine and laminate thickness change was measured by a linear variable differential transformer (LVDT). Shin and Hahn (2004) validated their coupled resin flow and heat transfer model by monitoring both the thickness change (distance between platens) and temperature (thermocouples) of 30 - 50 mm thick prepreg laminates manufactured in a heated press. They used a mould to control the resin flow conditions (1D or 2D) and placed layers

of bleeder cloth above the laminate for excess resin to flow into. Figure 2.22 shows the results for one of their validation experiments compared with the simulation.

In some other cases, authors validated their resin flow models against from thickness change data from existing publications (Oh and Lee, 2002; Costa and Sousa, 2003).

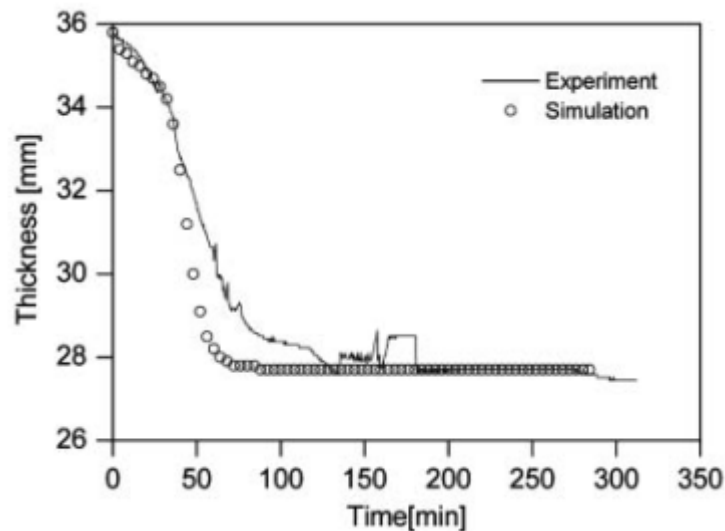


Figure 2.22. Experimental and simulated thickness data for a prepreg laminate as it is processed in a heated press; the thickness decreases due to resin flow (Shin and Hahn, 2004).

In terms of heat transfer model validation, thermocouples were universally chosen for measuring temperature variations within thick laminates. In general, thermocouples were distributed through the thickness of the laminate. For models with a 1D heat transfer assumption, the laminate edges were insulated in some way e.g. fibreglass, silicone rubber, or breather cloth as shown in Figure 2.23 (Loos and Springer, 1983; Bogetti and Gillespie, 1991; Twardowski, Lin and Geil, 1993; Shin and Hahn, 2004; Kratz *et al.*, 2012; Sorrentino, Polini and Bellini, 2014). In some cases of validating 2D or 3D models, thermocouples were distributed in-plane also (Oh and Lee, 2002; Wieland and Ropte, 2017).

Additional data was required in cases where the boundary conditions were modelled. Bogetti and Gillespie (1991) performed a parametric study to determine the effective

HTCs within an autoclave, and Twardowski *et al.* (1993) measured the temperatures between the surface of the hot press platens and the vacuum bagging.

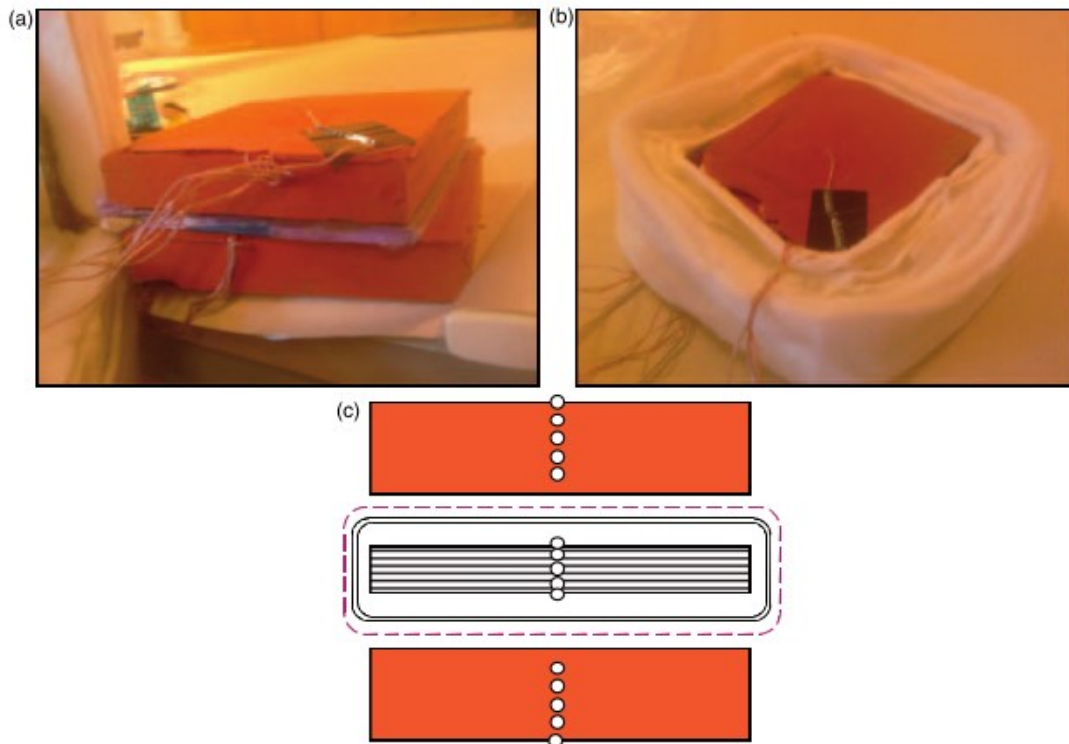


Figure 2.23. Experimental set up for validating a heat transfer and cure kinetics model. (a) The top and bottom surfaces of the laminate are insulated with silicone rubber. (b) The sides are insulated with breather cloth. (c) Illustration of the set-up with white dots denoting the position of thermocouples through the thickness (Kratz *et al.*, 2012).

In most cases, the accuracy of both the heat transfer and cure kinetics models were inferred from the closeness of the fit between simulated temperatures and experimental thermocouple data for the curing process. Using the experimental apparatus in Figure 2.23, Kratz *et al.* (2012) processed a flat CF/Epoxy laminate for a given temperature cycle, then repeated the cycle on the fully cured laminate. The repeat cycle allowed them to verify the accuracy of the heat transfer analysis in RAVEN when uncoupled from the curing effects, while the initial cycle validated the cure kinetics model. Other approaches to validating the cure kinetics model include in-situ measurement with dielectric sensors (Sorrentino and Bellini, 2015).

3. Experimental Characterisation of Epoxy Powder

3.1 Chapter Introduction and Overview

Epoxy powders are a commodity product which can be procured from a variety of sources. The various proprietary formulations offered by producers means that a wide range of processing properties are available. To select an epoxy powder which is suitable for manufacturing thick-section composite parts, it is necessary to experimentally characterise candidate powders.

This chapter describes the experimental characterisation of three epoxy powders; detailing the specific tests that were performed and the experimental methodology that was applied. The chosen methods focused mostly on the processing characteristics of the epoxy powders (i.e. cure kinetics, viscosity, etc.), but other aspects, such as storage stability and moisture uptake, were considered as well.

The results of testing are discussed and a rationale is presented for the downselection of one epoxy powder for further investigation.

3.2 Materials and Methodology

3.2.1 Epoxy Powder Selection

Three epoxy powders were chosen for investigation; GRN 918 (ÉireComposites Teo., 2013), HZH01R (Akzo Nobel Powder Coatings GmbH, 2016), and A-S-SET 02 (New Era Materials Sp. z o.o., 2014). GRN 918 was an epoxy powder coating chosen for composite manufacturing, HZH01R was designed as a binder for glass fibre impregnation, and A-S-SET 02 was specifically formulated for the manufacture of composite materials in an autoclave or heated press.

3.2.2 Thermogravimetric Analysis

As shown in Figure 3.1, a thermogravimetric analysis (TGA) test cell consists of a sample holder on a precision balance inside a furnace. The sample is exposed to an inert or reactive purge gas flow to control the test environment. Mass change is measured as the furnace is heated and cooled. Gases (due to boiling, decomposition, etc.) are exhausted from the furnace with the purge flow.

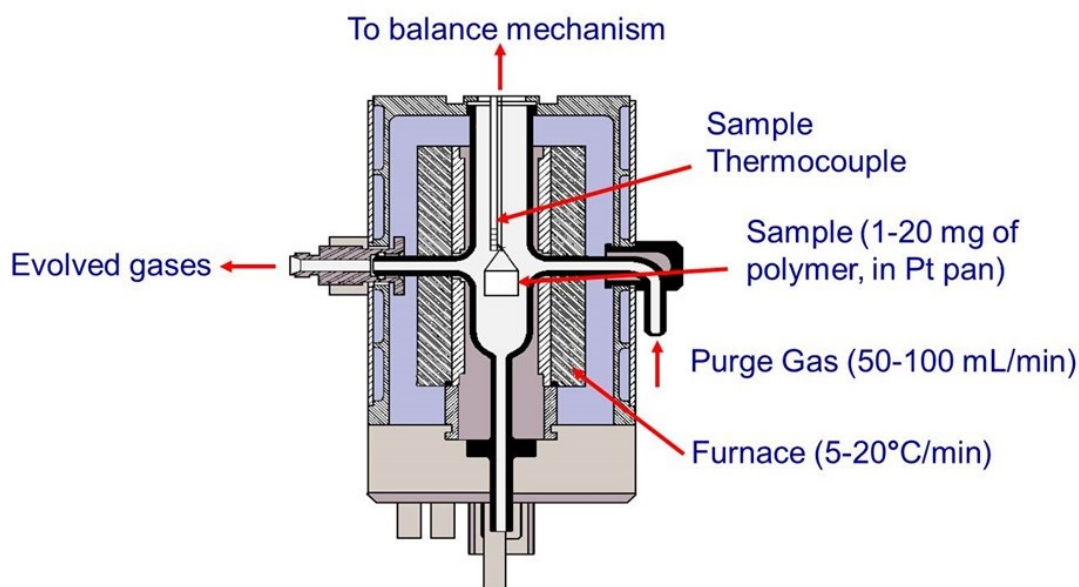


Figure 3.1. Schematic of a TGA test cell (Source: TA Instruments).

TGA was used to determine the upper processing temperature limit for the epoxy powders by evaluating their thermal stability over a broad range of temperatures. Tests were performed for GRN 918 and A-S-SET 02 using a SDT-Q600 TGA/DSC (TA Instruments), while HZH01R was tested using a Mettler Toledo TGA/DSC 3+. The tests on GRN 918 and AS-SET 02 were performed by Mr. Simon Hodge at the NIACE Centre in Belfast, UK. All tests followed the specifications of ISO 11358-1 (2014). Samples were tested in aluminium oxide (a.k.a. alumina) crucibles. The initial mass was 12.5 ± 0.6 mg for all GRN 918 and A-S-SET 02 samples, and 16.0 ± 0.5 mg for all HZH01R samples. Tests were carried out in an inert nitrogen atmosphere using a nitrogen purge gas with a flow rate of 50 ml/min. Temperature scans were carried out at a ramp rate of $10^{\circ}\text{C}/\text{min}$ between 25°C and 600°C . Additional isothermal tests were performed for GRN 918 and A-S-SET 02 at 210°C and 180°C , respectively.

3.2.3 Differential Scanning Calorimetry

As outlined by ISO 11357-1 (2009), two types of differential scanning calorimetry (DSC) are suitable for testing plastics; heat-flux DSC, and power-compensation DSC (see Figure 3.2). For heat-flux DSC, a sample crucible and a reference crucible are placed within an oven. As the oven is heated, the temperature difference between the sample and the reference is used to determine the difference in heat flows. For power-compensation DSC, the sample and reference crucibles are heated independently and the difference in the electrical power required to keep both crucibles at the same temperature is used to determine the heat flow. In both cases, a purge flow is used to control the atmospheric conditions around the sample.

DSC tests were carried out on GRN 918 and HZH01R using a DSC Q200 (TA Instruments), while A-S-SET 02 was tested using a Pyris 1 DSC (Perkin Elmer). Testing of A-S-SET 02 was performed by Mr. Ananda Roy at ICOMP in Limerick, ROI. Several DSC tests were performed to characterise the epoxy powders; in general, these tests were performed to the specifications of ISO 11357-1 (2009) and ISO 11357-5 (2013). For GRN 918 and HZH01R, all samples weighed 6.5 ± 0.4 mg. The mean

sample mass for A-S-SET 02 was 10.3 mg. All samples were loaded into ventilated aluminium crucibles. A nitrogen purge gas flow of 50 ml/min was used for all testing.

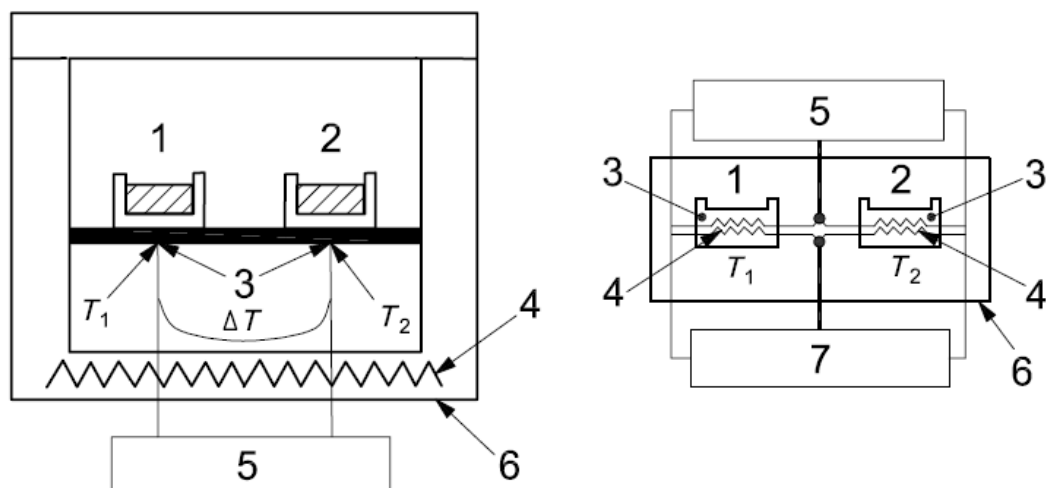


Figure 3.2. Schematic of a heat-flux DSC (left) and a power-compensation DSC (right): (1) Sample position; (2) Reference position; (3) Thermocouple; (4) Heater; (5) Temperature measurement circuit; (6) Enclosure; (7) Heat-flux compensation circuit (ISO 11357-1, 2009).

Temperature scans were used to determine the basic characteristics of the three epoxy powders and make a comparison between them. According to ISO 11357-5 (2013), the temperature scanning method can be performed with ramp rates ranging from 5°C/min to 20°C/min. A heating rate of 10°C/min was used for the comparison of different samples.

Temperature scans were also used to compare several samples of GRN 918 that had been conditioned. For wind turbine manufacturers operating in tropical climates, such as Suzlon Energy Ltd. (India), storage and working conditions are important manufacturing considerations. The motivation for conditioning the samples was to determine whether high temperature and high humidity had any permanent effect on the powder after being dried. For conditioned testing, as-supplied powder samples and melted powder samples were placed within an environmental oven at 35°C and approx. 70% relative humidity (RH) for 1 week. These conditions were chosen based on

average weather conditions for summer months in Bhuj, India. The samples were subsequently dried under vacuum at 40°C for at least 12 hours.

3.2.4 Parallel-plate Rheometry

Although rheometers can be configured in several ways, parallel-plate rheometry (PPR) is the most common arrangement for studying the cure effects of thermosets under low shear rate conditions (Halley and Mackay, 1996). PPR tests can be either strain rate-controlled or stress-controlled i.e. the former method applies a specified shear strain rate to the sample via the rotating upper plate (see Figure 3.3), while the latter method applies a specified shear stress.

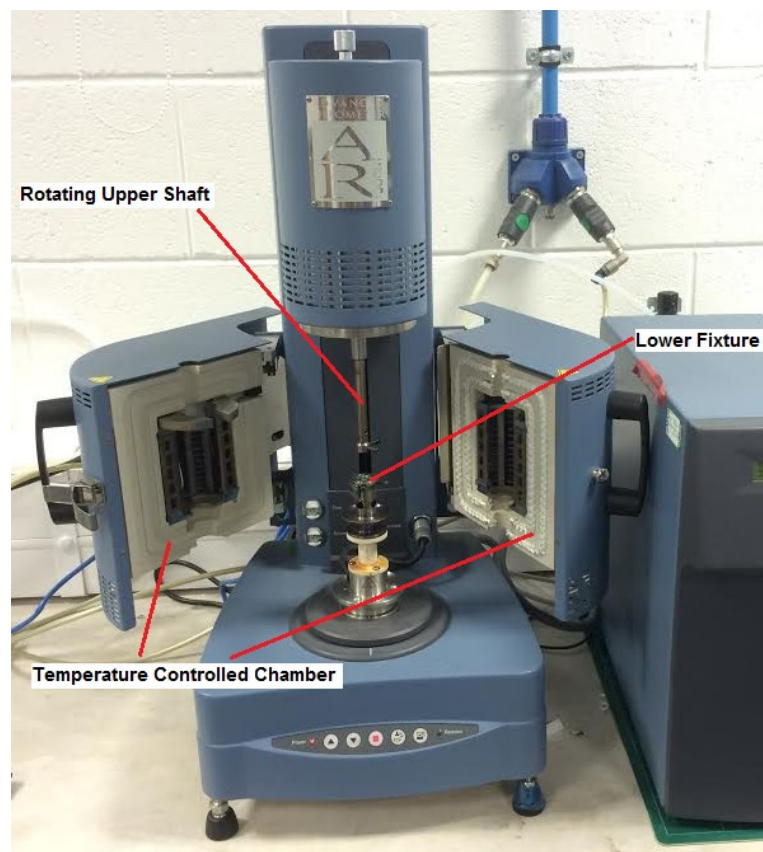


Figure 3.3. Photo of an AR 2000 rheometer with a temperature-controlled chamber for testing polymer melts at elevated temperatures.

Tests can be performed in rotational mode (continuous rotation), or in oscillation mode. As discussed in Chapter 2, Section 2.2.3, oscillation mode is preferred for studying thermoset polymers as continuous rotation damages the formation of crosslinking networks. In oscillation mode, PPR operates by measuring the oscillating torque or displacement, converting it into shear stress or shear strain, respectively, and then calculating the complex modulus and complex viscosity of the sample material. The complex modulus and complex viscosity can be separated into the elastic component (storage modulus/storage viscosity) and the viscous component (loss modulus/dynamic viscosity).

To study cure effects, the sample must be heated until gelation occurs; this is achieved either by direct heating of the plates (e.g. via a Peltier module) or heating of the surrounding environment (e.g. via a heated chamber that encloses the plates and sample, as shown in Figure 3.3).

An AR 2000ex rheometer (TA Instruments) was used to test GRN 918 and HZH01R in oscillation mode. Tests were performed to the specifications of ISO 6721-10 (1999). A temperature-controlled chamber, as shown in Figure 3.3, was used to heat the samples and the parallel-plate fixtures. Heating was achieved, via forced convection, using an air flow of 20 l/min. Disposable aluminium plates (diameter: 25 mm) were used for testing. Approximately 900 mg of epoxy powder was used for each test sample. The powder was loaded onto the lower plate at ambient conditions. A melt ring was used to stop powder spilling onto the rest of the test apparatus. For all tests, the sample temperature was increased from ambient to 100°C in approx. 3 min so that the powder could melt and form a homogenous layer (the air flow rate was initially reduced to 10 l/min so that the powder was not disturbed before melting). The samples were allowed to equilibrate at 100°C for 5 min, and then the gap height was reduced to 1000 μm . Excess resin was removed carefully with a thin, flat edged scraper. The temperature-controlled chamber was closed and brought to 70°C (i.e. the starting temperature for all tests). The samples typically took 5 min to cool, and were allowed to equilibrate for 1 min at 70°C before tests began. Using the cure kinetics model

described in Chapter 4, curing was estimated to progress by less than 1% during the aforementioned set-up steps.

To select an appropriate frequency and amplitude (i.e. % strain) for testing, it was necessary to determine the linear viscoelastic region for the epoxy powders. This was achieved by performing strain sweeps at 70°C, 90°C, and 120°C (plots for the frequency sweeps are given in the Appendices: A. Epoxy Powder Characterisation Data, Figure A.1, Figure A.2, and Figure A.3). At 90°C and 120°C, the response only became non-linear above 50% strain. It was found that high strains gave better signal resolution when the viscosity became low (i.e. at 120°C), however, at 70°C the rheometer had already reached its torque limit at 3% strain. Given these limiting factors, a strain of 1% and an angular frequency of 5 rad/s were chosen for all remaining tests so that the viscosity could be measured for a broad range of temperatures.

Note that for all tests it was assumed that the Cox-Merz relation (Schramm, 1994) was applicable i.e. the complex viscosity was equivalent to the dynamic viscosity at low shear rates. This relation has already been applied to epoxy powder coatings by Osterhold and Niggemann (1998).

Temperature scans were performed to determine how the epoxy powders' viscosities varied with temperature and DoC. A temperature ramp rate of 5°C/min was used for comparing GRN 918 and HZH01R, as well as some of the conditioned GRN 918 samples.

It should be noted that A-S-SET 02 was not included in the PPR testing as it had been eliminated already via the downselection process (discussed further in Section 3.3.1 and 3.3.5).

3.2.5 Dynamic Mechanical Thermal Analysis

Dynamic mechanical thermal analysis (DMTA) is used to determine how the modulus of a material changes w.r.t. temperature. This is achieved by applying a sinusoidal force or displacement to a material specimen as it is heated. Similar to PPR, it is

commonly used to characterise the viscoelastic behaviour of polymeric materials by measuring the complex modulus, however, DMTA is better suited to studying polymers in a glassy or rubbery phase as opposed to liquids.

DMTA was used to determine the crosslink density of the GRN 918 epoxy powder and compare it Ampreg 22 (Gurit). This latter system is a VARTM-grade epoxy which has been studied previously for tidal turbine applications, and has been shown to perform well in immersed conditions i.e. relatively low water uptake and good immersed fatigue properties (Kennedy, 2013).

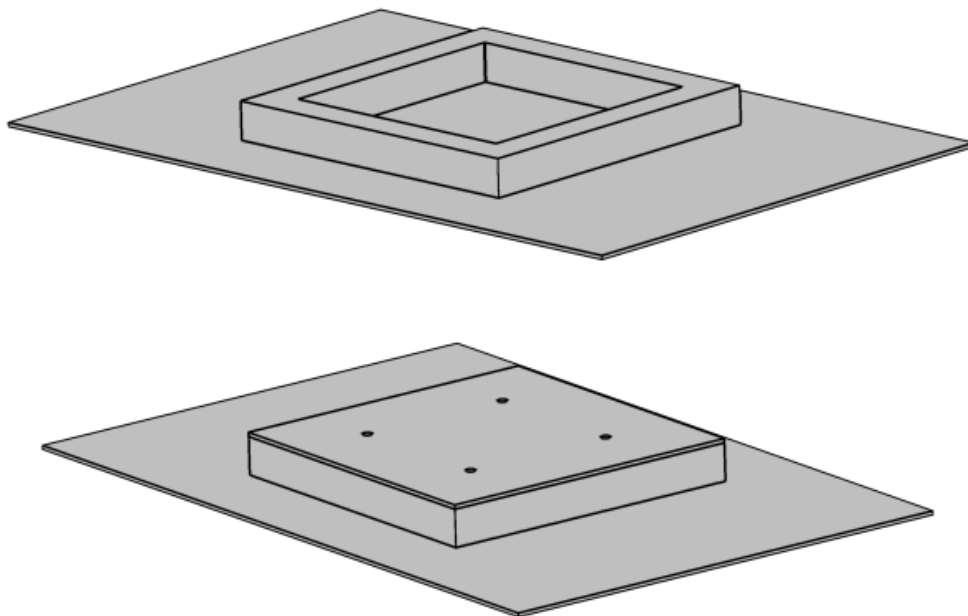


Figure 3.4. Rendered image of the picture-frame mould and flat backing plate that were used to manufacture neat resin specimens for DMTA (top), and the same mould with a perforated lid to allow for the release of vaporised gases (bottom).

Typically, the storage modulus used to calculate the crosslink density (see Equation 2.14) is < 100 MPa because the sample is tested above its T_g . For such cases, ISO 6721-5 (1996) suggests that “relatively short, thick specimens may be required to achieve sufficient accuracy in the measurement of force”. Consequently, it was decided that the test specimens should be 40 mm long, 10 mm wide, and 3 mm thick.

A picture-frame mould, as shown in Figure 3.4, was used to manufacture neat epoxy panels (100 x 100 x 3 mm).

For GRN 918 test panels, approximately 37 g of powder (cured density of approx. 1220 kg/m³) was dispersed within the mould. A perforated steel lid was used so that the mould could be vacuum bagged and vaporised gases could be evacuated. The following temperature cycle was used: dried under vacuum at 45°C for 4 hr, ramped to 120°C at 1.5°C/min, held at 120°C for 60 min, ramped at 1.5°C/min to 170°C, held at 170°C for 90 min, and then cooled to ambient conditions.

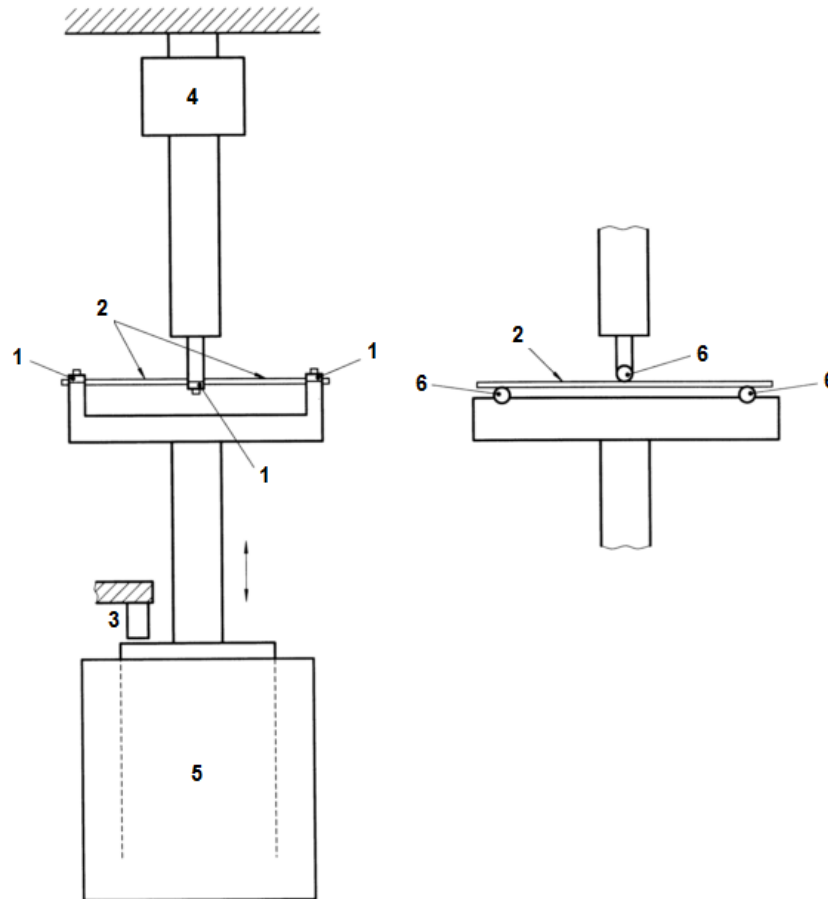


Figure 3.5. Schematic of DMTA flexural test fixtures for a clamped specimen (dual cantilever) (left), and a simply supported specimen (right). Identifiers are as follows: (1) Clamps, (2) Specimen, (3) Displacement transducer, (4) Force transducer, (5) Vibrator, (6) Roller supports (ISO 6721-5, 1996).

For Ampreg 22 test panels, the resin was mixed with a slow hardener using a ratio of 100:28 (by weight) as recommended by Gurit (Gurit Holding AG, 2015). The mixture was degassed, and then approx. 33 g of the mixture (mixed density of 1100 kg/m³) was carefully poured into the picture-frame mould. The epoxy mixture was left to cure at room temperature for 48 hr, and was postcured at 80°C for 5 hr before being demoulded.

Several DMTA specimens (40 x 10 x 3 mm) were cut from each of the neat epoxy panels. They were tested in a Triton 2000 Dynamic Mechanical Analyzer (Triton Technology Ltd.) using a clamped flexural fixture (as illustrated in Figure 3.5,) with a span of 30 mm. Multi-frequency tests (1 Hz and 10 Hz) were performed with a displacement of 0.05 mm. The specimens were heated from ambient to 180°C at 3°C/min during the tests.

From the resulting data, a storage modulus value was taken for each specimen at a temperature well above their T_g (i.e. 50°C above). With this value and the corresponding temperature, the crosslink density was calculated using Equation 2.14 in Chapter 2, Section 2.2.2.

3.2.6 Dynamic Vapour Sorption

Dynamic vapour sorption (DVS) is a gravimetric technique that involves weighing a sample, under isothermal conditions, as water vapour is passed over it (see Figure 3.6). The water vapour is formed by flowing dry nitrogen gas through a water bath. The relative humidity (RH) of the test environment is controlled then by varying the ratio of wet and dry nitrogen flow. As the gas mixture passes over the sample at one RH level, water vapour is adsorbed or desorbed until the sample reaches an equilibrium. This process is repeated for increasing and decreasing RH levels to determine the equilibrium moisture content at each RH.

DVS was used to measure the mass change of GRN 918 at various RH levels. By measuring mass change w.r.t. time, it was possible to gain an understanding of the sorption characteristics of the epoxy powder and investigate its storage stability.

DVS experiments were performed using an Aquadyne DVS-2 from Quantachrome Instruments. Samples were weighed using glass crucibles; each powder sample weighed 60 ± 13 mg. Minimum and maximum nitrogen gas flow was limited to $50 \text{ cm}^3/\text{min}$ and $150 \text{ cm}^3/\text{min}$, respectively.

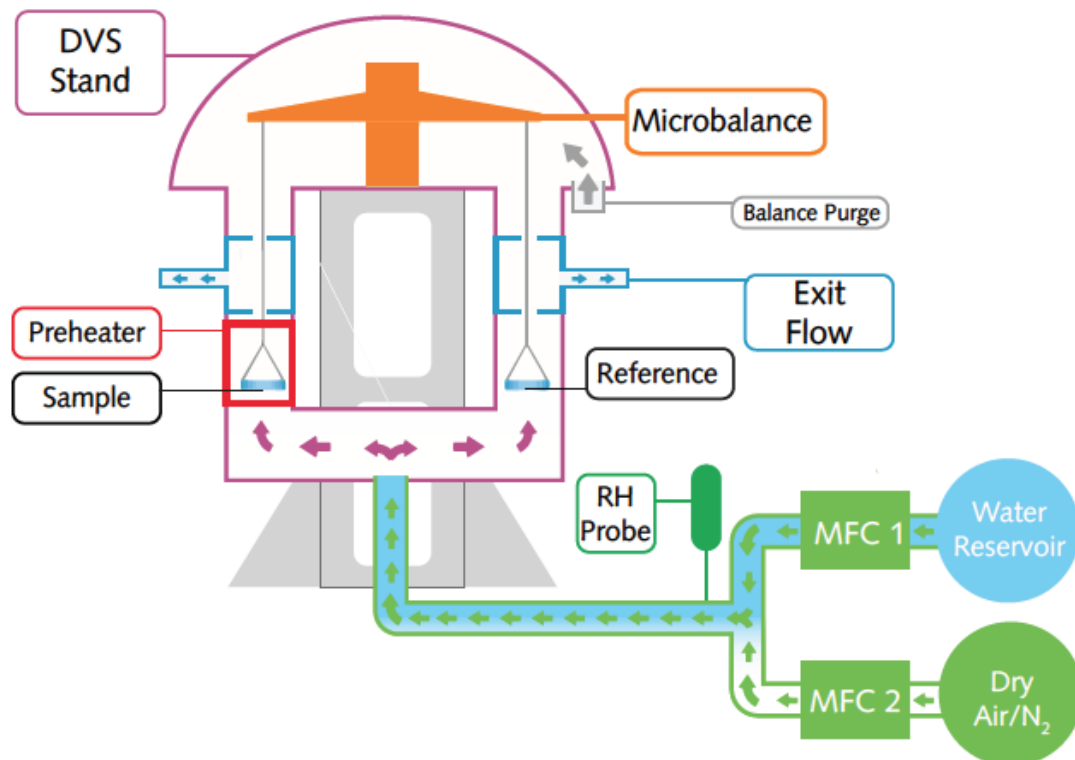


Figure 3.6. A schematic diagram of a DVS analyser. Water is mixed with a dry gas to create water vapour which then flows over the sample and reference crucibles. The microbalance then measures the mass change due to adsorption/desorption w.r.t. time (Surface Measurement Systems, 2018).

GRN 918 epoxy powder was tested at three temperatures: 23°C , 35°C , and 45°C . Weight calibration was performed every time the test temperature was changed. For each test, the powder was initially dried until equilibrium at the lowest possible RH (approx. 1-2% RH). Then, the RH level was increased to 90% RH in increments of 15% RH, before decreasing again in increments of 15% RH. Typically, if time permitted, the samples were allowed to reach equilibrium at each RH level. The only

exception to this procedure was for the samples at 45°C because it was found that the powder fully sintered above 60% RH. Sintering caused the sorption characteristics to change significantly. In light of this behaviour, the following additional tests were carried out:

- A test at 35°C with a sintered epoxy sample
- Tests on powder samples at 45°C and 50°C, increasing the RH from 1-2% RH to 90% RH in increments of approx. 1% RH every 6 mins, then decreasing the RH at the same rate.

These tests were performed in order to examine the storage stability of the powder and demonstrate the significant change in the sorption characteristics.

3.3 Results and Discussion

3.3.1 Downselection of Powders

During the process of characterising the three candidate epoxy powders, it was necessary to eliminate two of the options so that further studies could be completed in an effective manner. Downselection was performed on the basis of which epoxy powder was most suitable for manufacturing thick-section composite structures.

It should be noted that the three epoxy powders were procured at different times during this project and, therefore, they were not all tested simultaneously. Furthermore, some tests were carried out after one or more of the epoxy powders had been eliminated already.

3.3.2 Thermal Stability

The TGA temperature scans in Figure 3.7 show that the onset of decomposition for all three epoxy powders (approximately 340 - 350°C) was well above their typical processing temperatures (i.e. 150 - 180°C). Additional 3 hr isothermal tests were performed for GRN 918 and A-S-SET 02, at 210°C and 180°C respectively, to check the thermal stability for extended high-temperature exposure. A mass loss of approx.

1% was recorded in both cases; the data plot is available in Figure A.4 of the Appendices: A. Epoxy Powder Characterisation Data. This small mass loss was considered negligible and was attributed to evaporation of moisture and potentially residual solvents from the powder production process.

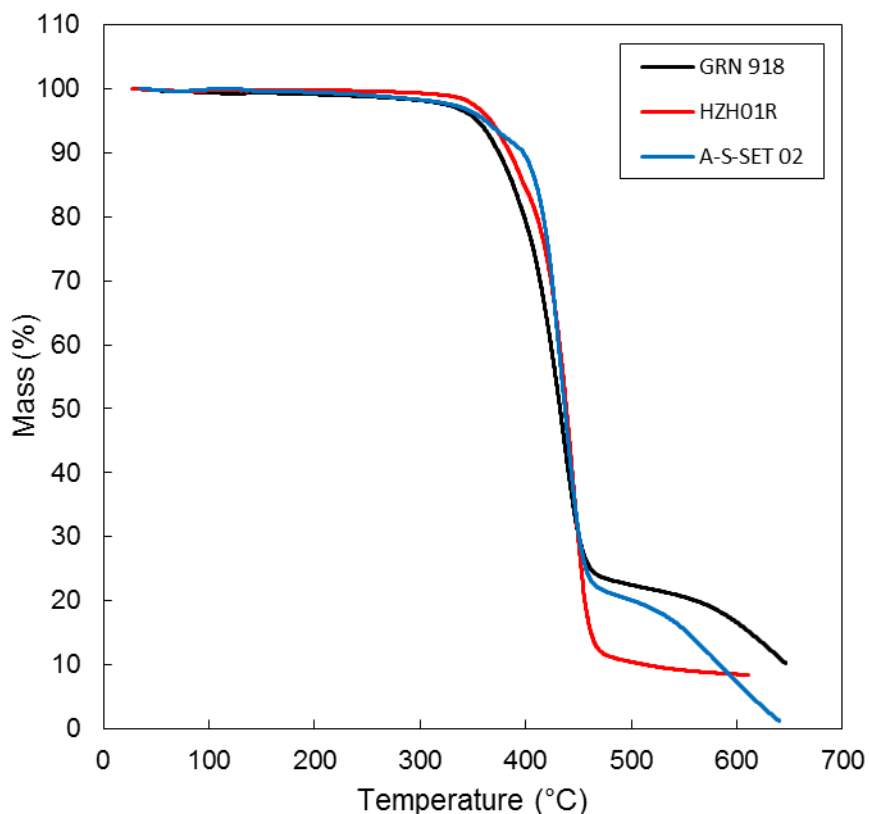


Figure 3.7. Mass change of the epoxy powders w.r.t. temperature. All powders showed relatively good thermal stability up to at least 300°C. At higher temperatures significant mass loss was recorded due to thermal decomposition.

3.3.3 Curing

Figure 3.8 shows the heat flow data for GRN 918 and HZH01R when subjected to a temperature scan at 10°C/min (the plot of a 1.5°C/min temperature scan for A-S-SET 02 is given in Figure A.5 the Appendices: A. Epoxy Powder Characterisation Data).

All three powders displayed an overlapping endothermic peak and step change in heat flow; a common characteristic of epoxy powders which was previously discussed in Chapter 2, Section 2.2.1. To recap, the step change signifies the glass-liquid transition, while the endothermic peak is an indirect result of enthalpic relaxation in the epoxy. It can be seen in Figure 3.9 that this endothermic peak did not occur when the powder was melted prior to testing (i.e. the powder was heated to 100°C and then cooled before beginning the test), leaving only the step change of the glass-liquid transition. This was because the epoxy had insufficient time to relax to thermodynamic equilibrium after being melted initially.

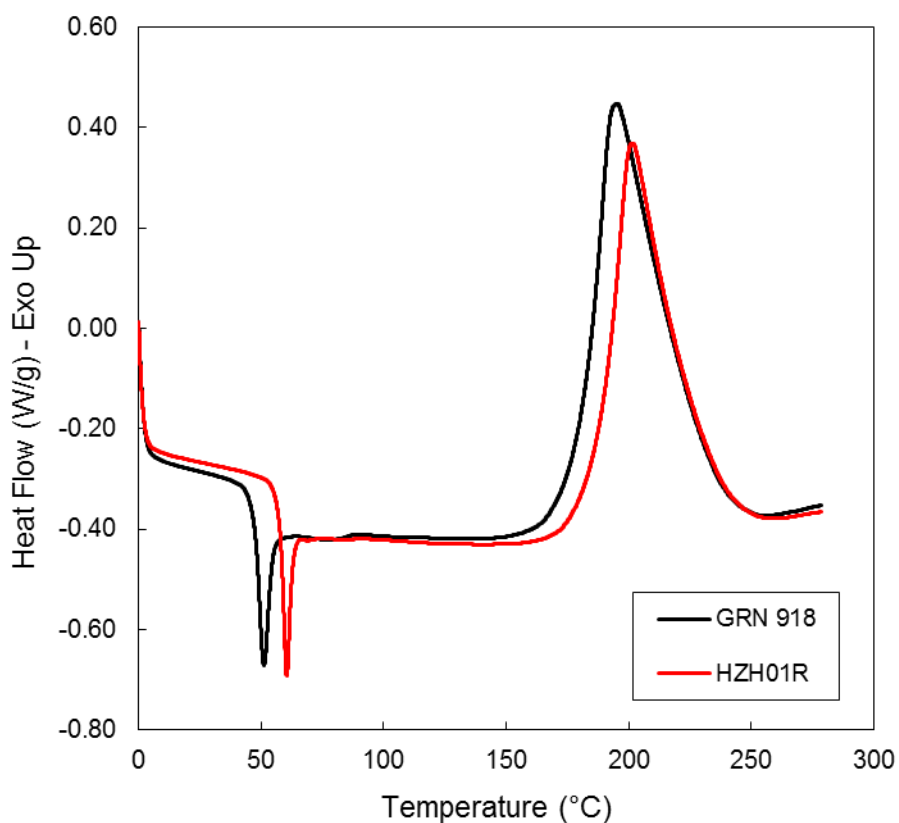


Figure 3.8. DSC heat flow data for two epoxy powders during temperature scan tests at 10°C/min. The powders displayed similar behaviour with the exception that HZH01R had a higher initial T_g and onset temperature for curing. Note: Positive exothermic heat flow.

The T_g of the powders was recorded as being approx. 40 - 60°C depending on which epoxy powder was being tested and the heating rate that was used. Combined with the use of latent curing agents, the high initial T_g of the epoxy powders meant that they had exceptional storage stability/out-life i.e. up to 4 months at 23°C for HZH01R (Akzo Nobel Powder Coatings GmbH, 2016).

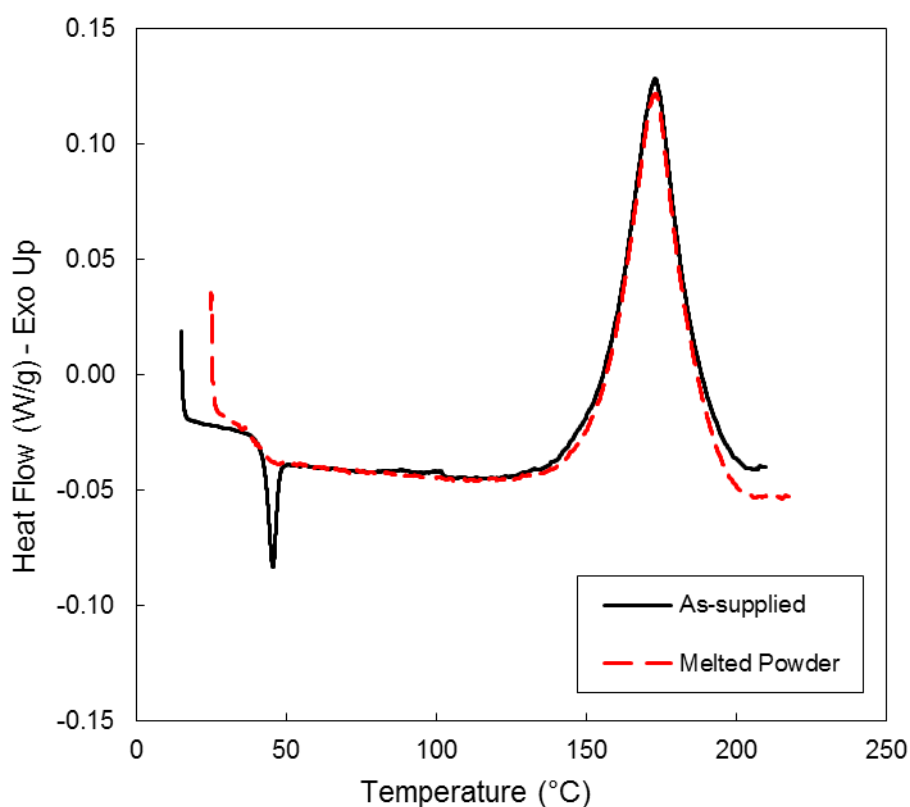


Figure 3.9. DSC heat flow data for two samples of GRN 918: an as-supplied powder sample, and a sample that had been heated to 100°C at 10°C/min and then cooled again at the same rate. In the latter case, the powder was melted and there was no endothermic peak upon reheating.

All three powders also showed a narrow band of curing temperatures (i.e. the temperatures between onset and cessation of the exothermic peak). This represented the acute temperature dependency of the curing reaction; a characteristic of heat-activated curing systems.

As previously mentioned in Chapter 1, Section 1.4, epoxy powder coatings were known to have a less exothermic curing reaction than conventional epoxy systems. Table 3.1 shows the total enthalpy of reaction for each epoxy powder that was tested. A-S-SET 02 produced the least heat during cure, however, the enthalpies of reaction for GRN 918 and HZH01R were also less than half of what was reported for conventional epoxy systems. Obviously, this feature would reduce the risk of thermal runaway in thick-section laminates

Another feature to consider is the onset of curing for the epoxy powder samples. The onset temperature for GRN 918 was 5 – 10°C lower than for HZH01R, while the onset temperature of A-S-SET 02 was much lower again (approx. 40°C lower). Naturally, manufacturers prefer to process at lower temperatures due to constraints on tooling, cost of heating, increased likelihood of thermal mismatch, etc. Nevertheless, specialised tooling has been developed for high temperature processing of epoxy powder composites (Ó Brádaigh *et al.*, 2011).

Table 3.1. Max total enthalpy of reaction for each of the epoxy powders

Epoxy powder	Total enthalpy of reaction [J/g]	Reduction in heat [%]*
GRN 918	184.0	60.7
HZH01R	138.0	70.5
A-S-SET 02	105.5**	77.5

* Compared to mean total enthalpy of reaction for the conventional epoxy resin systems presented in Table 1.1 (i.e. 468.9 J/g).

** Measured under isothermal conditions.

As discussed in Section 3.2.3, an additional area of interest was how the powder would behave after conditioning at an elevated storage temperature and relative humidity (RH). The results in Table 3.2 showed that, after vacuum drying at 40°C for at least 12 hours, no significant change to the curing behaviour of GRN 918 could be discerned

from the DSC data. It was found, however, that GRN 918 samples conditioned at 35°C and 70% RH had transitioned from a loose powder to a porous solid (i.e. partially sintered powder). Partial sintering of the powder would be undesirable during storage as it would increase the difficulty of handling. This could be circumvented by producing VBO prepreg under controlled conditions, and using backing paper to prevent plies from adhering to each other.

Table 3.2. DSC results for conditioned and unconditioned GRN 918 epoxy powder samples.

Epoxy form	Conditioning	Drying*	Initial T_g [°C]	Final T_g [°C]	Total enthalpy of reaction [J/g]
Powder	As-supplied	No	52.4	110.0	161.7
Powder	As-supplied	Yes	51.2	110.0	166.2
Powder	35°C, 70% RH	Yes	52.4	109.6	170.3
Melted	As-supplied	Yes	51.5	110.3	164.6
Melted	35°C, 70% RH	Yes	52.2	109.9	165.3

* *Drying under vacuum at 40°C for at least 12 hr.*

3.3.4 Chemorheology

For VBO processes, it has been suggested that a viscosity of < 100 Pa.s is required for infusion (Kratz *et al.*, 2012) due to the limited compaction pressure i.e. 101.325 kPa. For thermosetting resin systems, the time available at < 100 Pa.s is limited by the progression of cure, which makes the latent reactivity of epoxy powders an attractive feature for processing. This latter consideration is particularly important for thick-section composites due to the additional time required to transfer heat through the material.

With these criteria in mind, Figure 3.10 shows that both the GRN 918 and HZH01R reached suitably low viscosities for VBO prepreg processing; achieving minimum viscosities of 1 Pa.s and 2.3 Pa.s, respectively, for a heating rate of 5°C/min. Nevertheless, it was clear that GRN 918 offered greater processing flexibility i.e. it reached 100 Pa.s at 100°C, which was 15°C lower than for HZH01R. While this factor was used to downselect GRN 918 for further study, HZH01R was still considered a viable option for composite manufacturing and, as discussed in Chapter 6, Section 6.3.6, and Chapter 8, Section 8.2, may offer an opportunity to reduce the thermal gradients in thick-section parts when combined with GRN 918, or another suitable epoxy powder.

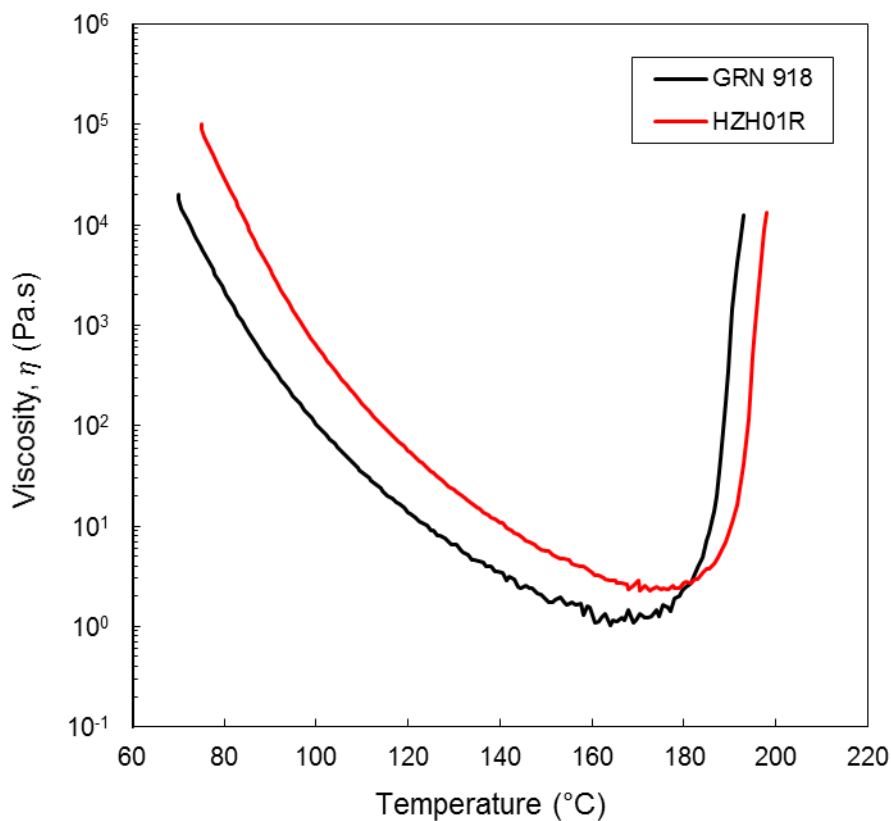


Figure 3.10. Comparison of the viscosity profiles for GRN 918 and HZH01R during a temperature scan at 5°C/min in a parallel-plate rheometer.

Tests were not performed for A-S-SET 02 due to downselection of the powders (see Section 3.3.5), however viscosity curves from the product datasheet are provided in Figure A.6 and Figure A.7 of the Appendices: A. Epoxy Powder Characterisation Data.

Tests were also carried out on conditioned samples (stored at 35°C, 70% RH for 1 week and then dried under vacuum at 40°C for at least 12 hr) to determine if there were any permanent effects on viscosity. Unlike the DSC tests which lacked enough sensitivity to measure any discernible change in the samples, the greater sensitivity of the rheometer measured a slight increase in viscosity for the conditioned samples (22% increase at 120°C), as shown in Figure 3.11. The difference may be attributed to a small increase in the DoC during conditioning, which was imperceptible with DSC.

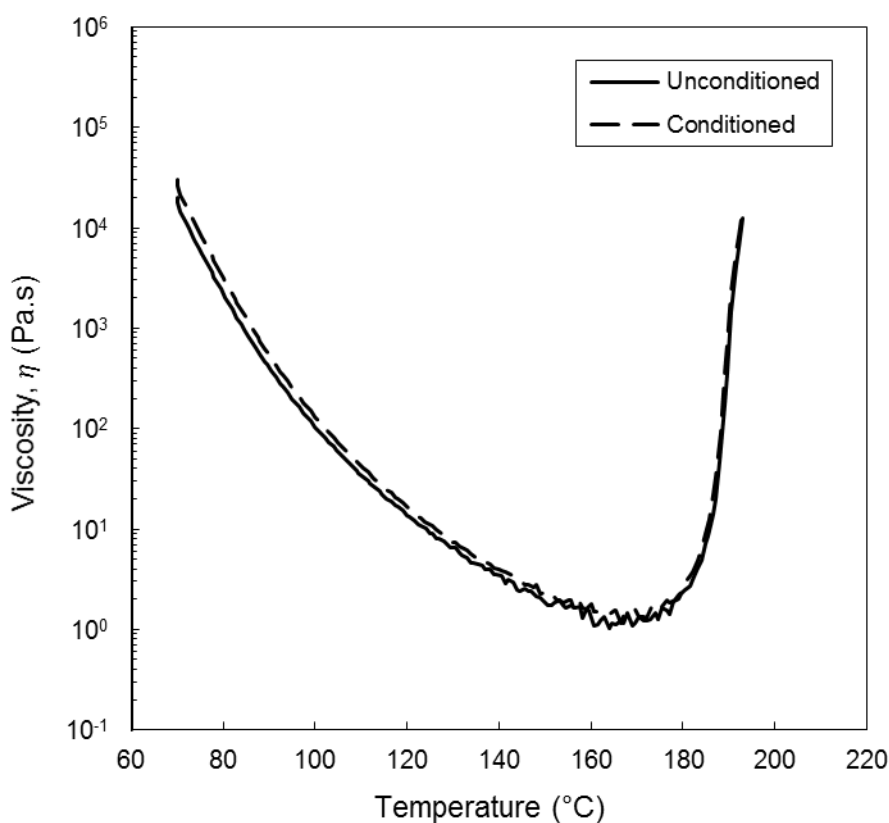


Figure 3.11. Comparison of viscosity profiles for conditioned and unconditioned GRN 918 samples tested at 5°C/min.

3.3.5 Crosslink Density

The crosslink densities for GRN 918 and Ampreg 22 are shown in Figure 3.12. The mean crosslink density of the Ampreg 22 specimens was approx. 2.7 times higher than the mean crosslink density of GRN 918.

It is known that the fracture toughness of ideal epoxy networks increases as the crosslink density decreases (Pascault *et al.*, 2002). This correlated with observations that the epoxy powders tended to be less brittle than typical untoughened epoxy systems. For example, Mamalis *et al.* (2018) found that the epoxy would plastically deform but not fracture during flexural testing.

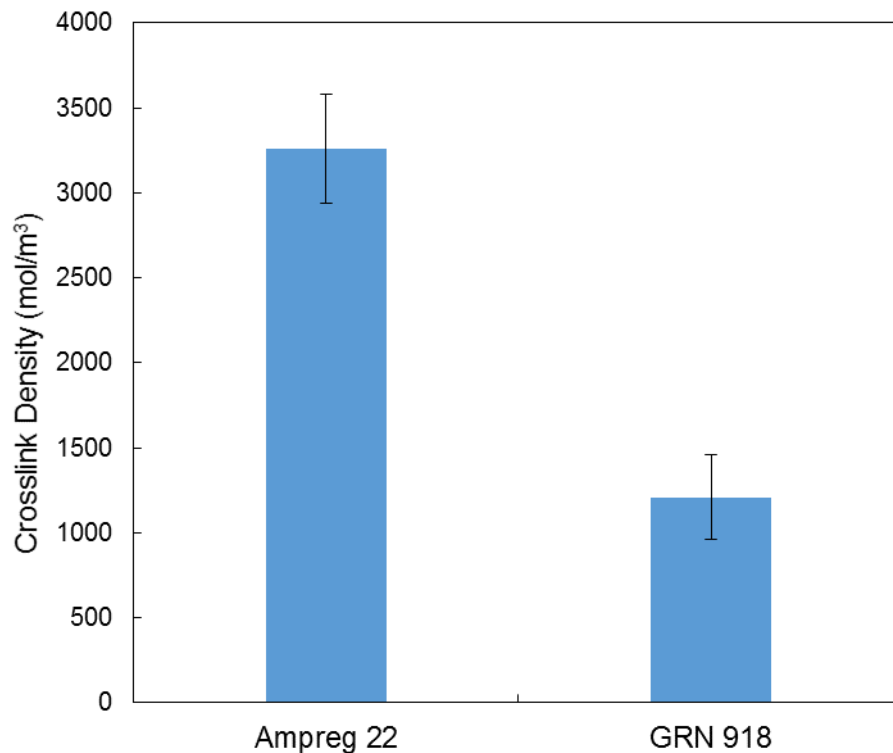


Figure 3.12. Comparison of crosslink densities for GRN 918 and Ampreg 22. The error bars represent ± 2 standard deviations.

As discussed in Chapter 2, Section 2.1.2, epoxy powders have already been successfully used as binders to toughen RTM-infused thermoset composites (Brody

and Gillespie, 2005a). At the time of writing, other researchers at The University of Edinburgh are investigating the interlaminar fracture toughness of fibre-reinforced epoxy powder (GRN 918) in combination with various fibre sizings. This is an important area of research for the design and manufacture of wind turbine blades due to the risk of composite delamination resulting in blade failures (Jacob *et al.*, 2009).

Another important consideration was how this relates to the moisture uptake and immersed ageing of composite materials. Grogan *et al.* (2018) showed that moisture was faster to diffuse into GF/Ampreg 22 composite specimens than for GF/GRN 918 composites, and that GF/Ampreg 22 exhibited a higher weight gain (approx. 1.2% w.r.t dry weight) than GF/GRN 918 (approx. 0.85% w.r.t dry weight). While the latter was attributed to the higher void content in the GF/Ampreg 22, the difference in rate of moisture uptake may also be connected to the difference in crosslink density. Highly crosslinked amine cured epoxies are known to exhibit high levels of hydrophilicity, with moisture uptake resulting in matrix swelling and plasticisation (Davies and Rajapakse, 2014). With this in mind, it is interesting to note that Grogan *et al.* (2018) measured a larger and more immediate increase in volume (swelling) for their immersed GF/Ampreg 22 samples than for their fibre-reinforced GRN 918 samples.

It should be noted that testing of A-S-SET 02 was also planned, however, it became apparent while manufacturing the test samples that it was not possible to process the A-S-SET 02 under vacuum due to the development of severe porosity (most likely due to volatilisation of some component in its formulation – see Figure A.8 in the Appendices: A. Epoxy Powder Characterisation Data). Additional manufacturing trials were attempted without vacuum, but the specimens were of very poor quality. As such A-S-SET 02 was eliminated from further study.

3.3.6 Water Vapour Sorption

At the outset of the project, it was known that epoxy powders were slightly hygroscopic, and initial testing showed that this had an adverse effect on the void content of the composite unless a drying cycle was used (Flanagan *et al.*, 2015). Figure 3.13 shows the sorption characteristics of GRN 918 under isothermal conditions

(23°C). The sample reached a maximum mass change of approx. 1.1%, however, it was clear that the sample had not reached equilibrium.

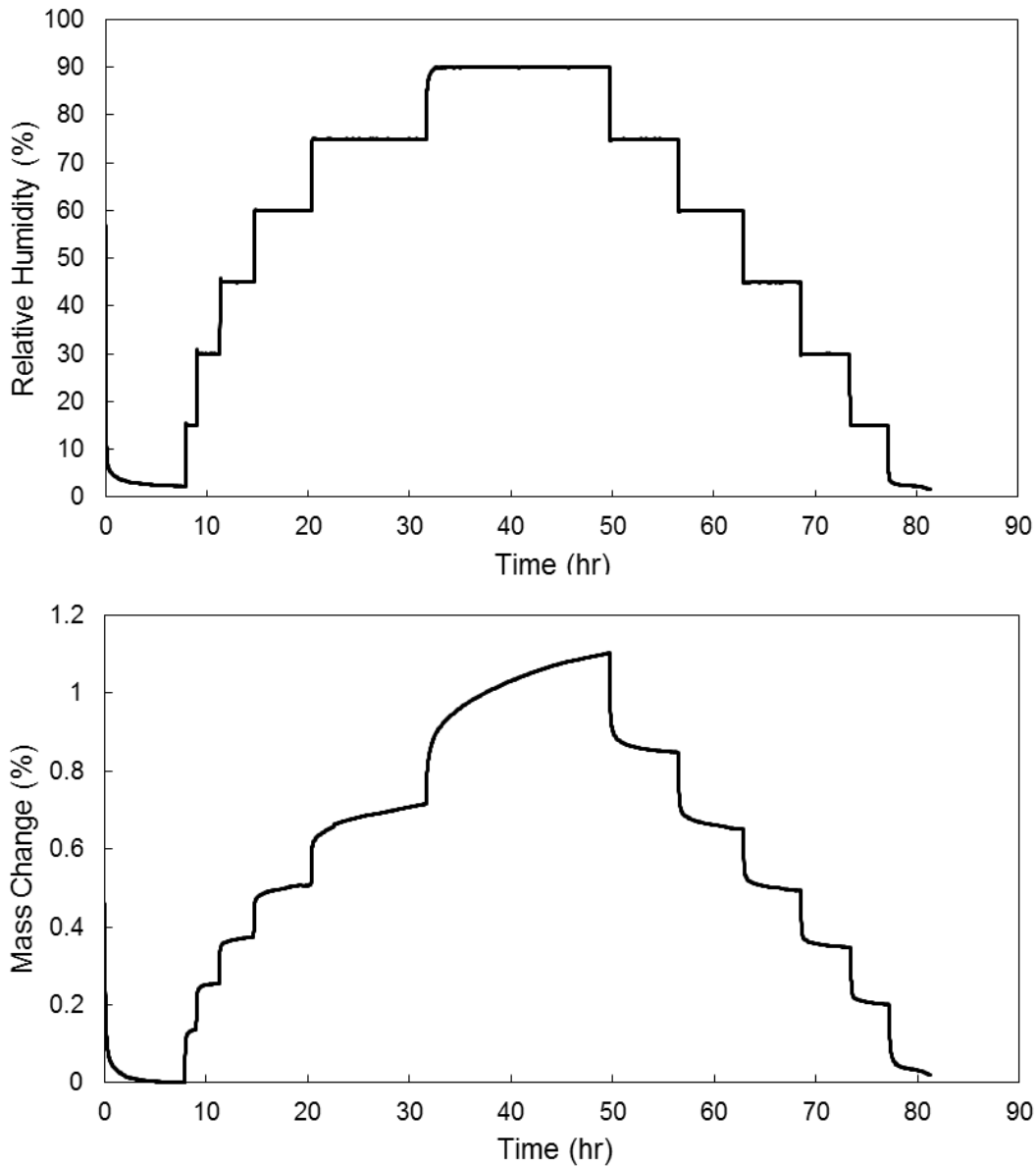


Figure 3.13. DVS of GRN 918 under isothermal conditions (23°C). (Top) The change in relative humidities (RH) w.r.t time. (Bottom) The mass change due to adsorption and desorption of water vapour.

Below 60% RH, GRN 918 showed a relatively fast response in mass change, equilibrating within an hour. At higher RH, however, the kinetics of adsorption changed with the initial fast response followed by more gradual mass change over several hours; possibly suggesting diffusion of water molecules into the bulk polymer. In relation to this latter point, hysteresis in the desorption curve suggested that some moisture was being retained in the powder until the RH was reduced further.

Additional isothermal tests were run at higher temperatures. Figure 3.14 shows that the rate of sorption was significantly affected by temperature; equilibrium was reached in 30 – 60 mins at 35°C, while the time to equilibrium was reduced to several minutes at 45°C. The total mass change at each RH also changed with temperature; reaching up to 1.36% for 35°C.

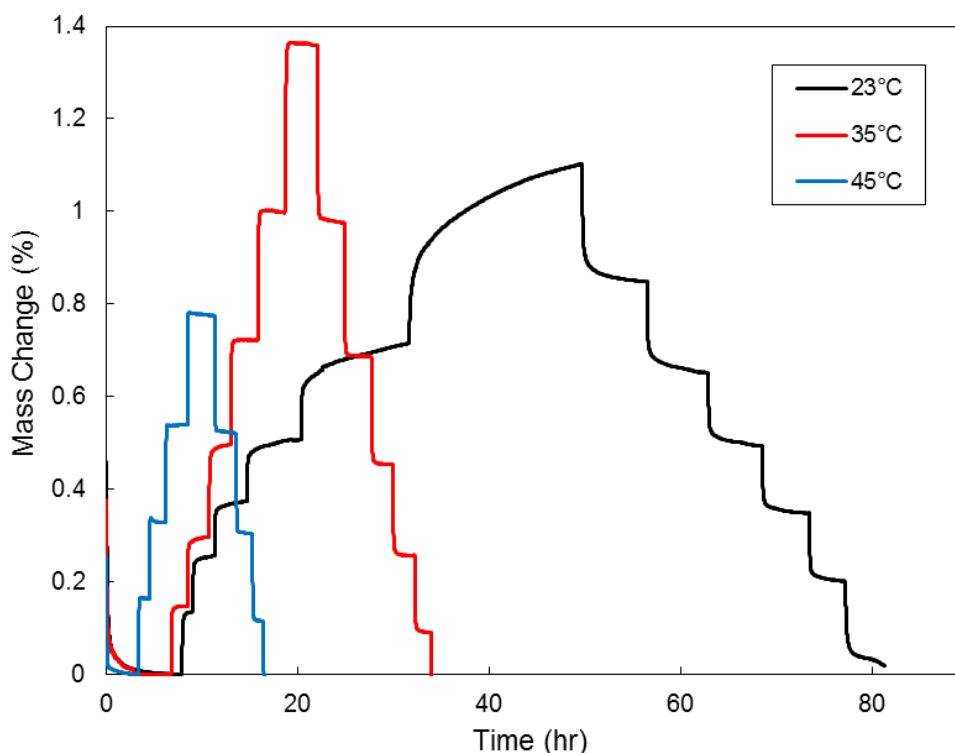


Figure 3.14. Mass change for GRN 918 at three different temperatures. Adsorption was highly temperature dependent, needing as little as several minutes to equilibrate at 45°C.

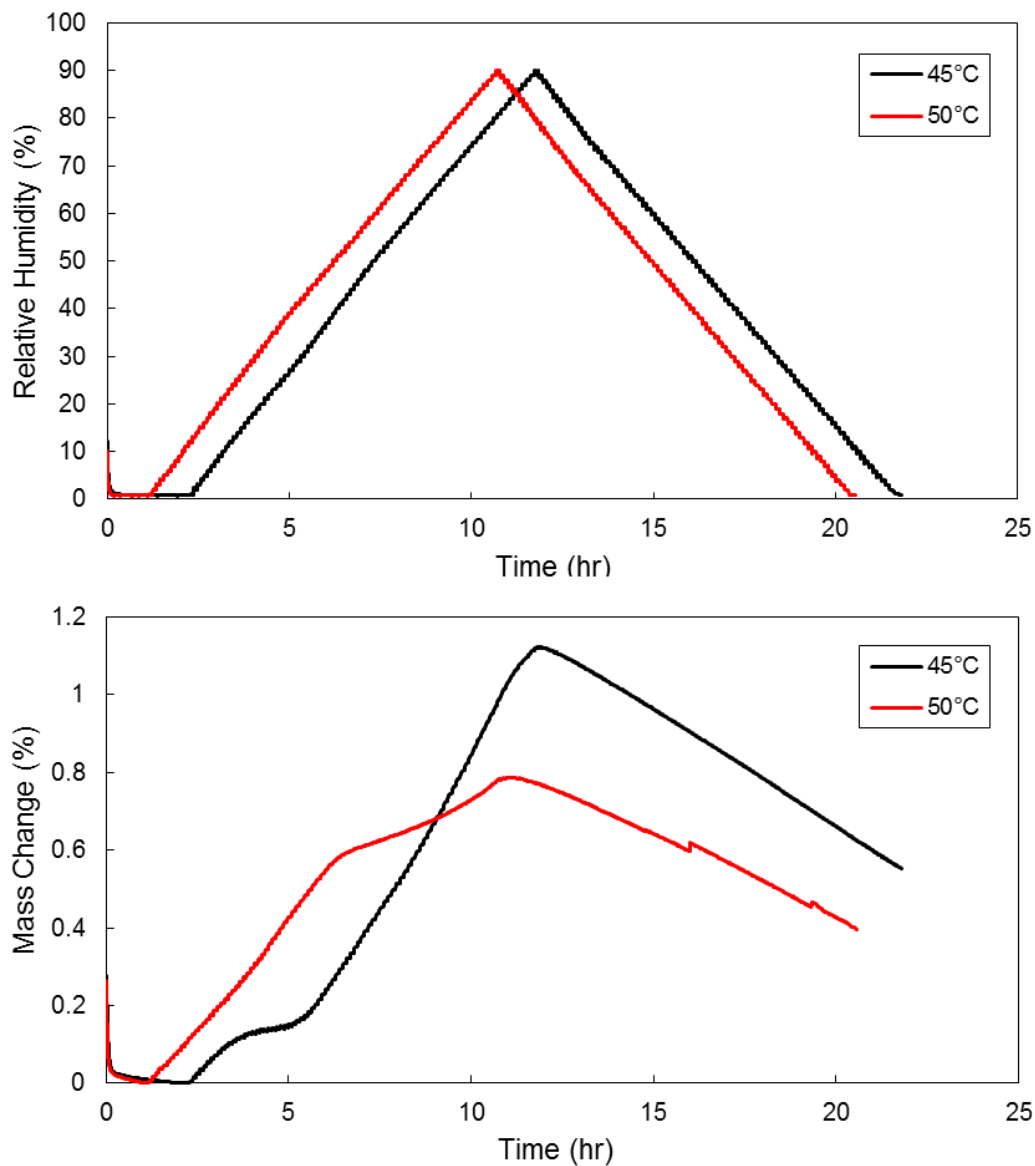


Figure 3.15. Mass change for GRN 918 at 45°C and 50°C using smaller increments of RH. The step in mass change for 45°C (at approx. 10% RH) may have been the glass-rubber transition, but it was only at higher RH that the powder sintered and became a rubbery liquid. In this latter form, the sorption behaviour changed dramatically. This effect was more evident for the 50°C isotherm, where the slope of the adsorption curve suddenly changed at 50% RH.

During testing at 45°C, it was noticed that above 60% RH, the powder underwent a glass-rubber transition. This showed that the storage stability was subject to both the temperature and RH conditions. The glass-rubber transition was investigated further,

using isothermal tests with smaller increments of RH. Figure 3.15 shows the result of the two tests at 45°C and 50°C. At 45°C, the powder underwent a transition that caused its mass to temporarily equilibrate between 16% RH and 26% RH. This was followed by further mass change until the powder reached a low enough viscosity that it sintered together under its own self-weight. The effect of sintering was more apparent for the test at 50°C, with the slope of the adsorption curve changing suddenly at approx. 50% RH. Visual observation of the test samples confirmed that the powder had completely sintered. Again, this showed the T_g of the powder was dependent on RH as well as temperature, but it also showed that the sorption characteristics were dependent on the form of the epoxy, with powder offering a far greater ratio of outer surface area to volume.

The latter point was made evident by testing sintered flakes of GRN 918 at 35°C, as shown in Figure 3.16. The kinetics of the mass change were greatly altered, most likely dominated by diffusion of water into the polymer bulk due to the reduced outer surface area of the epoxy. The samples failed to reach equilibrium at all levels of RH, and test was stopped prematurely due to time restrictions.

This behaviour may shed some light on why current drying cycles are so lengthy for conventional VBO prepregs (> 16 hr for large laminates (Centea, Grunenfelder and Nutt, 2015)). Having a powdered VBO prepreg may transition the drying process away from being diffusion-controlled, and to improve the through-thickness air permeability, thus allowing for significant reductions in drying time.

While these results are promising, they should be considered preliminary. Sorption science is a complex field of its own, and more analysis/modelling is required to test the above hypothesis.

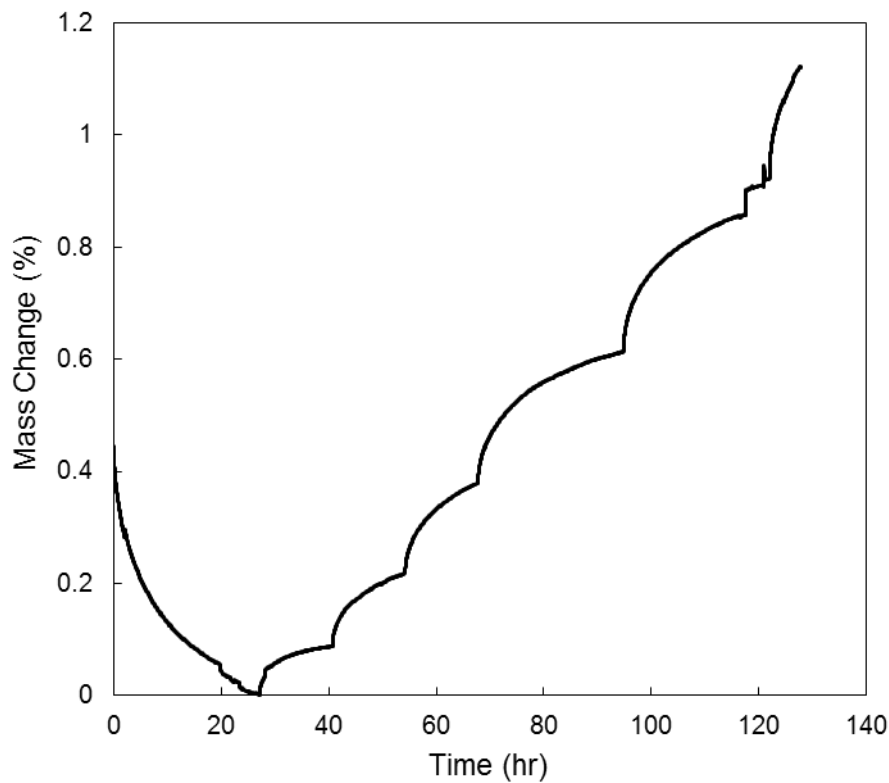


Figure 3.16. Mass change for flakes of sintered epoxy at 35°C. The response to changes in RH was much slower than for powder samples, with the sample failing to reach equilibrium at any stage. The test was cut short due to time restrictions.

3.4 Conclusions

Three epoxy powders have been experimentally characterised using several analysis techniques. The characterisation focused mainly on the processing behaviour of the powders and their suitability for manufacturing thick-section composites.

In all cases, the epoxy powders exhibited latent curing behaviour i.e. they had exceptional storage stability at ambient conditions, and curing peaked at high temperatures (between 150°C and 200°C). The latent behaviour also meant that curing occurred over a narrower temperature range, and the epoxy was fast reacting in this range. High curing rates can be an attractive feature for manufacturers, however, for thick-section composites, this advantage is often offset by the risk of thermal runaway.

Nevertheless, it was shown that epoxy powders produce relatively little heat (between 105.5 and 184 J/g) compared with conventional epoxy systems (> 400 J/g), and were thermally stable up to 350°C . For GRN 918, DMTA results showed that its lower enthalpy of reaction correlated with a relatively low crosslink density when compared to an infusion-grade epoxy system. This had implications for the mechanical properties of the cured epoxy, and may be linked to the immersed performance of the epoxy also. In terms of material downselection, manufacturing DMTA specimens revealed that A-S-SET 02 was not suitable for VBO processing due to the release of volatiles. As such, it was subsequently eliminated from further testing. The remaining two epoxy powders were tested using PPR. It was shown that both powders achieved sufficiently low viscosities for fibre-bed impregnation, however, GRN 918 was able to maintain a low viscosity over a wider temperature range prior to gelation. Consequently, GRN 918 was downselected due to the importance of processing flexibility for manufacturing thick-section composites.

As a secondary objective, it was of interest to the MARINCOMP project to determine how the epoxy powder would behave if used for manufacturing in countries with warmer climates, such as India. Additional DSC and PPR testing showed that a week of storage in tropical conditions (35°C , 70% relative humidity (RH)) had an insignificant effect on the cure kinetics or viscosity of GRN 918 as long as the samples were sufficiently dried after conditioning. Despite this, DVS tests showed that the T_g of GRN 918 was a function of both temperature and relative humidity (RH), and that sintering of the powder significantly affected the sorption characteristics of the powder, making it much more time-consuming to dry. Furthermore, melting/sintering of the powder would significantly change how it can be handled (i.e. it would no longer be possible to transport or deposit it as a powder). As such, the storage conditions must be a serious consideration when manufacturing with epoxy powders in warmer climates.

In summary, it has been shown that at least two of the investigated epoxy powders were suitable for VBO prepreg processing (i.e. GRN 918 and HZH01R). As has been discussed, however, GRN 918 displayed the most advantageous processing

characteristics for thick-section composites, while the other epoxy powders were in some way limited i.e. higher viscosity for HZH01R and extreme porosity for A-S-SET 02 due to volatilisation under vacuum. As such, the remaining chapters in this thesis were focused primarily on the use of GRN 918 in manufacturing thick-section composites.

4. Material Modelling of Epoxy Powder

4.1 Chapter Introduction and Overview

To understand more about how the chosen epoxy powder behaves under various processing conditions, it is beneficial to fit mathematical material models to the experimental characterisation data. Material models allow for the simulation of a material's response to external stimuli such as temperature and pressure.

This chapter outlines the selection and development of suitable material models for the GRN 918 epoxy powder, including models for cure kinetics, chemorheology, and powder sintering. The models are developed for use in process simulations for thick-section composite parts. Some simple simulations are carried out in this Chapter with the cure kinetics and chemorheological models to demonstrate the suitability of the downselected epoxy powder for vacuum-bag-only (VBO) processing.

4.2 Methodology

4.2.1 Differential Scanning Calorimetry

Additional DSC testing was required for fitting a semi-empirical cure kinetics model to GRN 918. The general test set-up was as described in Chapter 3, Section 3.2.3. The isothermal test temperatures of 160°C, 170°C, and 180°C were chosen based on the

curing behaviour recorded in the temperature scans in Chapter 3, Section 3.3.3. In all cases, an initial heating rate of 50°C/min was used to ramp the sample to the isothermal test temperature as quickly as possible.

Based on the 10°C/min temperature scans in Chapter 3, Section 3.3.3, the rate of curing peaked at temperatures above 120°C, however, in a realistic temperature cycle for thick-section parts, the resin would be cured at much slower ramp rates. As such, ramp rates of 0.5 - 1.5°C/min were used to gather additional information about the cure kinetics at temperatures lower than 120°C.

Additional DSC testing was carried out to determine the relationship between T_g and DoC for GRN 918. This testing was performed by Dr. Kapileswar Nayak at SE Blades Technology B.V. in Hengelo, the Netherlands. Samples were partially cured at 160°C, cooled to ambient temperature, and then re-heated using a temperature scan at 1.5°C/min. The data from these scans was used to determine the new T_g and corresponding DoC. The heat flow data from the DSC tests was converted into DoC values using Equations 2.5 and 2.6; the maximum total enthalpy of reaction, H_T , was 184.0 J/g (see Table 3.1 in Chapter 3, Section 3.3.3).

A final DSC test, which replicated the temperature cycle for composite processing, was performed on the GRN 918 powder to confirm the accuracy of the cure kinetics model. Details of this cycle are given in Section 4.3.1.

4.2.2 Parallel-plate Rheometry

In addition to the PPR tests described in Chapter 3, Section 3.2.4, isothermal PPR tests were carried out at 160°C, 170°C, and 180°C to assist in fitting GRN 918 to a chemorheological model. For the isothermal tests, the samples were ramped as quickly as possible to the test temperature; temperature overshoot was kept within 3°C for all tests, and thermal equilibrium was achieved within 30 s of reaching the test temperature. Similar to DSC testing, an additional PPR test was performed which replicated a realistic composite processing cycle. The aforementioned PPR tests were

performed using the general set-up and apparatus (AR 2000ex rheometer) described in Chapter 3, Section 3.2.4.

A HAAKE MARS II rheometer (Thermo Scientific) was used to perform a separate set of PPR tests which measured the compaction of the powder due to sintering. Khoun *et al.* (2009, 2010) showed that it was possible to measure the thickness change of an epoxy sample by monitoring the gap height between the parallel plates for a given normal force, as shown in Figure 4.1. For the MARS II rheometer, a Peltier module was used to heat the lower plate, and a PEEK sample hood was used for insulation. For all tests, the top plate was lowered onto the powder sample until it resisted compaction (the rheometer had a limiting normal force of 50 N). It was found that a normal force of 50 N was approximately equivalent to 52 kPa of pressure for 35 mm plates. Isothermal tests at 50°C, 55°C, and 60°C were carried out. The rheometer began recording the sample thickness as soon as the test temperature was reached.

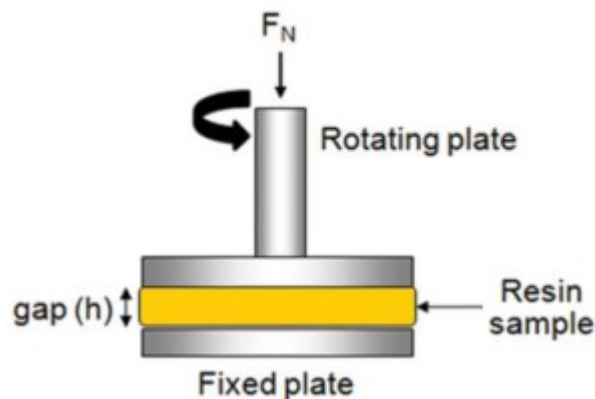


Figure 4.1. Illustration of a resin sample tested with a parallel-plate geometry; the gap height may be measured while a normal force is applied (Khoun and Hubert, 2010).

4.2.3 Cure Kinetics Modelling

Initial testing and modelling of epoxy powders (Maguire *et al.*, 2015) focused on fitting the powders to the Kamal-Sourour model (Equation 2.7) combined with a diffusion factor (Equation 2.11), however, the model lacked accuracy at lower

temperatures. The presence of a latent, heat-activated curing agent meant that the fitting of the rate constant, k_α [s^{-1}], was dominated by data at high temperatures and curing at low temperatures was misrepresented.

As such, an additional rate constant, $k_{\alpha 1}$, was added to the Kamal model (Equation 2.8) so that it could describe the curing behaviour at low temperatures. This modified model, which also included a diffusion factor, was written as follows:

$$\frac{d\alpha}{dt} = \frac{(k_{\alpha 1} + k_{\alpha 2} + k_{\alpha 3}\alpha^m)(1 - \alpha)^n}{1 + \exp[C(\alpha - \alpha_c)]} \quad (4.1)$$

The high temperature rate constants, $k_{\alpha 2}$ and $k_{\alpha 3}$, in Equation 4.1 were fitted to DoC data from the isothermal DSC tests at 160°C, 170°C, and 180°C. The low temperature rate constant, $k_{\alpha 1}$, was fitted to DoC data from the low rate temperature scans (i.e. 0.5°C/min, 1.0°C/min, and 1.5°C/min). MATLAB's in-built nonlinear least-squares curve fitting tool, "lsqcurvefit", was used to generate initial fitting parameters. These parameters were manually adjusted to achieve an exponential temperature dependence for each of the cure rate constants, $k_{\alpha i}$, as shown in Figure 4.2. Similar adjustments were performed to achieve a linear temperature dependence for the critical DoC, α_c . The remaining parameters were fitted constants. The cure kinetics model parameters for GRN 918 are given in Table 4.1.

It should be noted that the cure activation energies, E_2 and E_3 , were higher than what was reported typically for other epoxy systems [(Kenny and Opalicki, 1993; Khoun, Centea and Hubert, 2009; Kratz *et al.*, 2012; Garschke *et al.*, 2013; Lionetto, Moscatello and Maffezzoli, 2016)]. This was indicative of the epoxy powder's acute temperature dependency at higher temperatures. The presence of heat-activated curing agents in the epoxy powder formulation meant that curing occurred rapidly at high temperatures, while at lower temperatures the uncatalyzed reaction was significantly slower. This difference between the curing rates justified the inclusion of the additional cure rate constant in Equation 4.1.

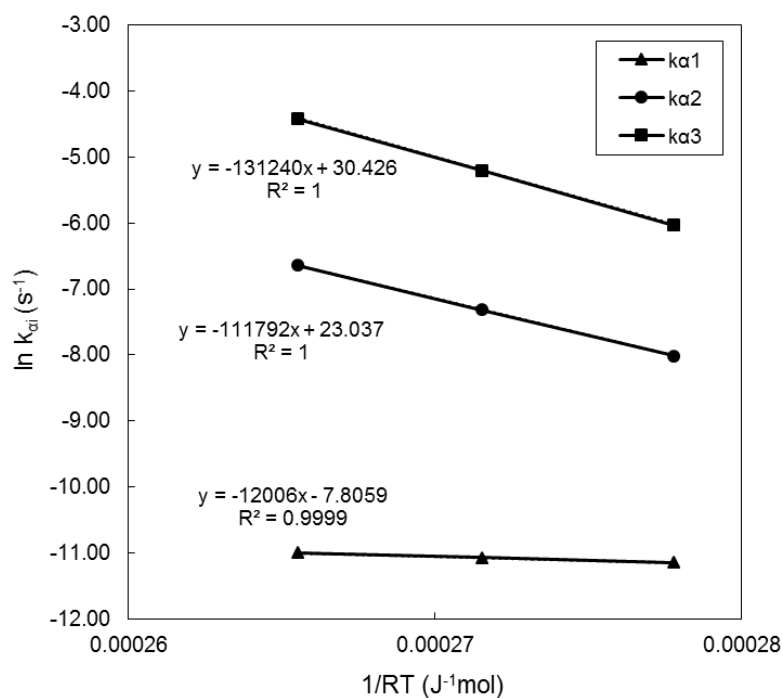


Figure 4.2. The log of each rate constant varied linearly as a function of temperature. The cure activation energy was the slope of the line, and the pre-exponential constant was determined from the exponential of the intercept.

Table 4.1. Fitted cure kinetics parameters for GRN 918 epoxy powder.

Parameter [units]	Value	Parameter [units]	Value
$A_{\alpha 1}$ [s^{-1}]	4.073×10^{-4}	m	1.24
$E_{\alpha 1}$ [J/mol]	12006	n	1.8
$A_{\alpha 2}$ [s^{-1}]	10.112×10^9	C	50
$E_{\alpha 2}$ [J/mol]	111792	α_c	$0.006 T - 1.748$
$A_{\alpha 3}$ [s^{-1}]	1.636×10^{13}		
$E_{\alpha 3}$ [J/mol]	131240		

$$\frac{d\alpha}{dt} = \frac{(k_{\alpha 1} + k_{\alpha 2} + k_{\alpha 3}\alpha^m)(1 - \alpha)^n}{1 + \exp[C(\alpha - \alpha_c)]}, \quad k_{\alpha i} = A_{\alpha i} \exp\left(\frac{-E_{\alpha i}}{RT}\right), \quad i = 1, 2, 3$$

The DiBenedetto equation (Equation 2.13) was used to fit the relationship of DoC and T_g . The T_g was taken as being the onset of the step change in DSC heat flow data. The initial glass transition temperature, T_{g0} , and the final glass transition temperature, $T_{g\infty}$, were determined from data for uncured and fully cured GRN 918, respectively. Intermediate values of DoC, and the corresponding T_g , were determined using additional temperature scan data of partially cured samples. A heating rate of 1.5°C/min was used to determine the T_g in each case. This heating rate was chosen as being representative of the heating rates used for processing thick-section composite parts. The DiBenedetto model parameters for GRN 918 are given in Table 4.2.

Table 4.2. Parameters for the DiBenedetto model.

Parameter [units]	Value
T_{g0} [°C]	40
$T_{g\infty}$ [°C]	106
λ	0.53

$$\frac{T_g - T_{g0}}{T_{g\infty} - T_{g0}} = \frac{\lambda\alpha}{1 - (1 - \lambda)\alpha}$$

4.2.4 Chemorheological Modelling

Initial chemorheological modelling focused on fitting the epoxy powder behaviour to the Castro-Macosko model (Equation 2.16) (Maguire *et al.*, 2015). It was found to be unsuitable, however, because the temperature dependence of the uncured resin viscosity could not be fitted to the Arrhenius expression (Equation 2.17). Instead, when plotted on a log scale, the viscosity changed in a non-linear fashion regardless of the heating rate that was used (see Figure 4.3).

As such, chemorheological data for GRN 918 was fitted to Equation 2.18; a Williams-Landel-Ferry (WLF) type model, which was developed by (Kenny and Opalicki, 1993)

because they found similar discrepancies when fitting toughened epoxies to the Castro-Macosko model. Parameters $C_{\eta 1}$ and $C_{\eta 2}$, along with the unreacted resin viscosity, η_{g0} , were fitted to temperature scan data from the PPR tests. The fitting constant, A , was determined using isothermal data. The intersection of the storage modulus and loss modulus data was used to determine the gel point for the various PPR tests. By combining this information with the cure kinetics model, as shown in Figure 4.4, it was possible to determine the DoC at the gel point, α_g . The chemorheological model parameters for GRN 918 are given in Table 4.3. It should be noted that the cure kinetics model and DiBenedetto model were used to inform the chemorheological model in terms of α and T_g , respectively.

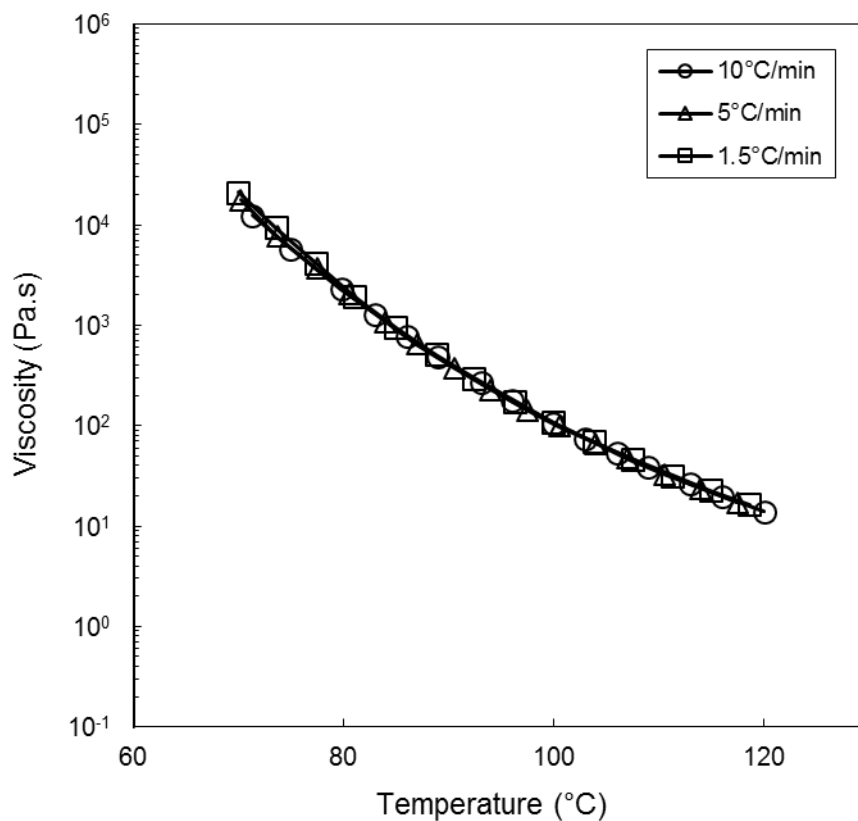


Figure 4.3. The initial viscosity of GRN 918 epoxy powder. The viscosity changed w.r.t. temperature was the same regardless of heating rate. This suggested that this behaviour was unrelated to the DoC of the epoxy because DoC was rate dependent.

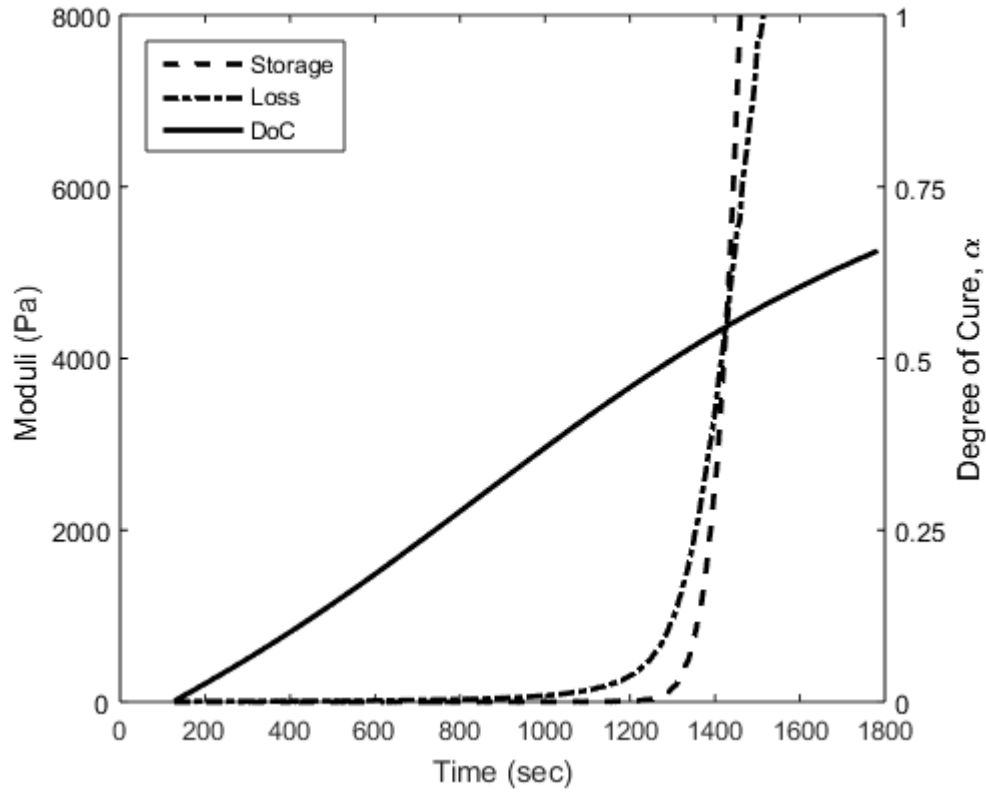


Figure 4.4. The gel point of the epoxy was assumed to occur at the crossover in storage and loss moduli. The cure kinetics model was used to estimate the corresponding DoC.

Table 4.3. Chemorheological model parameters for GRN 918 epoxy powder.

Parameter [units]	Value
η_{g0} [Pa.s]	2×10^{11}
$C_{\eta 1}$	32.25
$C_{\eta 2}$	30
α_g	0.56
A	1.6

$$\eta = \eta_{g0} \exp\left(\frac{-C_{\eta 1}[T - T_g(\alpha)]}{C_{\eta 2} + T - T_g(\alpha)}\right) \left(\frac{\alpha_g}{\alpha_g - \alpha}\right)^A$$

4.2.5 Modelling of Powder Melting and Sintering

As has been discussed in Chapter 2, Section 2.3.2, being able to determine the heat flow to/from the epoxy resin was an important consideration for heat transfer analysis of the overall system. In the same way that the cure kinetics model was required to describe the exothermic heat flow from the epoxy as it cured, another model was required to describe the endothermic heat flow due to the reversal of enthalpic relaxation. Equation 2.1, a model for powder melting, was fitted to DSC temperature scan data of GRN 918. The endothermic heat flow data was converted into the degree of melt (DoM, θ ; see Equation 2.1) in the same manner that exothermic heat flow data was converted into DoC data in Section 4.2.3 (the total enthalpy of relaxation was 7.1 J/g). The fitted parameters are given in Table 4.4. It was found that the melting point of the powder, T_m , varied as a function of the heating rate, S (units of K/min). This was expected as Equation 2.1 was based on a simple temperature-dependent function that did not account for any time dependency.

Table 4.4. Parameters for powder melting model.

Parameter [units]	Value
k_m	1.83
T_m [K]	$3.43 \times S + 313.48$
d	4.65

$$\frac{d\theta}{dT} = k_m e^{(-k_m(T-T_m))} [1 + (d-1)e^{(-k_m(T-T_m))}]^{d/(1-d)}$$

While Equation 2.1 describes the melting of the powder, it was shown by Greco and Maffezzoli (2003) that the melting process did not result in instantaneous sintering and compaction. As discussed in Chapter 2, Section 2.2.1, the process of sintering was dependent on viscosity reduction and surface tension, and had been previously modelled by Kandis and Bergman (1997) using an Arrhenius type semi-empirical

model. Initial attempts to fit the sintering data to this model were unsuccessful. Given that the viscosity data could not be fitted to an Arrhenius type model either, an attempt was made to model the sintering behaviour of the epoxy powder using the following WLF type model,

$$\frac{d\chi}{dt} = -\chi_0 \exp\left(\frac{C_{\chi 1}[T - T_{\theta}]}{C_{\chi 2} + T - T_{\theta}}\right) (\chi - \chi_{\infty})^B \quad (4.2)$$

Where χ_0 is a pre-exponential rate constant, χ_{∞} is the powder void fraction at infinity time, and T_{θ} is the onset temperature for melting [K]. $C_{\chi 1}$, $C_{\chi 2}$, and B are fitting constants.

The above model was fitted to data from the isothermal PPR tests described in Section 4.2.2, with the WLF type equation giving a better representation of the powder's sintering behaviour. The sintering model parameters for GRN 918 are given in Table 4.5.

From the PPR tests, the initial powder void fraction was estimated as being approx. 0.503. This was confirmed by manually compacting powder in a 5 ml graduated cylinder and weighing it on a microbalance.

Table 4.5. Parameters for the sintering model.

Parameter [units]	Value
χ_0	3×10^{-5}
$C_{\chi 1}$	11.5
$C_{\chi 2}$	24.5
T_{θ} [K]	313.48
χ_{∞}	0.0
B	0.5

$$\frac{d\chi}{dt} = -\chi_0 \exp\left(\frac{C_{\chi 1}[T - T_{\theta}]}{C_{\chi 2} + T - T_{\theta}}\right) (\chi - \chi_{\infty})^B$$

4.3 Results and Discussion

4.3.1 Cure Kinetics

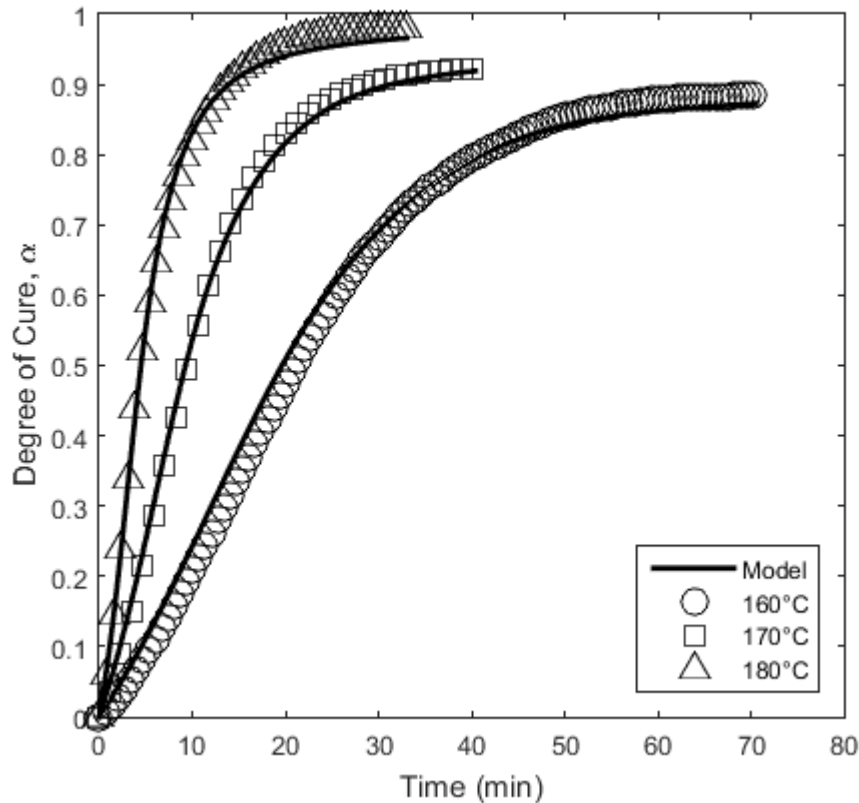


Figure 4.5. Comparison of the isothermal DoC data and cure kinetics model for GRN 918.

Figure 4.5 and Figure 4.6 show the experimental DoC data compared to the cure kinetics models. The overall agreement between the model and experiments was good, with the transition to a diffusion-controlled reaction evident in Figure 4.5. At high temperatures and fast heating rates, the kinetics of the catalysed reaction were dominant. Nevertheless, Figure 4.6 shows that a small amount of cure (approx. 5% conversion) developed at temperatures under 120°C when a slower heating rate was used (1.5°C/min). The ability to model this behaviour was important due to the time scales and heating rates involved in manufacturing thick-sections. Neglecting the cure kinetics at lower temperatures could result in poor predictions of the processing viscosity and subsequently poor impregnation of the fibre reinforcement.

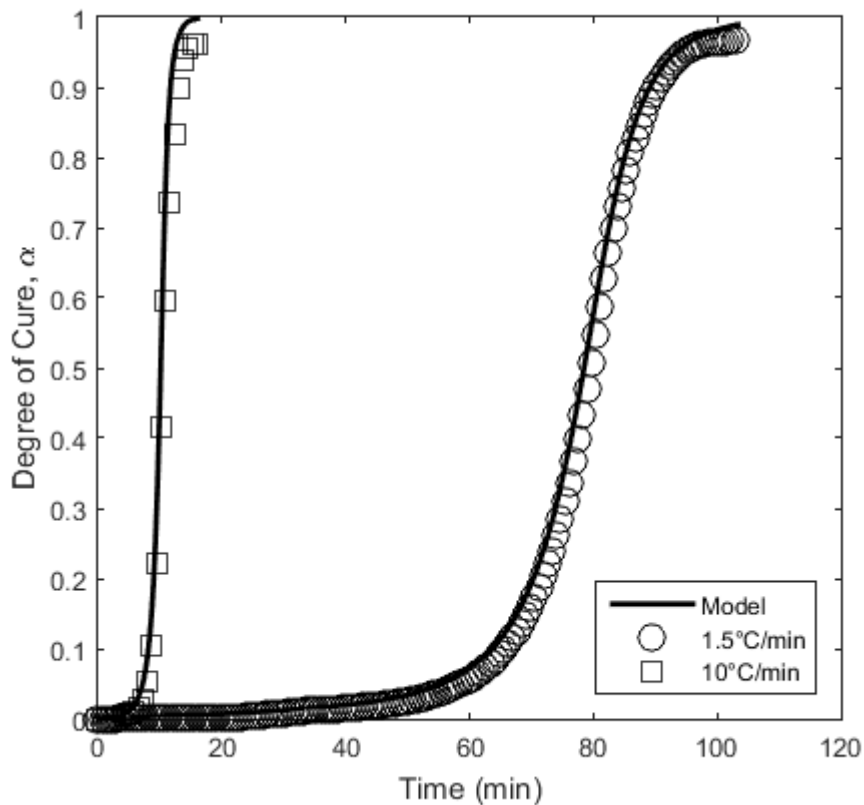


Figure 4.6. Comparison of the temperature scan data and cure kinetics model for GRN 918.

Plots of the isothermal DSC data, as well as additional temperature scan plots at lower ramp rates, are given in the Appendices: A. Epoxy Powder Characterisation Data (Figure A.9 and Figure A.10, respectively). Also given in the Appendices is Table A.1, which shows the total enthalpy of reaction for each DSC test used in performing the cure kinetics modelling.

To better illustrate the importance of the model's accuracy at lower temperatures, it was useful to simulate a temperature cycle for composite processing and validate it using DoC data from a DSC test. The DSC test was run for the following temperature cycle (the purpose of each stage is outlined):

- Stage 1: The temperature was ramped to 120°C at 1.5°C/min and held at that temperature for 60 min. This stage would be used to consolidate an individual part such as a wind turbine skin or spar.

- Stage 2: The temperature was ramped down to ambient conditions at 1.5°C/min. This would allow the composite part to solidify so that it could be assembled with the other parts.
- Stage 3: Stage 1 was repeated. This stage would be performed on the assembled composite parts so that the epoxy could fuse at the bond lines to form a single structure.
- Stage 4: The temperature was ramped to 180°C at 1.5°C/min. This stage would allow the assembled parts to be co-cured.

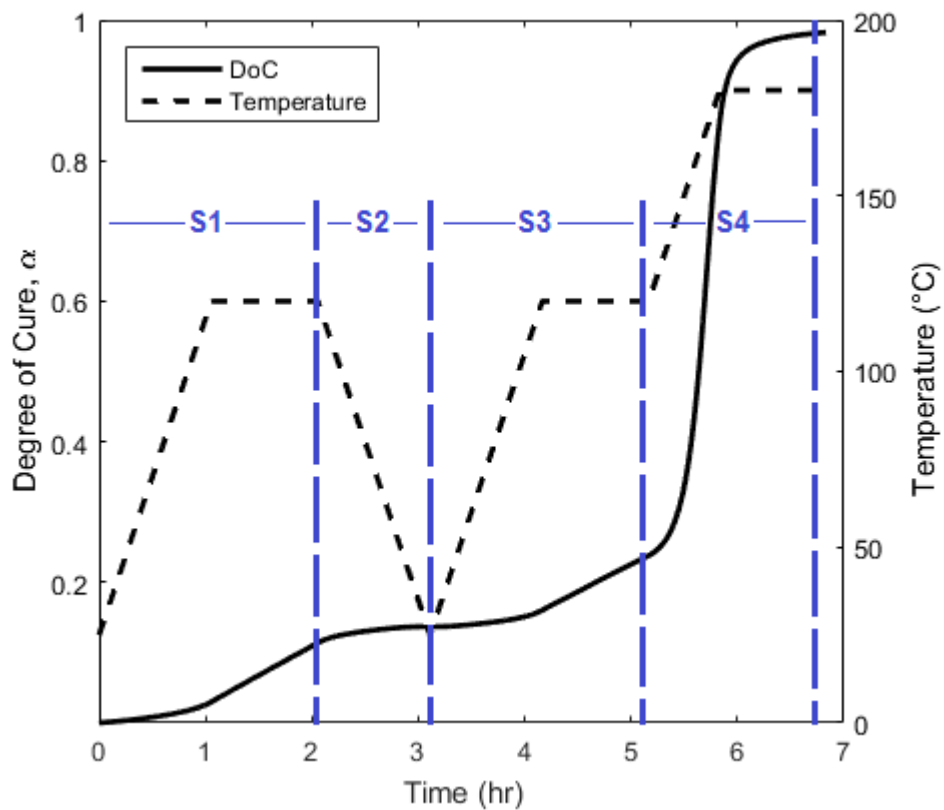


Figure 4.7. Cure kinetics simulation of a typical temperature cycle for processing epoxy powder composites. The stages of the cycle are outlined (i.e. S1 is Stage 1, etc.).

During the low temperature stages of the temperature cycle (Stages 1 – 3), the cure kinetics model predicted 24% conversion (see Figure 4.7). The progression of cure for these stages was difficult to measure from the DSC test data due to the relatively small

exothermic heat flow that was generated. Nevertheless, by measuring the residual enthalpy of reaction for Stage 4, it was possible to determine that 22.8% conversion had been achieved during Stages 1 – 3. This confirmed the accuracy of the model at low temperatures. As a comparison, another simulation was performed without the additional rate constant in Equation 4.1, and 12.1% conversion was predicted.

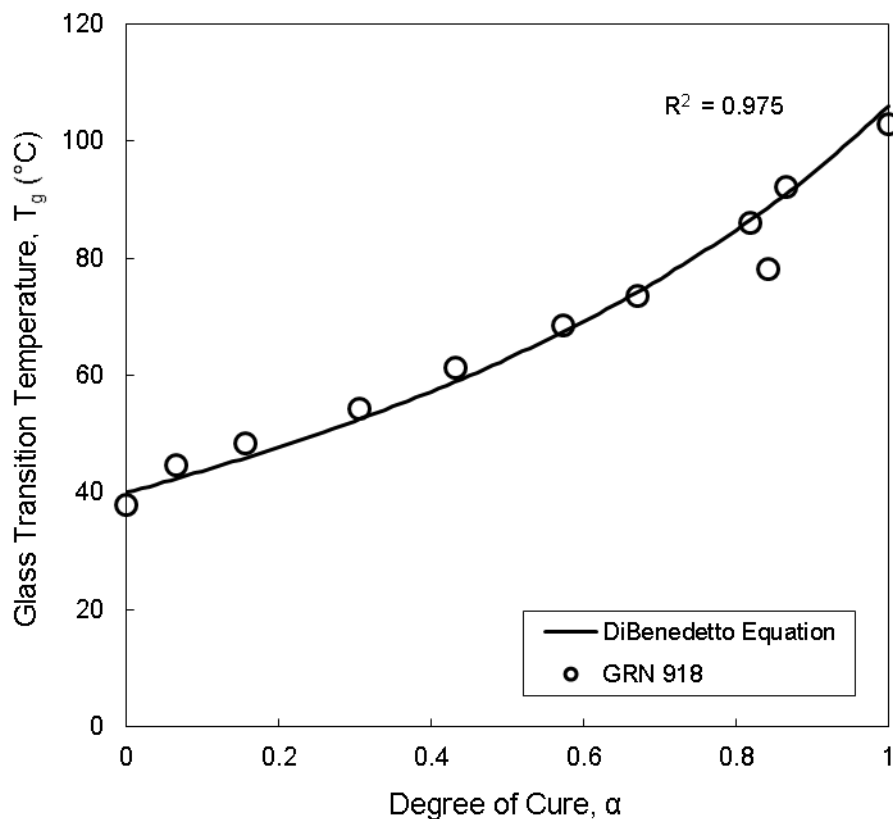


Figure 4.8. Plot of the DSC test results showing the non-linear relationship between T_g and DoC. The DiBenedetto Equation (Equation 2.13) was fitted to the data.

Given the difficulty of measuring the heat flow at lower temperatures, it was expected that even better accuracy could be achieved for the cure kinetics model by holding the samples isothermally between the powder's T_g and 120°C for prescribed lengths of time and then measure the residual enthalpy of reaction to determine the DoC

advancement. The downside of this approach is that it would be time-consuming; requiring many more tests to be performed.

The relationship between the DoC and T_g for GRN 918 is shown in Figure 4.8. It was found that the relationship became non-linear above the gel point (at DoC = 0.56); a characteristic that was captured by the DiBenedetto Equation (Equation 2.13). This model was used to determine the T_g and to inform the chemorheological model (Equation 2.18).

4.3.2 Chemorheology

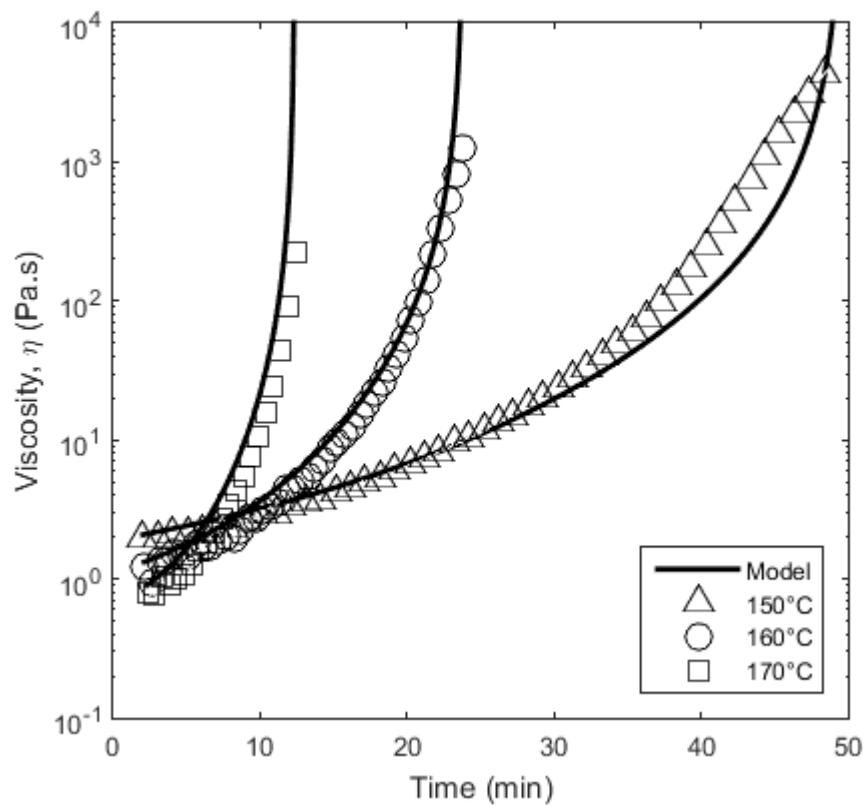


Figure 4.9. Comparison of the isothermal viscosity data and the chemorheological model for GRN 918. The viscosity increased due to the curing of the epoxy.

The Kenny-Opalicki model (Equation 2.18) was able to accurately capture the chemorheological behaviour of GRN 918, as shown in Figure 4.9 and Figure 4.10.

As previously mentioned, conventional epoxy systems display a logarithmic decrease in viscosity as a function of temperature, and can be modelled using the well-known Castro-Macosko model. This was clearly not the case for GRN 918 which behaved like a toughened epoxy system. The accuracy of the model in describing the initial viscosity reduction (shown in Figure 4.10) was particularly important for modelling resin flow in thick-section composites due to the highly non-isothermal nature of the process.

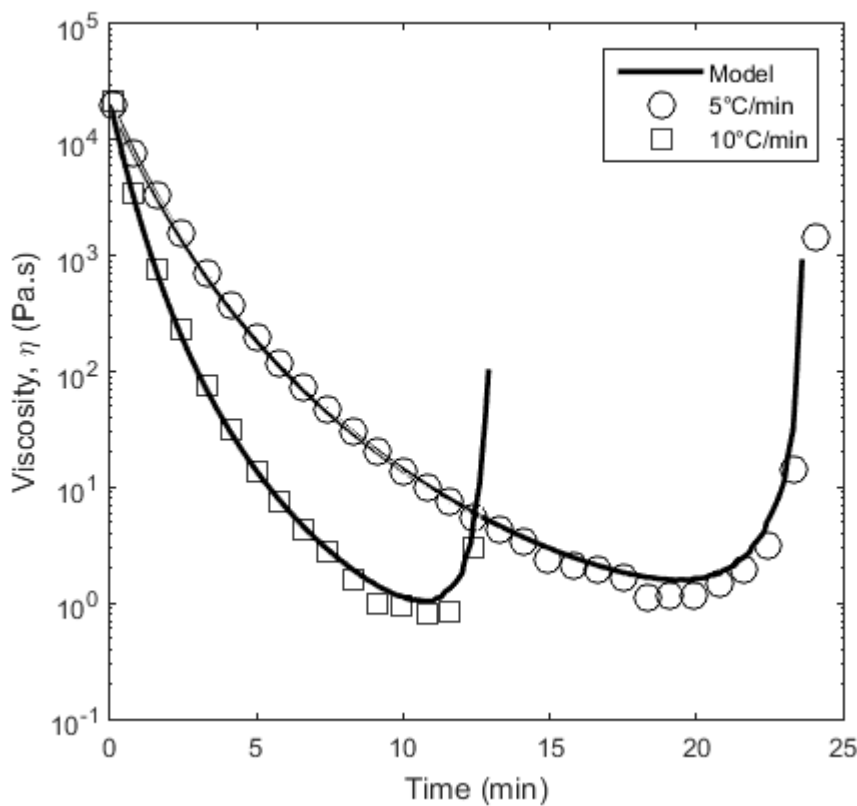


Figure 4.10. Comparison of viscosity data for a temperature scan and the chemorheological model data for GRN 918.

In each test case shown, the viscosity sharply rose as it approached the gel point; a characteristic feature of crosslinking systems. The model treated this increase in viscosity as tending towards infinity. In practice, this would result in the cessation of resin flow and act as a natural upper limit in the processing window. This upper limit

dictated the processing flexibility of the polymer matrix and was an important aspect for manufacturing thick-section composite parts.

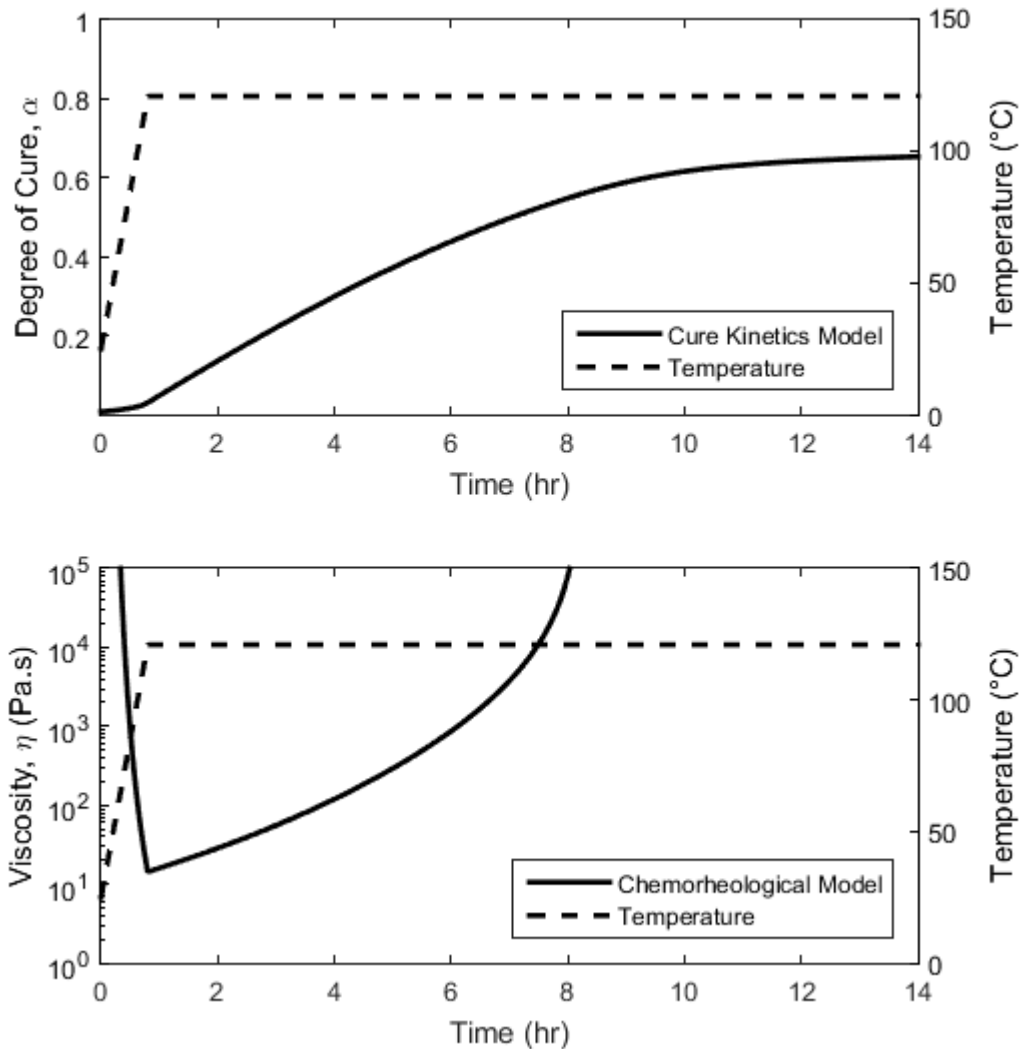


Figure 4.11. DoC and viscosity profiles (top and bottom plots, respectively) for GRN 918. The temperature cycle was a 2°C/min temperature ramp to 121°C and then held isothermally.

Kratz *et al.* (2012) used chemorheological models to demonstrate the processing flexibility of two VBO prepreg resin systems (Cytac Cycom 5320-1, and ACG MTM45-1) and an autoclave prepreg resin system (Hexcel Hexply 8552). They calculated the DoC and viscosity, w.r.t. time, for a basic temperature cycle; a 2°C/min temperature ramp to 121°C, followed by an isothermal dwell for several hours).

Replicating this simulation with the models for GRN 918 showed that the epoxy powder was relatively stable at 121°C (see Figure 4.11); it took several hours for it to reach the gel point (i.e. 56% conversion) and then the DoC plateaued.

To quantify the processing window, Kratz *et al.* (2012) used the chemorheological models to determine the “flow time” as a function of temperature (defined as the time at which the resin viscosity was < 100 Pa.s). They showed that the maximum flow time achievable for the two VBO prepreg resins was approximately 2 hr. This method was replicated for GRN 918, with the results showing that just over 3 hr of “flow time” was possible with the GRN 918 (see Figure 4.12). The “flow time” peaked at approx. 117°C; above which it steadily decreased. This was due to an increasing cure rate as the latent curing agent was activated.

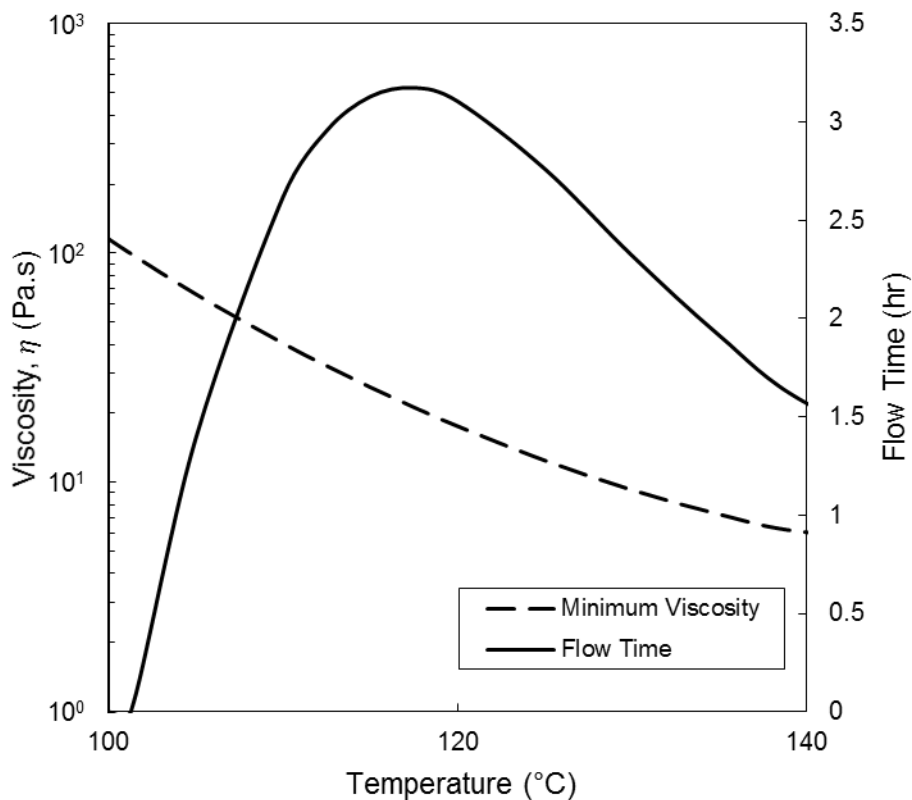


Figure 4.12. The “flow time” as a function of temperature for GRN 918, and minimum viscosity at each temperature. The values were determined by ramping to a set temperature at 2°C/min and then holding isothermally until the viscosity increased above 100 Pa.s.

The minimum viscosity, w.r.t temperature, was plotted in Figure 4.12 also. The minimum viscosity is temperature-dependent and has an important role in reducing the infusion time i.e. the viscosity is inversely proportional to the flow velocity (see Equation 2.19 in Chapter 2, Section 2.3.1). For example, processing at 110°C or 127°C would result in the same “flow time”, but the minimum viscosity at 110°C would 2.5 times higher than at 127°C.

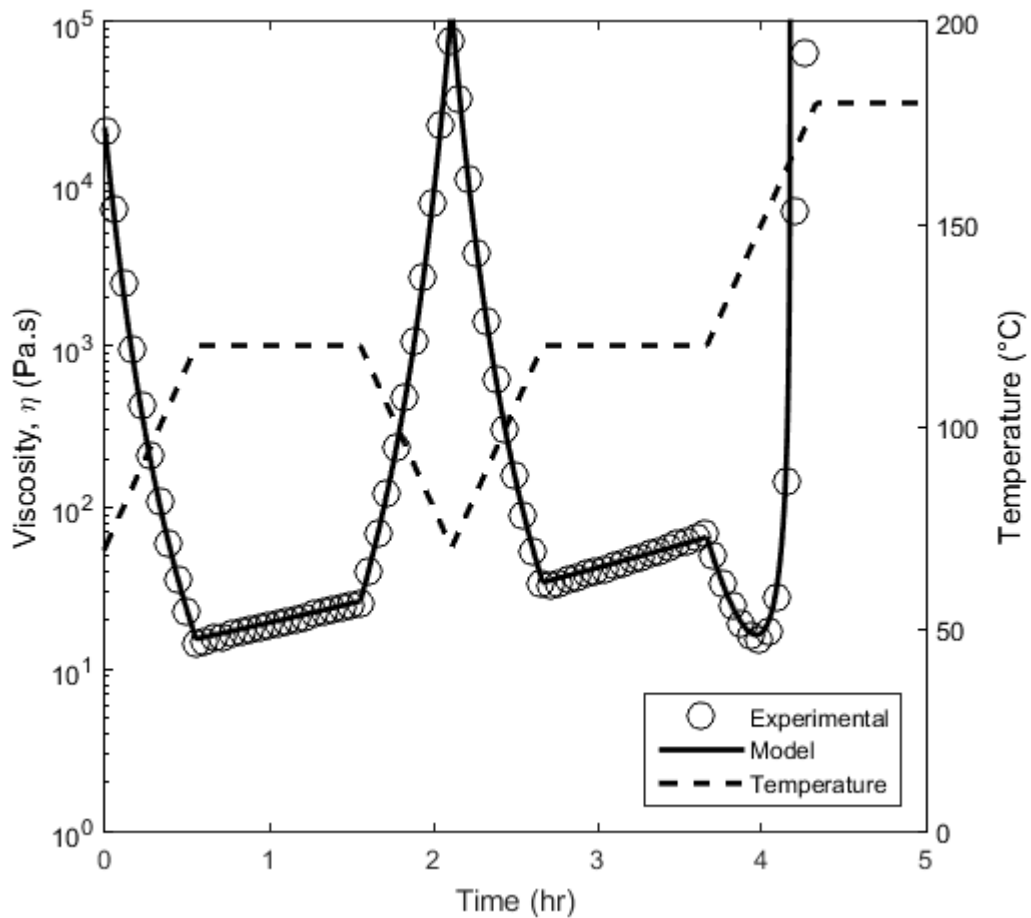


Figure 4.13. Comparison of experimental viscosity data and the chemorheological model data for the temperature cycle described in Section 4.3.1.

The temperature cycle described in Section 4.3.1 was used to further investigate the processing flexibility of the powder epoxy and validate the chemorheological model for a typical temperature cycle. Due to the stability of the curing reaction below 120°C,

and the above ambient T_g of the epoxy powder, Figure 4.13 confirms that the epoxy powder can behave similarly to a thermoplastic polymer at lower temperatures, i.e. it can be melted, solidified, and then re-melted. It should be noted, however, that this ability was limited by the gradual increase in DoC which caused a corresponding increase in viscosity. Over the duration of the two isothermal stages at 120°C, the viscosity rose by 54 Pa.s. While this meant that the viscosity was still below 100 Pa.s by the time the curing stage began, the temperatures within thick-section composites will not adhere strictly to the prescribed temperature cycle due to the lag in through-thickness heat transfer.

It is expected that full consolidation of thick-sections (> 50 mm thick) would require most of the resin's available "flow time". Nevertheless, subsequently co-curing the thick-section part (e.g. a wind turbine blade spar) to other sections (e.g. the blade skins) would not require < 100 Pa.s. Instead, the parts would simply need to achieve intimate contact at the bonding interface and be at a sufficiently low DoC to allow interdiffusion and crosslinking of the polymers so that a strong bond is formed. At the time of writing, there was no data on the relationship between initial DoC and the bond strength of co-cured laminates, but it is suggested that this would be an interesting and beneficial area of research.

4.3.3 Powder Melting and Sintering

Figure 4.14 shows the results of the powder melting model compared to the DSC data, which has been converted into DoM values. As can be seen, the melting transition was dependent on the heating rate used. Given this time-dependency, powder melting and enthalpic relaxation may be better described by using an Arrhenius type expression. Nevertheless, Equation 2.1 was deemed sufficient for the current application because enthalpic relaxation was expected to have a relatively small impact on heat transfer in thick-section composites; the total enthalpy of relaxation was 7.1 J/g.

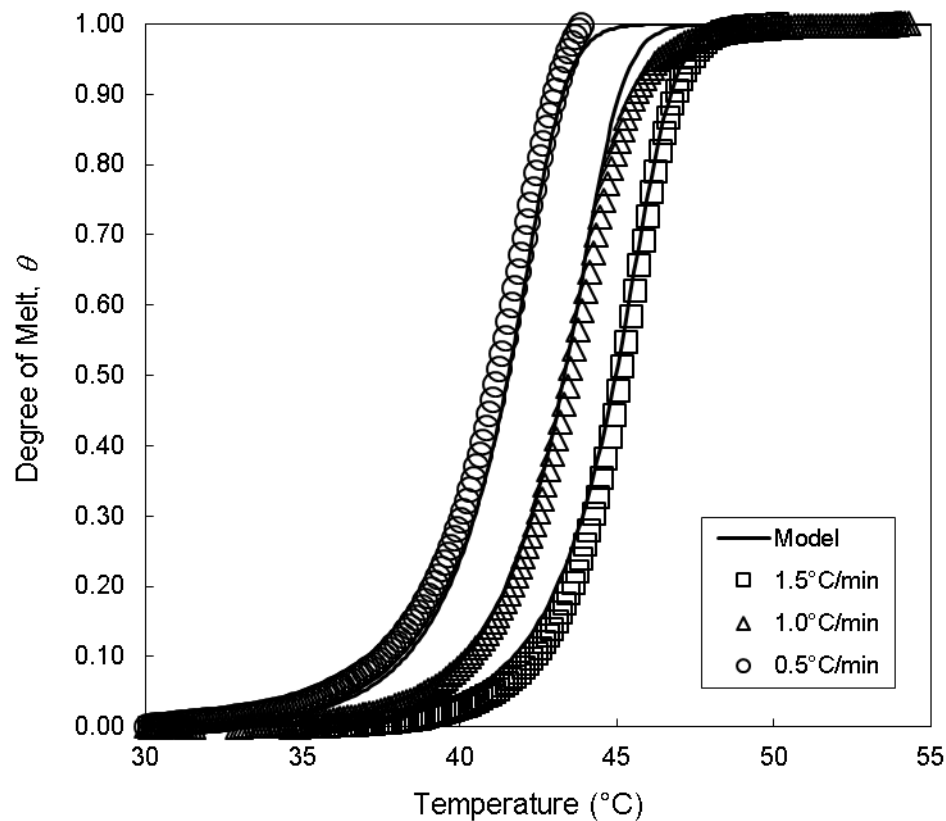


Figure 4.14. Comparison of the experimental data for GRN 918 and the model used to describe the powder melting process (Equation 2.1). There was a noticeable shift in the melting transition when the heating rate was increased.

While the melting model was used to describe the enthalpic relaxation of the powder, the actual transition from powder to liquid was described by the sintering model. As shown in Figure 4.15, Equation 4.2 was relatively accurate in describing the sintering behaviour of the GRN 918 powder. The sintering process corresponded to a 50% reduction of the powder sample's thickness. This highlighted that using epoxy powder would significantly increase the initial thickness of a composite preform compared to liquid epoxy.

Discrepancies between the data and model could be a result of the experimental set-up, which relied upon one-sided heating and an insulating sample hood. Use of a full environmental chamber may have given better temperature control, but it was unavailable at the time of testing.

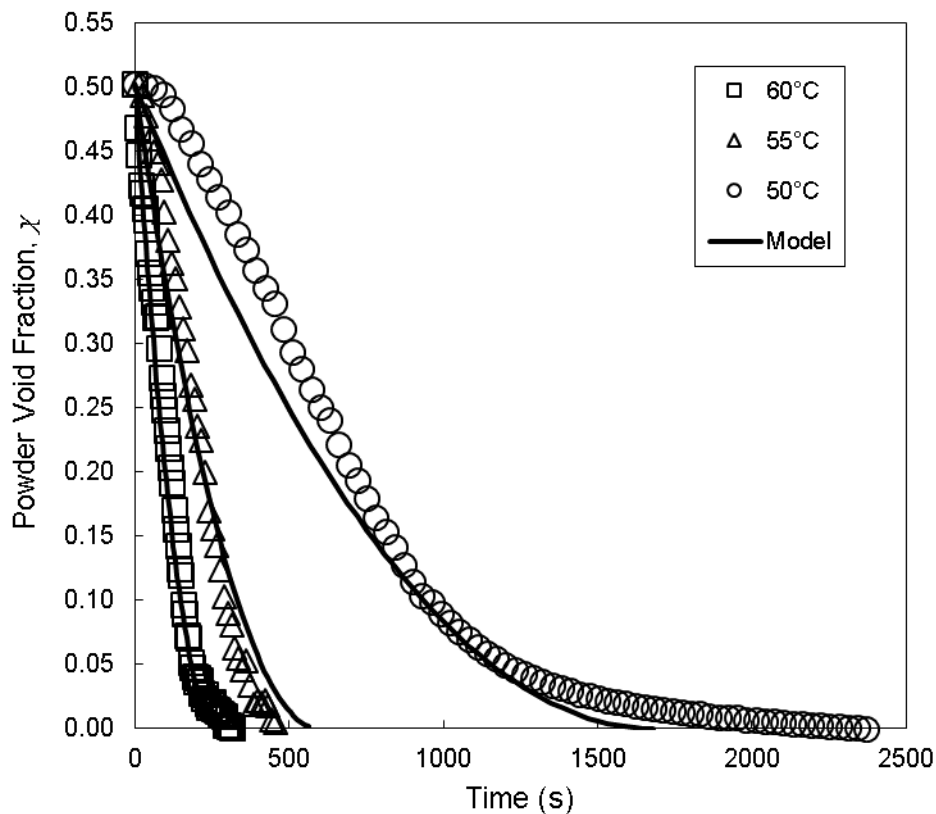


Figure 4.15. Results of the sintering model and experimental data for GRN 918. Note that the sintering process occurred at a higher temperature than the powder melting process. This was due to initial viscosity of the powder particles being too high to overcome their surface tension.

Another limitation of the test results was that the applied pressure was 52 kPa rather than 101.35 kPa (i.e. it was roughly half the pressure that would be expected for VBO processing). As such, the relationship of applied pressure and rate of sintering is not fully understood, and an improvement would be to repeat tests under various levels of applied pressure and determine if there was any significant effect. With the rheometer's max normal force being limited to 50 N, the easiest way to achieve this would be to use smaller plates (i.e. 25 mm diameter plates) and then to vary the applied force.

4.4 Conclusions

Several material models have been fitted to experimental data for GRN 918 epoxy powder. These models described the epoxy's cure kinetics, the evolution of its T_g , its chemorheological behaviour, and the sintering of the powder.

DSC data was used to develop a cure kinetic model which could describe the curing behaviour of epoxy powders over a wide range of temperatures. At low temperatures, the epoxy powder displayed slow rates of curing, however, upon activation of latent curing agents at higher temperatures ($> 120^\circ\text{C}$), the temperature-dependency of the cure rate changed significantly. It was found that the addition of a third cure rate constant to the well-known Kamal model allowed the model to capture this behaviour. The accuracy of the model was verified by experimentally replicating a typical composite temperature cycle and comparing the cure evolution to simulated results.

DSC data was also used to characterise the relationship between the degree of cure and the epoxy's T_g . It was found that DiBenedetto Equation accurately captured the non-linear increase in the T_g above the epoxy's gel point.

The cure kinetics model and DiBenedetto Equation were used in conjunction with experimental viscosity data to determine the fitting parameters for a chemorheological model. It was shown that the epoxy powder could be modelled accurately using an existing chemorheological model for toughened epoxy systems. Simulations with the chemorheological model confirmed the relative stability of the epoxy powder at 121°C . At this temperature, GRN 918 could maintain a viscosity below 100 Pa.s for up to 3 hours, while achieving a minimum viscosity of 10 - 20 Pa.s. Furthermore, it was shown that the epoxy took several hours to reach its' gel point when held isothermally at this temperature.

Similar to DSC testing, a typical composite temperature cycle was replicated using parallel-plate rheometry. The results showed that, at and below 120°C , the epoxy could be processed in a similar manner to a thermoplastic polymer, (melting and re-melting without significant increases in the DoC). This process flexibility could allow composite parts to be infused separately and then co-cured to form a finished structure

without the need for adhesive bond lines or fastened joints. The relationship between DoC and the strength of co-cured joints remains unclear, however, and may warrant further study.

A final use of the DSC data was to model the reversal of the enthalpic relaxation of the epoxy powder. This reversal resulted in an endothermic peak in the heat flow data which was fitted to a simple function for modelling the melting of thermoplastic powders. Although small, the endothermic peak was expected to make some contribution to the overall temperature distribution within a thick-section composite part during processing.

A separate model was developed to describe the sintering of the powder. To capture this behaviour, experiments were performed in a parallel-plate rheometer which monitored the thickness of a powder sample as the sintering process occurred. A WLF type equation was developed because existing models could not sufficiently describe the temperature dependence of the sintering process. It was shown that the volume of the GRN 918 epoxy powder reduced by approx. 50% during sintering.

Overall, the GRN 918 epoxy powder was shown to have good processing flexibility when compared to other commercial epoxy systems for VBO prepregs, and reasonable accuracy was achieved for the material models presented.

5. One-dimensional Process Simulations

5.1 Chapter Introduction and Overview

Prior to this chapter, the thesis has been focussed on the analysis of small epoxy powder samples using programmed temperature cycles, however, divergence from these cycles is unavoidable when manufacturing thick-section composite parts. It is impossible to know whether the overall manufacturing process will benefit from the seemingly advantageous characteristics of the epoxy powder without taking a more holistic view of the system. This system includes key processes such as resin flow and heat transfer, which can be modelled mathematically.

This chapter focuses on the development of a finite difference code for simulating the manufacture of thick-section structures using epoxy powder technology. Process models are presented for coupled resin flow and heat transfer. These process models are combined with the material models developed in earlier Chapters to describe how temperature, degree of cure (DoC), degree-of-impregnation (DoI), viscosity, and thickness evolve during the manufacturing process.

5.2 Methodology

5.2.1 Resin Flow Model

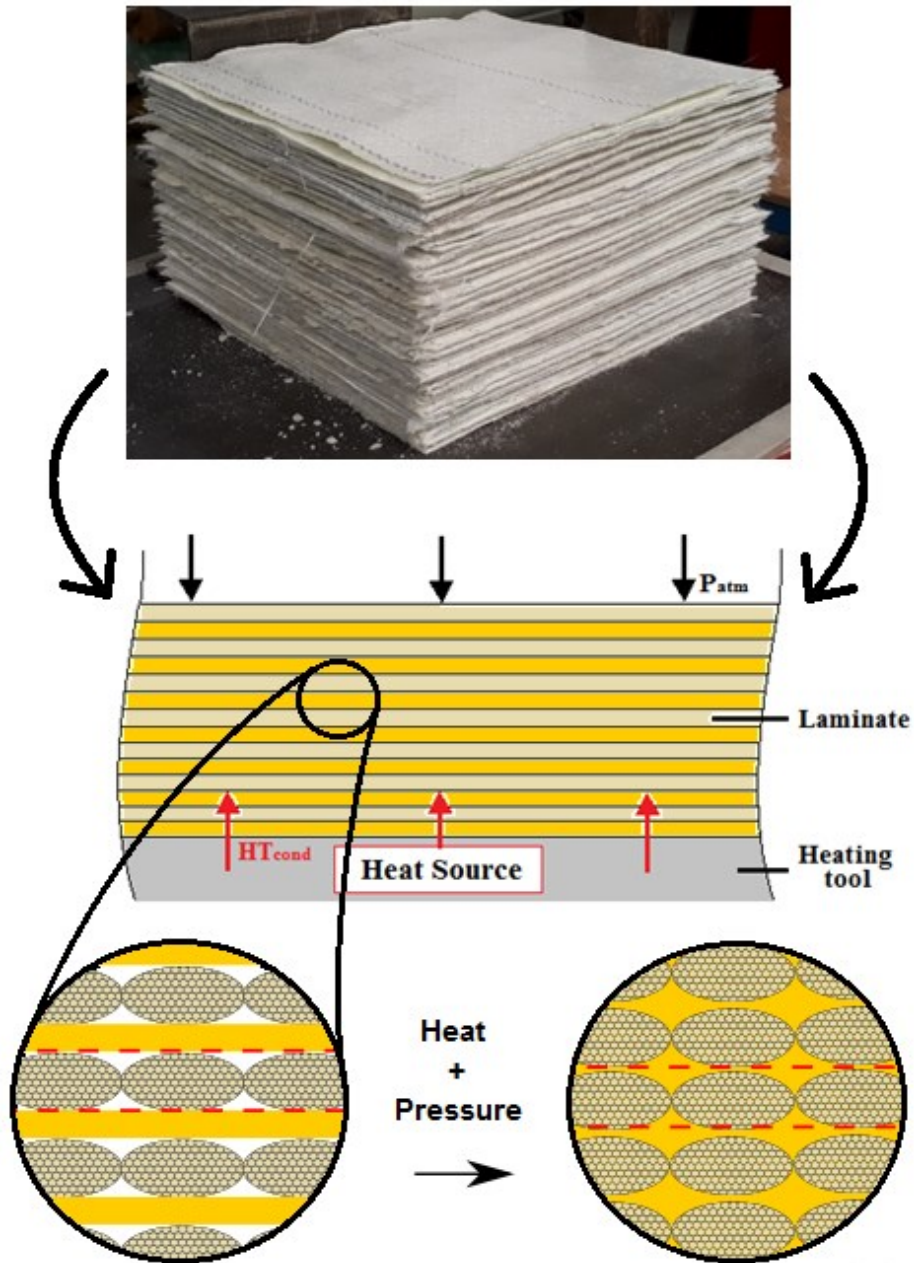


Figure 5.1. (Top) A thick laminate lay-up of glass-fibre/epoxy-powder VBO prepreg plies. (Middle) Schematic representation of the VBO prepreg with alternating layers of resin and fabric. (Bottom) Zoomed-in images of the VBO prepreg arrangement. As heat and pressure are applied, the resin flows into the fabric layers.

As previously described in Chapter 2, Section 2.3.1, vacuum-bag-only (VBO) prepregs are plies of fabric reinforcement partially impregnated with resin on one or both sides. When manufacturing thick laminates, a prescribed number of plies are stacked on top of each other, as shown in Figure 5.1. At the beginning of the manufacturing process, the lay-up of plies is effectively a system of alternating resin and fabric layers. As heat and pressure are applied, the resin viscosity drops, and the resin is forced to flow into the fabric layer, leading to a change in laminate thickness.

Figure 5.2 illustrates the resin flow pattern which is expected for an epoxy powder based VBO prepreg i.e. resin flow around the fibre tows (inter-tow flow), followed by resin flow into the fibre tows (intra-tow flow).

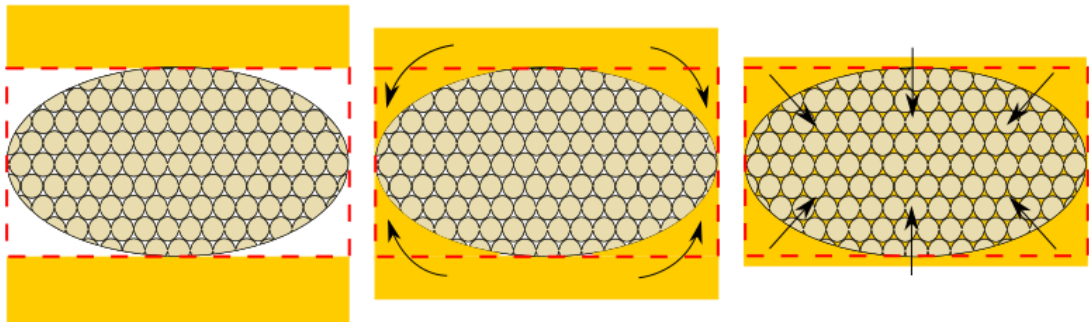


Figure 5.2. Schematic of the flow pattern in VBO prepregs. (Left) Assuming the DoI is zero, no resin has flowed into the fabric layer (red dashed line). (Middle) Resin flows first into the inter-tow space due to its higher permeability. (Right) Resin then flows into the low permeability tow.

For the model development, the following assumptions are made:

- Compaction due to gas evacuation is instantaneous
- The resulting fibre-bed is incompressible
- Nesting of fibre tows is negligible
- Resin flows through-thickness only (i.e. no in-plane flow)
- Resin flows into the adjacent fabric layers only (i.e. no global resin flow through multiple layers)

Under these assumed conditions, there is a fixed volume of inter-tow space and intra-tow space that the resin could flow into and fill. The dual scale resin flow models

developed by Cender *et al.* (2013) (Equations 2.22 and 2.23 in Chapter 2, Section 2.3.1) are chosen as a suitable basis for modelling the epoxy powder VBO prepreg system. Some modifications are required, however, to adapt the equations for the highly transient temperature conditions of thick-section composite processing.

To solve for transient temperature conditions (i.e. accounting for viscosity change due to temperature and degree of cure (DoC)), Darcy's Law (Equation 2.19) is rewritten as,

$$\frac{dl}{dt} = -\frac{K}{\varphi\eta(T, \alpha)} \cdot \frac{dP}{dx} \quad (5.1)$$

Where l is the flow front position [m] at any time t [s], K is the permeability [m^2], φ is the porosity, $\eta(T, \alpha)$ is the temperature and cure dependent resin viscosity [Pa.s], and P is pressure [Pa].

Equation 5.1 is integrated over the pressure boundary conditions for inter-tow flow, $P|_{x=0} = P_{app}$ and $P|_{x=l} = 0$,

$$\int_0^l \frac{dl}{dt} dx = \int_{P_{app}}^0 -\frac{K}{\varphi\eta(T, \alpha)} \cdot \frac{dP}{dx} dx \quad , \quad l < L_1 \quad (5.2)$$

$$\frac{dl}{dt} = \frac{K_1}{\varphi_1\eta(T, \alpha)} \frac{P_{app}}{l} \quad , \quad l < L_1 \quad (5.3)$$

Where L_1 is the characteristic length of the inter-tow region [m], K_1 is the inter-tow permeability [m^2], φ_1 is the inter-tow porosity, and P_{app} is the pressure applied by the vacuum bagging [Pa]. The viscosity, $\eta(T, \alpha)$, is modelled using the method outlined in Chapter 4, Section 4.2.4. The viscosity couples the resin flow model to the heat transfer and cure kinetics models via the temperature dependency and DoC dependency, respectively.

For intra-tow flow, Equation 5.1 is integrated over pressure boundary conditions of $P|_{x=0} = P_{L1}$ and $P|_{x=l} = 0$,

$$\frac{dl}{dt} = \frac{K_2}{\varphi_2\eta(T, \alpha)} \cdot \frac{K_1 P_{app}}{K_2 L_1 + K_1(l - L_1)} \quad , \quad l \geq L_1 \quad (5.4)$$

Where the pressure at the boundary of the intra-tow region is,

$$P_{L1} = \frac{K_1 P_{app} (l - L_1)}{K_2 L_1 + K_1 (l - L_1)} \quad (5.5)$$

Where K_2 is the intra-tow permeability [m^2], and φ_2 is the intra-tow porosity. The derivation of Equation 5.5 is given in the Appendices: B. Process Models.

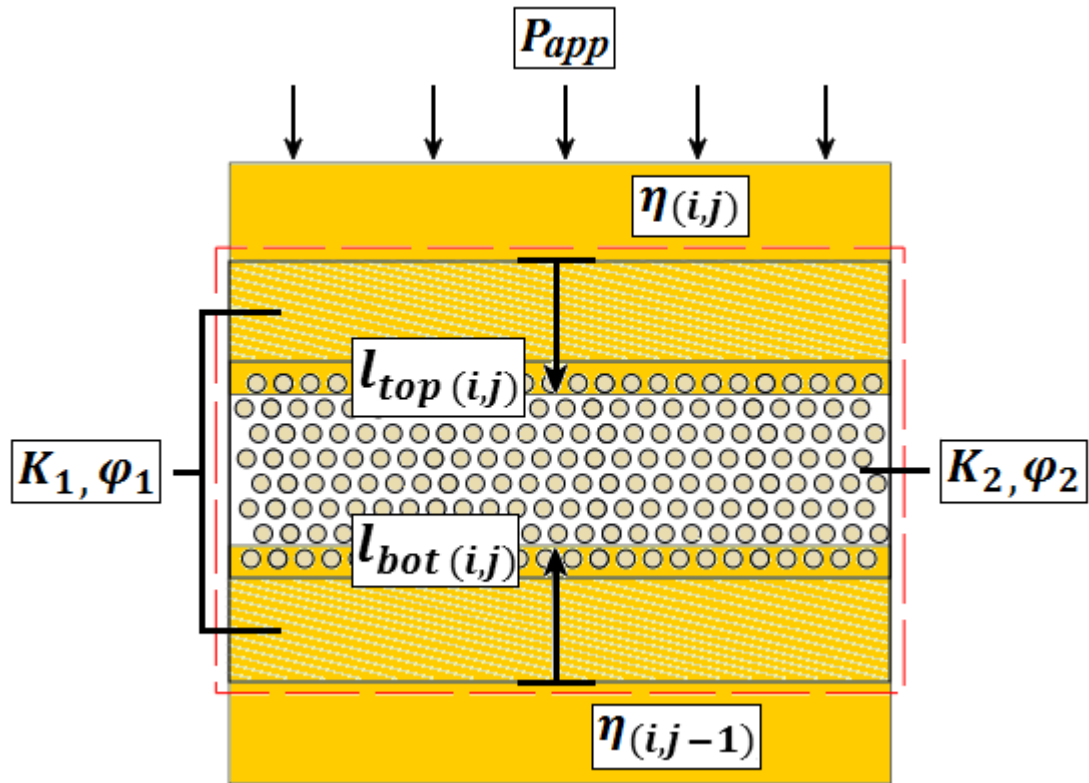


Figure 5.3. Physical representation of the 1D resin flow model at nodal position j and time step i . Resin flows into the fabric layer from above and below. The fabric layer is separated into inter-tow and intra-tow regions which are series.

Cender *et al.* (2013) showed that the fill time is proportional to the square of the flow distance i.e. halving the flow distance results in a factor of four reduction in the time taken to fill the fabric. For this reason, it is important to account for resin flow into the fabric layer from above and below, as illustrated in Figure 5.3. The total impregnation

depth for each ply, $l_{tot(i,j)}$ [m], is given by combining the resin flow front position from the top ($l_{top(i,j)}$) and bottom ($l_{bot(i,j)}$),

$$l_{tot(i,j)} = l_{top(i,j)} + l_{bot(i,j)} \quad (5.6)$$

Centea and Hubert (2013) showed that resin flow in VBO prepregs corresponded with a reduction in laminate thickness as the resin flowed into the fabric layers. For the finite difference code developed herein, a simplified ply microstructure is defined so that this thickness change can be computed. The simplified ply microstructure is segmented into a resin layer thickness, h_r [m], a fabric layer thickness, h_{fab} [m], and the total impregnation depth, l_{tot} (see Figure 5.4). By summing these quantities it is possible to determine the total laminate thickness, h_{lam} [m], for each time step, i ,

$$h_{lam,i} = \sum_{j=1}^q l_{tot(i,j)} + \sum_{j=1}^q (h_{fab} - l_{tot(i,j)}) + \sum_{j=1}^q h_{r(i,j)} \quad (5.7)$$

Where q is the number of plies in the laminate.

As impregnation progresses, the thickness of the resin layer diminishes from its initial value, $h_{r(0,j)}$,

$$h_{r(i,j)} = h_{r(0,j)} - \beta(\varphi_{fab} h_{fab}) \quad (5.8)$$

Where φ_{fab} is the porosity of the fabric layer, β is the degree of impregnation (DoI), which can be written as,

$$\beta = \frac{l_{tot}}{\varphi_{fab} h_{fab}} \quad , \quad l_{tot} < L_1 \quad (5.9)$$

$$\beta = \frac{\varphi_1 h_{fab} + (l_{tot} - \varphi_1 h_{fab}) \varphi_2}{\varphi_{fab} h_{fab}} \quad , \quad l_{tot} \geq L_1 \quad (5.10)$$

The characteristic length, L_1 , is assumed to be equivalent to the inter-tow thickness i.e. $\varphi_1 h_{fab}$.

Note, the DoI is also used in the finite difference code to determine when the fabric layer has been filled completely.

Assuming that there are no significant gaps between tows in the same fabric layer (i.e. the vertices of each tow touch the vertices of the adjacent tows), the inter-tow porosity, φ_1 , is constant for an elliptical tow geometry bound, at its vertices and co-vertices, by a rectangular cross-section (red dashed line in Figure 5.2),

$$\varphi_1 = \frac{A_{rec} - A_{ell}}{A_{rec}} = \text{constant} \cong 0.2146 \quad (5.11)$$

Where A_{rec} is the total area of the rectangular cross-section [m²] (outlined in Figure 5.2), and A_{ell} is the area of the elliptical tow [m²].

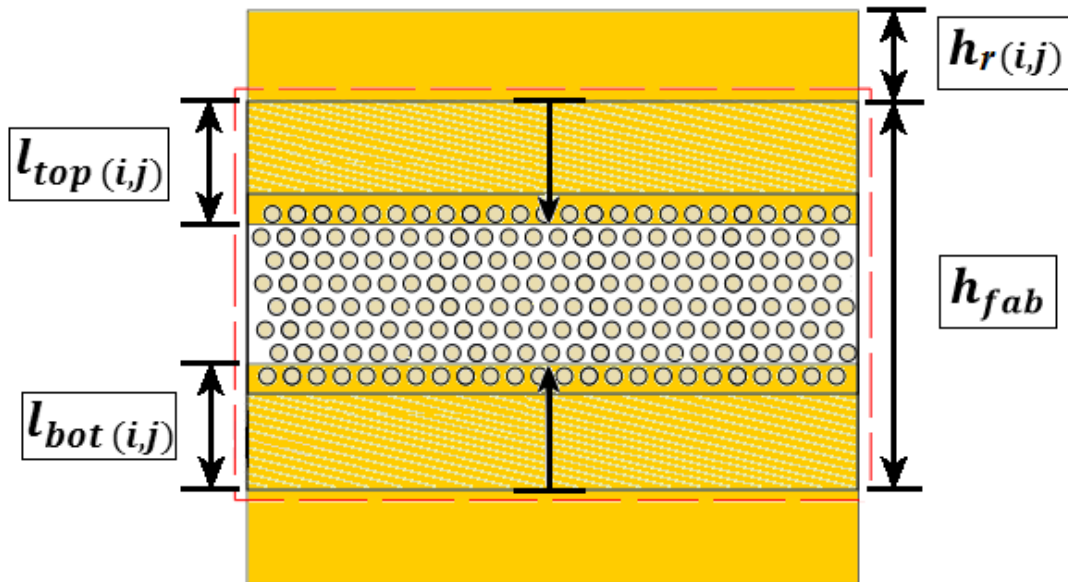


Figure 5.4. Illustration of the segmented layers in the 1D resin flow model. The layer thicknesses are summed to calculate the total laminate thickness change.

For a known intra-tow porosity, φ_2 , the porosity of the fabric layer, φ_{fab} , is determined as follows (Amico and Lekakou, 2004; Tahir, Hallström and Åkermo, 2014),

$$\varphi_{fab} = \varphi_1 + \varphi_2 - \varphi_1\varphi_2 \quad (5.12)$$

Note: the intra-tow porosity is often reported w.r.t to the area of the tow, as is the case for the above equation.

For a fully impregnated ply, l_{tot} is equivalent to h_{fab} such that the second term on the righthand side of Equation 5.7 cancels out. Naturally, the calculation of ply thickness, h_{ply} , reduces to the summation of the fabric thickness and any excess resin layer that remains:

$$h_{ply} = h_{fab} + h_r \quad (5.13)$$

The resin volume fraction, φ , of this ply can be written as,

$$\varphi = \frac{\varphi_{fab} h_{fab} + h_r}{h_{fab} + h_r} \quad (5.14)$$

Rearranging,

$$h_r = h_{fab} \left(\frac{\varphi - \varphi_{fab}}{1 - \varphi} \right) \quad (5.15)$$

Combining Equations 5.13 and 5.15, h_{fab} is approximated for a given φ ,

$$h_{fab} = h_{ply} \left(\frac{1 - \varphi}{1 - \varphi_{fab}} \right) \quad (5.16)$$

As can be seen, with the above set of equations, only the cure ply thickness, h_{ply} , the resin volume fraction, φ , and the intra-tow porosity, φ_2 , are required to fully describe the simplified ply microstructure in Figure 5.4. The cured ply thickness and the resin volume fraction can be measured experimentally, while values of intra-tow porosity can be found in the literature. As such, this is a rather inexpensive method. By comparison, microscopy and image analysis may allow for a more accurate description of the ply microstructure, but these techniques are time consuming to perform for each fabric type.

Another important consideration for modelling the thickness change is the initial form of the epoxy resin i.e. powdered or solid resin layer. For a powder layer, significant thickness reduction is expected during the sintering process. As such, the thickness of the resin layer, $h_{r(i,j)}$, is recalculated using,

$$h_{r(i,j)} = \frac{h_{r(i,j)}^*}{1 - \chi(i,j)} \quad (5.17)$$

Where $h_{r(i,j)}^*$ is the thickness of the fully sintered resin layer, and the powder void fraction, $\chi_{(i,j)}$, is modelled using Equation 4.2 in Chapter 4, Section 4.2.5.

5.2.2 Heat Transfer Model

Transient one-dimensional (1D) heat conduction in a plane wall is used as the basis for the heat transfer model under the assumption that convective heat transfer due to resin flow was negligible. The heat transfer equation is written using an explicit forward time, centered space finite difference formulation (illustrated in Figure 5.5). For the model developed here, Δz can vary as a function of resin flow in each fabric layer.

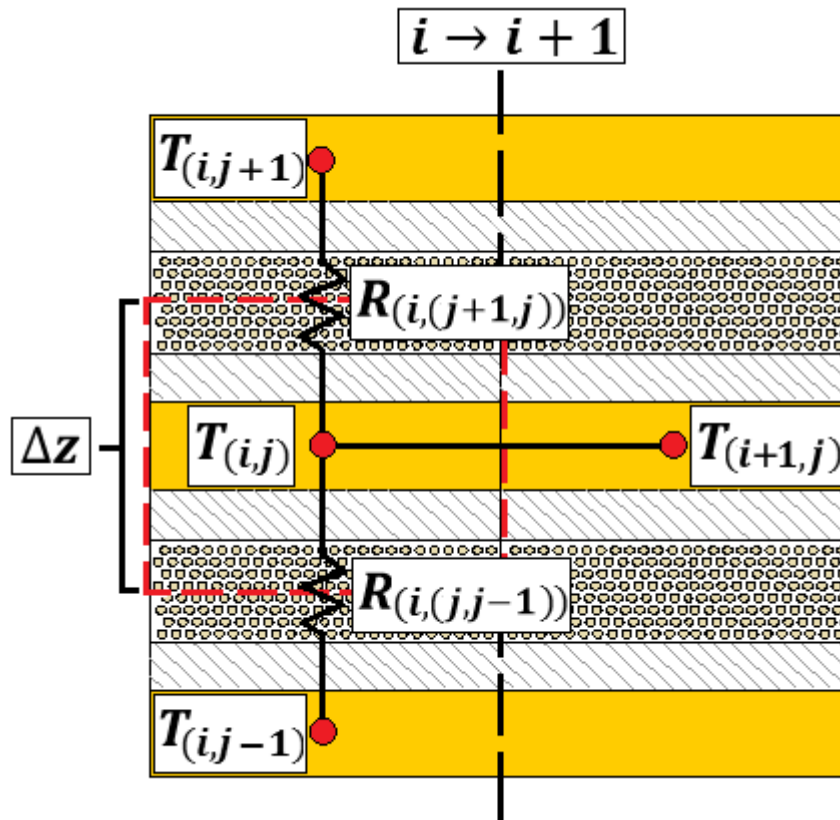


Figure 5.5. Schematic of the forward time, centred space scheme used for the heat transfer model. The temperature for the time step, $i + 1$, is calculated explicitly based on the conditions at time step, i . The various layers of resin, dry fabric and impregnated fabric are approximated as thermal resistances in series.

The structure of the heat transfer model is also approximated as individual layers of resin (h_r), fabric (h_{fab}), and impregnated fabric (l_{tot}) in series (see Figure 5.4 and Figure 5.5). Each layer is treated as a separate material with a unique thermal conductivity, which can be modelled as thermal resistances in series. These resistances change based on the state of the resin (powder or liquid) and the progression of resin flow. The contact resistance between these layers is assumed to be negligible.

As such, the *heat equation* is approximated as,

$$\begin{aligned} \left(\frac{T_{i+1} - T_i}{\Delta t} \right)_j &= \left(\frac{1}{\Delta z \rho c_p} \right)_{i,j} \left(\frac{T_{j-1} - T_j}{R_{j,j-1}} + \frac{T_{j+1} - T_j}{R_{j+1,j}} \right)_i \\ &+ \left(\frac{m_r}{c_p} \left(H_T \frac{d\alpha}{dt} - H_U \frac{d\theta}{dT} \right) \right)_{i,j} \end{aligned} \quad (5.18)$$

Where subscripts i and j represent the time step and nodal position, respectively, T is temperature [K], Δt is the time step size [s], Δz is the element thickness of node j [m], ρ is density [kg/m³], c_p is specific heat capacity [J/kg.K], $R_{j,j-1}$ is the thermal resistance of the material [m²K/W] between nodes j and $j - 1$, m_r is the resin mass fraction, H_T is the total enthalpy of the curing reaction [J/g], α is the degree of cure, H_U is the total enthalpy of relaxation [J/g], and θ is the degree of melting.

The element thickness is approximated by,

$$\Delta z_{(i,j)} = h_{r(i,j)} + h_{fab} \quad (5.19)$$

The density of the material at each node is approximated by,

$$\rho_{(i,j)} = \rho_c \frac{h_{ply}}{h_{fab} + h_{r(i,j)}} \quad (5.20)$$

Where ρ_c was determined via rule of mixtures (see Equation 2.27).

The specific heat capacity, c_p , is also determined via the rule of mixtures method (see Equation 2.28).

The thermal resistances $R_{(i,(j,j-1))}$ and $R_{(i,(j+1,j))}$ are written as,

$$R_{(i,(j,j-1))} = \frac{h_{r(i,j-1)}}{2\kappa_{r(i,j)}} + \frac{l_{tot(i,j)}}{\kappa_{c(i,j)}} + \frac{h_{fab} - l_{tot(i,j)}}{\kappa_f} + \frac{h_{r(i,j)}}{2\kappa_{r(i,j)}} \quad (5.21)$$

$$R_{(i,(j+1,j))} = \frac{h_{r(i,j)}}{2\kappa_{r(i,j)}} + \frac{l_{tot(i,j+1)}}{\kappa_{c(i,j+1)}} + \frac{h_{fab} - l_{tot(i,j+1)}}{\kappa_f} + \frac{h_{r(i,j+1)}}{2\kappa_{r(i,j+1)}} \quad (5.22)$$

The resin mass fraction, m_r , is,

$$m_{r(i,j)} = \frac{\rho_{r(i,j)}(1 - V_f)}{\rho_f V_f + \rho_{r(i,j)}(1 - V_f)} \quad (5.23)$$

The time derivatives of cure and melt are solved separately for the T_i , using Equations 4.1 in Chapter 4, Section 4.2.3, and Equation 2.1 in Chapter 2, Section 2.2.1, respectively.

5.2.3 Thermal Boundary Conditions

Two sets of boundary conditions (BCs) are considered for this work: specified temperature BCs for heated tooling; and forced convection BCs for oven heating.

As described by Bogetti and Gillespie (1991), the specified temperature BC is implemented by setting the surface node temperature at time step i , $T_{(i,s)}$ [K], equal to the programmed temperature cycle, $T_{P(i)}$ [K];

$$T_{(i,s)} = T_{P(i)} \quad (5.24)$$

For describing heat transfer by forced convection, the following expression from (Çengel, 2003) is used,

$$\rho c_P \frac{\Delta z}{2} \frac{T_{(i+1,s)} - T_{(i,s)}}{\Delta t} = h(T_{P(i)} - T_{(i,s)}) + \kappa \frac{T_{(i,s\pm 1)} - T_{(i,s)}}{\Delta z} \quad (5.25)$$

Where h is the heat transfer coefficient (HTC) [W/m²K], and $T_{(i,s\pm 1)}$ is equal to $T_{(i,s+1)}$ for the bottom BC and $T_{(i,s-1)}$ for the top BC. It is assumed that any heat transfer due to radiation in the oven is negligible compared to convection.

The material parameters in Equation 5.25 depend on the surface composition. For VBO prepreg manufacturing it is expected that the top boundary would consist of

bagging materials, while the bottom boundary would be the underside of the mould tool. Oh and Lee (2002) assumed negligible thermal contact resistance between the bagging, laminate, and tooling; the same assumption is made in this work.

Conduction through any additional layers (i.e. tooling, bagging, insulation, etc.) is modelled for all BCs. These additional layers are also modelled as thermal resistances in series. The corresponding equations are given in the Appendices: B. Process Models.

5.2.4 Material Properties

This work focusses on manufacturing simulations for GRN 918 epoxy powder with glass-fibre fabrics.

Some key properties for GRN 918 epoxy powder were characterised and modelled in the previous two chapters, however, additional data for thermal conductivity and specific heat capacity is required for heat transfer modelling. The thermal conductivity of epoxy resins has been reported in the literature as being between 0.167 and 0.27 W/m.K (Loos and Springer, 1983; Oh and Lee, 2002; Kratz *et al.*, 2012; Shi, 2016). The wide range in values may be due to temperature/cure dependencies. Shin and Hahn (2004) used the following empirical relationship to describe the thermal conductivity as a function of temperature and DoC,

$$\kappa_{r,liq} = 0.04184 [3.85 + (0.035 T - 0.41) \alpha] \quad (5.26)$$

Where T is in °C.

To the author's knowledge, no data was available for the thermal conductivity of epoxy powders, however, the thermal conductivity of polyamide powder, $\kappa_{r,pow}$, was reported to be 0.05 – 0.0913 W/m.K (Xue and Barlow, 1990; Tian *et al.*, 2018). Given that the bulk thermal conductivity of polyamide and epoxy is similar (0.15 – 0.25 W/m.K), data for polyamide powder is judged to be a reasonable approximation. The transition from powder to liquid resin is described for thermal conductivity using the following expression,

$$\kappa_r = \kappa_{r,pow} \frac{\chi}{\chi_0} + \kappa_{r,liq} \left(1 - \frac{\chi}{\chi_0}\right) \quad (5.27)$$

Where χ is the void fraction of the powder as determined by Equation 4.2 in Chapter 4, Section 4.2.5, and χ_0 is the initial void fraction of the powder.

The specific heat capacity of epoxy was often reported as being 1260 J/kg.K (Loos and Springer, 1983; Shin and Hahn, 2004; Kratz *et al.*, 2012), while others reported higher values (e.g. 1740 J/kg.K (Oh and Lee, 2002)). Again, the range in values may be attributed to a dependency on temperature and DoC. Abou Msallem *et al.* (2010) proposed an empirical relationship for specific heat capacity as a function of temperature and DoC, however, they measured very high values for cured epoxy (2750 – 3000 J/kg.K) using an in-house apparatus. Shin and Hahn (2004) used the following empirical relationship to describe the specific heat capacity as a function of temperature and DoC,

$$c_{p,r} = 4184(0.468 + 5.975 \times 10^{-4}T - 0.141\alpha) \quad (5.28)$$

Where T is in °C.

It is assumed that the above relationship is valid for epoxy in both its powder and liquid form, as it is a quantity which is independent of volume.

Table 5.1 shows the thermal properties used for epoxy in this chapter.

Characterisation of the fibre-bed was not within the scope of this project. For this reason, most of the fibre-bed properties have been taken from the literature. Properties for stitched uni-directional (UD) fabrics and stitched triaxial fabrics were used in this thesis; blade spars are predominantly made using UD because of the large bending loads they experience, while triaxial fabrics are used in the blade root because of bending and torsional load transfer to rotor hub (Wieland and Ropte, 2017).

Table 5.1. Thermal properties used to model heat transfer in GRN 918.

Property [units]	Value	Source
Thermal conductivity of liquid epoxy [W/m.°C]*	Equation 5.26	(Shin and Hahn, 2004)
Thermal conductivity of powder epoxy [W/m.K]	0.075**	-
Specific heat capacity of epoxy [J/kg.°C]*	Equation 5.28	(Shin and Hahn, 2004)

* Predicted temperatures within the simulation are converted to °C so that the empirical relationships can be used.

** Average value taken from (Xue and Barlow, 1990; Tian *et al.*, 2018)

As discussed in Chapter 2, Section 2.3.2, the Springer-Tsai model (Equation 2.29) has been used widely in process simulations for through-thickness thermal conductivity, $\kappa_{c,T}$, of UD composite materials. Another similar model was also proposed by Clayton (1971),

$$\frac{\kappa_{c,T}}{\kappa_r} = \frac{1}{4} \left[\sqrt{(1 - V_f)^2 \left(\frac{\kappa_f}{\kappa_r} - 1\right)^2 + \frac{4\kappa_f}{\kappa_r}} - (1 - V_f) \left(\frac{\kappa_f}{\kappa_r} - 1\right) \right]^2 \quad (5.29)$$

Where κ_r is the thermal conductivity of the resin [W/m.K], κ_f is the thermal conductivity of the fibre [W/m.K], and V_f is the fibre volume fraction.

With the Springer-Tsai model, many authors used the longitudinal (a.k.a. axial) thermal conductivity of the fibre for κ_f , however, El-Hage *et al.* (2018) noted that the transverse thermal conductivity of fibres were lower than the longitudinal thermal conductivities. They highlighted that the transverse thermal conductivity of fibres was less commonly reported in the literature but that it should be used for modelling through-thickness thermal conductivity. Thermal conductivities for glass fibres have been reported in the range of 0.417 – 1.3 W/m.K without clear distinction as to whether

they were values for transverse or longitudinal thermal conductivity of the fibres (Hsiao, Laudorn and Advani, 2001; Oh and Lee, 2002; Shi, 2016).

The through-thickness thermal conductivity of dry fabric under vacuum is impossible to calculate using the Springer-Tsai or Clayton models because the matrix conductivity term, κ_r , becomes zero (i.e. vacuum has no conductivity). As such, some authors have experimentally measured the through-thickness conductivity of dry fabric under vacuum (Lee, 2004; El-Hage, Hind and Robitaille, 2018). For dry GF fabric, they measured through-thickness thermal conductivities of 0.1 – 0.2 W/m.K, depending on the fibre architecture (i.e. stitched UD, plain weave, twill weave, etc.).

The density of E-glass fibre was reported as being approx. 2560 kg/m³, while the specific heat capacity varied between 670 and 920 J/kg.K (Oh and Lee, 2002; Tan and Pillai, 2012; Shi, 2016).

Some properties and parameters are required to describe the fibre-bed for the flow models also. As discussed in Chapter 2, Section 2.3.1, the permeability of a fibre-bed can be modelled or measured experimentally, however, reported values can vary significantly. The Gebart model for a quadratic packing structure (Equation 2.24) is used to calculate the intra-tow permeability for all simulations presented here. This model requires additional information on the fibre radius and the FVF of the tow. A value of 0.67 is used for the FVF of the tow; this FVF was experimentally measured by Amico and Lekakou (2004) for a single E-glass fibre tow. The datasheet for Johns Manville 086 glass fibre for epoxies reports a fibre diameter of 16 μm for 1200 and 2400 tex rovings (Johns Manville, 2018).

Experimentally measured inter-tow permeabilities for GF fabrics range between 7.2×10^{-10} and 21.3×10^{-10} m², depending on the fabric architecture (Kuentzer *et al.*, 2006; Zhou *et al.*, 2006). For the materials studied in this thesis, inter-tow permeabilities for stitched UD fabrics are assumed.

Table 5.2 compiles the fibre-bed properties and parameters that are used for the process simulations.

Table 5.2. Properties and parameters used for glass fibre fabric.

Property/Parameter [units]	Value	Source
Thermal conductivity of impregnated GF fabric [W/m.K]*	Equation 5.29	(Clayton, 1971)
Thermal conductivity of glass fibre [W/m.K]	0.417	(Hsiao, Laudorn and Advani, 2001)
Thermal conductivity of dry GF fabric [W/m.K]	0.2	(Lee, 2004)
Density of E-glass fibre [kg/m ³]	2560	(Tan and Pillai, 2012)
Specific heat capacity of E-glass fibre [J/kg.K]	810	(Shi, 2016)
Inter-tow permeability of stitched GF fabric [m ²]**	13.675×10^{-10}	(Kuentzer <i>et al.</i> , 2006)
Intra-tow permeability of GF [m ²]	Equation 2.24	(Gebart, 1992)
Glass fibre diameter [m]	16.0×10^{-6}	(Johns Manville, 2018)
Fibre volume fraction of glass fibre tow	0.67	(Amico and Lekakou, 2004)

* The Springer-Tsai model (Equation 2.29) can also be used with little change to the overall result.

** Average value for stitched GF fabric.

Additional material properties are required for the bagging materials and the mould tooling. Joshi *et al.* (1999) modelled heat transfer through bagging which consisted of one layer of release film, one layer of nylon bag, and two layers of breather. They treated the bagging as a single layer with averaged values for density, specific heat capacity, and thermal conductivity. Oh and Lee (2002) gave values of the same bagging properties, but broke them down into individual components of the bagging layer. Both studies reported properties for an aluminium tool as well.

For simplicity of modelling, the bagging is treated as one layer and the values reported by Joshi *et al.* (1999) are used (see Table 5.3). The bagging layer thickness is assumed to be 1.5 mm.

Table 5.3. Properties used for bagging and tooling materials.

Property [units]	Value	Source
Thermal conductivity of bagging [W/m.K]	0.069	(Joshi <i>et al.</i> , 1999)
Thermal conductivity of aluminium [W/m.K]	216.3	(Joshi <i>et al.</i> , 1999)
Thermal conductivity of tool steel [W/m.K]	53.35	(Kluge <i>et al.</i> , 2016)
Density of bagging [kg/m ³]	355.6	(Joshi <i>et al.</i> , 1999)
Density of aluminium [kg/m ³]	2692.1	(Joshi <i>et al.</i> , 1999)
Density of tool steel [kg/m ³]	7822.8	(Kluge <i>et al.</i> , 2016)
Specific heat capacity of bagging [J/kg.K]	1256.0	(Joshi <i>et al.</i> , 1999)
Specific heat capacity of aluminium [J/kg.K]	916.9	(Joshi <i>et al.</i> , 1999)
Specific heat capacity of tool steel [J/kg.K]	485.0	(Kluge <i>et al.</i> , 2016)

5.2.5 Initial Conditions

To initialise the models, several parameters have to be given values. In this chapter, a 100-ply laminate is used for simulations, with a cured ply thickness (h_{CPT}) of 0.001 m (1 mm). The initial FVF is controlled during prepregging process with the use of automated powder deposition. In-plane resin flow is expected to be negligible during processing, so it is assumed that the final FVF was approximately the same as the initial FVF i.e. no significant resin bleeding. A FVF of 0.5 is chosen for all simulations in this chapter.

It is assumed that during powder deposition, the powder would partially infiltrate the fiber-bed. As such, an initial DoI of 0.113 is chosen arbitrarily; this equates to a quarter of the available inter-tow space being filled. It is assumed that the epoxy powder is brought above its T_g during the prepregging so that it adheres to the fibre-bed, but still retains its powder form (e.g. 30 seconds at 50°C would result in a powder void fraction of approx. 0.485). It is assumed that the prepregging process has a negligible effect on

the DoC and there are negligible out-time effects between prepregging and laminate processing (i.e. initial DoC of 0.01).

Based on real-world observations of vacuum bagged parts, an applied pressure of 90×10^3 Pa (90 kPa) is used for simulating laminate manufacture; it has been shown that deficient pressure conditions commonly occur and can be an important factor in VBO processing (Centea and Hubert, 2013).

The initial temperature throughout the laminate, tooling, and bagging is set to 23°C for all simulations in this chapter.

Table 5.4 summarises the initial conditions that are used for the process simulations.

Table 5.4. Initial conditions used for the process simulations.

Parameter [units]	Value
No. of plies	100
Cured ply thickness [m]	0.001
Fibre volume fraction	0.5
Degree of impregnation	0.113
Powder void fraction	0.485
Degree of cure	0.01
Applied pressure [Pa]	90×10^3
Laminate/bagging/tool temperature [°C]	23

5.2.6 Numerical Computation

To simulate the processing of a thick-section laminate, the laminate is discretized through the thickness, and the process models are numerically solved at the nodes. Many explicit and implicit finite difference methods exist for solving the *heat*

equation, however, as indicated in Section 5.2.2, an explicit forward time, central space scheme is used in this work. This is a first-order scheme, so it has limited accuracy (due to a large temporal truncation error), however, it is very simple to implement and stable, if the following criterion is met (Çengel, 2003; Recktenwald, 2011),

$$\gamma \frac{\Delta t}{\Delta z^2} < \frac{1}{2} \quad (5.30)$$

Where γ is the thermal diffusivity [m^2/s],

$$\gamma = \frac{\kappa}{\rho c_p} \quad (5.31)$$

Similarly, the Euler method is implemented for solving any ODEs in the simulation (e.g. cure kinetics, resin flow, etc.). Again, this is an explicit first order method which is simple to implement but has limited accuracy.

The code was developed in MATLAB R2015a. A nested for-loop structure is used to compute the finite difference scheme; time increases incrementally in the outer loop, while the inner loop iterates through the spatial nodes. The code is given in the Appendices: C. Numerical Codes.

The spatial discretization is based on the thickness of the plies i.e.,

$$N_{nodes} = N_{plies} + 1 \quad (5.32)$$

Where N_{nodes} is the number of nodes, and N_{plies} is the number of plies.

The thermal diffusivity of the laminate, as well as the bagging and tooling, has to be considered when choosing the maximum allowable time step size for a simulation. In cases where aluminium or steel tooling is used, the thermal diffusivity of the tooling is much higher than the composite material itself and limits the time step size.

The maximum allowable time step size for a 1 mm ply of GF/Epoxy-powder is approx. 2.80 s (see Figure D.1Figure D. in the Appendices: D. Simulation Results), while, it is 0.57 s for a 10 mm aluminium tool, and 3.55 s for a 10 mm steel tool.

For a small enough time step, first order methods provide sufficient accuracy due to the low rates of change associated with manufacturing thick-section composites i.e. slow ramp rates are used. As such, a time step of 0.5 s is chosen for all simulations using an aluminium tool, while a time step of 2.5 s is chosen for all simulations using a steel tool. Simulations show that there is no loss of accuracy when increasing from 0.5 s to 2.5 s increments for a steel tool (see Figure D.2 in the Appendices: D. Simulation Results).

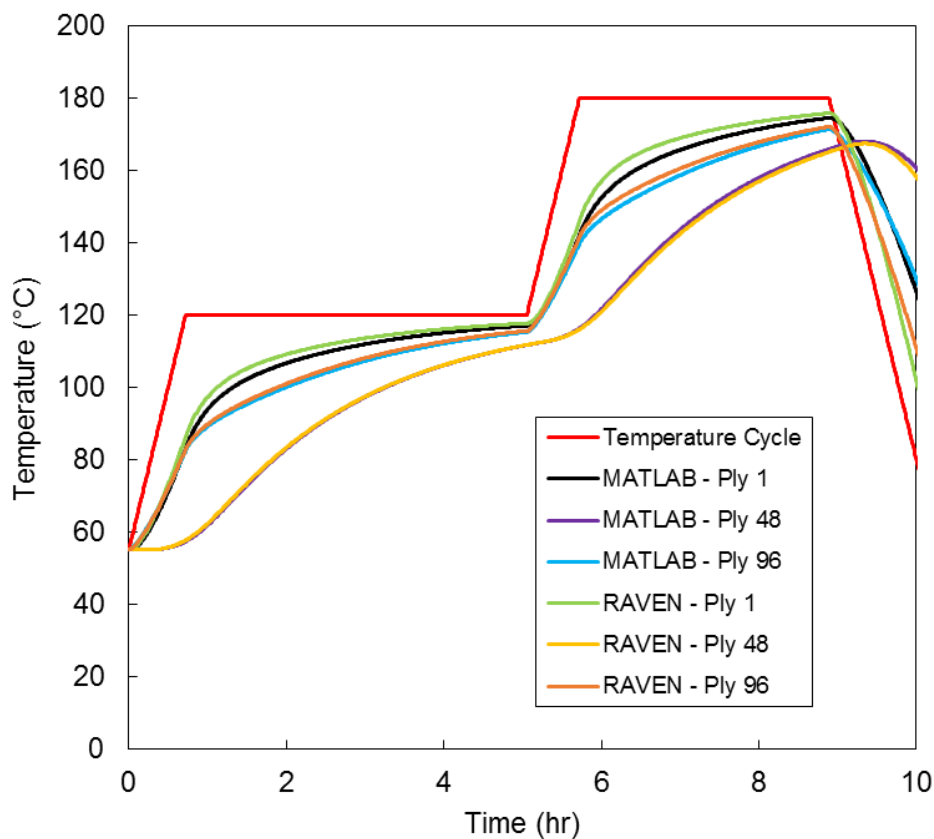


Figure 5.6. Comparison of the results from RAVEN and from the finite difference code developed in MATLAB. The simulations were carried out for a 96-ply GF/Epoxy-powder laminate heated on a 10 mm steel plate in an oven.

As a final verification of the numerical methods, the solution of the finite difference code is compared with results from RAVEN, a commercially available software for

performing 1D heat transfer and cure kinetics simulations on composite laminates. Figure 5.6 shows that there is little difference between the solutions ($< 5^{\circ}\text{C}$ at any time). The simulations did not include compaction due to resin flow because it was not a featured capability of RAVEN. Furthermore, cure kinetics were excluded as it was not possible to implement a user-defined cure kinetics model in RAVEN which could simulate the cure kinetics of the GRN 918 epoxy powder.

5.3 Results and Discussion

5.3.1 Case Study – Oven Processing of a 100-ply Laminate

As a starting point for investigating thick-section processing, it was worthwhile to consider the standard manufacturing process for a 100-ply laminate. A thick-section laminate of GF/Epoxy-powder may be processed on a heated tool or in an oven using an extended version of the standard temperature cycle used for thin laminates i.e. with longer isothermal dwells to allow heat to transfer through all the plies. For this case study, the simulations focussed on a laminate being processed in an oven, on a steel plate with one layer of vacuum bagging around it.

The following temperature cycle was used:

- Drying stage: Ramp to 55°C and hold for 900 min
- Impregnation stage: Ramp to 120°C at $1.5^{\circ}\text{C}/\text{min}$ and hold for 360 min
- Cure stage: Ramp to 180°C at $1.5^{\circ}\text{C}/\text{min}$ and hold for 200 min
- Cool down

For forced convection BCs, Zimmermann and Van Den Broucke (2012) recommended that a convective HTC of $10 - 100 \text{ W}/\text{m}^2\text{K}$ be used for gases in an autoclave. Similarly, average convective HTCs have been experimentally measured in the range of $10 - 40 \text{ W}/\text{m}^2\text{K}$ for autoclaves (Monaghan, Brogan and Oosthuizen, 1991; Kluge *et al.*, 2016). A convective HTC of $40 \text{ W}/\text{m}^2\text{K}$ was chosen for the simulation.

All other initial conditions were as described in Table 5.4.

5.3.2 Temperature Profiles

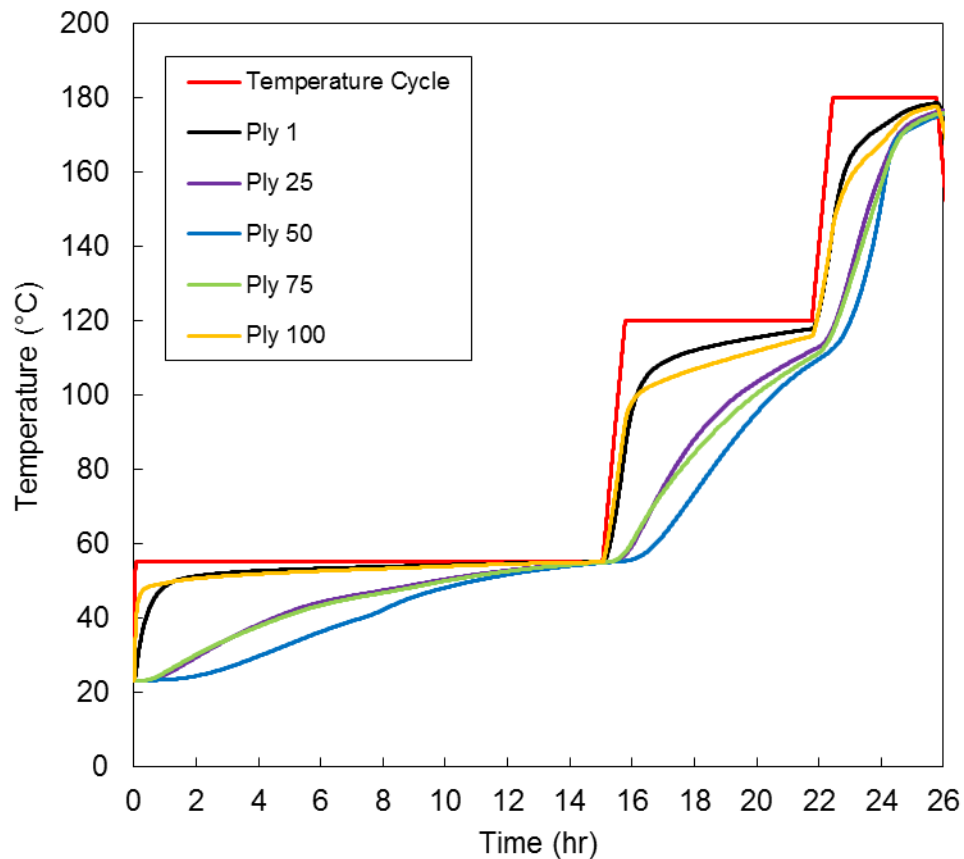


Figure 5.7. Plot of simulated ply temperatures within a 100-ply laminate. There was no temperature overshoot predicted, however, large thermal gradients were still present.

Figure 5.7 shows how the temperature evolved within the laminate with respect to time. Despite having symmetric thermal BCs, the temperatures at the bottom and top of the laminate (Ply 1 and Ply 100, respectively) were asymmetric because of the presence of the tool and bagging. Due to GRN 918's low enthalpy of reaction, there was no thermal overshoot predicted for the laminate during the cure stage (i.e. above 120°C). While this was beneficial for mitigating the adverse effects associated with thermal overshoot/runaway, there were still significant thermal gradients due to the insulating properties of the laminate.

To give some indication of the magnitude of the thermal gradients within the laminate during processing, Figure 5.8 shows a plot of the maximum temperature difference within the laminate as a function of time. The temperature difference peaked at the beginning of each ramp stage as the outside of the laminate was rapidly heated and the temperature at the centre of the laminate lagged.

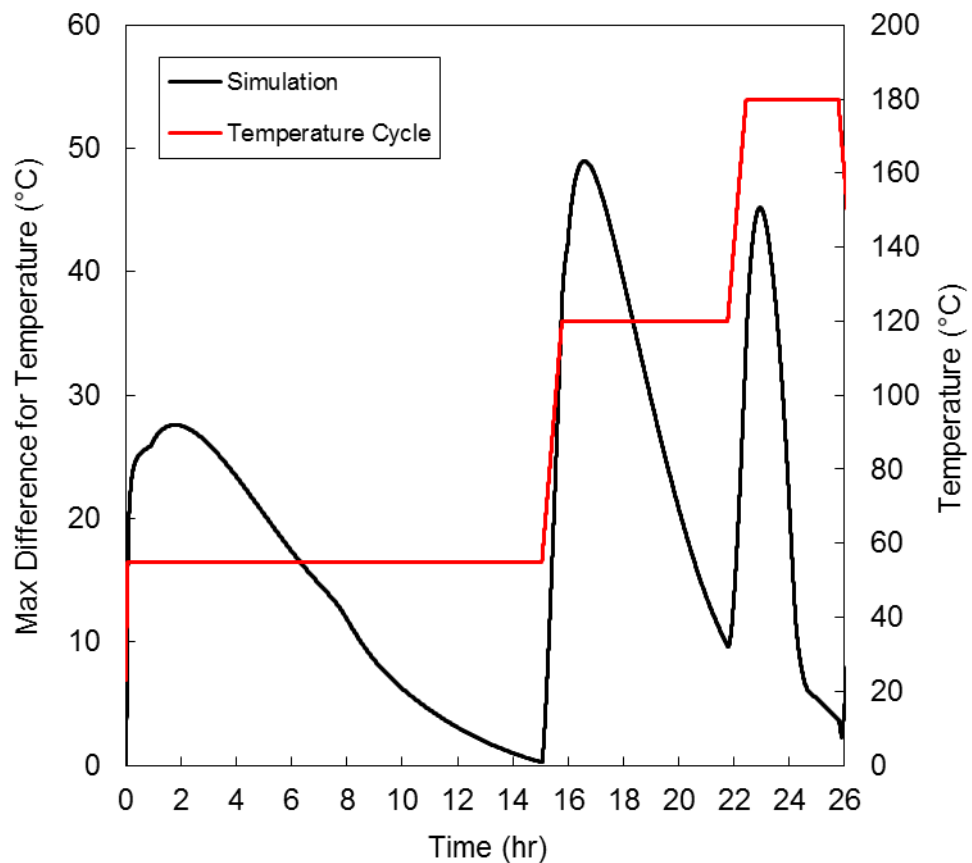


Figure 5.8. Plot of the maximum temperature difference within the laminate vs time. Significant temperature differences evolved during temperature ramps due to the lag in heat transfer through the thickness. The spike in temperature difference during the cure stage ($> 120^{\circ}\text{C}$) could result in “locked-in” residual stresses as the epoxy gels.

The width of each peak in Figure 5.8 represented the time lag in heat transfer during the corresponding stage. It was interesting to note that the time lag of each stage was less than the stage which preceded it. This was due to the increasing thermal diffusivity

of the material as the laminate compacted and the thermal properties of the resin changed w.r.t. temperature and DoC (see Figure D.3, Figure D.4, Figure D.5, and Figure D.6 in the Appendices: D. Simulation Results). During the cure stage, heat transfer was also aided by the heat generation of the chemical reaction (see Figure D.7 in the Appendices: D. Simulation Results).

5.3.3 Cure Profile

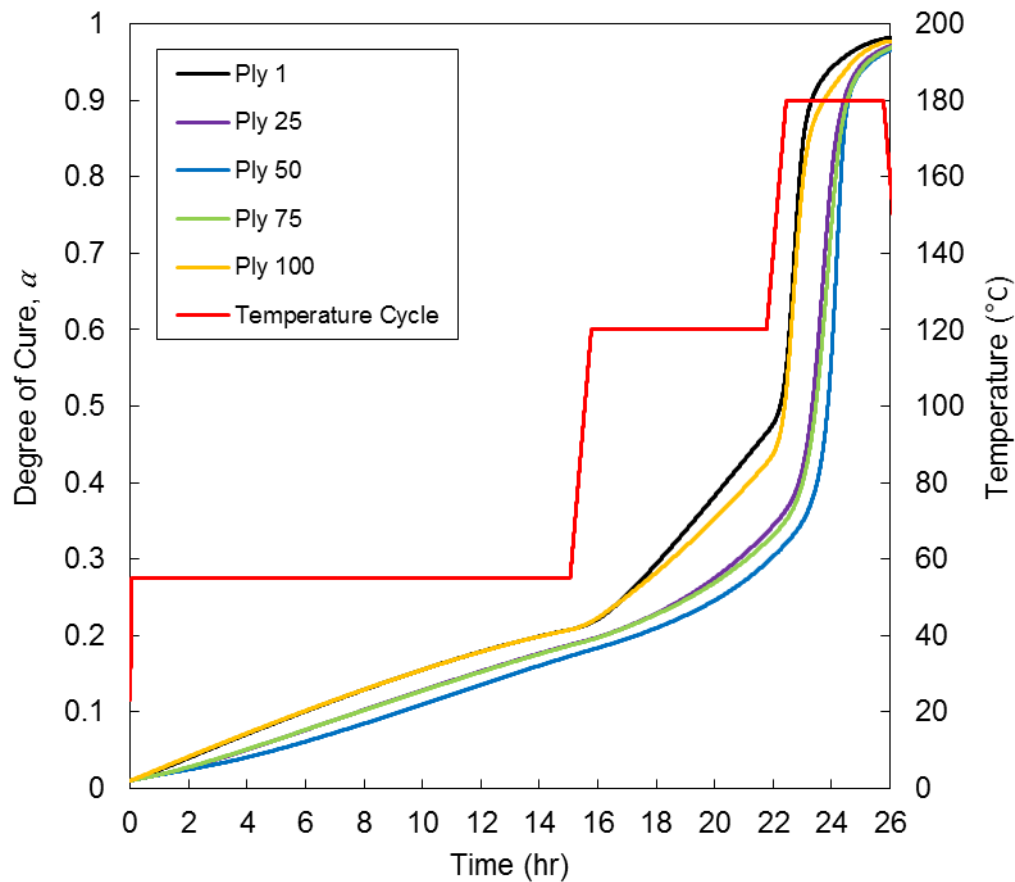


Figure 5.9. Plot of the simulated DoC evolution within the laminate.

Despite having the least time lag for heat transfer, the peak in temperature difference during the cure stage represented the largest processing hazard due to the risk of creating “locked-in” residual stresses. As shown in Figure 5.9, the DoC increased slowly during the drying and impregnation stages, and none of the plies reached the

gel point (i.e. DoC of 0.56) prior to the cure stage. Upon heating past 120°C, the DoC increased rapidly as the latent curing agent was activated. This rapid curing gave rise to a large cure gradient within the laminate, as represented by the maximum DoC difference plotted in Figure 5.10.

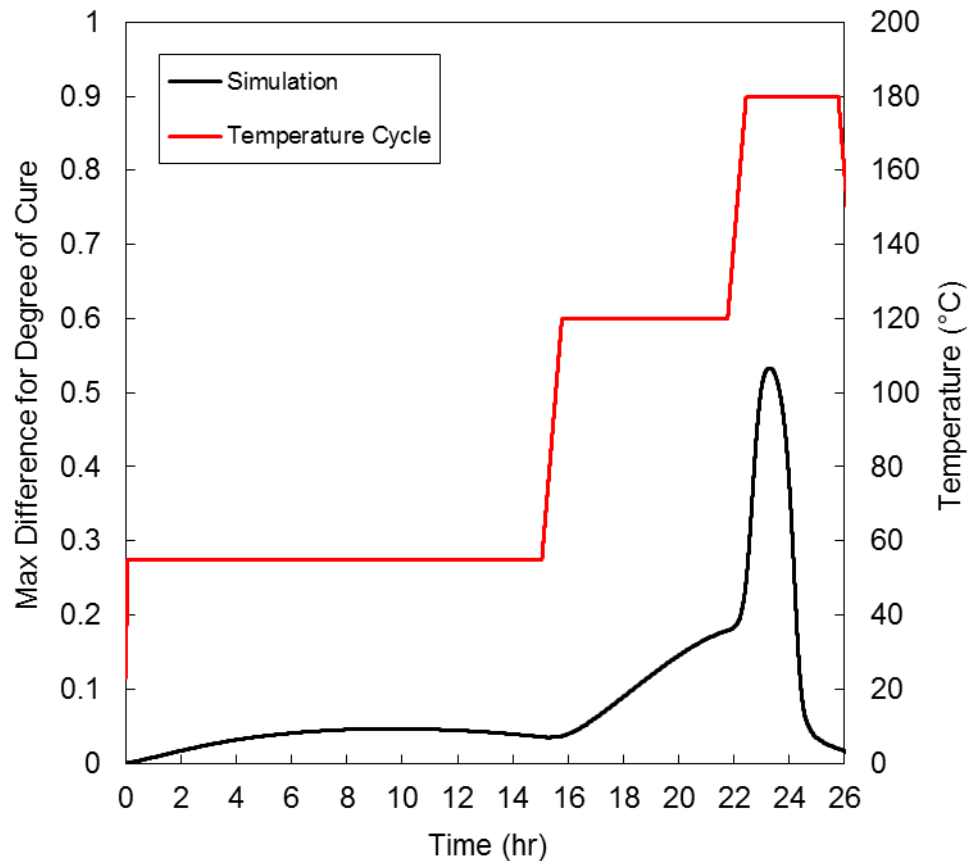


Figure 5.10. Plot of the maximum DoC difference within the laminate for each point in time. Crucially, the maximum difference peaked as the resin was reaching its gel point in multiple plies. This could adversely affect the laminate by locking in residual stresses.

It should be noted that the peak in the max DoC difference coincided with both the peak in temperature difference (Figure 5.8) and the gel point of multiple plies. This suggested that the laminate could be subject to large, locked-in residual stresses arising from mismatches in both thermal expansion and cure shrinkage. This is discussed further in Chapter 6, Section 6.3.6.

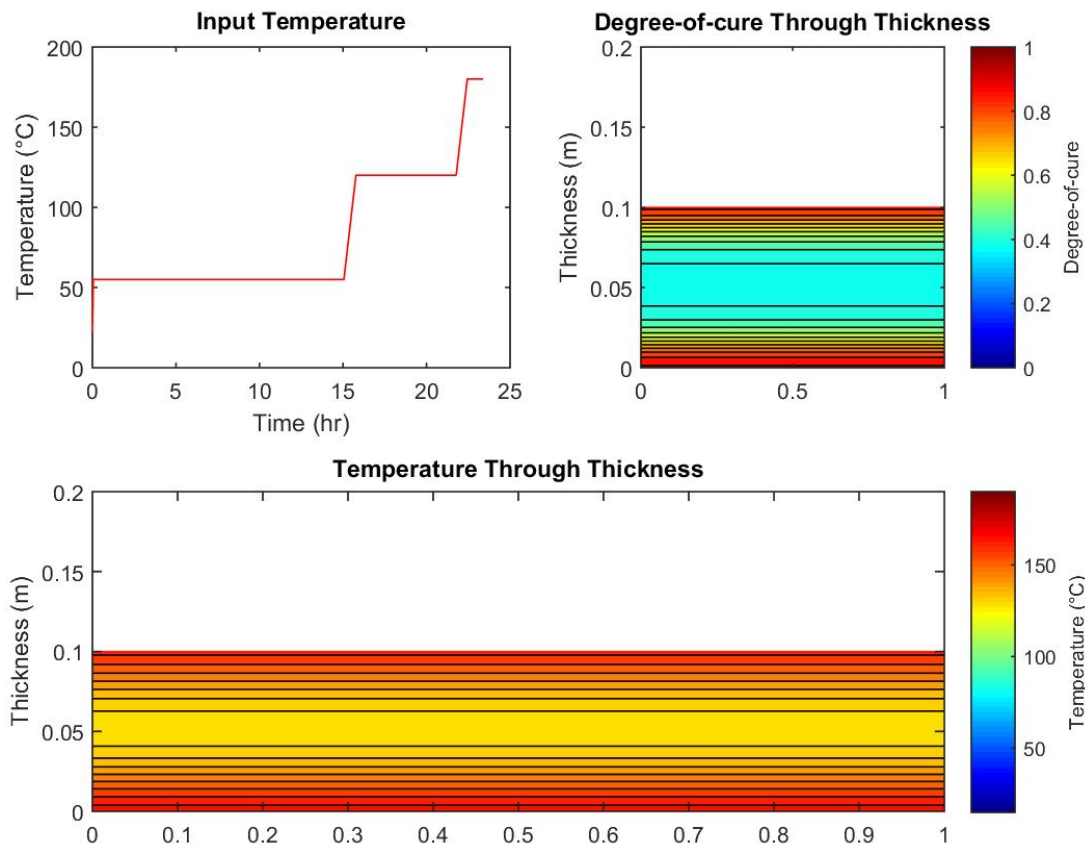


Figure 5.11. Simulation results at approx. 23.3 hr into the temperature cycle. Large cure gradients were predicted between the outside and inside of the laminate; indicated by the colour contour (top right). This coincided with temperature gradients within the laminate, corresponding to a temperature difference of 40°C between the surface and centre of the laminate (bottom).

Another important factor to consider was that, when the cure difference was highest (23.3 hr into the cycle), the outside of the laminate was above the gel point and the inside of the laminate was not. As discussed in Chapter 2, Section 2.3.2, this outside-to-inside curing (shown in Figure 5.11) was considered undesirable due to the potential for large tensile and compressive stresses in the inside and outside of the laminate, respectively. Bogetti and Gillespie (1992) showed that these stresses were enough to initiate transverse matrix cracking in GF/Polyester laminates.

The outside-to-inside curing profile was related to the cure kinetics of the epoxy powder; above 120°C, the cure rate of the outer plies increased rapidly due to

activation of the latent curing agent, while the central plies lagged due to the low enthalpy of reaction. For a standard epoxy system this would not normally happen as the resin at the centre of the laminate generates sufficient heat to auto-accelerate the curing; commonly resulting in an inside-to-outside cure profile.

For the above reasons, the manufacture of thick-section composite parts may benefit from the use of two epoxy powders used in parallel. An epoxy powder with a higher temperature cure-activation, such as HZH01R (see Chapter 3), could be used in the outer layers of the laminate to inhibit early curing and reduce both the temperature and cure gradients. Due to the deposition of the powder across the fabric, it would be expected that the two powders would maintain their position within the laminate, and only flow locally into the empty fibre tows. This is discussed further in Chapter 6, Section 6.3.6.

5.3.4 Thickness Change

As previously mentioned, another aspect that influenced the severity of the thermal gradients was the thickness of the laminate. In the powder format, the epoxy introduced considerable bulk to the initial preform. Figure 5.12 shows that the thickness of the laminate was predicted to reduce by approx. 45%. When coupled with the lower thermal conductivity of the powder and dry fabric (see Figure D.5 Appendices: D. Simulation Results), this format of VBO prepreg had a significant effect on the heat transfer within the laminate.

The drying temperature currently used by industry partner, ÉireComposites Teo., was chosen to improve the rate of moisture evacuation, however, in Chapters 3 and 4, it was shown that the T_g of GRN 918 was as low as 40°C. Consequently, it was found that the powder melted and then sintered as the viscosity of the epoxy resin decreased (see Figure D.8 in Appendices: D. Simulation Results). This resulted in a significant decrease in the laminate thickness and an increase in the thermal conductivity of the plies. These changes benefitted heat transfer within the laminate, however, melting and sintering the powder may have an adverse effect also.

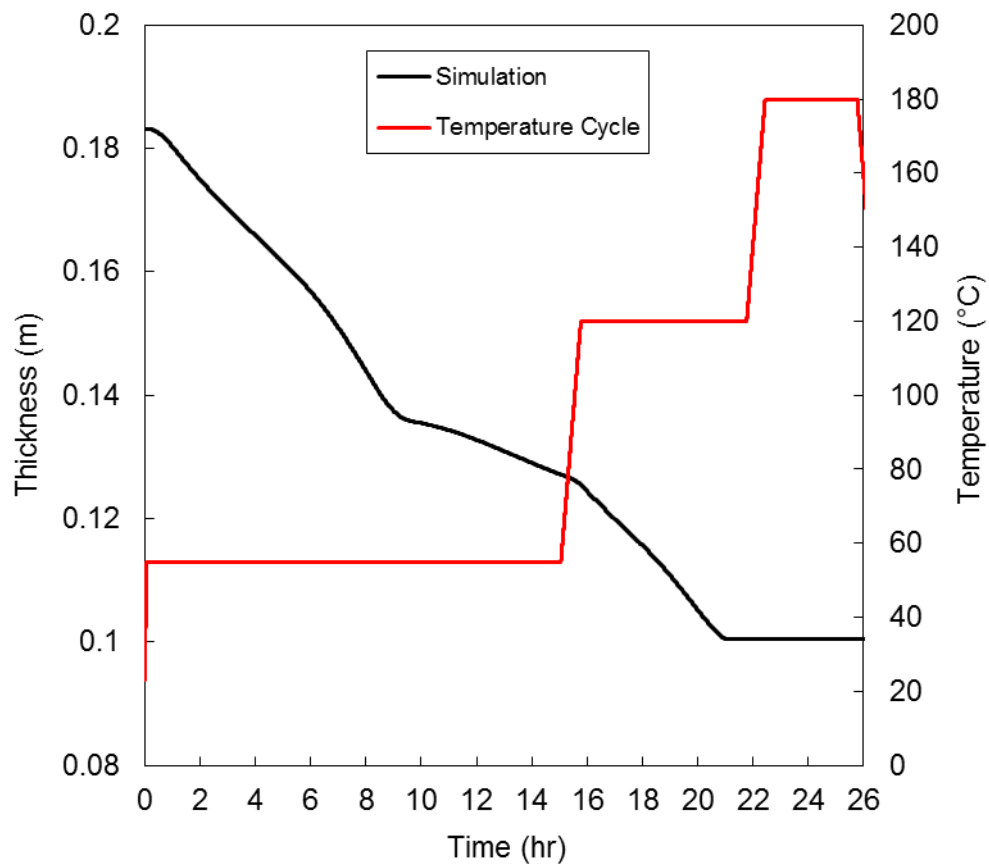


Figure 5.12. The thickness change plot of the GF/Epoxy-powder laminate during the temperature cycle. During the drying stage, there was a large reduction in thickness due to the sintering of the powder. After the cessation of sintering, the resin continued to slowly flow into and fill the inter-tow region of the fibre-bed. During the impregnation stage, the viscosity of the resin reduced, the resin filled the fibre tows, and the laminate thickness decreased again.

As discussed in Chapter 3, Section 3.3.6, by sintering the powder, moisture can no longer desorb from the surface of the particle and must diffuse through the bulk polymer. Furthermore, the powder acts as permeable layer through which gases can be evacuated. By sintering the powder, the epoxy forms a barrier and the gases must pass through the dry fibre tows. Ideally, a shortened drying stage would be carried out below the T_g of the epoxy powder (due to the advantageous sorption properties of the powder), and then an additional stage could be introduced for sintering. To optimise

the drying stage, more research is required which is outside the scope of this work. Instead, it is suggested as future work (see Chapter 8, Section 8.2).

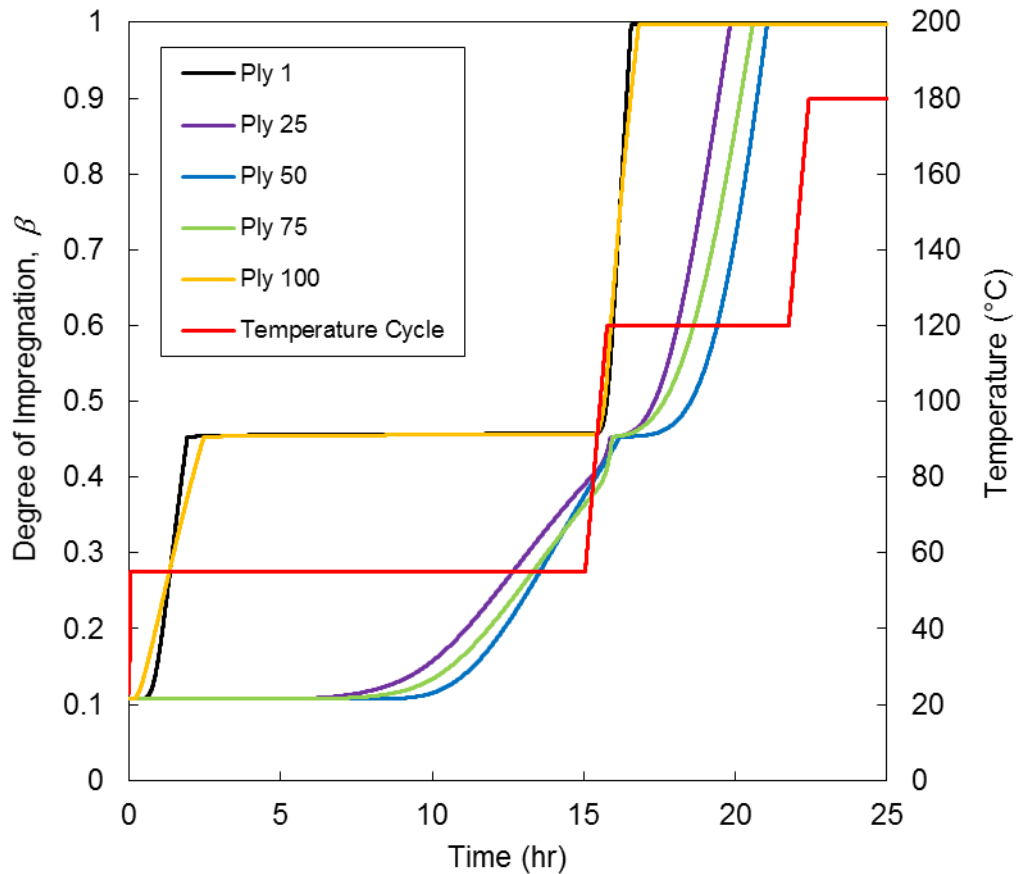


Figure 5.13. Plot of the degree of impregnation during the simulated temperature cycle. The inter-tow region ($DoI < 0.45$) filled during the curing cycle, but lower viscosities were required for filling the fibre tows ($DoI > 0.45$).

After the drying stage, the remaining thickness reduction in Figure 5.12 was due to resin flow. As shown in Figure 5.13, the simulation predicted that the inter-tow region ($DoI < 0.45$) would fill during the drying stage when powder had melted and reached a sufficiently low viscosity to flow between the tows. The inter-tow filling of the outer plies was predicted within the first few hours of the process, however, the inner plies lagged by several hours due to slow heat transfer. In contrast, intra-tow filling ($DoI >$

0.45) was relatively fast when a sufficiently low viscosity was achieved (see Figure 5.14).

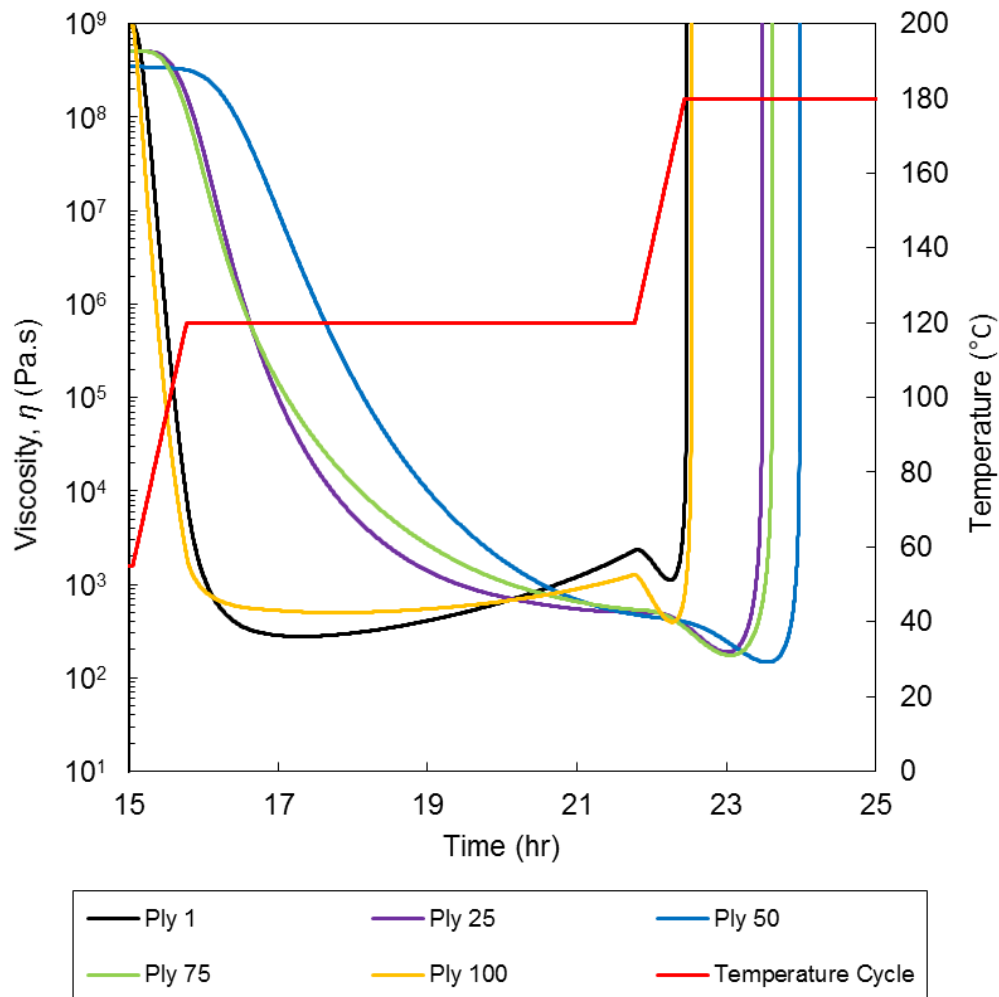


Figure 5.14. Plot of the resin viscosity during the impregnation and cure stages of the temperature cycle (note the time span on the horizontal axis). The viscosities dropped significantly when the temperature was increased to 120°C. Upon heating above 120°C, the epoxy reached its gel point, and the viscosity tended towards infinity.

The simulated viscosities (in Figure 5.14) seemed very high for impregnation, but a quick calculation with the analytical version of Darcy’s Law (Equation 2.22) confirmed that, even for 1000 Pa.s, a ply could be fully impregnated within 80 mins.

Whether this was the case in reality remained unclear as other factors can inhibit the completion of filling (e.g. pressure sharing of the fibre-bed, pressure deficient conditions, etc.; see Chapter 2, Section 2.3.1).

5.4 Conclusions

The development of a 1D finite difference code for manufacturing thick-section composites using epoxy powder has been described. The code included process models for coupled resin flow and heat transfer, and the material models previously described in Chapter 4. Using first order numerical methods, it was possible to solve these models for a typical composites temperature cycle. The accuracy of the heat transfer model was verified by comparing the results of the code to results from the commercial composite processing software, RAVEN. Due to limitations with RAVEN, it was not possible to verify or validate the cure kinetics model, resin flow model, or powder sintering model. It was decided that validation experiments would be required for this purpose; this is the subject of the Chapter 6.

A case study was carried out on a 100-ply laminate which was processed in an oven on steel tooling. The study was used to demonstrate the capability of the code and to analyse a typical temperature cycle used by industry for manufacturing thick-section composite parts. For the drying stage, it was found that the current drying temperature was high enough to melt and sinter the powder throughout the laminate. This played an important role in improving heat transfer within the laminate but may not have been efficient in terms of drying the epoxy. With more analysis and modelling of moisture desorption and gas evacuation, it would be possible to optimise the drying stage of the temperature cycle, however, this was outside the scope of the project.

An existing model for VBO prepreg was used as the basis of the resin flow model. This dual-scale model simulated resin flow around the fibre tows (inter-tow) and into the fibre tows (intra-tow). It was found that the resin viscosity profile varied significantly depending on the resin's position within the laminate. Due to the advancement of cure, the resin did not reach below 100 Pa.s, however, the resin flow

model still predicted that the fibre-bed would reach full impregnation during the 120°C dwell. The fabric impregnation, along with powder sintering, contributed to a 45% reduction in the thickness of the laminate. This thickness change was computed based on a simplified microstructural model which required values for the cured ply thickness and the fibre volume fraction of an individual ply. This microstructural model also played a role in coupling resin flow to the heat transfer model by updating each ply's thickness, and thermal diffusivity.

Temperature profiles for the 100-ply laminate showed that it did not experience any overshoot in temperature, thus eliminating the risk of thermal runaway. Despite, it was found that large thermal gradients still developed within laminate due to the poor thermal conductivity of the constituent materials, the thickness of the laminate, and the low enthalpy of reaction. Importantly, a peak of 44°C temperature difference during the final cure stage coincided with both resin gelation and a peak in the degree of cure difference, thus locking the laminate into an unknown stress state. Furthermore, it was shown that the laminate developed an *outside-to-inside* curing profile due to the lower enthalpy of reaction of the epoxy powder. It was suggested by Bogetti and Gillespie (1992) that this curing profile should be avoided during the manufacture of thick composite laminates.

Residual stress modelling was outside the scope of this project, and, until it is investigated further, the true stress state of the laminate is open to speculation. It is possible that these overlapping events would result in “locked-in” residual stresses due to mismatches in thermal expansion and cure shrinkage. On the other hand, it is also possible that thermal expansion and cure shrinkage would cancel each other out to achieve a near stress-free state, as described by Bogetti and Gillespie (1992). Nevertheless, it is known that minimising thermal and cure gradients within the laminate is desirable. As such, the deposition of more than one epoxy powder through the thickness of the laminate was posited as a possible means of achieving this goal. This hypothesis is investigated further in Chapter 6.

6. Experimental Validation of Process Simulations

6.1 Chapter Introduction and Overview

As powerful as numerical simulations can be, validating their accuracy is essential for their adoption in industry. In some cases, numerical simulations can be validated against analytical solutions, but, ultimately, the most attractive approach for industry is to validate via experimental testing.

This chapter describes experiments which were performed to validate the simulation tool developed in the previous chapter. The design of the experimental apparatus is presented along with details of the hardware and signal analysis used to measure temperature and thickness change. Results for the manufacture of three thick-section laminates are compared with simulated results to test their accuracy. Additional simulations are presented which investigate the format of the vacuum-bag-only (VBO) prepreg, heating methods, the importance of thickness change, and methods for improving the manufacturing process.

6.2 Materials and Methodology

6.2.1 Material Format

Two material formats were investigated:

- A 1200 gsm, stitched uni-directional (UD) glass fabric supplied by Johns Manville, with loose epoxy powder (GRN 918) manually dispersed between each ply.
- An 1800 gsm, stitched triaxial glass fabric that had been partially impregnated from one side with GRN 918 using an automated process. This VBO prepreg (a.k.a. semi-preg) was supplied by ÉireComposites Teo.

6.2.2 Experimental Apparatus Design

Due to the difficulty of directly measuring resin flow within thick-section composites, it was decided that the overall thickness change of the laminate would be used to validate the resin flow model indirectly, and temperature measurements from within the laminate would be used to validate the heat transfer model.

As discussed in Chapter 2, Section 2.3.3, Helmus *et al.* (2016) used experimental data for thickness change in VBO prepreps to validate their air evacuation and resin flow models. This experimental data – originally published by Centea and Hubert (2013) – was measured using a non-contact sensor within an apparatus which could control the pressure conditions. The apparatus itself was placed in a convective oven which meant that the measurements needed to be corrected for temperature drift in the sensor (rated to 150°C) and for thermal expansion of the apparatus itself.

One goal of this project's apparatus design was to minimise features which could potentially lead to the accumulation of error. To achieve this goal, it was decided that the sensor and main support structure for the sensor should be kept isolated from the main heat source to avoid any temperature effects. As such, oven heating was eliminated as a route for experimental validation. Instead, an existing heated tool was chosen as the heat source for the apparatus design. The heated tool consisted of a 750 × 750 × 10 mm flat, aluminium plate with a 600 × 600 mm silicone rubber heating mat adhesively glued to the underside of the plate. The plate was supported by an aluminium frame.

As illustrated in Figure 6.1, the concept of the design was to manufacture thick-section laminates on the heated tool, and use insulation to control the top and side boundary conditions. The temperatures would be measured using thermocouples and the thickness change would be measured using one or more linear variable differential transformers (LVDTs). LVDTs were chosen because they offer high resolution and a measurement range of >100 mm, making them well suited to the measurement of large thickness changes.

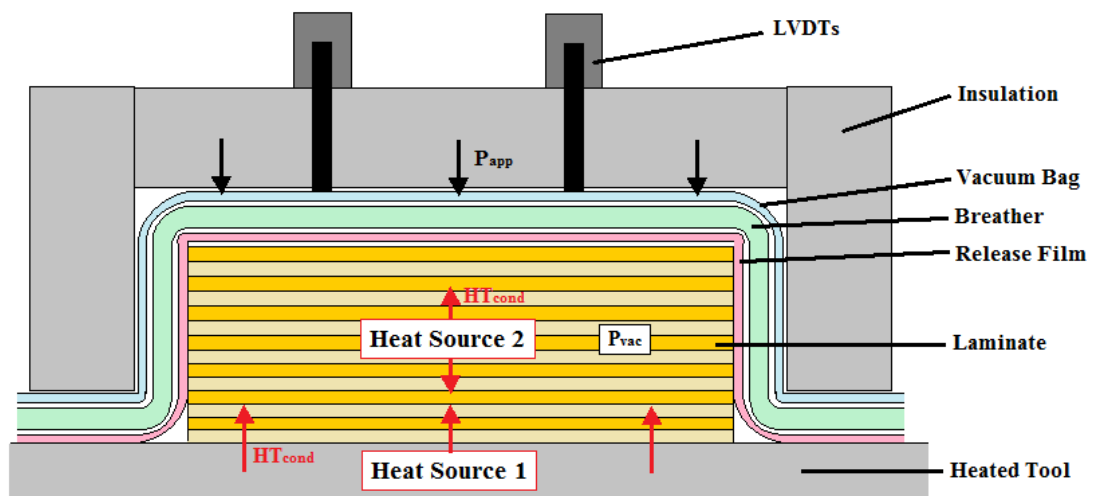


Figure 6.1. Conceptual design for the experimental validation apparatus.

The existing heated tool was rated to 200°C , but had poor temperature uniformity across its surface due to the mismatch between the size of the aluminium plate and the silicone rubber heating mat i.e. the excess aluminium at the perimeter acted as a heat sink. As shown in Figure 6.2, the tool was modified so that the excess aluminium was removed and plate was instead supported at its edges by vermiculite slabs which have a low thermal conductivity ($0.1 - 0.15$ W/m.K). An additional 100 mm thick glass wool insulation slab was placed underneath the tool to insulate it further. This improved the temperature uniformity across the plate and insulated the plate from the main tool frame.



Figure 6.2. Photo of the modified heated tool and tool frame.

GF insulation slabs were used to insulate the test laminates as well (see Figure 6.3). These 200 mm thick insulation slabs were wrapped in vacuum bagging to improve ease of handling. The side walls of the insulation were made in four separate parts and backed with aluminium plates to maintain their shape. Adjustable connectors on the aluminium backing allowed the insulation to be tightly fitted to the test laminate.

The LVDT support frame was designed to connect to the main tool frame so that it would not come in contact with any fixture which was subject to thermal expansion. The support frame could position one or more LVDTs directly above the laminate as it was being processed. A calcium silicate rod was used as an extension for the LVDT due to its low thermal conductivity (0.5 W/m.K) and low coefficient of thermal expansion (approx. $5 \times 10^{-6} \text{ K}^{-1}$). This ensured that temperature correction of the LVDT sensor would not be required, and any thermal expansion of the rod would be minimal.

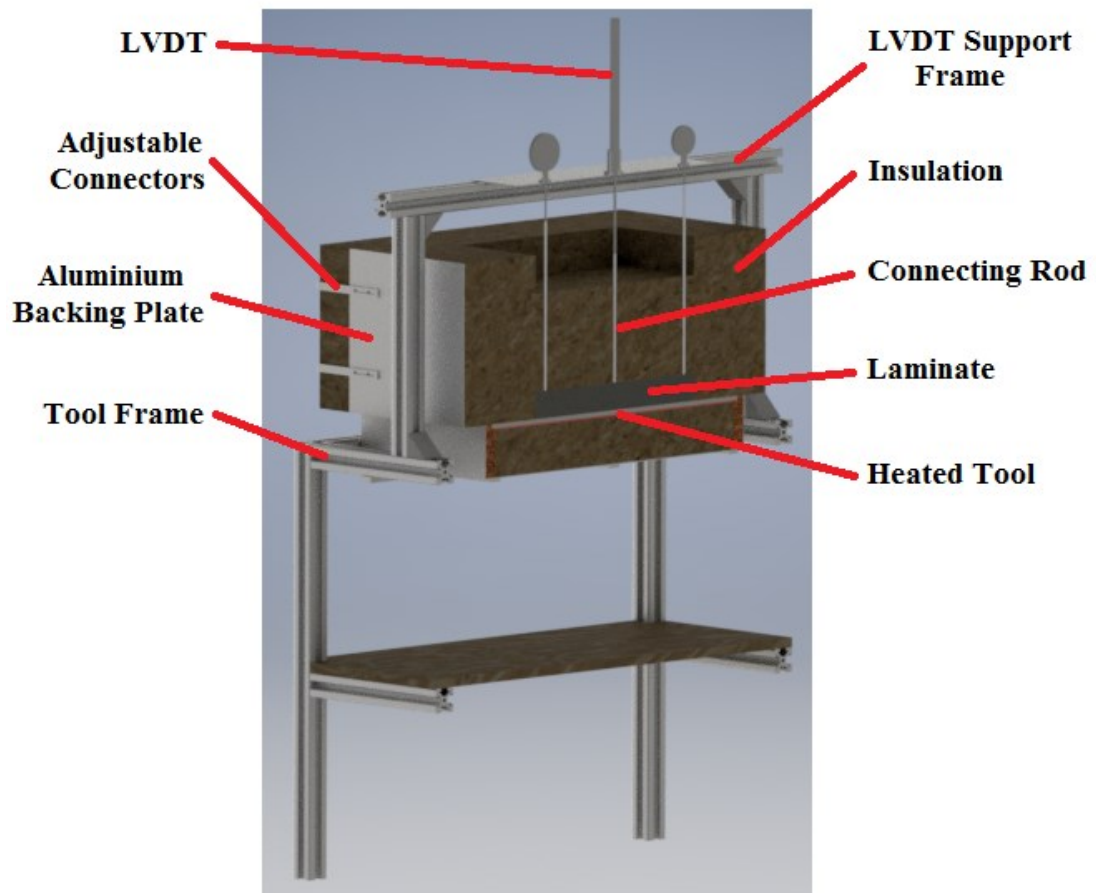


Figure 6.3. Half-section of the apparatus design, rendered in Autodesk Inventor.

6.2.3 Instrumentation and Signal Analysis

AC LVDTs consist of a movable core which passes through a concentric coil assembly, as shown in Figure 6.4. The primary winding of the coil assembly is excited by an AC source and, based on the position of the core relative to the windings, a corresponding AC voltage is induced in the secondary windings due to the coupling of their magnetic flux. This induced voltage is proportional to the distance of the core from the centre of the primary winding, with the phase of the AC signals determining the direction of the core displacement. Typically, the core is attached to an extending rod which is put in contact with the object being measured.

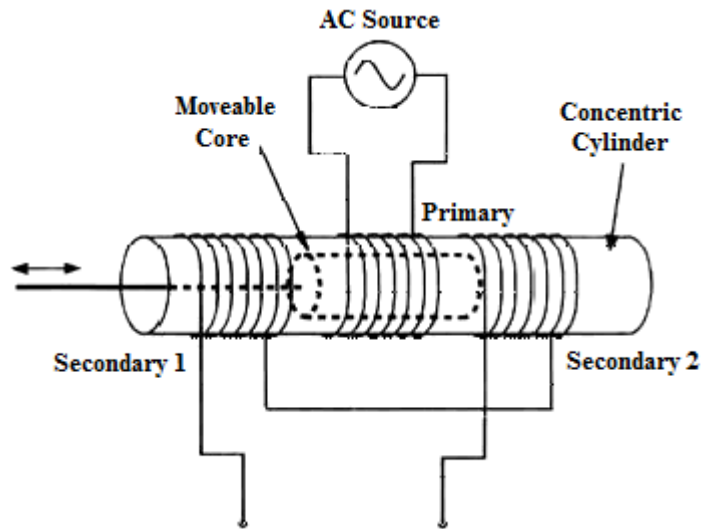


Figure 6.4. Schematic of an AC LVDT assembly (National Instruments, 2018).

A Monitran economy series, spring-loaded, AC LVDT was used for testing. The LVDT had a stroke of ± 50 mm and a 4-wire connection (two wires for excitation of the primary windings, and two wires for the voltage response of the secondary windings). A FeelTech arbitrary function signal generator was used to generate a 3 kHz AC signal with an amplitude of 7.07V (the LVDT was rated to 5V RMS). This input signal, along with the output signal of the secondary windings, was fed into a National Instruments (NI) USB 6009 (analog) module. Analysis of the LVDT signal was performed in LabVIEW. The LabVIEW program recorded the voltage amplitude and phase of the secondary winding, then used a linear relationship (voltage divided by a slope of 0.01154) to calculate the displacement of the core. As a 3 kHz signal was used, the program cycle only ran every 1 min to reduce the amount of data that was stored.

The LabVIEW program recorded temperature data from K-type thermocouples via two NI 9211 modules (four thermocouples each). In addition to this, a Pico USB TC-08 thermocouple data logger was used to record temperatures from eight additional K-type thermocouples.

6.2.4 Laminate Manufacturing

The first test laminate, henceforth referred to as Test Laminate 1, consisted of 60 plies of UD GF with GRN-918 powder manually dispersed between each GF ply. The weight of powder for each layer was measured so that a fibre volume fraction (FVF) of 0.5 was targeted. The lay-up of this laminate is shown in Figure 6.5, along with the lay-up of the second laminate, Test Laminate 2. Test Laminate 2 consisted of 44 plies of triaxial semi-preg. The automated prepregging process deposited sufficient resin for a target FVF of 0.5 also. The final laminate, Test Laminate 3, was a repeat of Test Laminate 1, but consisted of 48 plies and had a target FVF of 0.45.

As discussed in Section 6.2.2, the experimental apparatus was designed to heat the test laminates from one side and insulate the other sides. Under these conditions, the manufacture of 50 - 60 mm thick laminates were approximately equivalent to the manufacture of 100 – 120 mm thick laminates using two-sided heating; a more realistic thickness for the root section of a wind or tidal turbine blade. This effect will be discussed more in Sections 6.3.4 and 6.3.5.

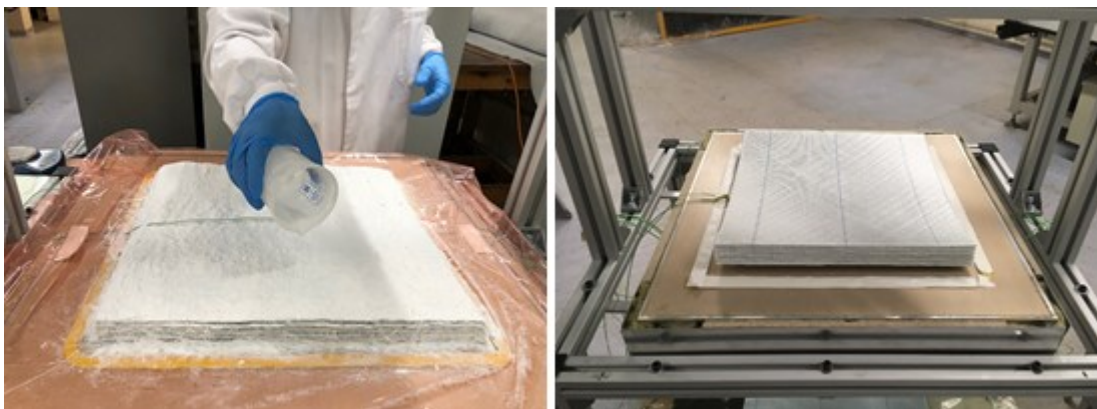


Figure 6.5. Lay-up of the thick-section laminates on the heated tool: (left) GRN 918 epoxy powder was weighed and then manually dispersed between each layer of GF fabric; (right) semi-preg plies were cut and stacked on the heated tool.

For each case, the laminates were symmetric and the ply orientation was kept constant. The plies were cut with dimensions of 400×400 mm, and were stacked at the centre

of the heated tool. During the lay-up, thermocouples were placed throughout the laminates to measure temperature variations. The positions of the thermocouples for Test Laminate 2 are shown in Figure 6.6; similar thermocouple positioning was used for the other test laminates. This arrangement of thermocouples was used to measure the through-thickness temperature variation, but also to ensure that the 1D approximation was valid for the experiment.

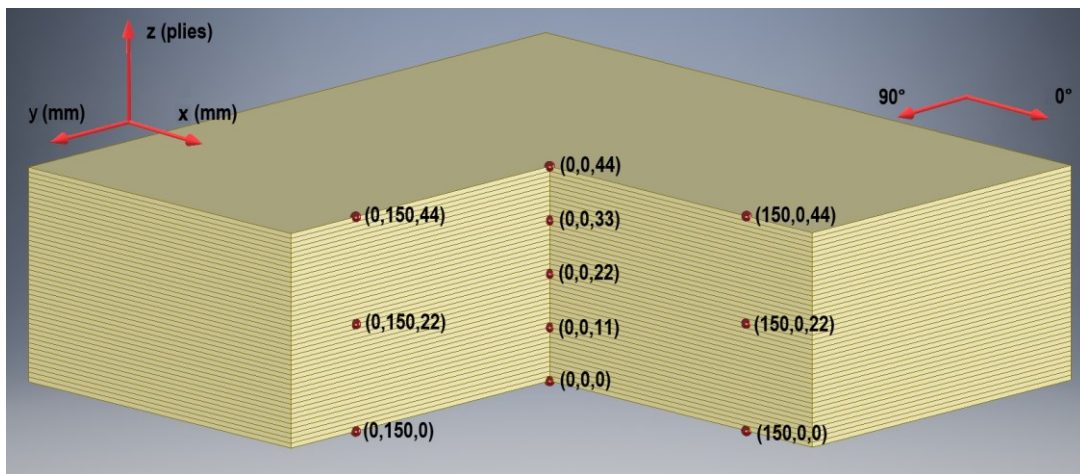


Figure 6.6. Rendered image showing the position of the thermocouples within Test Laminate 2. Refer to the axes (top left) for the coordinate system i.e. (x, y, z). The additional axes (top right) refer to the fibre direction.

After laying up all of the plies and positioning the thermocouples, the vacuum bagging procedure began. For each laminate, two concentric dams of sealant tape were positioned around the laminate. The inner dam prevented excess resin flow, but contained several dry fibre tows which acted as pathways for gases to be evacuated from the laminate. In addition to this, a perforated release film was placed over the laminate to assist with air evacuation and prevent excess resin bleed. One layer of breather cloth was used as porous media for gas transport to the vacuum port. As shown in Figure 6.7, an oversized pleat in the breather cloth was used to station the vacuum port away from the laminate so that it would not interfere with the positioning of the insulation or general heat transfer in the laminate. The vacuum bagging was pleated at the corners of the laminate to avoid obstructing the insulation i.e. the

insulation sides could close over the pleats and fit tightly to the laminate (see Figure 6.8).

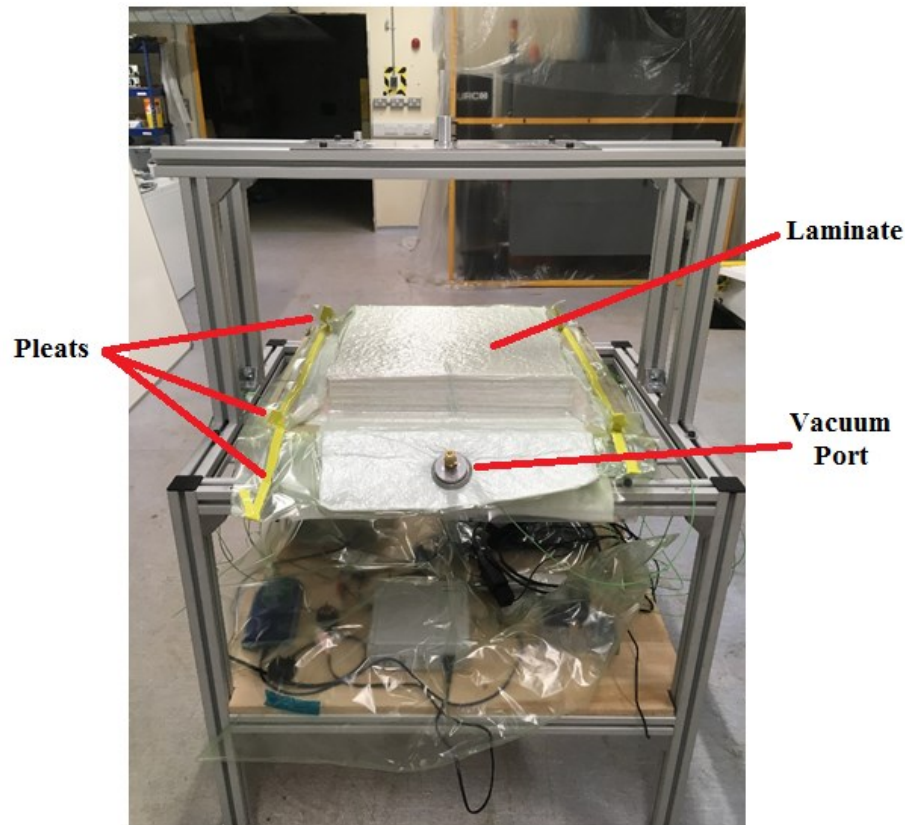


Figure 6.7. Photo of the laminate preform under vacuum pressure. For the insulation to fit tightly around the laminate, the vacuum bagging was pleated at the corners and an oversized pleat was used to station the vacuum port away from the laminate.

The vacuum bagging was checked for leaks and was considered fully sealed when the vacuum pressure did not drop after several minutes. A maximum pressure of approx. 85 kPa was recorded at the beginning of the tests. Measuring the thickness change due to gas evacuation was not included in this study. Instead, the initial thickness was taken as being the thickness after several minutes under vacuum. The LVDT took measurements from the centre of the laminate, as shown in Figure 6.8. The connecting rod was passed through a hole in the top insulation so that it came in contact with the top surface of the vacuum bagging. The in-built spring mechanism ensured that the

rod remained in contact with the surface throughout the experiment without indenting the laminate itself.

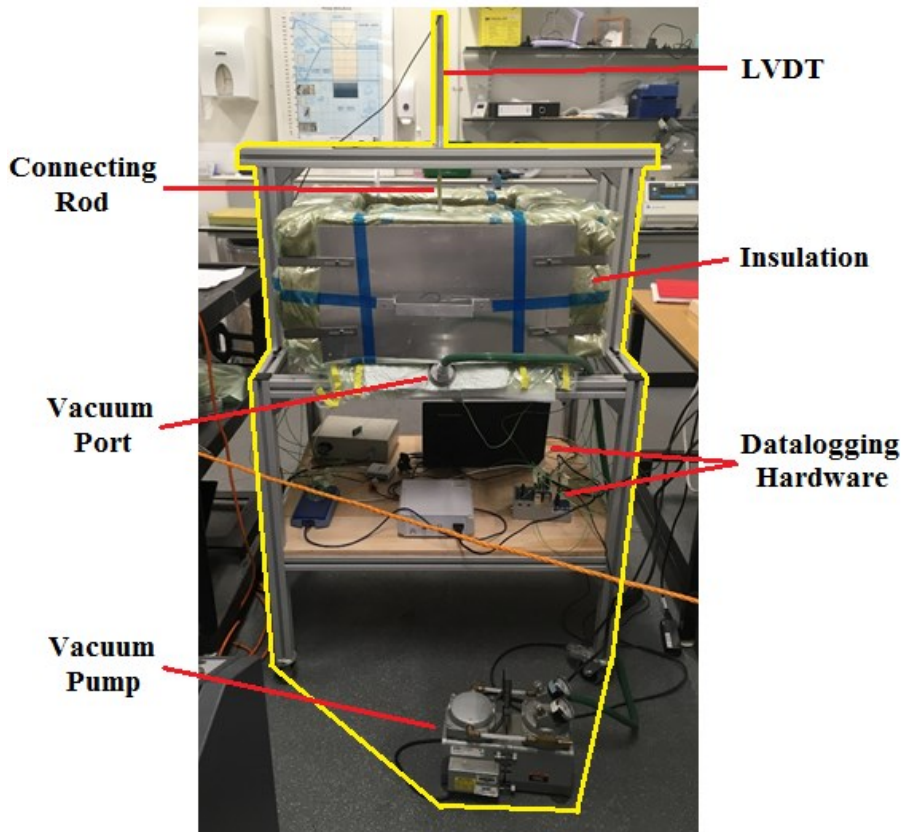


Figure 6.8. Photo of the apparatus (outlined in yellow) during an experiment.

6.2.5 Simulation of Test Laminate Processing

For the process simulations of Test Laminates 1, 2 and 3, the assumed material properties were as given in Table 5.1, Table 5.2, and Table 5.3 in Chapter 5, Section 5.2.4. The initial conditions used for each simulation are given in Table 6.1, Table 6.2, and Table 6.3 below. For each simulation, the ambient air temperature was assumed to remain constant at the values given in the tables. The initial temperature of the laminate, bagging, tool, etc. were assumed to be equal to the ambient temperature.

Table 6.1. Initial conditions for the simulation of Test Laminate 1.

Parameter [units]	Value
No. of plies	60
Cured ply thickness [m]	0.0009
Fibre volume fraction	0.5
Degree of impregnation	0.113
Powder void fraction	0.503
Degree of cure	0.2
Applied pressure [Pa]	85×10^3
Ambient temperature [°C]	21

Table 6.2. Initial conditions for the simulation of Test Laminate 2.

Parameter [units]	Value
No. of plies	44
Cured ply thickness [m]	0.0013
Fibre volume fraction	0.5
Degree of impregnation	0.575
Powder void fraction	0.175
Degree of cure	0.01
Applied pressure [Pa]	85×10^3
Ambient temperature [°C]	19

Table 6.3. Initial conditions for the simulation of Test Laminate 3.

Parameter [units]	Value
No. of plies	48
Cured ply thickness [m]	0.001
Fibre volume fraction	0.45
Degree of impregnation	0.113
Powder void fraction	0.503
Degree of cure	0.2
Applied pressure [Pa]	85×10^3
Ambient temperature [°C]	18

Note that the degree of cure (DoC) for Test Laminate 1 and 3 was set to 0.2. This was because 12 months had passed between initial DSC testing of the powder and manufacture of the test laminates. Subsequent DSC testing suggested that the DoC had increased in storage (i.e. out-time effects). These effects should be investigated further, but were outside the scope of this work.

For Test Laminate 3, the degree of impregnation (DoI) and powder void fraction were fitted to the experimentally measured thickness change. Their values were deemed realistic; the DoI was slightly more than enough to fill the inter-tow region (which was equivalent to a DoI of 0.4737), and the 0.175 void fraction accounted for any cracks in the brittle, uncured epoxy matrix, as well as gaps between the stiff semi-preg plies caused by surface roughness.

The simulations also accounted for conductive heat transfer through the insulation and the silicone rubber heating mat. Their thermal material properties are given in Table 6.4.

Table 6.4. Material properties used for the insulation and silicone rubber heating mat.

Property [units]	Value	Source
Thermal conductivity of insulation [W/m.K]	0.04	(Greenspec, 2018)
Thermal conductivity of silicone rubber [W/m.K]	0.53	(Kratz <i>et al.</i> , 2012)
Density of insulation [kg/m ³]	40.0	(Greenspec, 2018)
Density of aluminium [kg/m ³]	1540.0	(Kratz <i>et al.</i> , 2012)
Specific heat capacity of insulation [J/kg.K]	1030.0	(Greenspec, 2018)
Specific heat capacity of silicone rubber [J/kg.K]	1050.0	(Kratz <i>et al.</i> , 2012)

6.3 Results and Discussion

6.3.1 Uni-directional Laminates with Epoxy Powder

The results of Test Laminate 1 are compared with simulation results in Figure 6.9 and Figure 6.10. For Test Laminate 1, the drying cycle was split into two stages; one stage at 35°C and another stage at 55°C. At 35°C, there was little or no thickness change because the epoxy powder was below its T_g , and it was clear from the temperature evolution that heat transfer was slow due to the very low thermal conductivity of the powder. By comparison, the rate of heat transfer improved in the second stage of drying at 55°C. This was because the powder began to sinter, and the laminate thickness decreased significantly. The sintering model captured the general trend of the thickness decrease but lacked accuracy in describing the temperature dependence of the epoxy powder. This inaccuracy was most likely related to poor temperature control and pressure-dependent effects during the parallel-plate rheometry tests described in Chapter 4, Section 4.2.2. It may be improved via repeated testing using a temperature-controlled test chamber and smaller plates or, alternatively, using thermomechanical analysis (TMA).

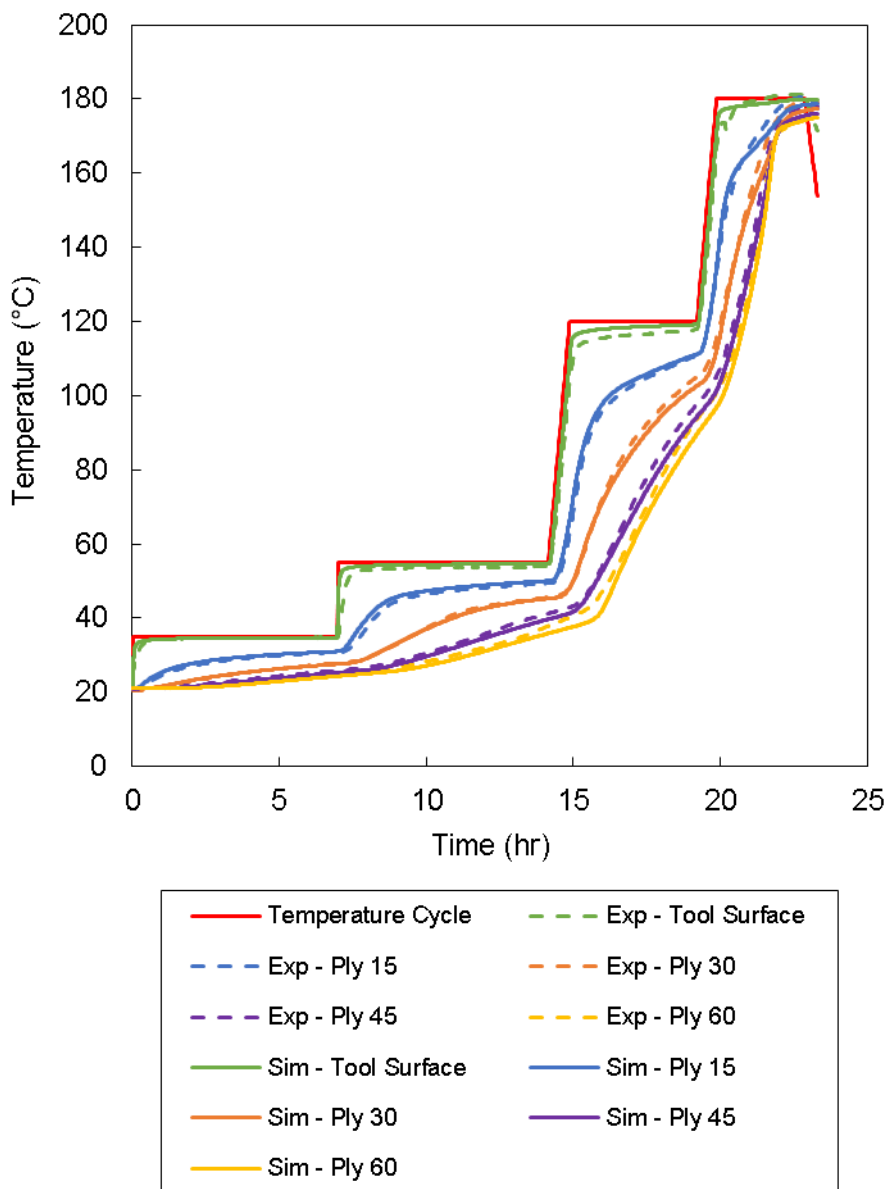


Figure 6.9. Comparison of simulated temperatures and thermocouple data for Test Laminate 1. The simulation was accurate in describing the temperature evolution.

The experimental and simulated thickness change data (Figure 6.10) converged during the impregnation stage as the powder finished sintering and resin flow became the dominant process. The resin flow model predicted a distinct transition from inter-tow flow to intra-tow flow (identified by a sudden change in slope for the thickness change curve, midway through the impregnation stage), however, this transition was

not distinguishable in the experimental data. This suggested that, in reality, fabric impregnation was characterised by a more gradual transition between the two flow domains. Similarly, the simulation predicted an abrupt plateau in thickness change after 20 hr, signally the end of resin flow, whereas the experiment showed a more gradual cessation. It was found that the simulation overestimated the total thickness change by approx. 2.5 mm.

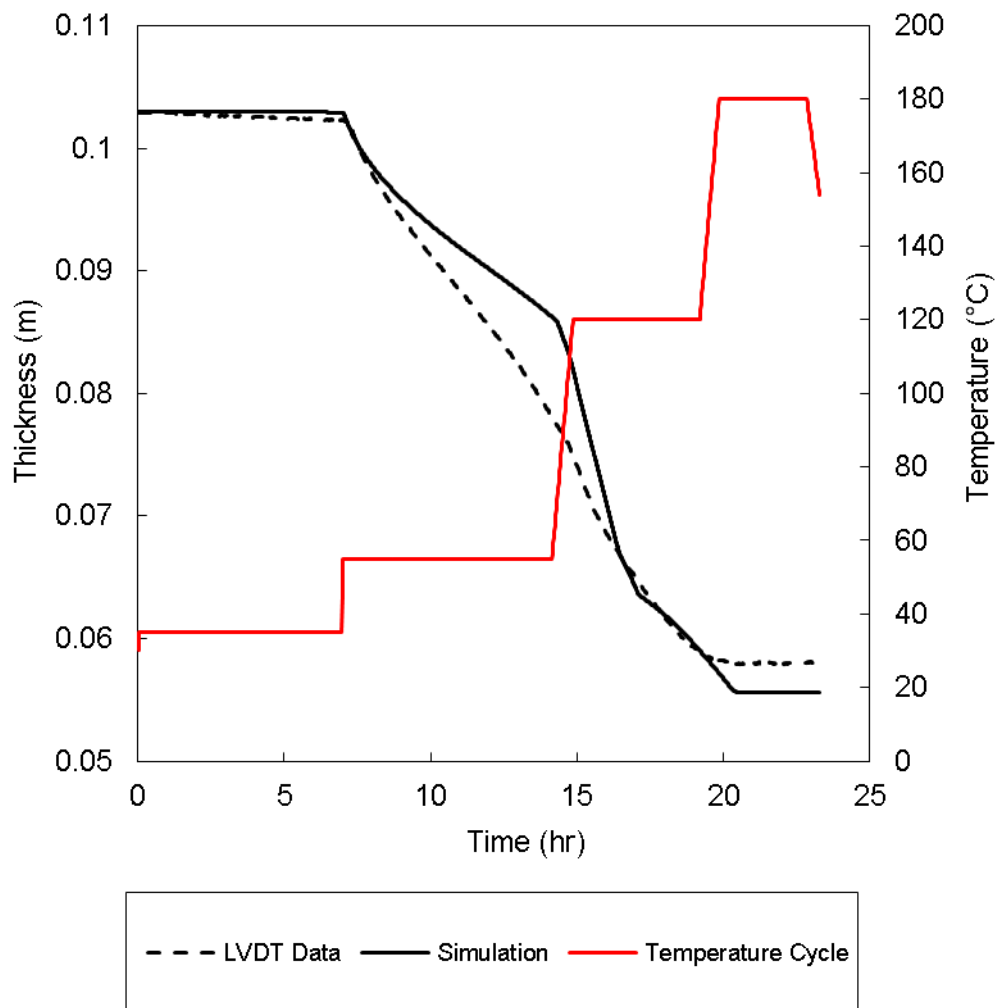


Figure 6.10. Comparison of the simulated thickness change and LVDT measurements for Test Laminate 1. The simulations captured the overall trend, however, there was some inaccuracy in the sintering model and in the prediction of the final thickness.

In terms of the heat transfer model, the simulation was accurate throughout, except for a slight underestimation of the temperature increase at the centre of the laminate during the drying and impregnation stages (approx. 3°C); most likely due to the inaccuracy of the sintering model. Both experiment and simulation showed that the exothermic curing reaction increased the rate of temperature change, but did not result in any thermal overshoot of the programmed temperature cycle.

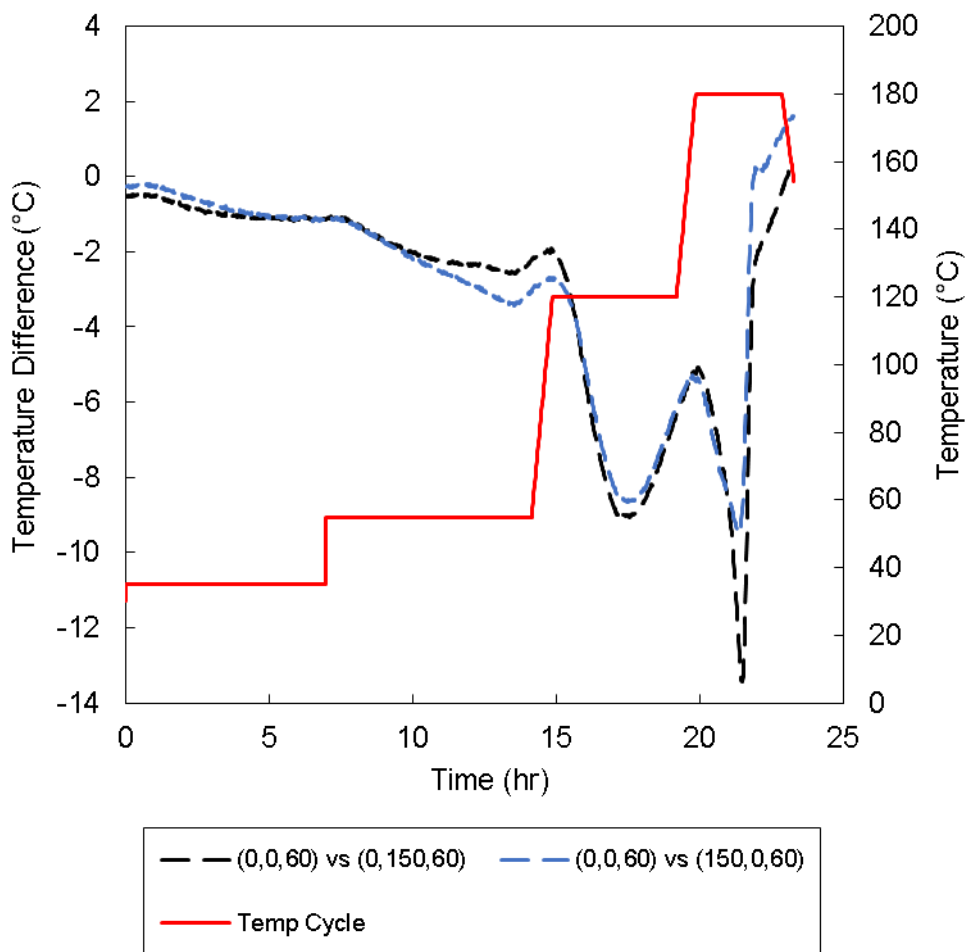


Figure 6.11. Plot of the temperature difference between the centre of Ply 60 and 150 mm towards the edge, in the x and y directions. In both cases, the centre thermally lags the edges, hence the negative values. The legend refers to the coordinate system given in Figure 6.6.

As discussed in Section 6.2.4, thermocouples were positioned at both the centre and near the edges of the laminate so that the 1D heat transfer assumption could be tested (see Figure 6.6). It was found that a temperature difference did exist between the centre and edges, with the centre typically lagging behind the edges, as shown in Figure 6.11. It was possible that edge effects would have an impact on the 1D approximation at the centre of the laminate, but given that the laminate experienced a peak of almost 80°C in through-thickness temperature difference, in-plane heat transfer would be relatively negligible. Nevertheless, efforts were made to reduce the temperature difference for the other test laminates by fitting the insulation tighter to their sides.

As shown in Figure 6.12, Test Laminate 1 was reheated to test the effects of thermal expansion. For an unknown reason, the laminate appeared to initially contract upon heating, then subsequently expand. This feature was present for all three test laminates when reheated. It was noted that the response on cooldown was also non-linear, with a peak in expansion as the laminate underwent its glass transition. As such, the two phenomena may be linked, however, further investigation was outside the scope of this work. Overall, it was found that the thermal expansion/contraction accounted for approx. $\pm 3\%$ of the total thickness change of Test Laminate 1. This was considered negligible in terms of validating the process simulations.

A greater source of error was the relatively uneven thickness of Test Laminate 1 ($\pm 6.8\%$ variation) due to the manual dispersion of powder between the plies. A section was cut from the laminate to inspect its interior (see Figure 6.13). Partially dry fibre tow, as well as inter-tow voids, were widespread in the upper third of the laminate. In addition to this, sporadic incomplete tow impregnation was visible in the lower two thirds of the laminate. Figure 6.14 shows the general defects that formed in the upper third of the laminate, while Figure 6.15 shows the intra-tow voids at the centre of the tows under increased magnification. These defects may have been the result of numerous factors including ageing of the epoxy powder (i.e. out-time effects), pressure sharing of the fibre, or entrapment of gases. The formation of these defects was not predicted by the process simulation and forms an obvious area of improvement for future development of the simulation tools.

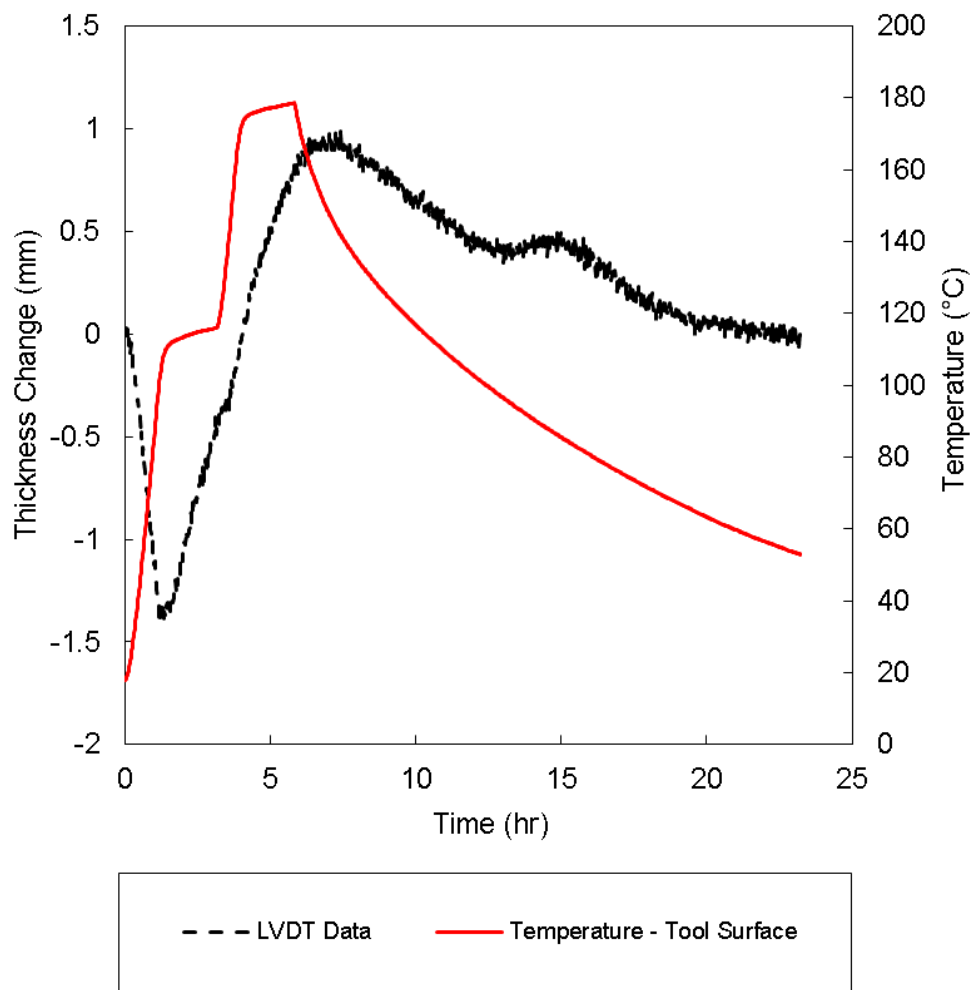


Figure 6.12. Plot of LVDT data for a reheat cycle on Test Laminate 1. Unusually, the laminate initially contracted upon heating and then expanded. Overall, the change was negligible compared to the laminate thickness change during the initial processing.



Figure 6.13. Cut-section of Test Laminate 1 showing the non-uniformity of thickness.



Figure 6.14. USB microscope image of the upper third of Test Laminate 1 (X1 magnification). Both incomplete tow impregnation and inter-tow voids are visible.

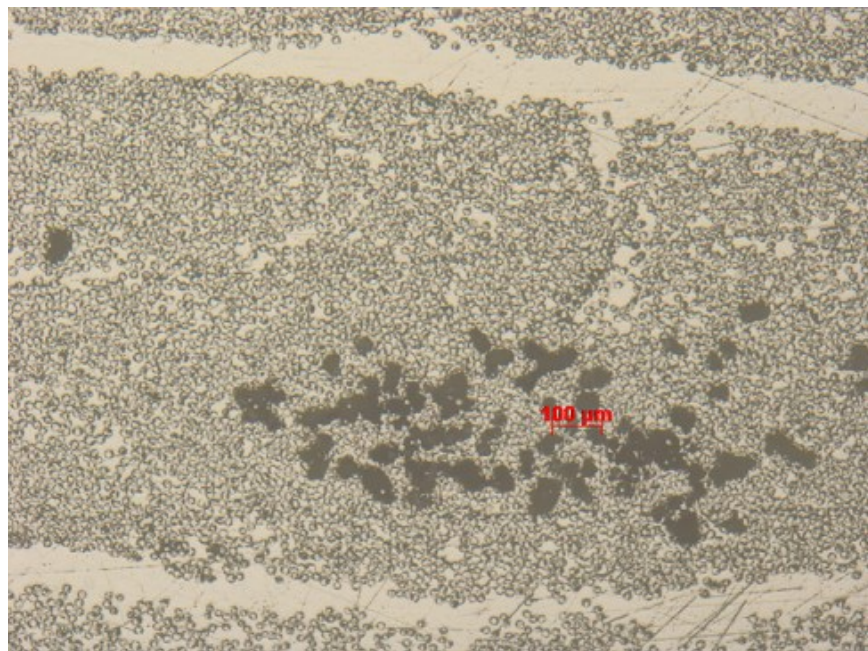


Figure 6.15. Optical microscope image of Test Laminate 1 (X5 magnification). The image reveals the intra-tow voids at the centre of the tow caused by incomplete impregnation.

As a result of the void formation in Test Laminate 1, an FVF of 0.45 was targeted for Test Laminate 3. It was thought that this may reduce any pressure sharing effects caused by the fibre-bed as the resin layers diminished. Other changes to the laminate included reducing its thickness to 48 plies and increasing the in-plane dimensions (420 x 420 mm) to prevent heat loss via gaps between the laminate and the insulation. The low temperature drying stage (at 35°C) was replaced with a continuous drying stage at 55°C. The results for Test Laminate 3 are shown in Figure 6.16 and Figure 6.17.

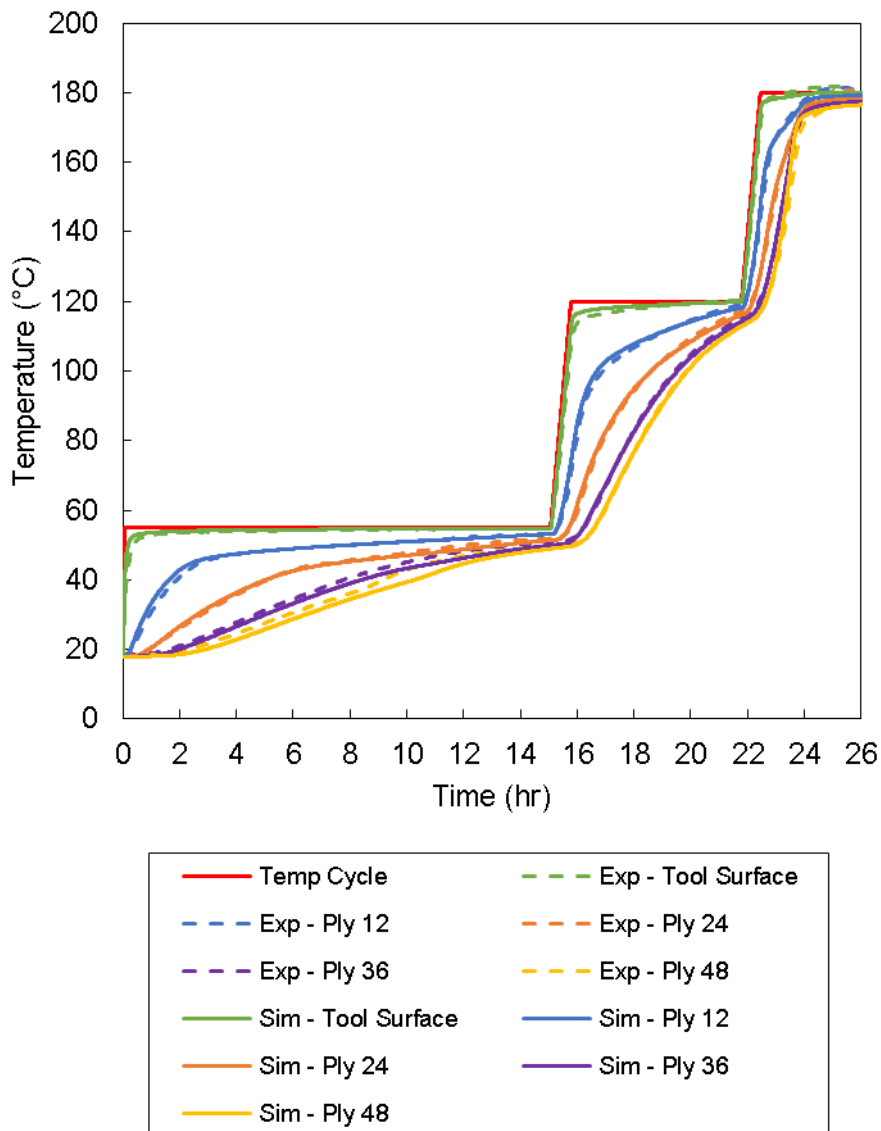


Figure 6.16. Thermocouple data for Test Laminate 3 compared with results of a simulation.

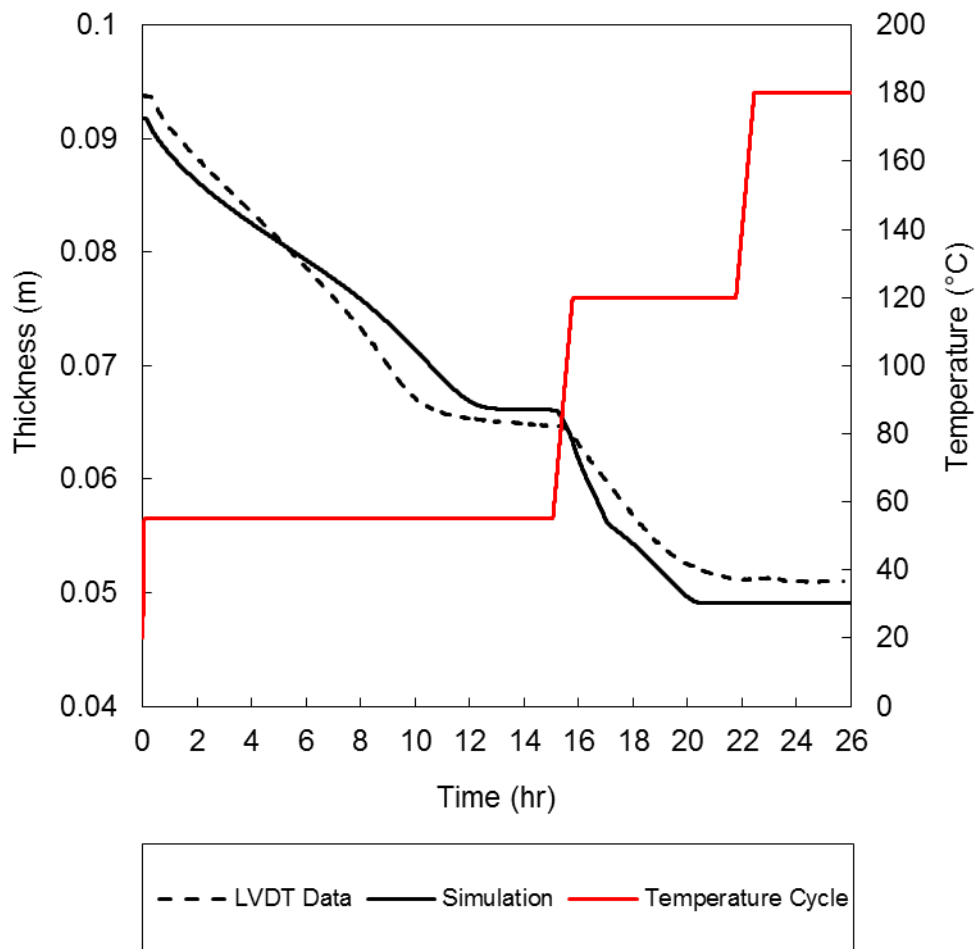


Figure 6.17. LVDT data for Test Laminate 3 compared with simulation results.

The simulations showed reasonable accuracy in capturing the general trends of the experiments. Once again, however, the simulations were slightly inaccurate in predicting the thickness change due to sintering, which has a knock-on effect with the accuracy of the temperature profile during the drying stage.

It was found that, when the whole drying stage was carried out at 55°C, sintering ceased after approx. 10 hr and the thickness change became dependent on inter-tow resin flow, which was slow at this temperature due to the high viscosity of the resin. Once again, the resin flow model predicted a noticeable transition from inter-tow flow to intra-tow flow during the impregnation stage, whereas, the LVDT data suggested a more gradual transition. Furthermore, the simulation once again predicted an abrupt

end to thickness change, but the LVDT data revealed a more gradual cessation. Helmus *et al.* (2016) showed a similar mismatch between simulation and experiment, where pressure deficient conditions resulted in a more gradual plateauing of experimentally measured thickness change. Despite careful checks for vacuum leakage, this could suggest that Test Laminates 1 and 3 suffered from pressure deficient conditions, however, more experiments and analysis would be required to investigate this further.

A section was cut from Test Laminate 3, and, upon inspection, it was confirmed that the laminate suffered from the same defects as Test Laminate 1 i.e. incomplete tow impregnation and inter-tow voids. Furthermore, Test Laminate 3 showed $\pm 7\%$ thickness variation along the cut edge and an in-plane temperature variation similar to Test Laminate 1. By this measure, the changes that were made for Test Laminate 3 had little or no effect.

6.3.2 Partially Impregnated Triaxial Laminate

As previously mentioned, Test Laminate 2 differed from the other test laminates in that it was a stitched triaxial fabric which had been partially impregnated with GRN 918 in an automated process. This meant that the powder dispersion was more uniform, and that the thickness change due to sintering was expected to be much less for the laminate.

The experimental data for Test Laminate 2 is compared against the results of the 1D simulations in Figure 6.18 and Figure 6.19. The finite difference code was adjusted to account for resin flow into the three layers of fibre tow in the triaxial fabric. The simulations were again accurate in capturing the general processing behaviour of the test laminate, however, in this case, the simulation underpredicted the temperature increase during the impregnation and curing. This may have been related to a difference in the through-thickness thermal conductivity of the triaxial fabric, or because of the lower void content of the laminate (discussed further at the end of this section). Another interesting feature of Figure 6.18 was that the temperature increased faster during the drying stage due to the absence of powder and the reduced initial thickness. The top ply of Test Laminate 2 reached 40°C after 5.66 hr, whereas Test

Laminate 3 took 9.16 hr to reach 40°C. Bearing in mind the advantages of drying the epoxy in powder form, this result showed that there was an obvious trade off in processing advantages between the two material forms.

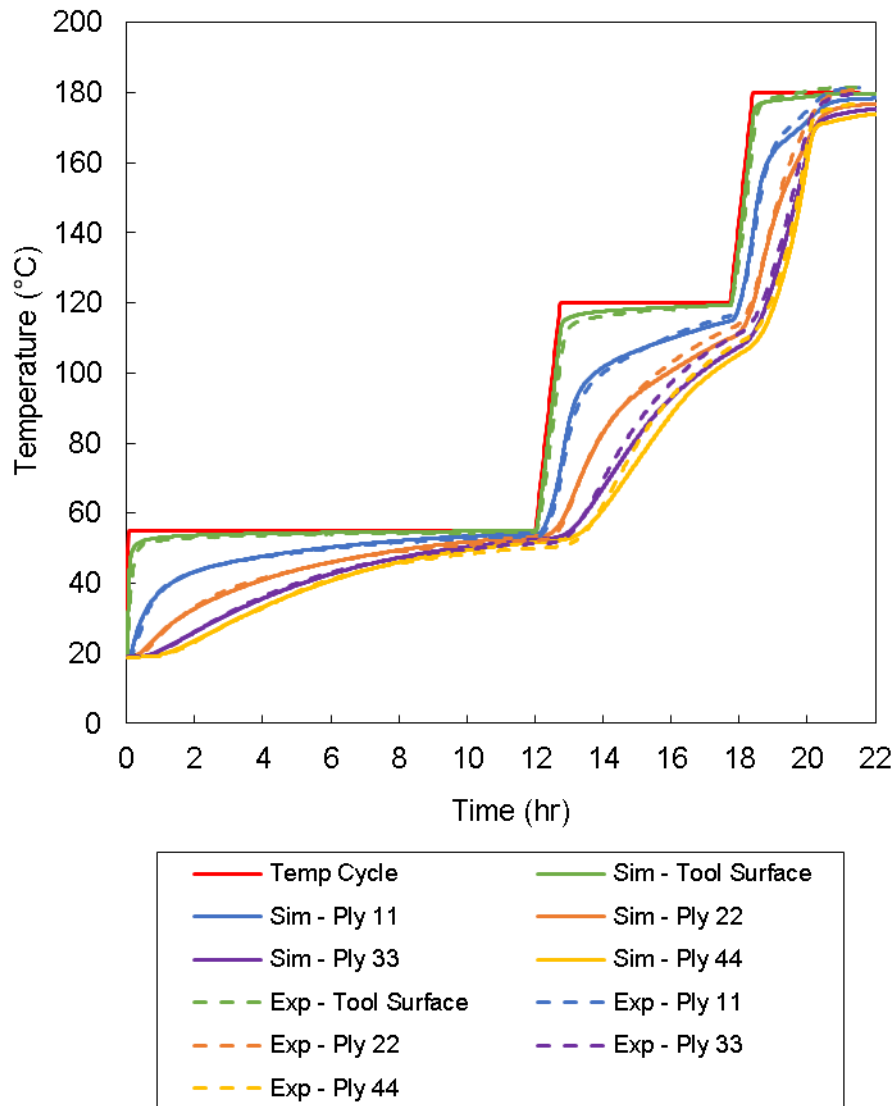


Figure 6.18. A plot of thermocouple data and simulated temperatures for Test Laminate 2.

In terms of the LVDT data (Figure 6.19), it was interesting to note that, despite the epoxy being fully sintered in the VBO prepreg production process, Test Laminate 2 was still compacted by several millimetres during the drying stage. To account for this,

the simulation was given an initial powder void fraction of 0.175. Most likely, there were two sources for the initial void fraction: (1) the formation of cracks in the brittle uncured epoxy matrix during handling, and (2) the formation of gaps between the stiff, board-like plies during lay-up.

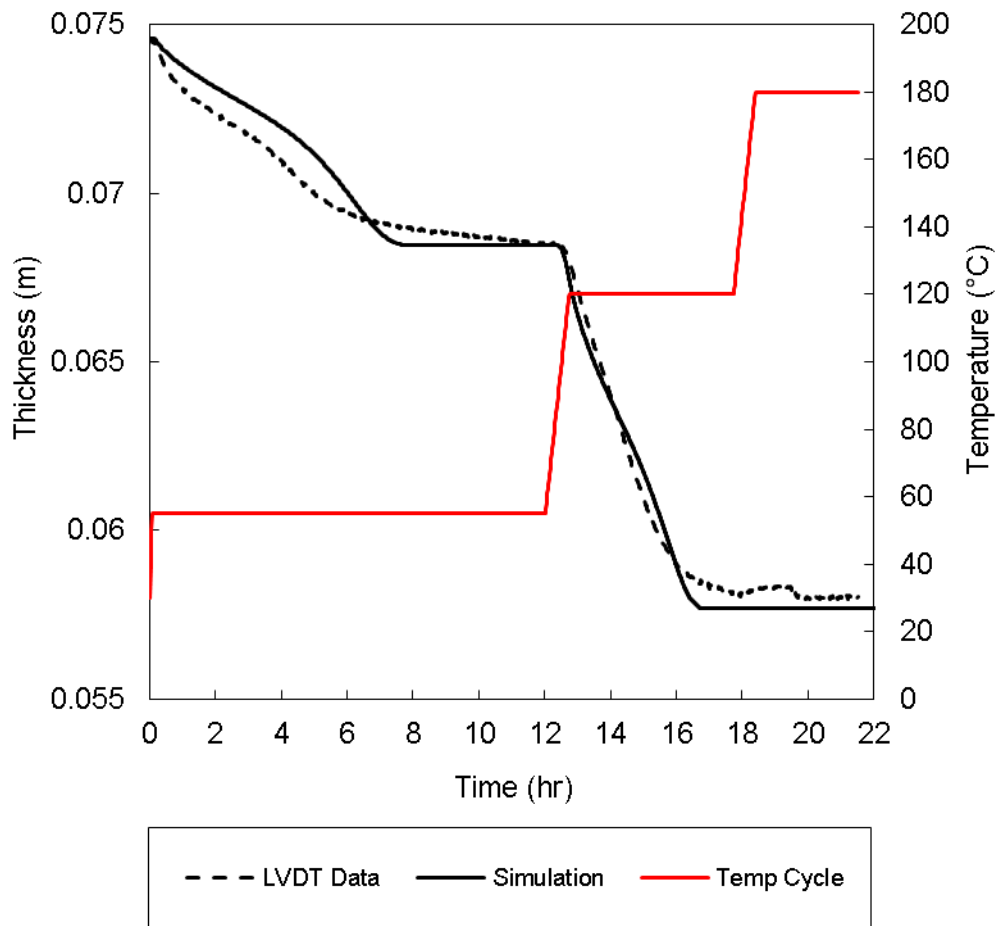


Figure 6.19. A plot of LVDT data and simulated thickness change for Test Laminate 2. Note that, although the epoxy powder had been fully sintered during the production of the VBO prepreg, the thickness of the laminate still reduced by several millimetres.

It was noted that the Test Laminate 2 had better in-plane temperature uniformity than Test Laminates 1 and 3 (see Figure 6.20). As such, greater confidence could be taken from the 1D heat transfer approximation.

As shown in Figure 6.21, Test Laminate 2 had much better thickness uniformity (variation of $\pm 1\%$) than the other laminates. It also seemed to have much less visible defects, however, optical microscopy of the cut-section (see Figure 6.22) revealed that there were cases of sporadic incomplete tow impregnation and larger inter-tow voids. The latter case was particularly true in the mid-plane of the laminate where prepreg plies had been stacked symmetrically so that their resin rich surfaces were in contact. Given the fully sintered form of the epoxy, this was possibly a result of entrapped gases, as air and water vapor would have had more resin to pass through in order to reach a dry fibre pathway for evacuation.

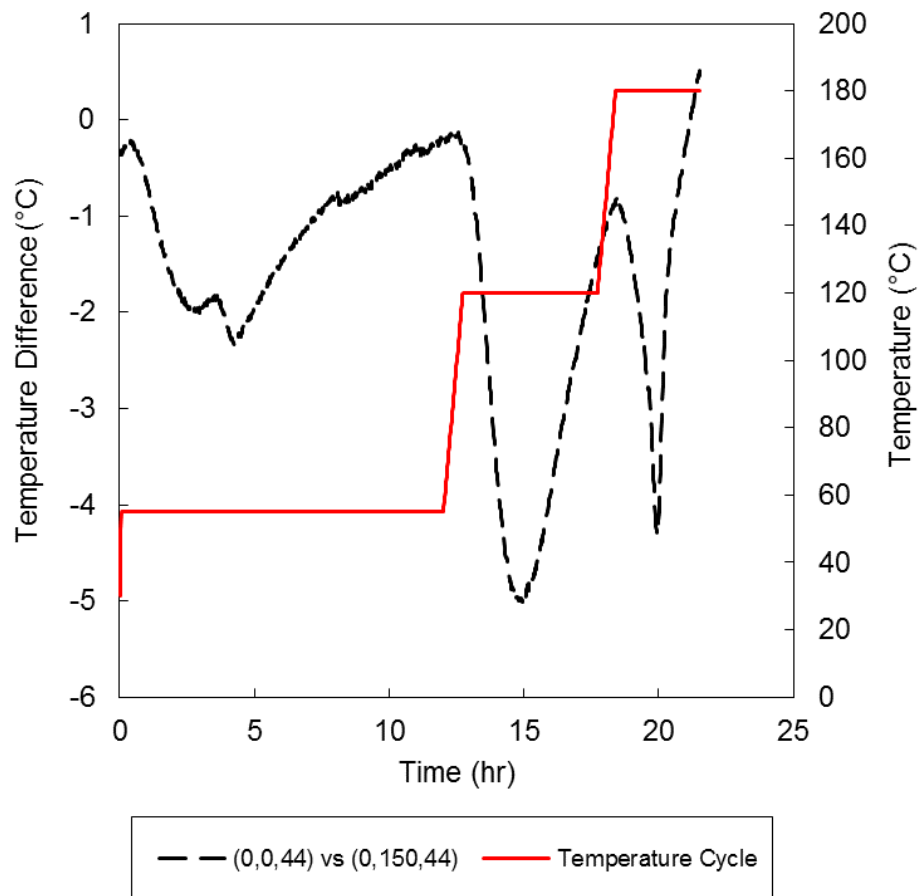


Figure 6.20. Plot of the in-plane temperature difference between (0,0,44) and (0,150,44) in Test Laminate 2. Refer to Figure 6.6 for the coordinate system.

Although the void content of the laminates was not quantified, the difference in void content was noticeably higher for Test Laminates 1 and 3 based on visual inspection. In terms of the heat transfer model underpredicting the temperature increase in Test Laminate 2, it was possible that the higher void content of Test Laminates 1 and 3 corresponded with lower thermal conductivity, as was the case with the powder void fraction. The thermal conductivities for simulations may be manually adjusted for differences in void content, but ideally a suitable model would be added to the numerical code which can account for such behaviour.



Figure 6.21. Cut-section of Test Laminate 2.

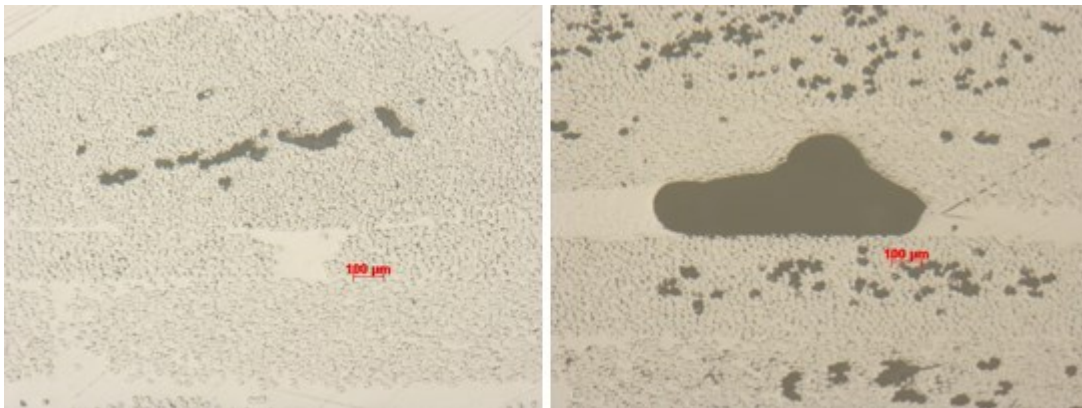


Figure 6.22. Micrographs of Test Laminate 2 at two locations. (L) Intra-tow voids caused incomplete tow impregnation. (R) Inter-tow and intra-tow voids caused by gases which were entrapped at the laminate midplane (i.e. plane of symmetry).

There were many factors which could have contributed to incomplete tow impregnation and void formation in Test Laminates 1, 2, and 3. Those that have already been mentioned include out-time effects, pressure sharing with the fibre-bed, and entrapped gases. Another factor, was the relatively poor vacuum that was achieved during the testing. Due to limitations with the vacuum pump, a max of 85 kPa was achieved for each test. Ideally, up to 101 kPa should be achieved for VBO processes, as it has been shown that pressure deficient conditions can result in up to 5.5% voids in thin laminates made from VBO prepregs (Centea and Hubert, 2013).

6.3.3 Investigation of VBO Prepreg Format

With the simulations validated for two different VBO prepreg formats, it was worthwhile considering the advantages and disadvantages of each format in more detail. From Chapter 3, Section 3.3.6, it was known that as-supplied epoxy powder performed significantly better w.r.t water desorption when compared to sintered epoxy. Furthermore, it was hypothesised that it would improve the through-thickness gas permeability of the VBO prepreg compared to a format with homogenous resin layers.

To offset these advantages, the experimental validation tests revealed that epoxy powder reduced the rate of heat transfer in the laminate. This was because it increased the initial bulk of the laminate preform by up to 30% and had a thermal conductivity which 55% lower than that of fully sintered epoxy. To determine the severity of this effect, the simulation of a 100-ply laminate (described in Chapter 5, Section 5.3.1) was performed again with three different initial values of powder void fraction. Figure 6.23 shows the temperature plots for Ply 50; the ply most affected by this phenomena). The results showed that only the drying stage was affected by the powder format, and the effect diminished as the powder sintered. Given this relatively small impact on heat transfer, the advantages of a powdered format may outweigh the advantages of a fully sintered VBO prepreg.

One aspect of the powdered format that must be investigated further, however, is the automated production of the VBO prepreg. It was noted, during the lay-up of Test

Laminates 1, 2, and 3, that the semi-preg material (Test Laminate 2) was much easier to work with, and produced a more uniform laminate due to the evenly deposited powder. This is an important aspect of manufacturing, and it is suggested that, if the powder format is to be explored further, the powder should be partially sintered onto a fabric in an automated prepreg production process also. In this case, an optimal degree of sintering would need to be determined to find the best trade-off between sorption properties and handling properties.

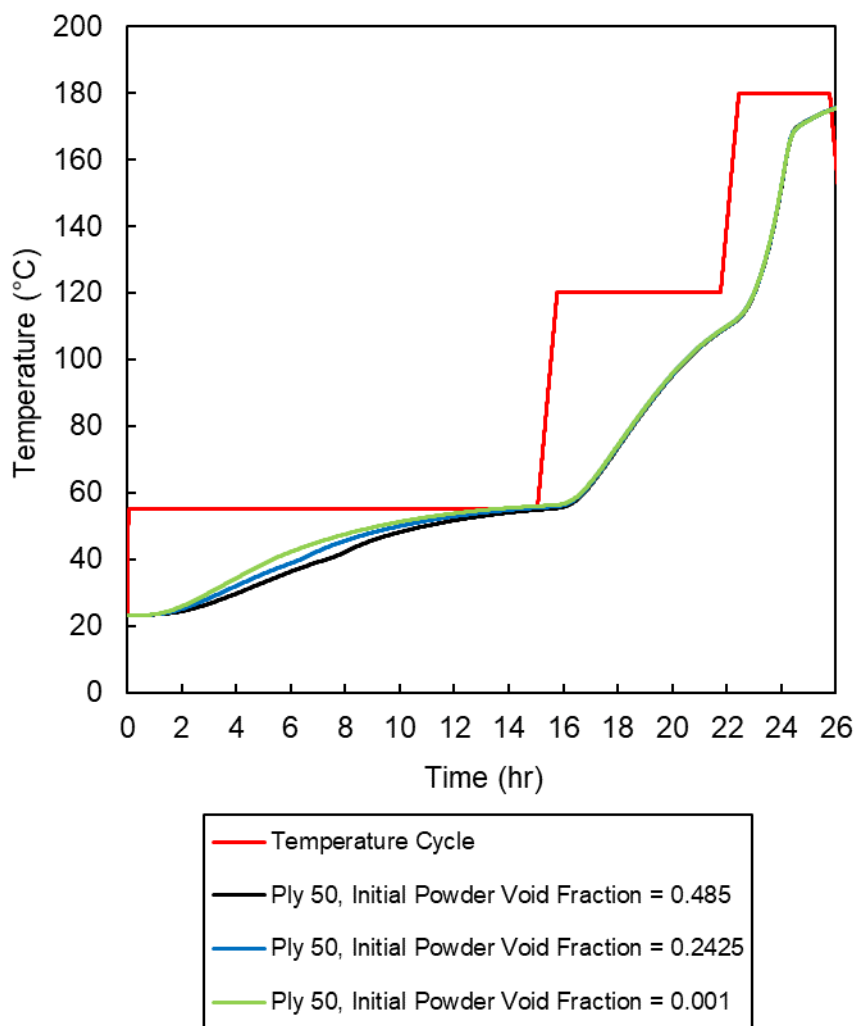


Figure 6.23. Plot of the temperature at Ply 50 for varying levels of initial powder void fraction.

6.3.4 Investigation of Thickness Effects

The relatively small effect of the powder void fraction w.r.t. heat transfer suggested that perhaps the coupling of heat transfer and thickness change was not as important as previously considered. To verify whether coupling these effects was necessary or not, another simulation of the 100-ply laminate from Chapter 5 was run for a fully consolidated laminate (i.e. no thickness change).

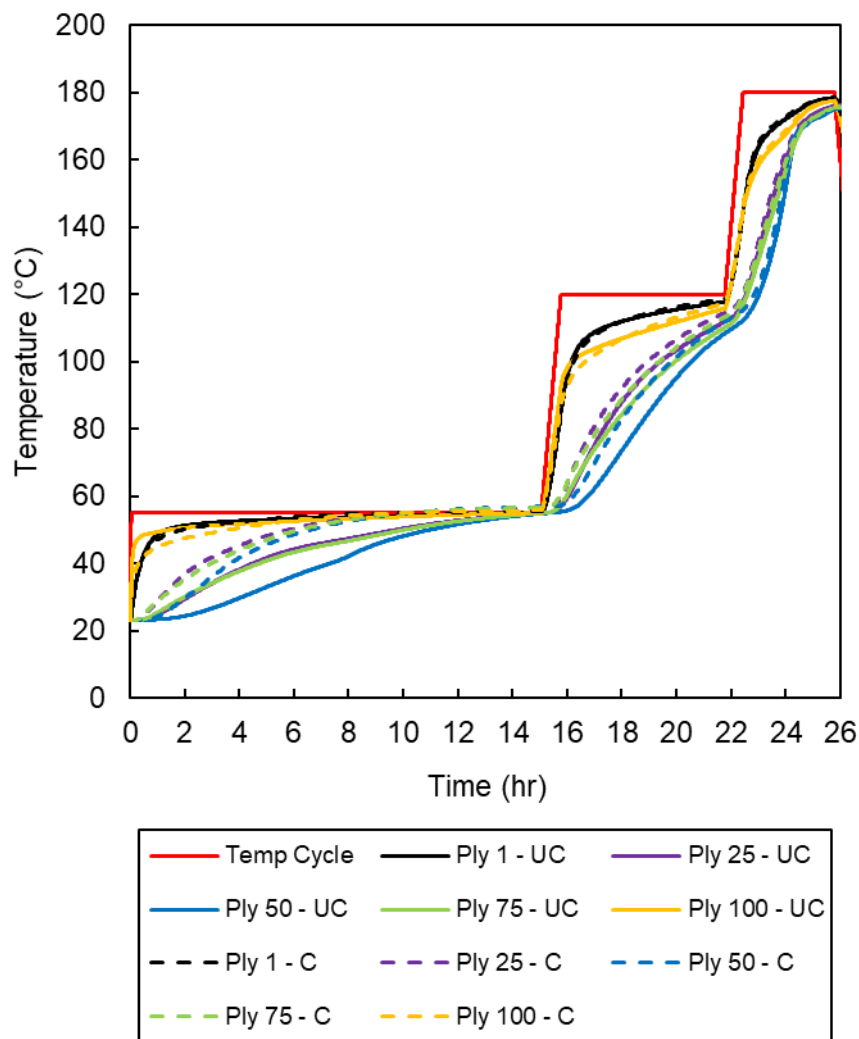


Figure 6.24. Comparison of simulations for a consolidated (C) laminate and an unconsolidated (UC) laminate. The consolidated laminate simulation assumed a constant thickness throughout.

As can be seen in Figure 6.24, there were relatively significant discrepancies between the two simulations during the drying and impregnation stages, while the solutions converged during the cure stage. The effect was more pronounced than in Figure 6.23 because the thickness change due to impregnation, as well as sintering, was unaccounted for in the fully consolidated case. Naturally, these discrepancies influenced other processes like fabric impregnation and cure evolution. As such, the importance of coupling the models for powder-based VBO prepregs was verified. In contrast, this effect was less prominent for the semi-preg used in Test Laminate 2, so decoupling could be possible for this format without a significant loss of accuracy in the simulated results.

6.3.5 Investigation of Heating Methods

As previously mentioned, two sets of heating methods were considered for this work; heated moulds/tooling (specified temperature BCs), and oven heating (forced convection BCs). Heated moulds are common for manufacturing large parts, such as wind turbine spars, skins, shear webs, etc., because they are inexpensive compared to purchasing and operating very large ovens. Looking back at the *heat equation* (Equation 2.26 in Chapter 2, Section 2.3.2), however, it is obvious that one-sided heating is an inefficient way to process thick-section parts because the conductivity term in the equation is dependent on the second spatial derivative of temperature. By halving the distance that the heat must transfer, the rate of change for temperature can be greatly increased. As a result, it is common to manufacture root sections of the blade separately in ovens so that the laminate can be heated from both sides. This effect can be seen in Figure 6.25, which shows that processing of the 100-ply laminate was significantly faster for two-sided heating. This was also evident from the temperature plots, Figure D.9 and Figure D.10, which are given in the Appendices: D. Simulation Results.

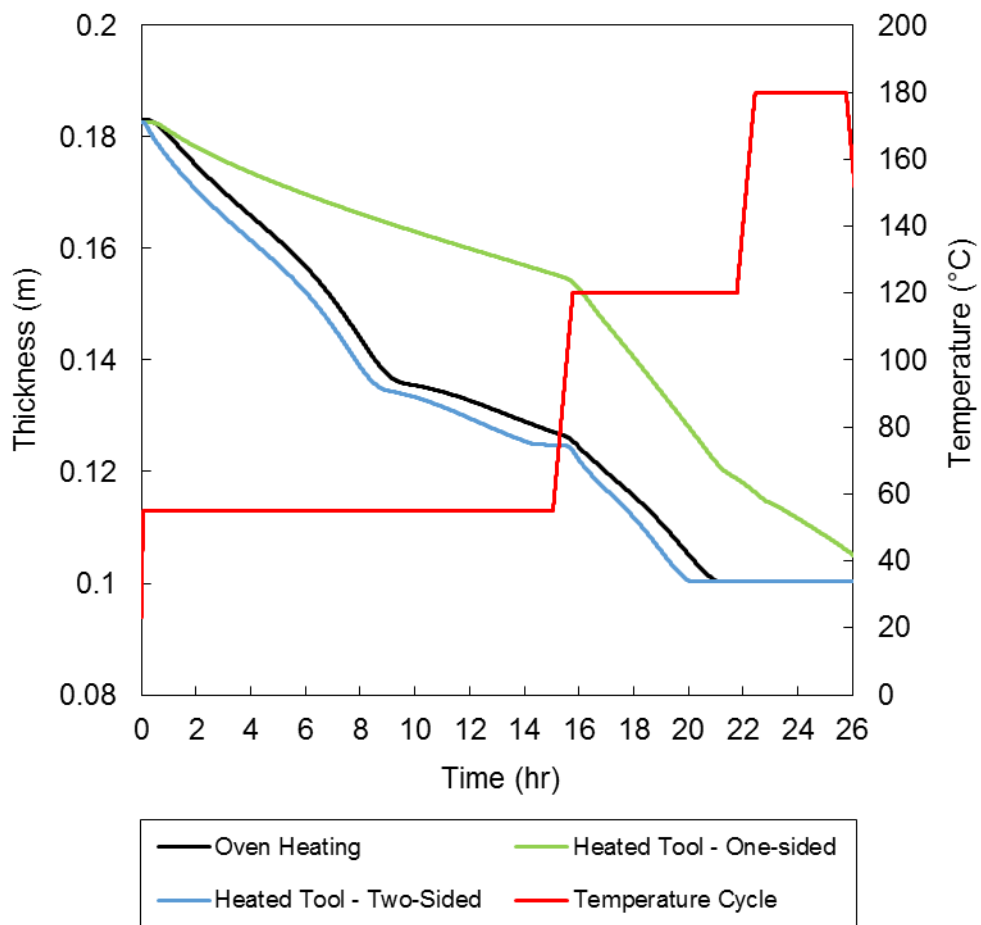


Figure 6.25. Simulated consolidation of three 100-ply laminates manufactured using different thermal boundary conditions. Consolidation was significantly slower for one-sided heated tooling when compared to two-sided heated tooling or oven heating (also two-sided heating).

Figure 6.25 also shows the results of a third arrangement which combined heated tooling with the use of silicone rubber heating mats on the top surface of the laminate. The aim of this additional arrangement was to explore an alternative method for two-sided heating which might achieve a lower capital cost than oven heating. For manufacturing a real, 3D geometry, the concept would be to use the heating mats only in areas of increased thickness as one-sided heating is sufficient for thin structures. Highly flexible, silicone rubber heating mats are available (O&M Heater Co. Ltd., 2018) which could conform to the part shape under a double vacuum bagged arrangement i.e. the heating mat could be placed between two vacuum bags.

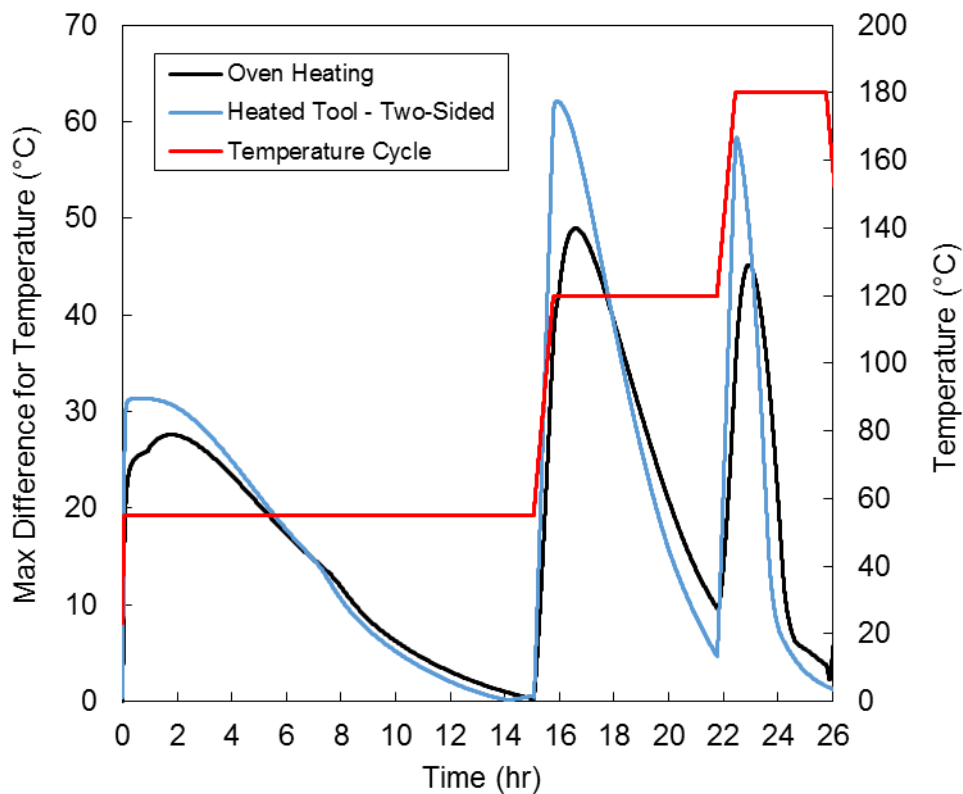


Figure 6.26. Comparison of the maximum temperature difference in two 100-ply laminates; one laminate manufactured in an oven, and the other manufactured using a heated tool and silicone rubber heating mat.

Focusing on the results of both two-sided heating methods in Figure 6.25, it can be seen that the heated tooling allowed for faster heat transfer and slightly reduced the time required for some of the processing stages. Nevertheless, oven heating had its own advantages in that it reduced the maximum temperature and cure differences within the laminate; see Figure 6.26 and Figure 6.27. The peaks during the cure stage were the primary concern as they may have some implications for the residual stress development in the final part. This topic is discussed further in the next section, Section 6.3.6.

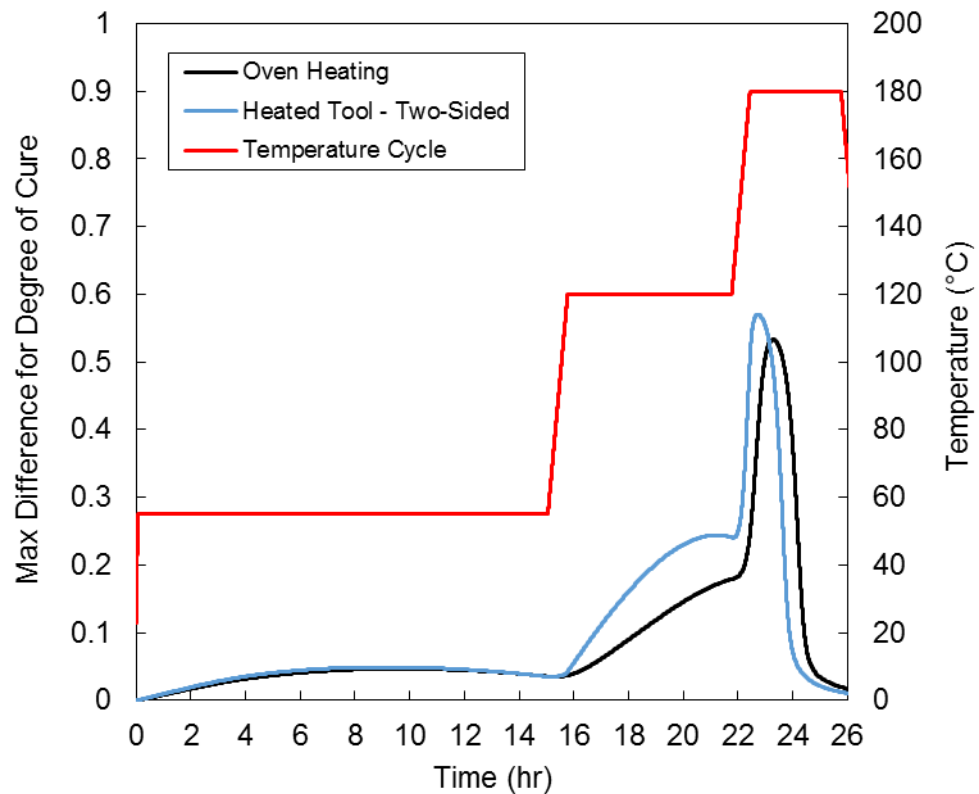


Figure 6.27. Comparison of the maximum degree of cure difference in two 100-ply laminates; one laminate manufactured in an oven, and the other manufactured using a heated tool and silicone rubber heating mat.

6.3.6 Methods for Reducing Thermal Gradients and Cure Gradients

As discussed in Chapter 2, Section 2.3, one of the main challenges with processing thick-section composite laminates is the development of large thermal gradients and cure gradients due to the highly exothermic nature of conventional thermoset systems. These gradients can cause large residual stresses in the material due to mismatches in expansion and contraction, which can be “locked in” when the resin reaches the gel point.

While it has been shown that use of the epoxy powder was successful in eliminating thermal overshoot as a processing hazard, it was clear that thermal gradients and cure gradients remained an issue for the manufacturer’s recommended temperature cycle due to the difficulty of transferring heat through the thickness of the laminate.

Moreover, when the gel point of the epoxy was identified for the whole laminate (see Figure 6.28) the timespan overlapped with peaks in temperature difference and in DoC difference, as shown in Figure 6.29. This meant that the laminate was gelling when the gradients were at their highest.

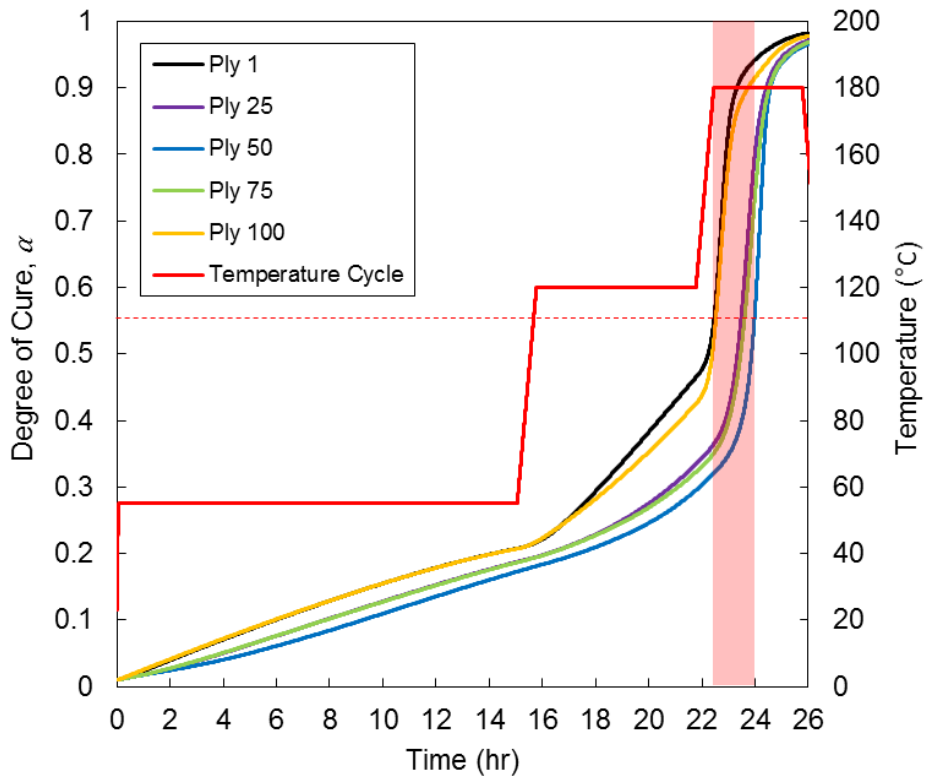


Figure 6.28. Simulated DoC evolution for the 100-ply laminate of UD GF/GRN 918. The horizontal dashed red line represents the gel point, while the shaded red area shows the timespan of gelation in the laminate.

Ultimately, without developing a residual stress model, it was impossible to know the implications of this event. Nevertheless, it was worthwhile to investigate how the gradients can be reduced. One concept was the use of a second epoxy powder with cure kinetics that differ from GRN 918 e.g. lower or higher heat activation temperature than GRN 918. By distributing the “low-temperature” epoxy powder at the centre of the laminate, and the “high-temperature” epoxy at the outside of the laminate, it was expected that curing could be partially synochronised across the thickness of the

laminate. This concept was formed on the basis that the epoxies maintained their global position within the laminate because each layer only flowed through-thickness into the adjacent fabric layer. For other VBO processes, such as VARTM, such an arrangement would not be possible because it would be impossible to control the through-thickness distribution of the resins during infusion.

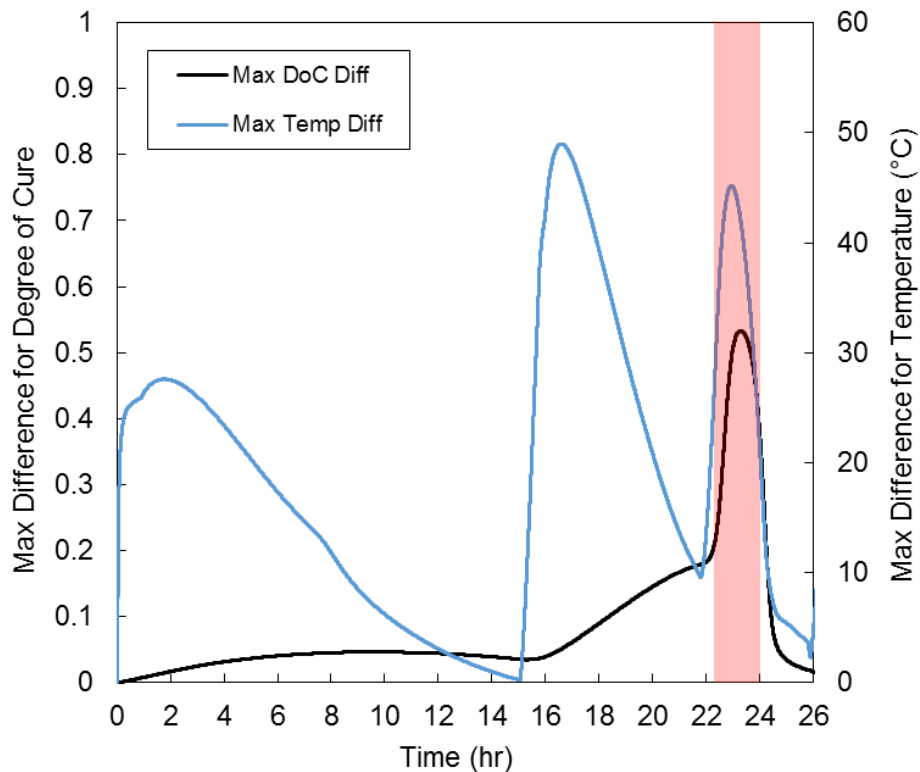


Figure 6.29. Plot of the maximum DoC difference and the maximum temperature difference.

The red shaded area shows that peaks in the max differences overlap with gelation of the laminate, meaning that any corresponding residual stresses would be locked in.

As a first approximation, the cure kinetic parameters of Equation 4.1 were estimated for HZH01R (the AkzoNobel epoxy powder which was investigated in Chapter 3). These parameters are given in Table 6.5. Note, full characterization of the parameters was not performed, and the given values were simply used as first approximation for proof of concept. For the modified laminate, HZH01R was placed between plies 1 and

25, and between plies 75 and 100. GRN 918 was placed between plies 25 and 75 because it had a lower activation temperature.

Table 6.5. First approximation of cure kinetics parameters for HZH01R.

Parameter [unit]	Value	Parameter [unit]	Value
A_1 [s^{-1}]	4.073×10^{-4}	m	1.24
E_1 [J/mol]	12006	n	1.8
A_2 [s^{-1}]	7.359×10^{12}	C	50
E_2 [J/mol]	137594	α_c	$0.006 T - 1.748$
A_3 [s^{-1}]	1.097×10^{13}		
E_3 [J/mol]	131251		

Another means of reducing the thermal gradients and cure gradients was modification of the temperature cycle. As discussed in Chapter 2, Section 2.3, much existing research focused on optimisation of the temperature/processing cycle. The development of optimization algorithms were outside the scope of this project. Nevertheless, it was possible to manually run simulations for several iterations of the temperature cycle. For each iteration, the temperature cycle was adjusted, using basic criteria, until the max temperature difference and DoC difference were significantly reduced during gelation.

For the criteria, primary importance was given to achieving full impregnation prior to gelation and minimizing the max temperature difference and max DoC difference at and above the gel point for all the laminate. It was assumed that residual cure stress development would begin at the gel point (i.e. DoC = 0.56) and that the effects of any gradients prior to gelation were negligible (Kravchenko, Kravchenko and Pipes, 2016). In addition, it was decided that the drying stage could be cease as soon as the powder was fully sintered, as any further desorption of moisture would be negligible.

The manually optimised cycle was as follows:

- Drying stage: Ramp to 55°C and hold for 540 min
- Impregnation stage: Ramp to 135°C at 1.5°C/min and hold for 480 min
- Cure stage: Ramp to 180°C at 0.25°C/min and hold for 300 min

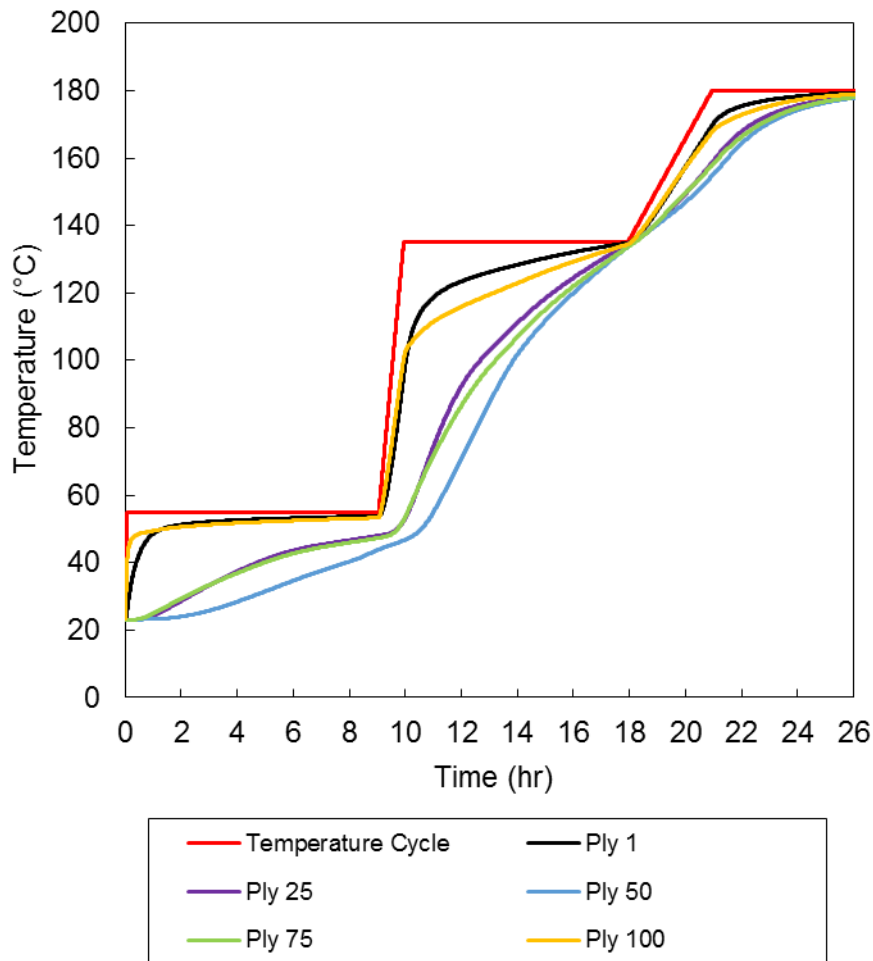


Figure 6.30. Plot of simulated temperatures for modified laminate and temperature cycle.

Figure 6.30 shows the simulated temperature distribution when two powders are used in combination with an optimised temperature cycle. The drying stage was significantly shorter than the recommended cycle, while the impregnation stage was longer. By increasing the duration of the impregnation stage, the ply temperatures

could converge prior to the start of the cure stage. The slower ramp to the final curing temperature then meant that the temperatures did not diverge significantly for the remainder of the temperature cycle, thus minimizing the thermal gradients.

Figure 6.31 shows the effect of the two modifications on the DoC evolution. The DoC at the centre of the laminate (i.e. Ply 50) overtook the DoC at Ply 75 during the impregnation stage (after approx. 16.5 hr). This was because GRN 918 (plies 25 to 74) had a lower heat activation temperature when compared to HZH01R (plies 1 to 24, and plies 75 to 100). Despite the period of gelation being increased, by activating the latent curing agents in the epoxy at the centre of the laminate, the maximum DoC difference could not grow as large as what it was in the standard 100-ply laminate. It was also noted that the fabric impregnation had completed after approx. 14 hr.

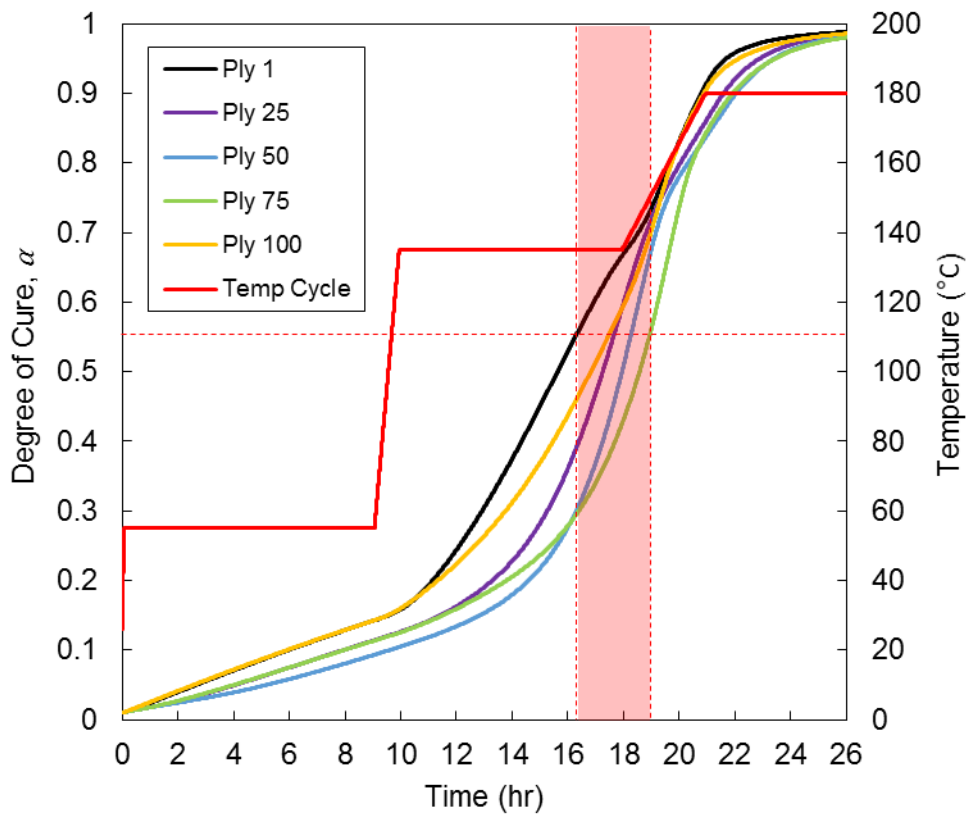


Figure 6.31. Plot of the DoC evolution for the modified laminate and temperature cycle. Once again, the horizontal dashed red line denotes the gel point, and the shaded red area outlines the period of gelation within the laminate.

Figure 6.32 highlights the improvements achieved via the modified laminate and temperature cycle. The period of gelation in the laminate (identified by the red shaded area) overlapped with a trough in max temperature difference, and the peak in max DoC difference was reduced from 0.53 to 0.28. One potential area of concern with using two epoxy powders, was that it could cause large localized gradients of DoC at the interface of the two epoxies. This risk may be reduced by mixing powders so that the transition from one powder to the other is more gradual, however, the epoxies would need to be compatible so that they do not create a region with poor interlaminar properties.

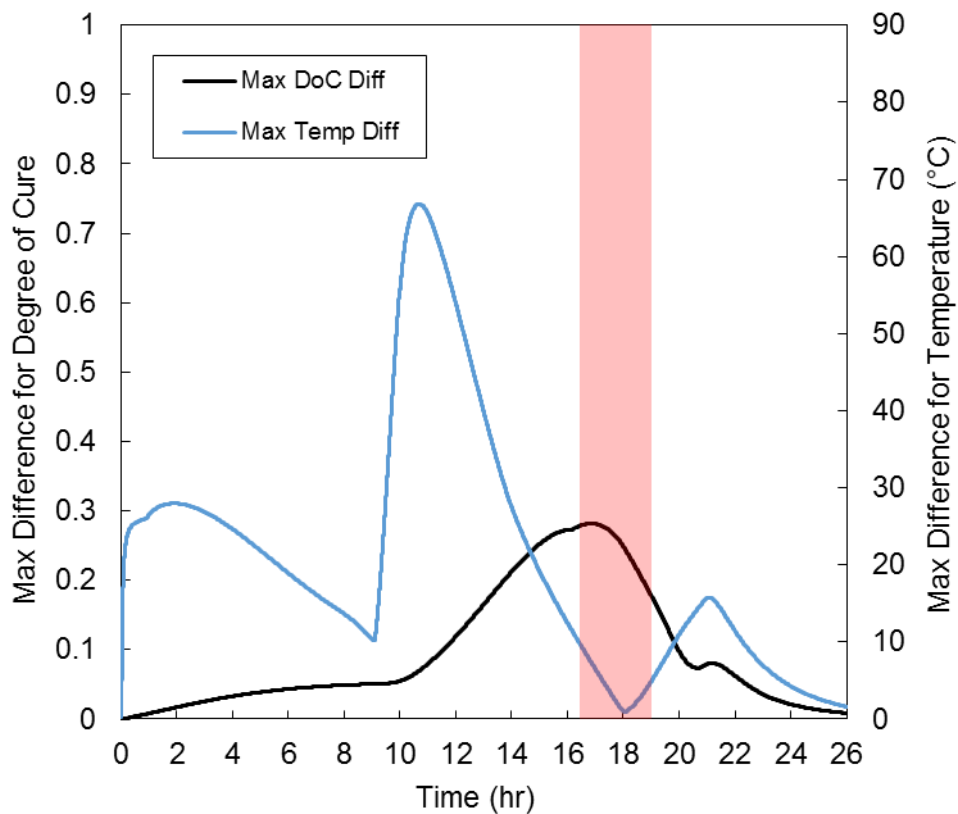


Figure 6.32. Plot of maximum DoC difference and maximum temperature difference for the modified laminate and temperature cycle. The shaded area shows that the temperature difference reached a minimum during gelation. While the peak in max DoC difference still occurred during gelation, it was reduced significantly with the introduction of another epoxy powder.

The manually optimized temperature cycle was also run for a 100-ply laminate which only contained GRN 918 as the polymer matrix, the results of which are given in Figure D.11, Figure D.12, and Figure D.13 in the Appendices: D. Simulation Results. The modified cycle also reduced the max temperature difference in this case but the effect on DoC was less pronounced without the use of a second epoxy powder.

6.4 Conclusions

Experimental validation of the 1D process simulations has been presented. Three test laminates were manufactured: Test Laminate 1 and 3 were manufactured using uni-directional glass-fibre (UD GF) fabric with epoxy powder (GRN 918) manually dispersed between plies; and Test Laminate 2 was manufactured using triaxial GF fabric which was partially impregnated with GRN 918 in an automated prepregging process. The laminates were manufactured on a heated tool which was modified for the experimental testing. Insulated thermal boundary conditions were created by fitting GF insulation slabs to the top and sides of each laminate. A linear variable differential transformer (LVDT) was used to measure the thickness change of the laminate, while K-type thermocouples were used to measure individual ply temperatures.

The results for Test Laminate 1 showed that, below the T_g of the epoxy powder, the laminate underwent little or no compaction. The results also showed that heat transfer was very slow due to the low thermal conductivity of the powder and the large initial thickness of the laminate. Above the T_g , there was significant thickness change due to sintering of the powder, and a corresponding improvement to the rate of heat transfer. During the impregnation stage, the thickness continued to decrease as resin flowed into the GF fabric. As expected, the laminate did not exhibit any thermal overshoot, however, it was clear that large thermal gradients developed in the laminate due to its low through-thickness thermal conductivity. Upon inspection of the laminate, it was shown that the manual dispersion of powder resulted in an uneven thickness throughout the laminate. Microscopy of a cut-section revealed that the laminate suffered from incomplete tow impregnation and inter-tow voids, particularly in the

upper third of the laminate. A few adjustments were made for manufacturing Test Laminate 3 to improve the laminate quality, however, the results were approximately the same as Test Laminate 1.

Test Laminate 2 was found to be much easier to manufacture due to the powder having been dispersed in an automated process. Initially, heat transfer was faster than the other test laminates, due to the powder having been fully sintered during the prepregging process. Despite this, the laminate underwent a small amount of compaction during drying. This was attributed to the re-sintering of cracked epoxy matrix (the epoxy was very brittle in its uncured form), and gaps between the stiff plies. Otherwise, Test Laminate 2 processed in a similar fashion to the other test laminates. When inspected visually, the laminate was found to be much more uniform (owing to the even dispersion of powder), and seemed to suffer less from defects. Regardless, optical microscopy revealed that the laminate was affected by void formation also, but to a lesser extent than Test Laminates 1 and 3.

Additional checks were carried to identify sources of error in the tests. A small in-plane temperature difference was measured for each laminate, with Test Laminate 1 and 3 having larger differences due to the non-uniformity of their thickness. Each test laminate was also re-heated to measure the effects of thermal expansion/contraction. The resulting values were considered negligible compared to the total laminate thickness change.

The data from the experiments was compared to simulations for each test laminate. The temperature predictions matched well with the experimental results. Thickness change predictions generally captured the behaviour of the laminate in terms of compaction due to powder sintering and fabric impregnation, however, improvement of the sintering model should improve the accuracy of the simulations. It was also noted that the transition from inter-tow flow to intra-tow flow could not be distinguished from the experimental data, whereas the transition was more apparent for the simulations. Similarly, the experiments exhibited a gradual cessation of thickness change, whereas the simulations predicted an abrupt end to consolidation.

Such behaviour was consistent with VBO prepreg consolidation under pressure deficient conditions (Helmus *et al.*, 2016).

Additional simulations were carried out to investigate several aspects of processing thick-section composites; how the form of the powder-based VBO prepreg affected processing, how thickness change affected heat transfer, how the method of heating affected processing, and how the laminate and temperature cycle could be modified to reduce the thermal gradients and cure gradients in the laminate.

It was found that the rate of heat transfer improved with decreasing powder void fraction due to the low thermal conductivity of the powder. This was weighed against the advantageous sorption properties of the powder, as observed in Chapter 3. It was concluded that further analysis and modelling was required to understand the effect of the VBO prepreg format on moisture desorption and gas evacuation during the drying stage.

It was shown that thickness change did have a significant effect on heat transfer in thick-section laminates manufactured using powder-based VBO prepreps. The effect was most noticeable for the drying and impregnation stages. As such, it was deemed necessary to couple heat transfer to thickness change for accurate predictions of powder-based, thick-section processing. Thickness change was less important for heat transfer in VBO prepreps with fully sintered resin.

Simulations of different heating methods confirmed that two-sided heating (i.e. heating of the top and bottom of the laminate) was required for efficient processing of thick-section laminates. A concept for locally heating thick-sections, using flexible heating mats, was presented as a means of achieving two-sided heating at a reduced cost compared to oven heating. The results for the two-sided heating methods were shown to be similar.

For the manufacturer's recommended temperature cycle, it was found that thick-section laminates developed large temperature differences and degree of cure (DoC) differences through the thickness of the laminate. For a 100-ply laminate, peaks in differences happened to overlap with gelation in the laminate. It was considered that

this occurrence would put the laminate at risk of developing large residual stresses due to mismatches in thermal expansion and chemical shrinkage. To reduce these differences, a modified laminate lay-up and temperature cycle were proposed. The modified lay-up replaced GRN 918, in the outer plies of the laminate, with HZH01R. The higher cure activation temperature for HZH01R meant that curing at the outside of the laminate would overlap with the curing of the GRN 918 epoxy powder at the centre of the laminate. The modified temperature cycle reduced the duration of the drying stage, and increased the duration of the impregnation stage, so that the temperatures within the laminate had more time to converge before reaching the gel point. A slower ramp rate was then implemented for the cure stage so that the temperatures would not then diverge again. The modifications resulted in the temperature difference reaching a minimum during gelation, and a 47% reduction in the maximum DoC difference. Despite these improvements, it was concluded that the residual stress development should be modelled as part of future work, so that it can be understood how the processing affects the final stress state of the cured laminate.

7. Two-dimensional and Three-dimensional Process Simulations

7.1 Chapter Introduction and Overview

Up to this point, one-dimensional simulations have been used to investigate the processing of thick-section composites using epoxy powder, however, not all part geometries have sufficiently large in-plane dimensions to satisfy the 1D assumption for heat transfer. As such, two-dimensional (2D) or three-dimensional (3D) tools may be required in certain cases where edge effects, or other in-plane effects, are expected to be prevalent.

This chapter introduces the use of a commercial finite element analysis (FEA) software, Abaqus FEA, for performing 1D, 2D and 3D simulations. A methodology is described for implementing various process models and material models within a coupled temperature-displacement analysis using user-defined subroutines. The accuracy of the simulation tool is verified against experimental results, and the convergence of solutions is tested for a range of time step sizes and element sizes. Simulations are performed for 2D and 3D geometries, including the tapered root section of a wind turbine blade. The influence of thermal conductivities is investigated for in-plane heating, and the validity of the 1D assumption is tested for different cases. Additional simulations are performed to improve the temperature cycle and explore the use of alternative heating methods.

7.2 Methodology

7.2.1 Numerical Computation

In this Chapter, numerical computation of the relevant process models and material models was performed using two user-defined subroutines in Abaqus FEA, namely, UMATHT and UEXPAN.

UMATHT allows for the definition of a material's thermal behaviour during a coupled temperature-displacement analysis. When the subroutine is called at a material calculation point, it solves the energy balance at that point using Newton's method for a given time increment and temperature increment. To assist in the definition of the material's thermal behaviour, UMATHT also allows for the use of solution-dependent state variables, the values of which are stored for each time increment.

The *heat equation*, described by Equation 2.26, was used as the governing equation for energy balance in the laminate. To calculate the heat generation term in Equation 2.26, it was necessary to solve the cure kinetic model within UMATHT. This was achieved by defining the DoC as a solution-dependent state variable within the UMATHT subroutine. Using the same principle, it was also possible to solve the sintering model, the chemorheological model, and the resin flow model. It was not possible, however, to update the element thickness (and, thereby, the laminate thickness) using UMATHT. Instead, the thickness change was updated via UEXPAN, a user subroutine which allows the user to define incremental thermal strains as a function of state variables.

Although many of the material properties were temperature-dependent, it was assumed that, within each time step, all material properties were constant and were evaluated at $T + \Delta T$ and $t + \Delta t$ i.e. values were not interpolated between the start and end of the increment. This simplified solving the energy balance, however, it also meant that the solution was sensitive to the increment size.

Another factor affecting the maximum allowable increment size was the numerical error associated with the methods being used to compute the cure kinetics and resin flow models. First order methods were used to compute these ODEs for the 1D finite

difference code in Chapter 5, however, they required small time increments to be used. To implement the same methods within the FEA code would severely hamper its computational efficiency, thereby negating one of the main advantages of using commercial FEA software. Instead, similar to Yi *et al.* (1997), a fourth order Runge-Kutta method was implemented in the subroutine to solve the ODEs. This method was numerically stable and was significantly more accurate than the first order Euler method which was previously used in the finite difference code (Kreyszig, Kreyszig and Norminton, 2011).

State variable data was not passed between elements within the FEA code. As such, the resin flow model was solved for each element in isolation (see Figure 7.1) i.e. resin could not flow between plies. Apart from this, the 1D resin flow and thickness change was computed using the methodology described in Chapter 5, Section 5.2.

The FORTRAN-based subroutines are available in the Appendices: C. Numerical Codes.

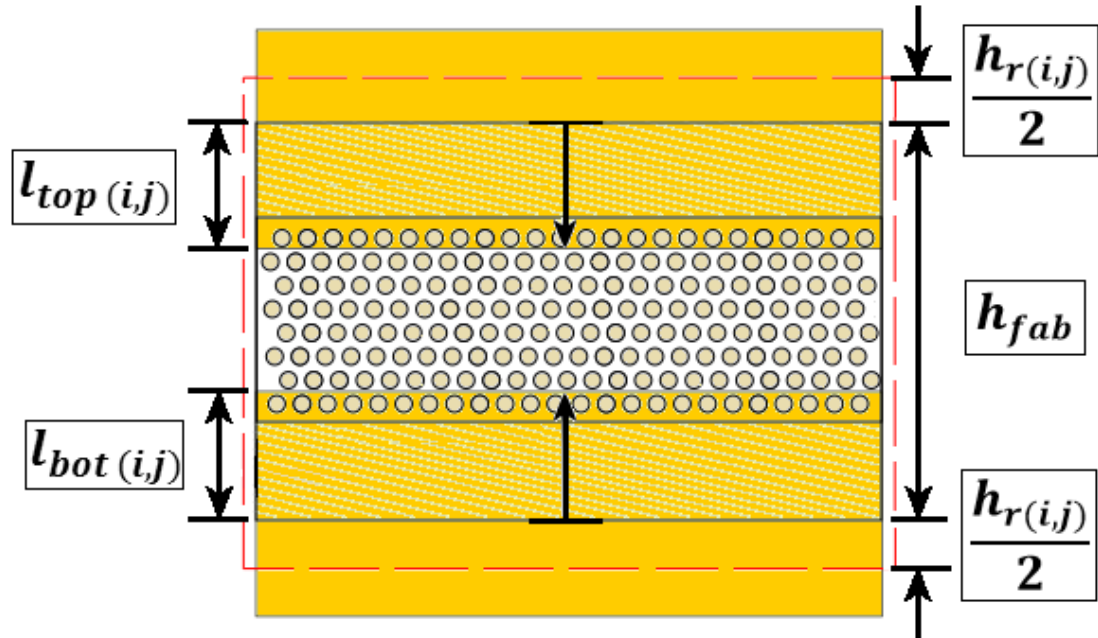


Figure 7.1. The simplified ply microstructure used in UMATHT. The boundary of the element is represented by the dashed red line. As such, the top and bottom resin layers were split in half and resin flow was solved for the each element in isolation i.e. as a closed system.

7.2.2 Virtual Composite Part Development

Virtual composite parts were developed in Abaqus FEA using the in-built graphical user interface (GUI). Three geometries were investigated, as shown in Figure 7.2: a 1D through-thickness section; a 3D quartered section of a flat laminate; and a 2D section of a tapered turbine blade root.

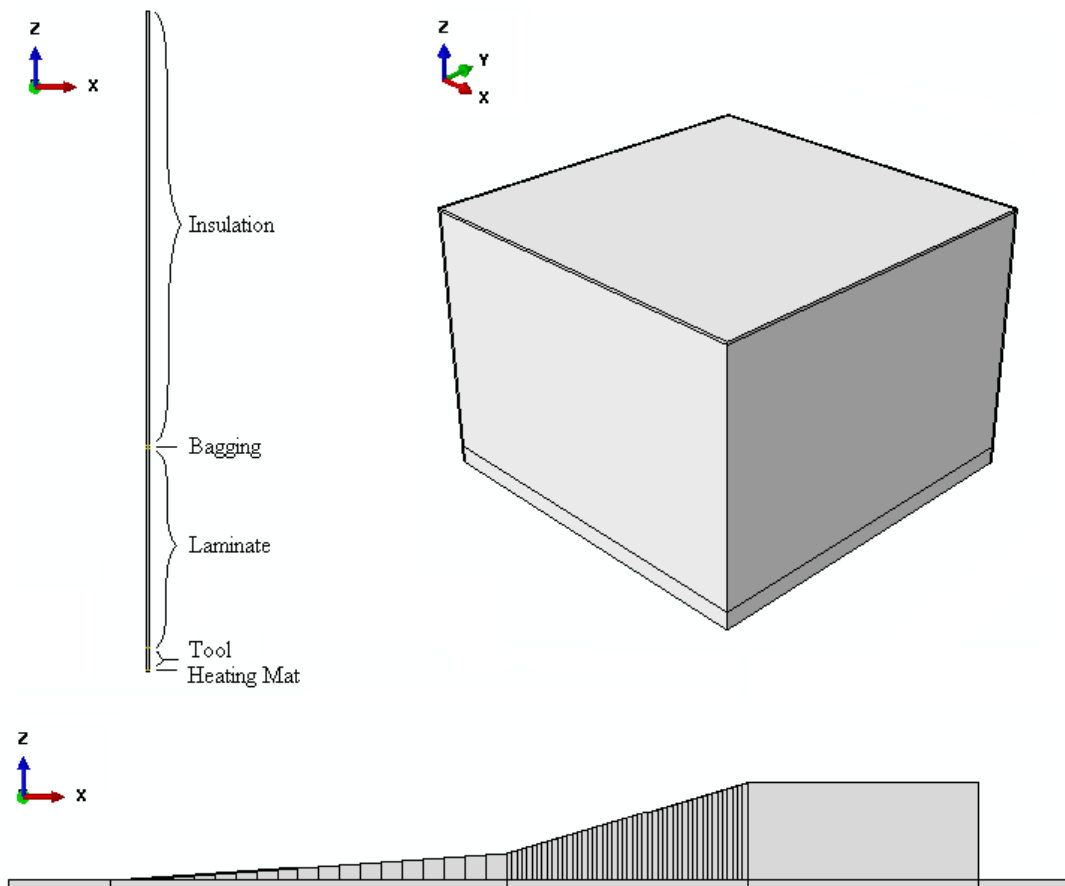


Figure 7.2. Three types of geometry were created for analysis in Abaqus FEA: (top left) a 1D through-thickness section; (top right) a quartered section of a laminate on a flat tool; (bottom) 2D section of a tapered wind turbine blade root, where the ply drops have been sectioned for meshing.

The 1D geometry was used to verify the numerical methods used and compare against the results of Test Laminates 1, 2, and 3. It was also used to test the 1D heat transfer assumption for the other geometries.

The 3D geometry represented a 420 mm x 420 mm x 100-ply laminate which was processed on a 10 mm steel tool in an oven (HTC of 40 W/m².K). This part was developed to investigate the effects of in-plane heat transfer in anisotropic materials. The symmetry of the flat laminate was used to reduce the geometry to a quarter section, thus reducing the computational cost of performing a simulation.

The 2D geometry represented a cross-section of a tapered wind turbine blade root. A full 3D demonstrator was designed by SE Blade Technology B.V. for the POWDERBLADE project, however, the geometry was reduced to a 2D section to save on computational cost. It was assumed that the root section was made on a 10 mm thick steel tool in an oven with a uniform heat transfer coefficient of 40 W/m².K, and that triaxial semi-preg (with GRN 918) was used. The section tapered from 67 plies down to 0 plies, with two gradients, over a 1040 mm span.

In all cases, the geometries were constructed as 3D deformable solids, but were given arbitrary thicknesses in any unused directions e.g. the 1D geometry was one element thick in the x and y directions, while the 2D geometry was one element thick in the y direction. When meshing the parts, only structured meshing with hexahedral (brick) elements was used so that elements would represent individual plies or groups of plies e.g. for 100 plies, there may be 100 elements through the thickness (i.e. one ply per element), or 20 elements (5 plies per element). Partitioning was used to create the separate material sections for the laminate, insulation, bagging, etc., and to ensure that structured meshing with hexahedral elements was possible, as shown in Figure 7.3. An 8-node thermally coupled brick, trilinear displacement and temperature (C3D8T) element was used for all simulations. Note that, due to difficulty with partitioning and meshing, the bagging layer was excluded from the 2D geometry of the tapered root section, which is discussed further in Section 7.3.2.

For each geometry, the bottom of the tool was given encastre mechanical boundary conditions, while any cut sections in the xz or yz planes were given mechanical

symmetry boundary conditions. A transient coupled temperature-displacement analysis step was created for each geometry with the non-linear geometry option activated. Within this analysis step, thermal boundary conditions (i.e. specified temperature or forced convection) were applied where appropriate for each geometry. On any surface where the thermal boundary condition was not specified, Abaqus FEA assumed that the surface was perfectly insulated.

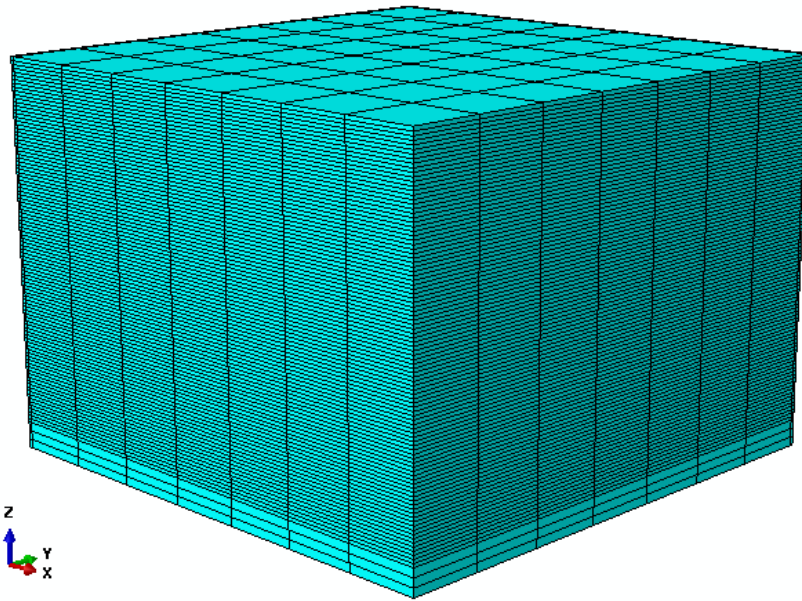


Figure 7.3. The 3D geometry after being meshed using hexahedral elements. The structured meshing was used to preserve the shape of the plies; in this case, the element thickness matched the ply thickness.

For geometries where in-plane heating was considered (i.e. the 2D and 3D geometries), it was necessary to create a thermal conductivity matrix, κ (Park *et al.*, 2003). Unidirectional (UD) plies were represented with an orthogonal thermal conductivity matrix,

$$\kappa_{UD} = \begin{bmatrix} \kappa_{xx} & 0 & 0 \\ 0 & \kappa_{yy} & 0 \\ 0 & 0 & \kappa_{zz} \end{bmatrix} \quad (7.1)$$

An effective thermal conductivity in the z direction (i.e. through-thickness), κ_{zz} , was back-calculated from the assumption of thermal resistances in series, as described in Chapter 5, Section 5.2.2. It was assumed that, for a unidirectional ply, the thermal conductivity in the y direction (i.e. transverse), κ_{yy} , was equal to κ_{zz} . The thermal conductivity in the x direction (i.e. longitudinal), κ_{xx} , was calculated using a rule of mixtures approach, where the longitudinal thermal conductivity of the fibres was assumed to be 1.3 W/m.K (Shi, 2016).

For plies with an angle, θ , the thermal conductivity matrix was transformed as follows (Park *et al.*, 2003),

$$\kappa_{\theta} = \mathbf{R}^T \kappa_{UD} \mathbf{R} \quad , \quad \text{where } \mathbf{R} = \begin{bmatrix} \cos \theta & \sin \theta & 0 \\ -\sin \theta & \cos \theta & 0 \\ 0 & 0 & 1 \end{bmatrix} \quad (7.2)$$

The values in Table 5.1, Table 5.2, and Table 5.3 in Chapter 5, Section 5.2.4 were used for all remaining material properties in this chapter, unless otherwise stated. Additional mechanical properties were required by Abaqus FEA also; the tool materials were given generic values for steel and aluminium, while the laminate and bagging materials were given arbitrary isotropic elastic values to allow them to deform easily.

Table 7.1. Initial conditions used for the tapered root section simulations.

Parameter [units]	Value
No. of plies	67 (tapered to 0)
Cured ply thickness [m]	0.0013
Fibre volume fraction	0.5
Degree of impregnation	0.575
Powder void fraction	0.175
Degree of cure	0.01
Applied pressure [Pa]	90×10^3
Laminate/bagging/tool temperature (°C)	23

The 1D geometry was used to simulate each of the Test Laminates; with each case using the corresponding initial conditions listed in Table 6.1, Table 6.2, and Table 6.3 in Chapter 6, Section 6.2.5. The initial conditions of the 3D geometry was assumed to be that of the 100-ply case study in Chapter 5 (i.e. Table 5.4 in Section 5.2.5). The initial conditions of the 2D simulations are given in Table 7.1.

7.2.3 Verification of the Numerical Methods

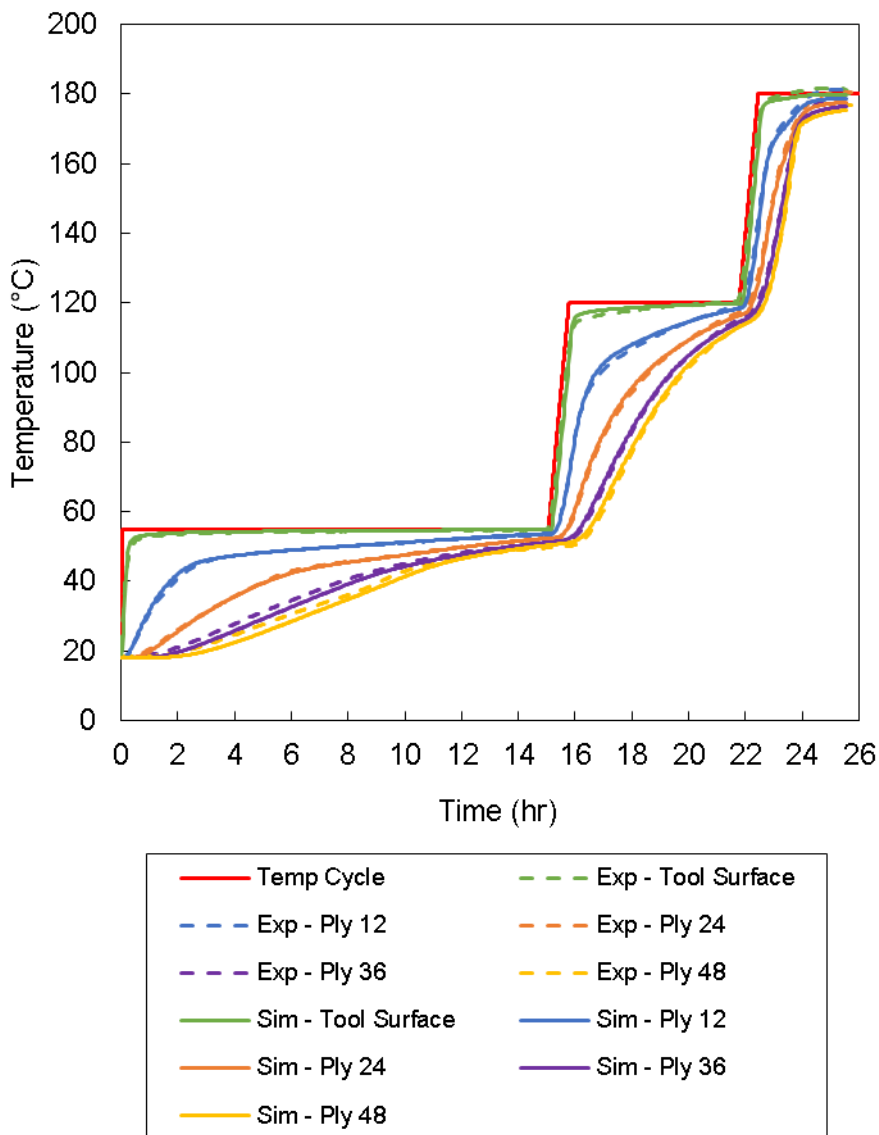


Figure 7.4. Comparison of the temperature distribution from a 1D simulation in Abaqus FEA and the thermocouple data for Test Laminate 3.

As previously mentioned, the 1D geometry was used to verify the accuracy of the numerical methods being used in the simulation. The results of the 1D geometry were compared against the experimental results of Test Laminates 1, 2, and 3. The plots for Test Laminate 3 are shown in Figure 7.4 and Figure 7.5, while the results for Test Laminates 1 and 2 can be found in the Appendices: D. Simulation Results, Figure D.14, Figure D.15, Figure D.16, and Figure D.17.

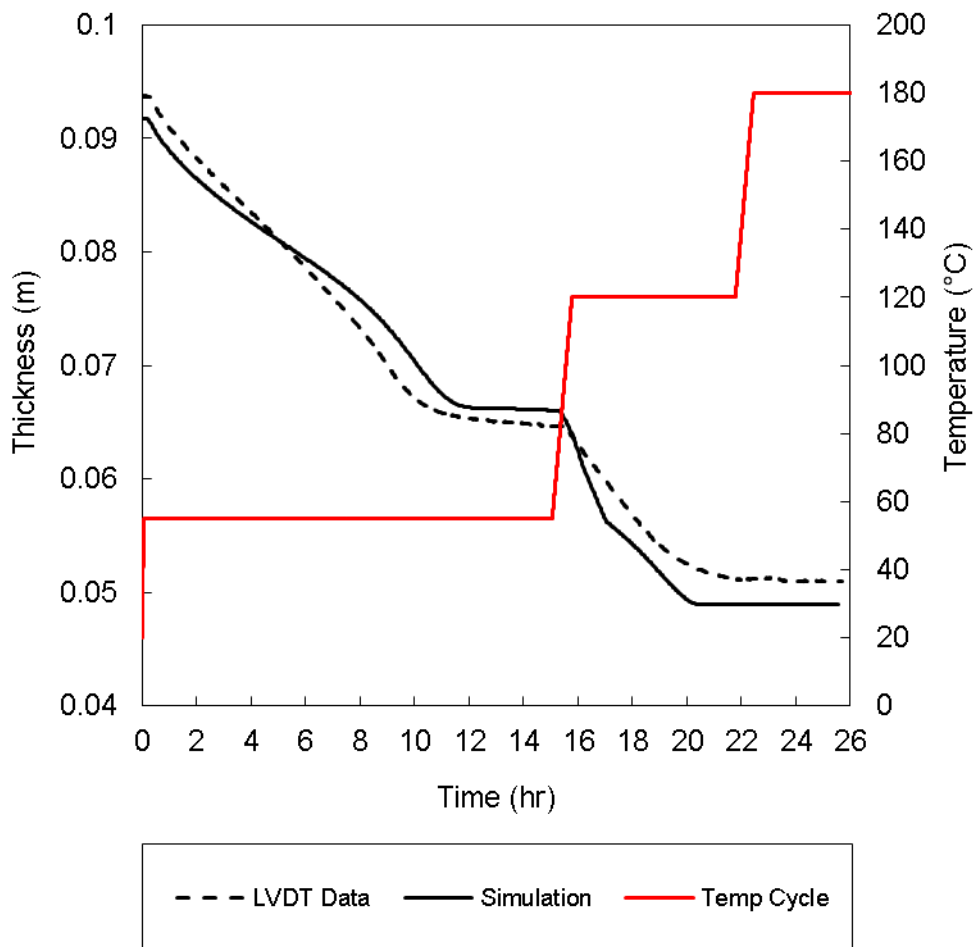


Figure 7.5. Comparison of the laminate thickness change from a 1D simulation in Abaqus FEA and the LVDT data for Test Laminate 3.

It was found that the Abaqus FEA simulations produced accurate predictions of both the laminate's through-thickness temperature distribution and thickness change such

that the results closely resembled those of the 1D finite difference code developed in MATLAB.

7.2.4 Convergence Study

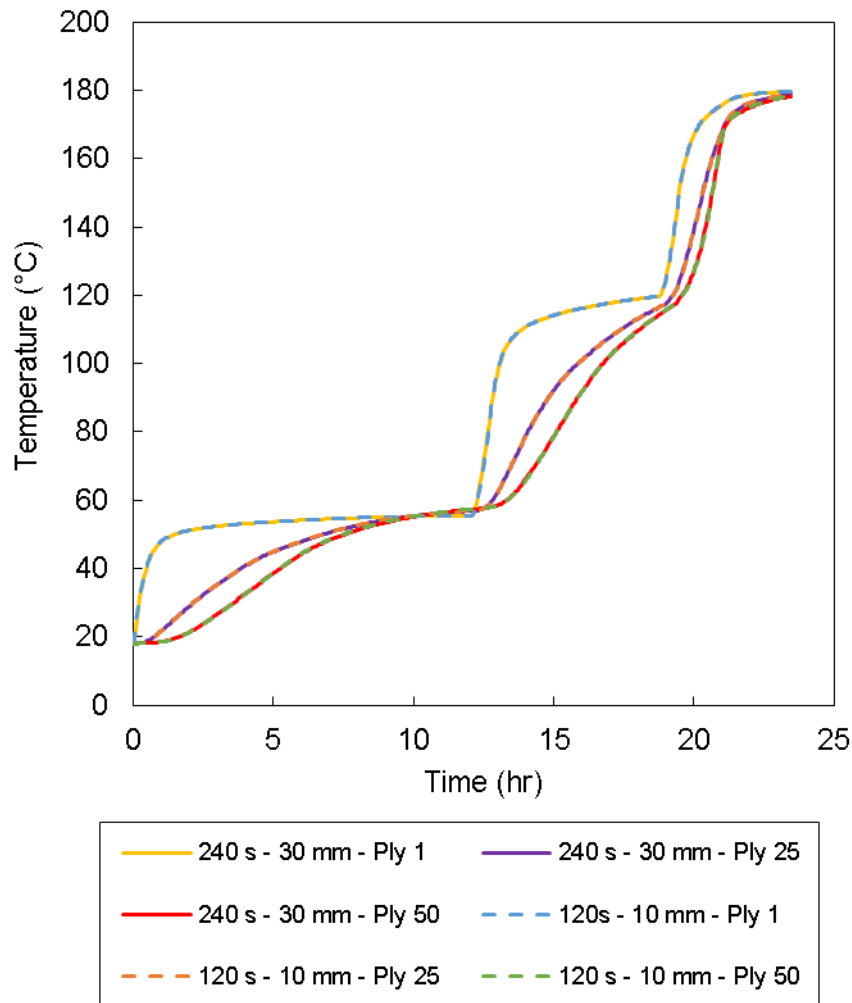


Figure 7.6. Simulated temperatures for a 3D 100-ply laminate. Simulation results are shown for two analyses with different element sizes and time step sizes. Note the temperatures were taken from the in-plane centre of the laminate.

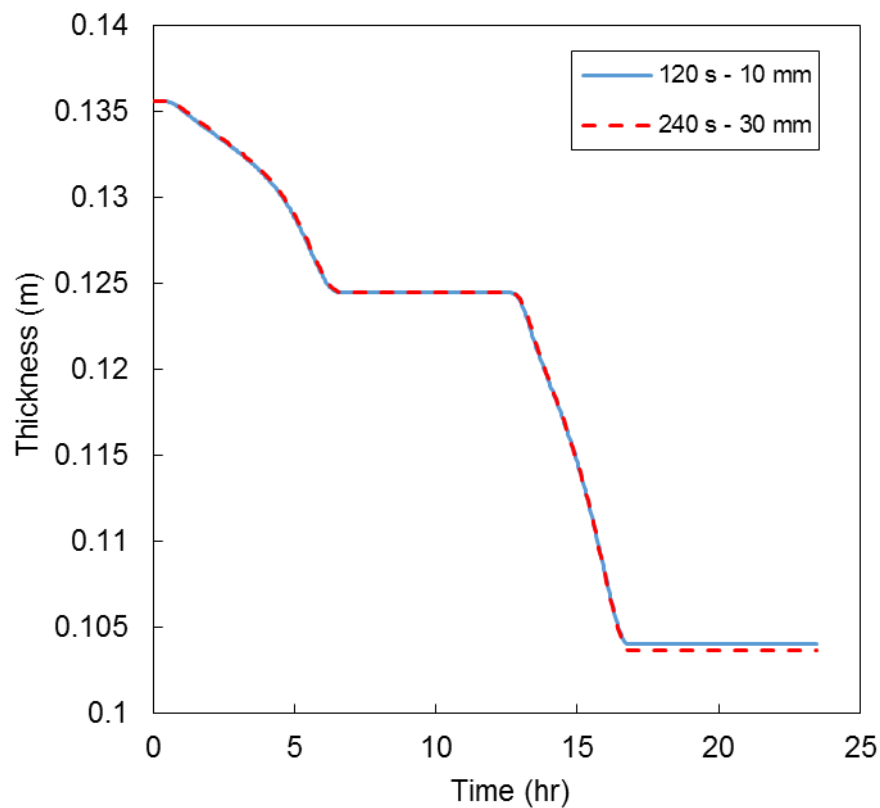


Figure 7.7. Simulated thickness change for a 3D 100-ply laminate. Simulation results are shown for two analyses with different element sizes and time step sizes.

The run time for a simulation was dependent on the number of calculations performed and, therefore, the number of elements in the FEA mesh. Naturally, reducing the mesh density reduced the number of calculations, however, there was potential for a loss of accuracy with coarser meshes. As such, it was necessary to perform a convergence study to find a balance between accuracy and efficiency.

In the context of this chapter, simulation efficiency was particularly important for 2D and 3D geometries where the number of elements required can become substantial, resulting in large run times. A convergence study on element size and time step size was performed for the 3D geometry. While it was possible to reduce the mesh density through-thickness, it was found that meshing composite part geometries with ply drops was easier when the element thickness was made equal to the ply thickness. As such,

changing the in-plane mesh density was a more effective way to increase efficiency for geometries such as the tapered blade root.

For a time step size of 120 s, the in-plane length and width of the elements was increased from 10 mm to 30 mm in increments of 5 mm. Then, for an element length/width of 30 mm, the time step size was increased from 60 s to 240 s in increments of 60 s. Rather than show the results from all the intermediary increments of element size and time step size, Figure 7.6 and Figure 7.7 show the results from two ends of the range, highlighting that the simulations were robust and showed little or no divergence for either temperature change or thickness change.

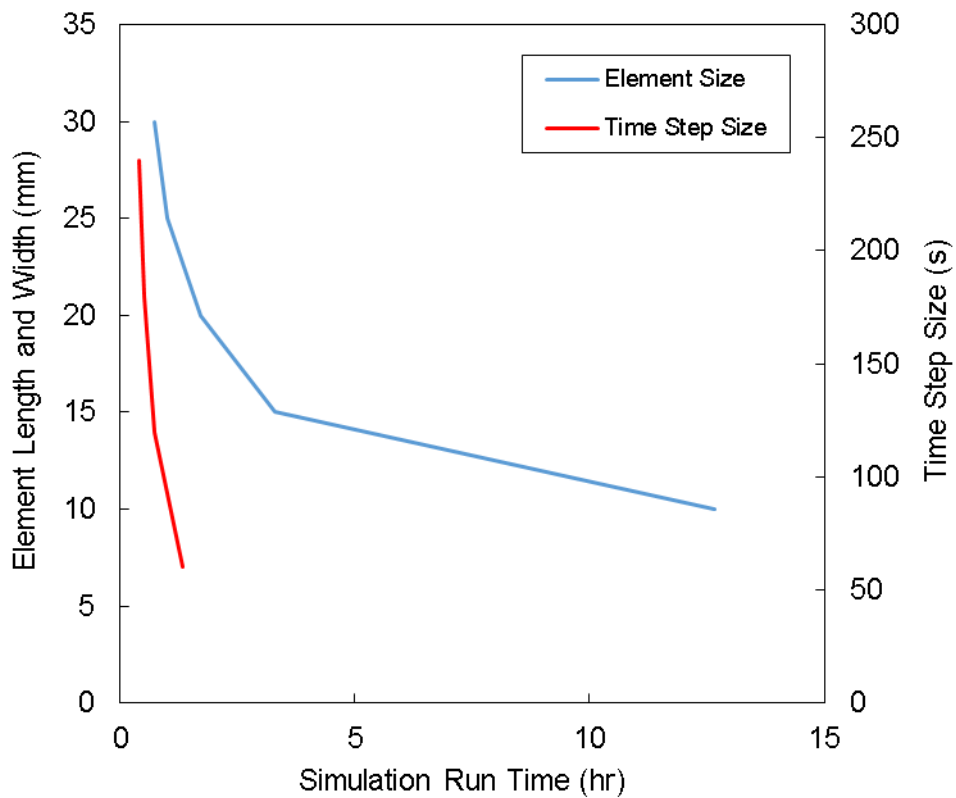


Figure 7.8. The influence of element size and time step size on the overall simulation run time. In both cases, increasing the size results in decreasing the run time. The time step size was kept at 120s for changes in element size, while the element length/width was kept at 30 mm for changes in time step size.

While it was possible to increase the in-plane element size and time step size further, Figure 7.8 shows that doing so would result in a relatively negligible improvement in simulation run time. For further improvements to efficiency, it was possible to increase the element thickness to 10 times the ply thickness without a significant loss to the accuracy of the results (using a time step size of 240 sec). This allowed for a simulation run time of under 4 min. If a better meshing strategy can be developed for more complex geometries (e.g. tapered sections with ply drops), using thicker elements would offer significant computational savings.

7.3 Results and Discussion

7.3.1 In-plane Heat Transfer

The simulation from Chapter 5 – a case study of a 100-ply UD GF/epoxy-powder laminate – was repeated for the 3D quartered geometry. Contour plots were produced for the drying stage, impregnation stage, and the cure stage of the temperature cycle; Figure 7.9, Figure 7.10, and Figure 7.11 respectively. Figure 7.12 indicates the time at which each contour was plotted w.r.t the overall temperature cycle. These contour plots illustrated the outside-to-inside nature of each temperature-dependent process (i.e. sintering, impregnation, and curing). Centea *et al.* (2017) have shown that these type of thermal gradients can result in high void contents when vacuum-bag-only (VBO) prepregs are used. This was due to gas pathways being sealed off at the laminate edges, essentially trapping gas in the centre of the laminate. Moreover, outside-to-inside curing can lead to the development of large residual stresses in the cured laminate, as previously discussed Chapter 2, Section 2.3.2.

Due to the relatively small difference between longitudinal and transverse thermal conductivity of UD GF/epoxy laminates, Oh and Lee (2002) showed that heat transfer was almost symmetric in the XZ and YZ planes. Figure 7.9 and Figure 7.10 show that this was not necessarily the case for powder-based laminates because, at the beginning of the temperature cycle, the low thermal conductivity of the powder meant that heat transfer along the fibres was dominant. For example, at 4 hr, the laminate's through-

thickness thermal conductivity, κ_{zz} , was between 0.127 and 0.2 W/m.K, whereas the thermal conductivity in the direction of the fibres, κ_{xx} , ranged between 0.69 and 0.737 W/m.K. This resulted in a ratio of anisotropy (κ_{xx}/κ_{zz}) as high as 5.43. By comparison, at 21 hr (i.e. the end of the impregnation stage) the ratio of anisotropy was reduced to 2.68. Effectively, as the epoxy sintered and began to impregnate the laminate, both the through-thickness and transverse thermal conductivities improved and the longitudinal component became less influential. This behavior was reflected in the comparison between the 1D model and the 3D model, shown in Figure 7.13. As can be seen, there was greater discrepancy between the two models when the ratio of anisotropy was higher (i.e. earlier in the temperature cycle).

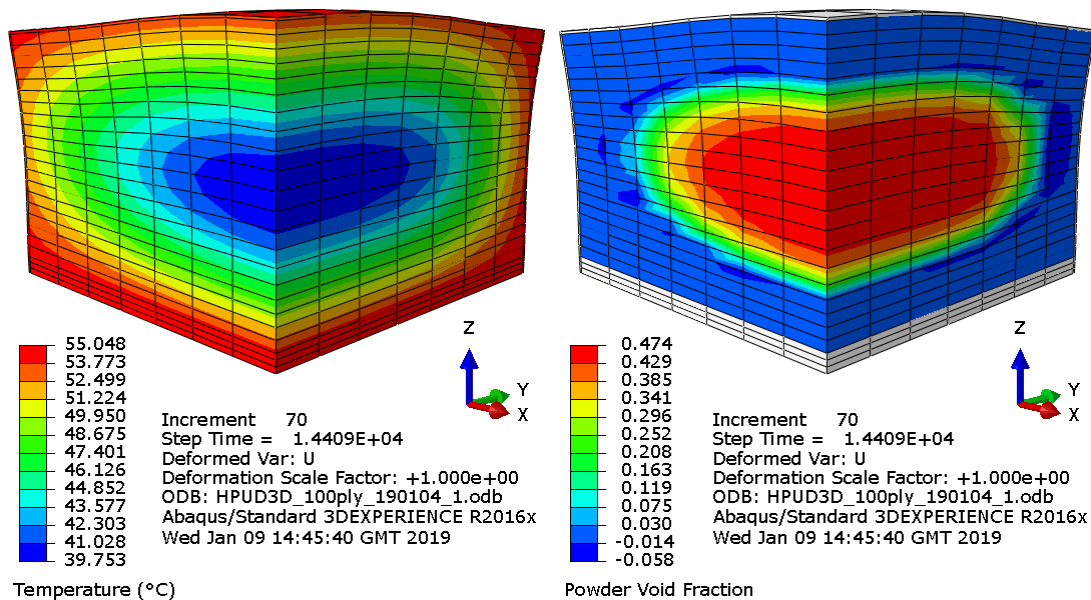


Figure 7.9. Contour plot of the 100-ply UD GF/epoxy laminate during the drying stage (i.e. 4 hrs into the cycle): (left) temperature; (right) powder void fraction. The powder sintered faster at the edges due to the higher temperatures, resulting in an uneven thickness change.

Two-dimensional and Three-dimensional Process Simulations

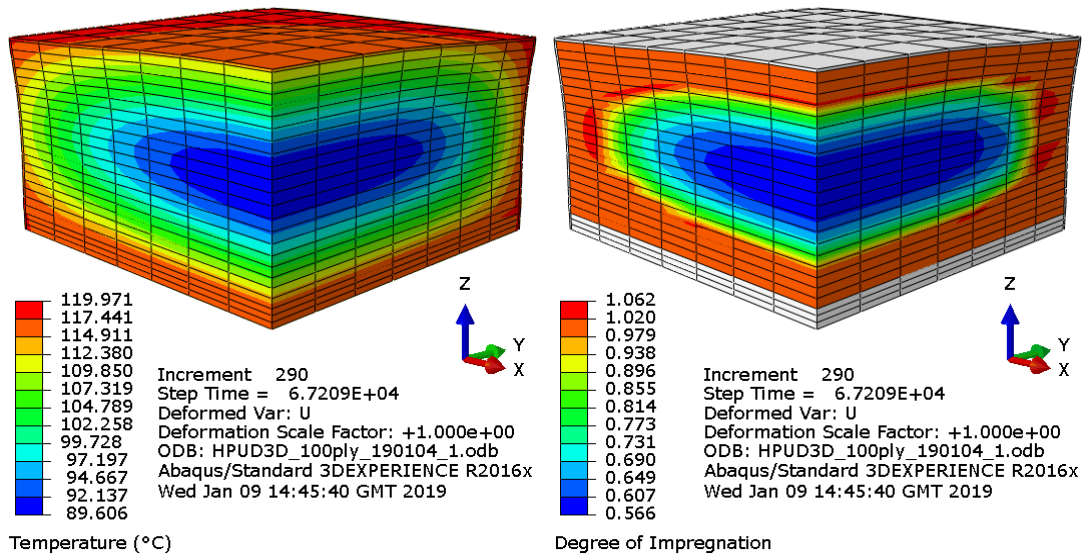


Figure 7.10. Contour plot of the 100-ply UD GF/epoxy laminate during the impregnation stage (i.e. 18.67 hr into the cycle): (left) temperature; (right) degree of impregnation. Fabric impregnation was faster at the edges of the laminate, which would impede gas evacuation.

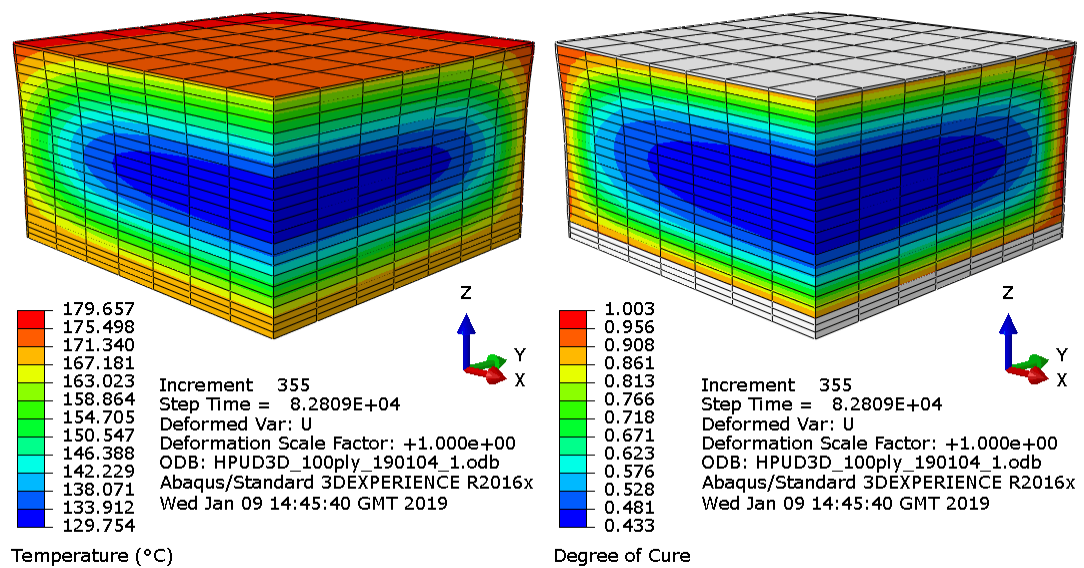


Figure 7.11. Contour plot of the 100-ply UD GF/epoxy laminate during the cure stage (i.e. 23 hr into the cycle): (left) temperature; (right) degree of cure. At 23 hr, the laminate was undergoing gelation and there were peaks in the thermal and cure gradients. The laminate exhibited outside-to-inside curing which created a solidified shell around the molten core.

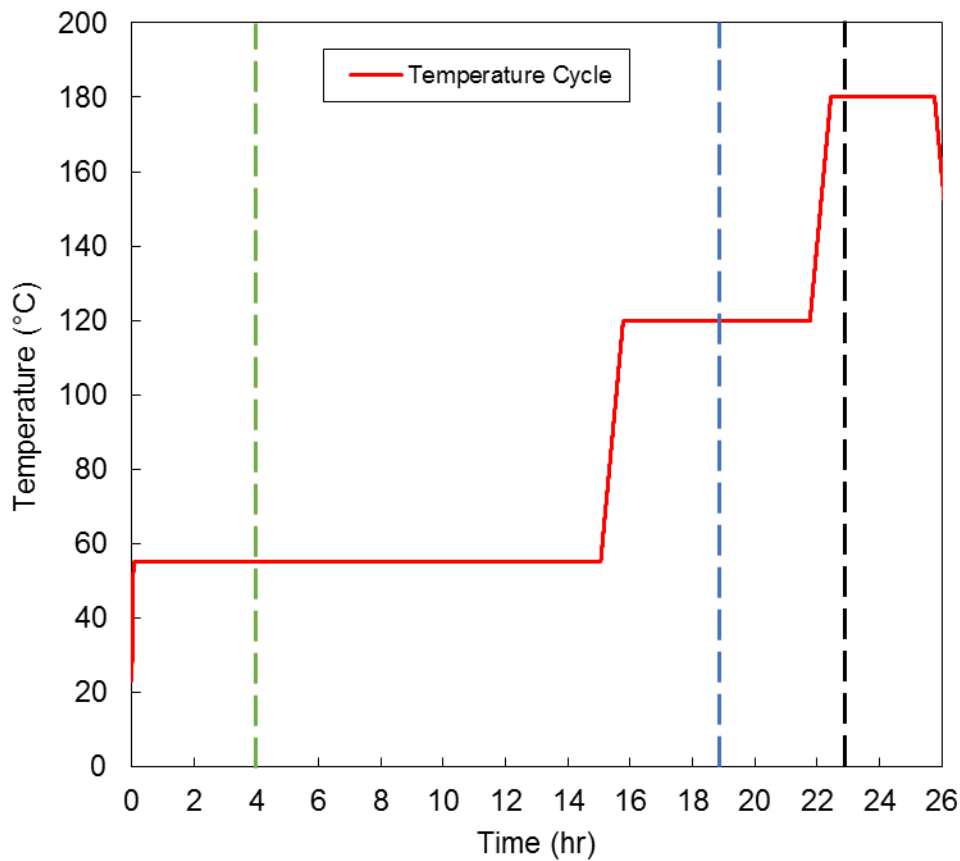


Figure 7.12. The time at which each contour was plotted w.r.t. the temperature cycle. The green dashed line represents the time step for Figure 7.9, while the blue and black dashed lines represent Figure 7.10 and Figure 7.11, respectively.

In most practical cases, thick section composites will be subject to 3D heat transfer, which brings into question the validity of using 1D simulations to optimize a temperature cycle. In the absence of a gas evacuation model and a residual stress model, it has been assumed that the completion of both fabric impregnation and curing were key criteria for processing thick section composites. As has can be seen in Figure 7.9 - Figure 7.11, these criteria were dependent on the processing conditions at the centre of the laminate i.e. the farthest point from any edges. Whether the 1D simulations, developed in Chapter 5 and 6, could accurately predict the processing conditions at the centre of a laminate depended on the ratio of laminate thickness to

in-plane dimensions (Oh, 2007), and the ratio of anisotropy w.r.t. the thermal conductivities (Yan, 2008).

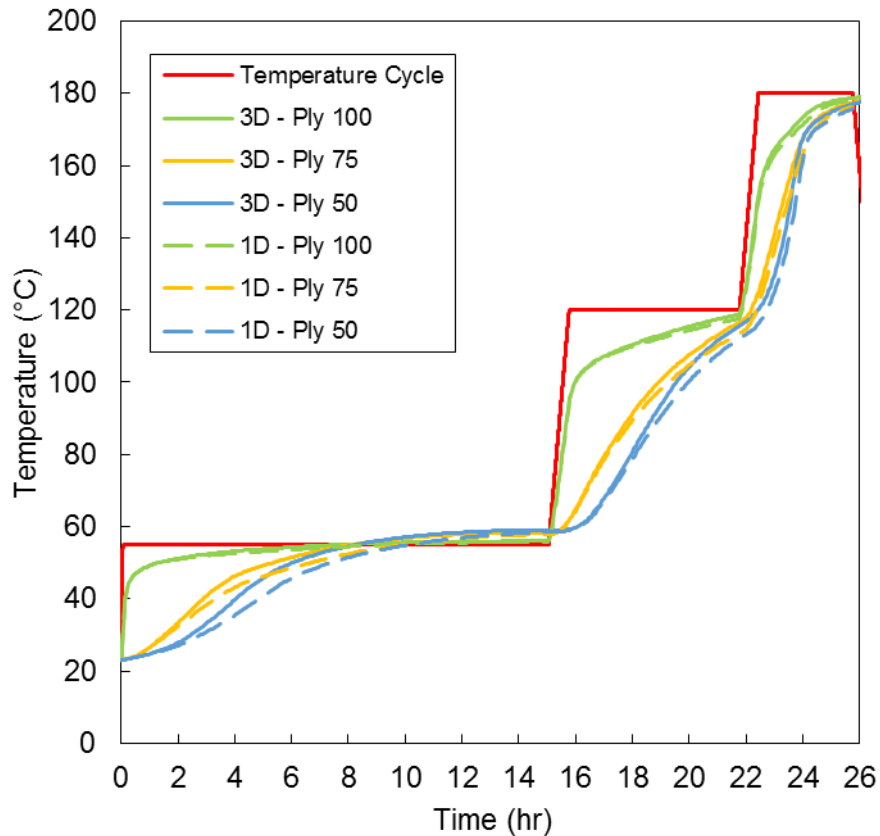


Figure 7.13. Comparison of 1D and 3D temperature predictions in a 100-ply UD glass-fibre laminate. The mismatch between the results was more prevalent when the epoxy was in powder form and the ratio of anisotropy was greater.

Figure 7.13 shows that 1D simulations offered a reasonable approximation of the 3D results, however, with respect to the ratio of anisotropy for thermal conductivities, it was interesting to consider the influence of edge effects for carbon-fibre (CF) based laminates. A simulation was repeated for the 3D quartered geometry using the material properties/parameters given in Table 7.2. All other properties/parameters remained the same as the previous simulation.

Table 7.2. Material properties/parameters used for carbon-fibre (CF) fabric.

Property/Parameter [units]	Value	Source
Thermal conductivity of impregnated CF fabric [W/m.K]	Equation 5.29	(Clayton, 1971)
Thermal conductivity of carbon fibre [W/m.K]	7.8	(Hsiao, Laudorn and Advani, 2001)
Thermal conductivity of dry stitched CF fabric [W/m.K]	0.287	(Lee, 2004)
Density of carbon fibre [kg/m ³]	1800	(Toray Carbon Fibers America, 2019)
Specific heat capacity of carbon fibre [J/kg.K]	753	(Toray Carbon Fibers America, 2019)
Inter-tow permeability of stitched CF fabric [m ²]*	8.45×10^{-10}	(Kuentzer <i>et al.</i> , 2006)
Intra-tow permeability of CF [m ²]	Equation 2.24	(Gebart, 1992)
Carbon fibre diameter [m]	7.0×10^{-6}	(Toray Carbon Fibers America, 2019)
Fibre volume fraction of glass fibre tow	0.73	(Centea and Hubert, 2012)

* Average value for biaxial woven CF fabric chosen as a first approximation.

As shown in Figure 7.14, the high thermal conductivity of the carbon fibres resulted in asymmetric in-plane heat transfer. When comparing the temperatures at the centre of the laminate to a 1D simulation (see Figure 7.15), it was clear that the difference between the models was significantly greater than for the GF laminate. Due to in-plane heat transfer, the entire laminate approached the programmed oven temperature much faster than GF laminates as well. This resulted in the powder sintering at an increased rate, which would have an effect on moisture desorption and gas evacuation.

Additionally, it was noted that the laminate did not reach full impregnation for the normal temperature cycle due to the lower permeability of CF tows (see Figure 7.16). Using the modified temperature cycle from Chapter 6, Section 6.3.6, it was possible to achieve full impregnation for the laminate due to the shortened drying stage and extended impregnation stage.

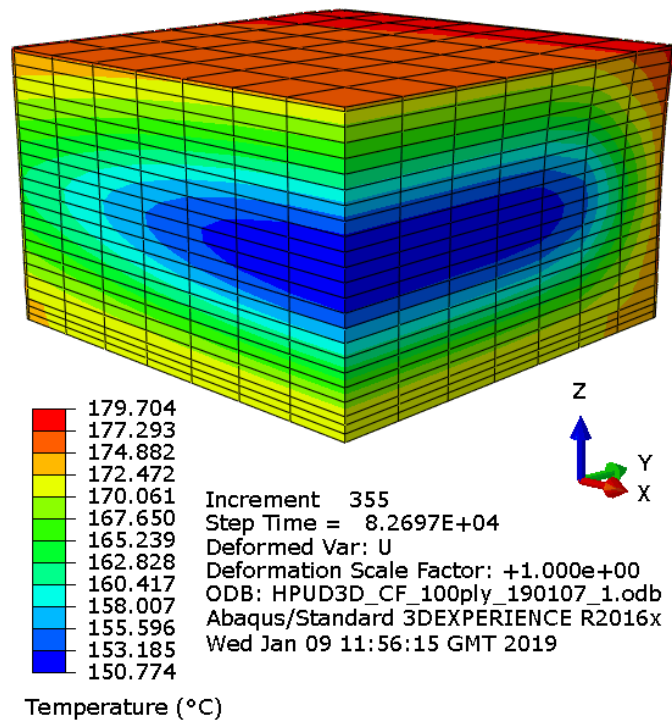


Figure 7.14. Contour plot of the 100-ply CF/epoxy laminate during the cure stage (i.e. 23 hr into the cycle). The temperature gradients in the XZ and YZ planes were asymmetric due to the high thermal conductivity of the laminate in the longitudinal (x) direction.

Simulations were performed for triaxial fabrics also (GF and CF). The ratios of anisotropy for each simulated laminate are given in Table 7.3; in each case, a range was given because the ratios varied over the duration of the temperature cycle as a function of the material state i.e. temperature, powder void fraction, degree of impregnation, etc. As expected, the ratio of anisotropy was significantly higher for the carbon fibre laminates.

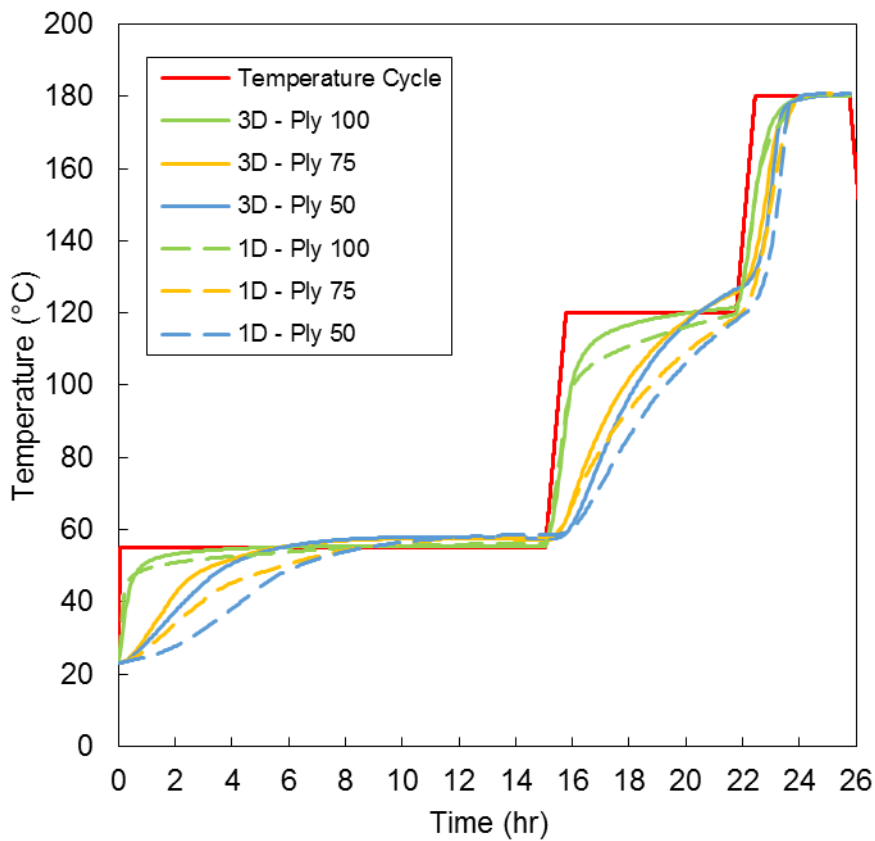


Figure 7.15. Comparison of 1D and 3D temperature predictions in a 100-ply UD CF laminate. There was a significantly greater difference between the results than there was for the equivalent GF laminate.

Table 7.3. Ratio of anisotropy for the various laminates that were simulated.

Material type	Ratio of anisotropy*
Uni-directional GF	2.08 – 5.55
Triaxial GF	1.80 – 4.42
Uni-directional CF	5.54 – 35.79
Triaxial CF	4.44 – 27.10

* Ratio of anisotropy between the longitudinal thermal conductivity and the through-thickness thermal conductivity

Overall, it was clear from the results that part dimensions and thermal conductivity must be carefully considered before using 1D simulations to optimize a temperature cycle.

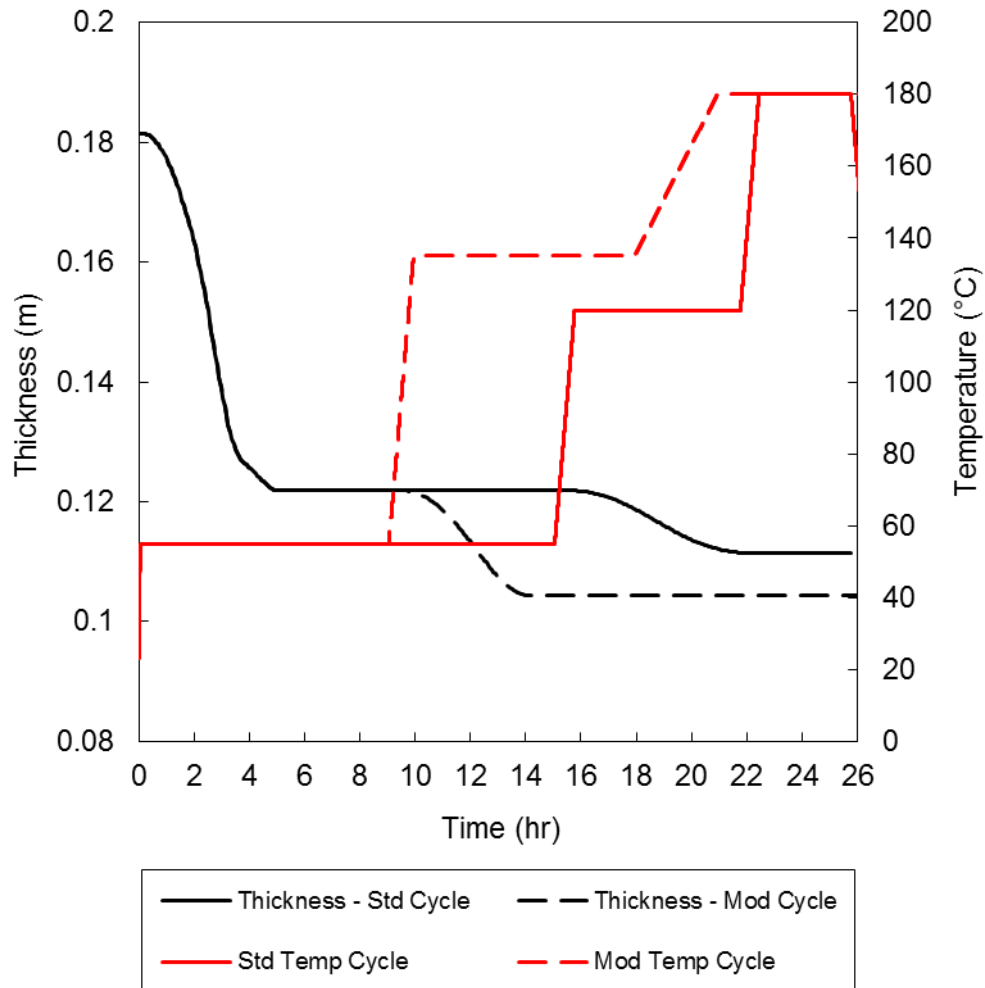


Figure 7.16. Simulated thickness change for the 100-ply UD CF laminate using the standard temperature cycle and the modified temperature cycle from Chapter 6, Section 6.3.6. The laminate failed to fully impregnate for the standard temperature cycle. By beginning the impregnation stage earlier, the modified cycle could achieve sufficiently low viscosities to impregnate the carbon fibre tows.

7.3.2 Simulations of Turbine Blade Manufacturing

The complexity of the geometry plays an additional role in determining which kind of simulation should be performed; 1D, 2D, or 3D. For the root-section of a turbine blade, as shown in Figure 7.17, the thickness tapered (via ply drops) along the blade axis (in the x direction) but was unchanged in the radial direction (about the x axis). As such, it was assumed that in-plane heating was negligible in the radial direction, and a 2D cross-section (in the XZ plane) was created using the triaxial semi-preg, as described in Section 7.2.2.

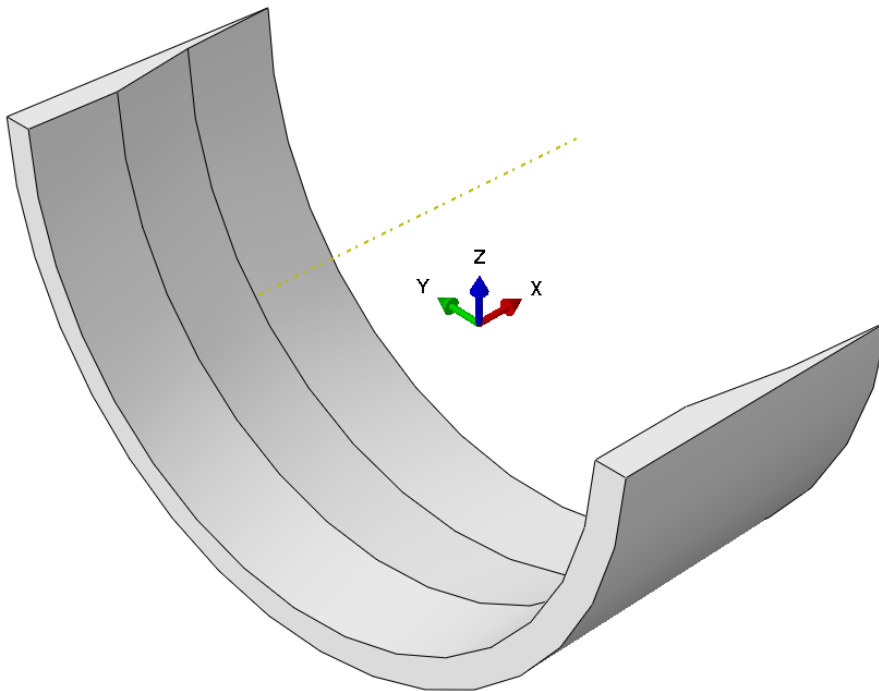


Figure 7.17. Half-section of a tapered wind turbine blade root, designed by SE Blade Technology B.V. as a manufacturing demonstrator for the POWDERBLADE project.

The standard temperature cycle, described in Chapter 5, Section 5.3.1, was used to perform initial simulations. It should be noted that, due to difficulties with meshing, the bagging layer was excluded from the simulations. The effects of this exclusion were not negligible (see Figure D.18 in the Appendices: D. Simulation Results),

however, for demonstration purposes, the results can be considered a good approximation of actual processing conditions.

Contour plots of temperature and DoC are shown in Figure 7.18 and Figure 7.19, respectively, for the 2D tapered section manufactured using the standard temperature cycle. While tooling was included in the simulations, it has been removed from view in the contour plots. Furthermore, the detail of the meshing has been removed from the contours to allow better image clarity.

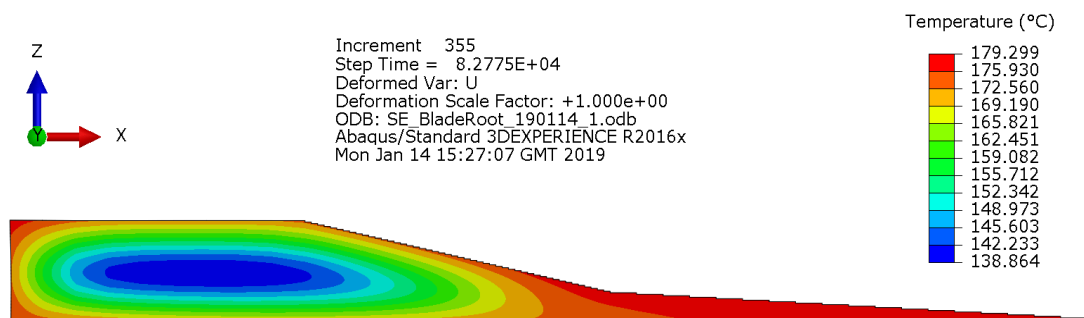


Figure 7.18. Temperature distribution along the XZ plane of a tapered root section during the cure stage of a standard temperature cycle (i.e. 23 hr into the cycle). Thermal gradients formed towards the thicker part of the section.

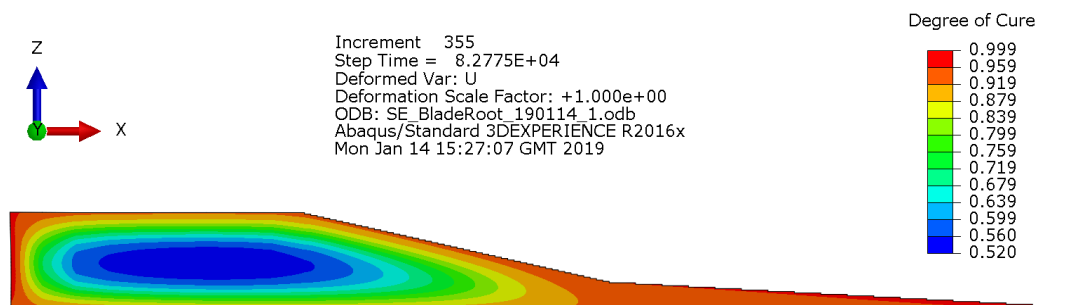


Figure 7.19. Degree of cure distribution along the XZ plane of a tapered root section during the cure stage of a standard temperature cycle (i.e. 23 hr into the cycle).

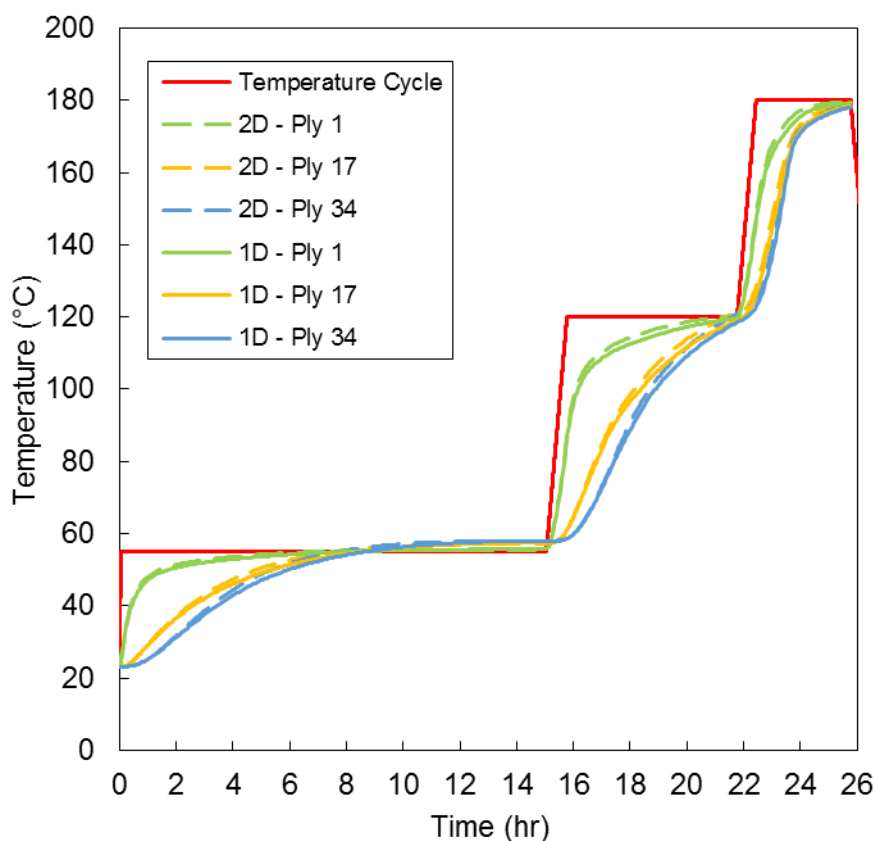


Figure 7.20. Comparison of temperature results for the 1D and 2D simulations. For the 2D geometry, temperatures were taken approx. 185 mm from the end of the section. There was relatively little difference between the results (max of approx. 2°C).

While the temperature and DoC remained uniform in the thinner end of the root, thermal gradients and cure gradients developed in the thicker end of the root. It was expected that the modified temperature cycle, described in Chapter 6, Section 6.3.6, would alleviate the gradients in the thicker region, however, it was found that temperature cycle needed to be adjusted further to account for difference between the semi-preg and powder-based prepreg. For an iterative task such as this, the 2D simulation was relatively inefficient (i.e. run time of 677 s) compared to 1D simulations (run time of 87 s or less). To test whether a 1D approximation would be valid for this case, 1D simulation results were compared with the 2D simulation; see Figure 7.20. For the 2D simulation, values were taken at $x = 185$ mm i.e. the point which seemed least affected by in-plane heat transfer. There was little variation

between the results, which suggested that the 1D approximation was valid. Consequently, 1D simulations were used for iterative modification of the temperature cycle.

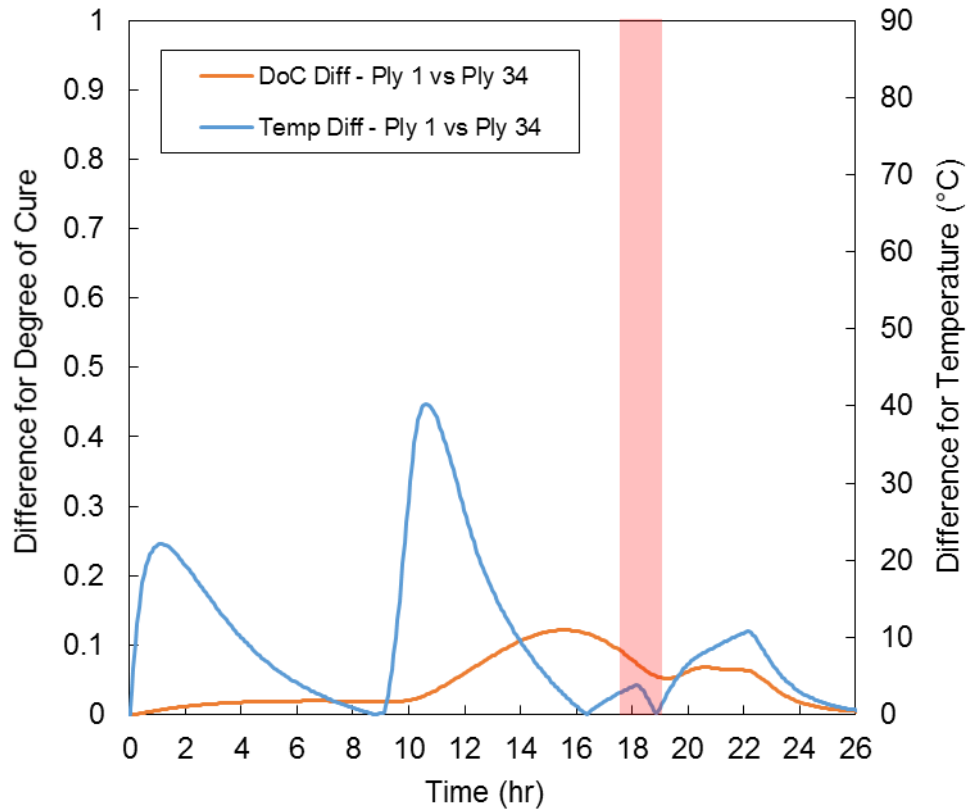


Figure 7.21. The temperature difference and DoC difference between the outside of the section (Ply 1) and the centre (Ply 34) for the new temperature cycle. The red shaded are represents the period of gelation within the section.

The new temperature cycle for this case was as follows:

- Drying stage: Ramp to 55°C and hold for 540 min
- Impregnation stage: Ramp to 120°C at 1.0°C/min and hold for 480 min
- Cure stage: Ramp to 180°C at 0.25°C/min and hold for 300 min

As can be seen in Figure 7.21, the new temperature cycle resulted in relatively small differences in temperature and DoC between the outside and centre of the laminate during gelation (less than 5°C and 0.1, respectively).

In Chapter 6, Section 6.3.5, the use of heated tooling and flexible heating mats were investigated as an alternative heating method which could potentially be more cost-effective for manufacturing thick parts than oven heating. Assuming that one-sided heating was sufficient to process the thinner end of the tapered blade root, it was considered worthwhile to re-explore this concept.

The new temperature cycle for the root section was implemented using specified temperature boundary conditions on both the underside of the steel tool and the top surface of the thickest part of the root (including the first 16 ply-drops), as shown in Figure 7.22. Insulated boundary conditions were assumed for all other surfaces.

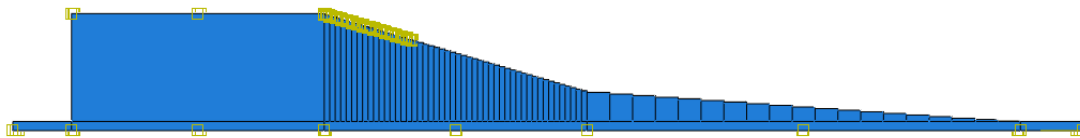


Figure 7.22. The tapered blade root geometry with yellow boxes marking where the specified temperature boundary conditions were applied.

Figure 7.23 and Figure 7.24 show the effects of using heated tooling and flexible heating mats. Due to localised heating, the thickest part of the geometry experienced two-sided heating, while the thinner region experienced one-sided heating. For the new temperature cycle, the thermal gradients and cure gradients were relatively low during gelation. Note that the thicker section of the root is undergoing gelation in Figure 7.23 and Figure 7.24.

Obviously, the length of the flexible heating mat can be increased to heat more of the top surface if necessary. This concept may be particularly useful for parts which are too large to fit into a conventional oven, such as blade spars. As multiple mats would be in use, it would also be possible to control the temperature cycle on a zone-by-zone basis to minimise in-plane gradients and energy usage.

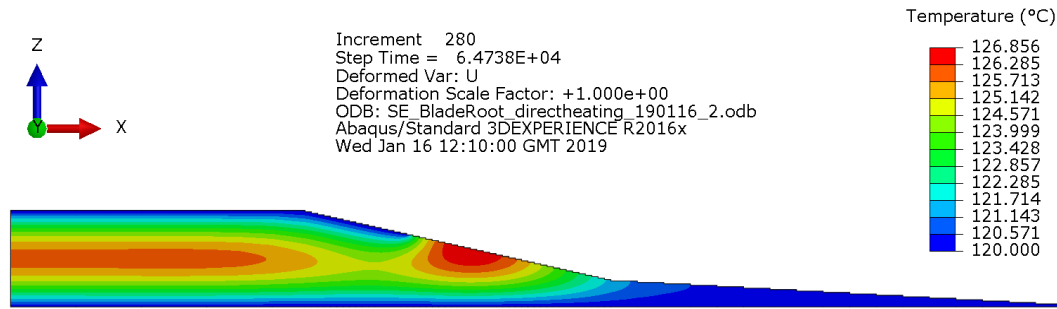


Figure 7.23. 2D simulation of the tapered root section with the temperature distribution represented by colour contours. The image was taken approx. 18 hr into the modified temperature cycle when the epoxy was undergoing gelation.

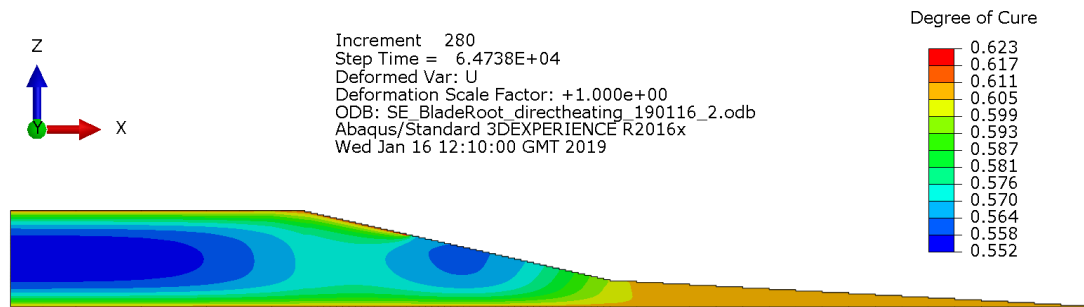


Figure 7.24. 2D simulation of the tapered root section with the DoC distribution represented by colour contours. Gelation had begun in the part, but the cure gradients were relatively small due to the used of the modified temperature cycle.

Although the root section of a turbine blade is typically made from glass-fibre composites, it was a worthwhile exercise to consider how the ratio of anisotropy would affect processing. For this reason, a simulation was performed with triaxial CF fabric using the new temperature cycle (the dimensions of the geometry were not altered). Figure 7.25 shows that heating was relatively uniform for much of the temperature cycle, which resulted in relatively small gradients in the thickest section of the part. This was due to a combination of the improved temperature cycle and the presence of carbon fibres which allowed larger amounts of in-plane heat transfer, particularly in the x direction. Note that the values were taken 185 mm from the end of the blade root (in the x direction).

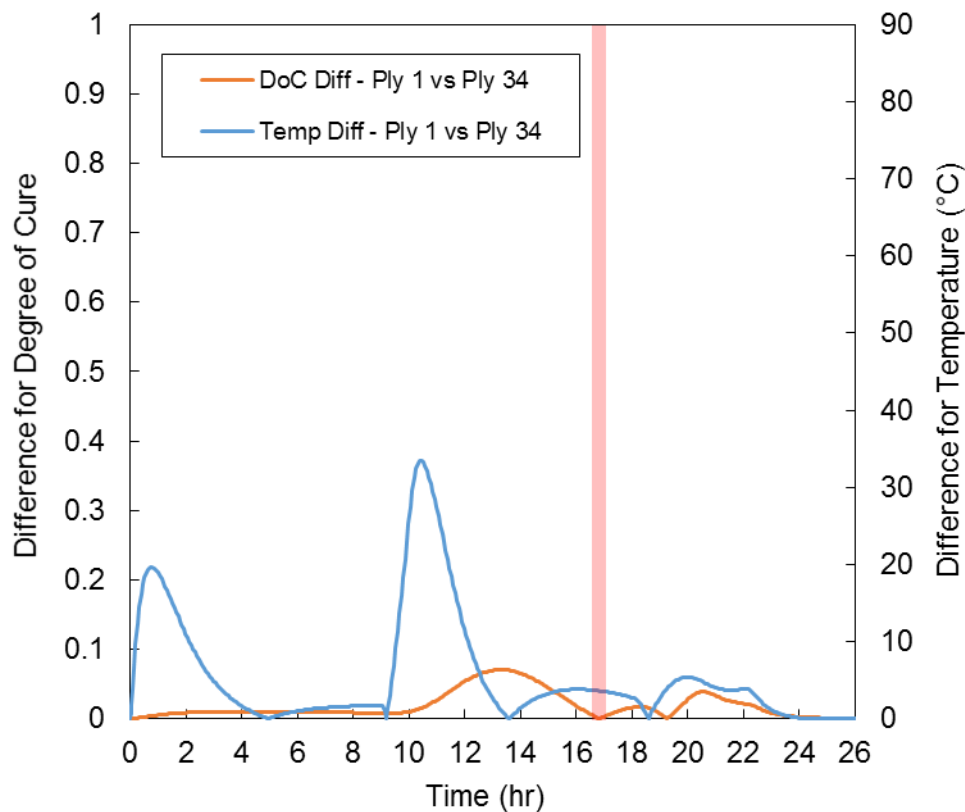


Figure 7.25. The temperature difference and DoC difference between the outside of the blade root (Ply 1) and the centre (Ply 34) when triaxial CF fabric was used. The period of gelation in the laminate was very short because there was little or no difference in the DoC (through-thickness) at that point in time. The data was taken 185 mm from the end of the section.

7.4 Conclusions

Numerical methods for performing 2D and 3D process simulations have been presented. The simulations focussed on the processing of thick-section laminates via VBO prepregs which use epoxy powder as the polymer matrix. The simulations were performed using coupled temperature-displacement analysis tools in Abaqus FEA along with user-defined subroutines which described the resin flow, powder sintering, and cure kinetics within the composite material. Three main geometries were considered; a 1D through-thickness geometry, a 3D quartered section of a flat

laminate, and a 2D cross-section of a wind turbine blade root. The 1D geometry was used to confirm the accuracy of the simulations against experimental data from Chapter 6, and a small convergence study showed that the numerical methods were robust for varying time step sizes and element sizes. In this sense, it can be concluded that the commercial software was highly efficient in comparison to the finite difference code developed in Chapter 5. Nevertheless, implementation of the process models in the user-defined subroutines was a challenging process and benefitted from the development of the finite difference code.

The effects of in-plane heat transfer were investigated using the 3D quartered section. It was found that heat transfer in the fibre direction had a greater influence in the first two stages of the temperature cycle while the powder was sintering and then flowing into the fabric. This was due to the low thermal conductivity of the powder and dry fabric, which inhibited through-thickness heat transfer. As a result, all the critical processes, such as powder sintering, fabric impregnation, and curing, occurred first at the outside of the laminate. Centea *et al.*, (2017) have shown that this behaviour in VBO prepreps can trap voids at the centre of the laminate. Outside-to-inside curing can result in large residual stresses in thick sections also.

The mismatch between in-plane and through-thickness heat transfer became more severe when carbon fibres were considered. In terms of thermal conductivity, it was shown that, depending on the stage of the temperature cycle, the ratio of anisotropy for carbon-fibre fabrics was up to an order of magnitude higher than for glass-fibre fabrics. It was also shown that fabric impregnation was significantly slower for carbon-fibre fabrics, and a modified cycle was required to achieve full impregnation with the GRN 918 epoxy powder.

Due to the influence of in-plane heating, the validity of a 1D (through-thickness) heat transfer assumption was tested for the 3D geometry. It was shown that the discrepancies between 1D and 3D simulations were significantly higher for carbon-fibre fabrics than for glass-fibre fabrics due to the higher ratio of anisotropy. As a result, the 1D assumption may be limited for many practical cases of thick-section

carbon-fibre laminates because the in-plane dimensions must be significantly larger than the laminate thickness.

Additionally, the choice of 1D, 2D, or 3D simulations was considered for a turbine blade root geometry which was tapered via ply-drops. As the cross-section was uniform radially, a 2D simulation was implemented, however, it was shown that 1D simulations could be used as well to determine key processing criteria such as the completion of impregnation and cure. Consequently, 1D simulations were used to modify the temperature cycle for that geometry and VBO prepreg format.

An alternative heating method, previously introduced in Chapter 6, was re-investigated for the tapered blade root section. This method used heated tooling and heating mats to apply two-sided heating locally to the thickest section of the root while the thinner part of geometry was heated from one side by the tool. It was shown that the blade root could be fully processed using this method, and, compared to conventional ovens, this arrangement should offer more energy efficient heating of large thick-section parts.

Finally, the implication of using carbon-fibre was considered for the turbine blade root. It was shown that, due to in-plane heating, the through-thickness temperature and DoC differences were relatively small. Although turbine blade roots are typically made using glass-fibre fabrics, increasingly, unidirectional carbon-fibre is being used to produce spars for very large turbine blades (> 60 m in length). As such, faster in-plane heat transfer may represent an added benefit of using carbon fibres in this application.

8. Conclusions and Recommendations

8.1 Conclusions

The increasing market share for renewable energy has pushed industry to scale up new technologies (tidal turbines) and existing technologies (wind turbines) to meet the demands. Scaling up the blade manufacturing process has been challenging due to the limitations of conventional resin systems for processing thick sections i.e. highly exothermic curing. This thesis has investigated the use of heat-activated epoxy powders as an alternative to conventional resin systems due to their lower exotherm, and their potential for making low-cost vacuum-bag-only (VBO) prepreg materials. With respect to the objectives outlined in Chapter 1, Section 1.6, the key conclusions of this thesis were the following:

1. At least one epoxy powder (GRN 918) was shown to have suitable characteristics for manufacturing thick-section fibre-reinforced composite parts using VBO processing i.e. it was stable under vacuum, it could maintain a suitable viscosity ($< 100 \text{ Pa}\cdot\text{s}$), and it generated a relatively small exotherm (184 J/g).

2. GRN 918 adsorbed/desorbed moisture faster in its powder form than when it was fully sintered, and its glass transition temperature was a function of relative humidity and temperature.
3. It was possible to describe the curing of GRN 918 by modifying an existing cure kinetics model. The modification was required due to the presence of latent curing agents in the epoxy's chemical formulation.
4. The chemorheological behaviour of GRN 918 resembled that of a toughened epoxy. As such, Williams-Landel-Ferry type models best described both the chemorheological behaviour and sintering behaviour of GRN 918.
5. It was possible to simulate the processing of a thick-section laminate – manufactured using powder-based VBO prepregs – by combining material models with existing models for heat transfer and resin flow.
6. The reduction in laminate thickness was as much as 45%. This was due to fabric impregnation and powder sintering.
7. Laminate thickness change, along with the initial state of the VBO prepreg plies (i.e. initial degree of impregnation, powder void fraction, etc.), has an important influence on heat transfer within the laminate.
8. Thick laminates, which were manufactured using GRN 918, do not exhibit any thermal overshoot, but large thermal and cure gradients still develop within the laminates when a standard temperature cycle is used. Due to these gradients, the laminates also undergo an *outside-to-inside* curing pattern.
9. The thermal and cure gradients can be reduced by modifying the temperature cycle. They can also be reduced by modifying the laminate lay-up to include different epoxy powders (with tailored cure kinetics) through the thickness of the laminate.
10. It was possible to experimentally recreate one-dimensional (1D) heat transfer conditions within a thick-section laminate and validate the heat transfer model against thermocouple data.
11. Based on comparisons with experimental data from a linear variable differential transformer (LVDT), the 1D resin flow and sintering models captured the general processing behaviour of the laminate, however, optical

microscopy revealed that the resin flow model could not accurately predict the cessation of flow at the centre of the tow.

12. Using user-defined subroutines, it was possible to implement the material models and process models (as well as laminate thickness change) in the commercial finite element analysis (FEA) software package, Abaqus FEA.
13. 1D simulation results from Abaqus FEA closely resembled the results from the finite difference code, but were more computationally efficient (up to 60 times faster).
14. For 2D/3D simulations, the ratio of in-plane thermal conductivity to through-thickness thermal conductivity (i.e. the ratio of anisotropy) varies w.r.t. the degree of impregnation (DoI) and powder void fraction.
15. The ratio of anisotropy is significantly higher for carbon-fibre (CF) laminates than for glass-fibre (GF) laminates.
16. Both the ratio of anisotropy and the laminate dimensions must be considered when determining whether 1D, 2D, or 3D heat transfer analyses should be used.
17. The effectiveness of a temperature cycle is dependent on part geometry and material format (i.e. powder void fraction, DoI, fibre type, etc.), and must be optimised on a case-by-case basis.
18. Alternative heating methods, such as flexible heating mats, can be used to provide localised heating of thick-section parts.

8.2 Recommendations

There are numerous areas of this research which could be expanded on, some more critical than others.

The sorption properties of powder-based polymers could present a significant advantage to VBO prepreg processing. It is clear that moisture desorbs faster from powder than from sintered resin, however, it would be greatly beneficial to develop process models which can describe the rates of sorption as a function of temperature

and powder void fraction. Moreover, much research has been carried out on modelling gas evacuation in VBO prepreg, and has pointed towards the importance of through-thickness gas permeability. It seems intuitive that porous powder layers have an advantage over conventional systems, however, this has not been quantified. By measuring the gas permeability and the sorption properties of the epoxy powder, it should be possible to combine them with a gas evacuation model and simulate the drying stage of the temperature cycle. This is critical to optimising the drying stage without adversely affecting the laminate quality i.e. due to entrapped gases.

It has been shown that optimising the temperature cycle depends on the part geometry and material format. To increase efficiency, it would be beneficial to develop an optimisation algorithm for automating this process. The optimisation of composite temperature/processing cycles has been widely researched, and a few examples for thick-section processing are given in Chapter 2, Section 2.3.2.

Despite optimisation, large thermal and cure gradients are still a risk for thick-section composite parts due to the high temperature processing of epoxy powder. As such, the process simulations would significantly benefit from the addition of residual stress analysis models. Without some form of residual stress analysis, it is impossible to know the actual effect of any gradients that are formed within the laminate.

The concept of using more than one powder to reduce thermal and cure gradients has been briefly explored, but warrants further study. Such a study could include an investigation of powder compatibility, both in terms of processing and mechanical properties (i.e. do they inhibit or promote curing when mixed, and do they bond well together, etc.). It could also include an investigation into how the powders are mixed through-thickness i.e. gradual or abrupt transition.

From a commercial perspective, it would be worthwhile to consider the concept of using flexible heating mats and test whether the concept is feasible in a practical setting.

It has been suggested that epoxy powder based parts can be consolidated separately and co-cured. This is a novel and beneficial feature of the resin system, however, more

research must be carried out to quantify the bond strength of co-cured joints, and to determine how the bond strength varies as a function of the degree of cure (DoC). Due to the long cycle times and *outside-to-inside* curing, it may be difficult to co-cure thick-section parts.

The experimental validation showed that the cessation of fabric impregnation was more gradual than what was predicted by the current resin flow model. It is possible that the cause of this is pressure deficient conditions. As these conditions are not uncommon in reality, the process simulations would also benefit from an improved resin flow model which can account for the resulting void formation.

The experimental validation also revealed that the epoxy powder had a higher initial DoC due to having been in storage longer than the semi-preg material. As such, it would be worthwhile to investigate the effects of long-term storage on the epoxy powder, using characterisation techniques such as differential scanning calorimetry and parallel-plate rheometry.

Finally, improvements could be made to the current sintering model by repeating tests using a controlled temperature chamber on the parallel-plate rheometry and by varying the applied pressure to determine its effect, if any, on the sintering process.

Appendices

A. Epoxy Powder Characterisation Data

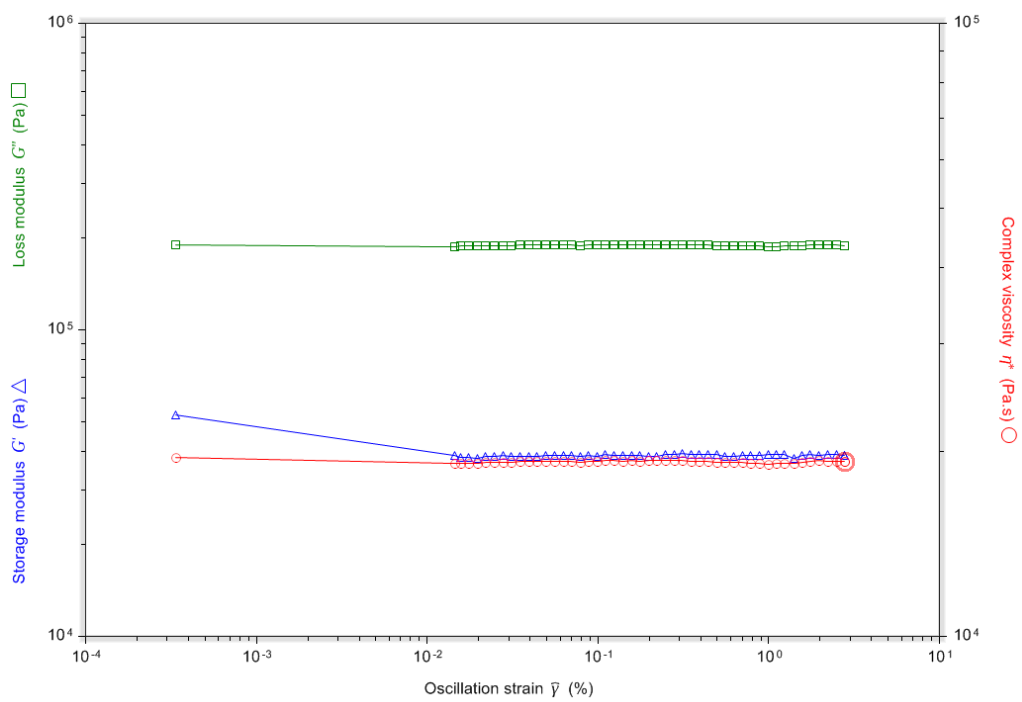


Figure A.1. Rheometer data for a strain sweep at 70°C. Note that the data stopped at approx. 3% strain because the torque limit of the rheometer was reached.

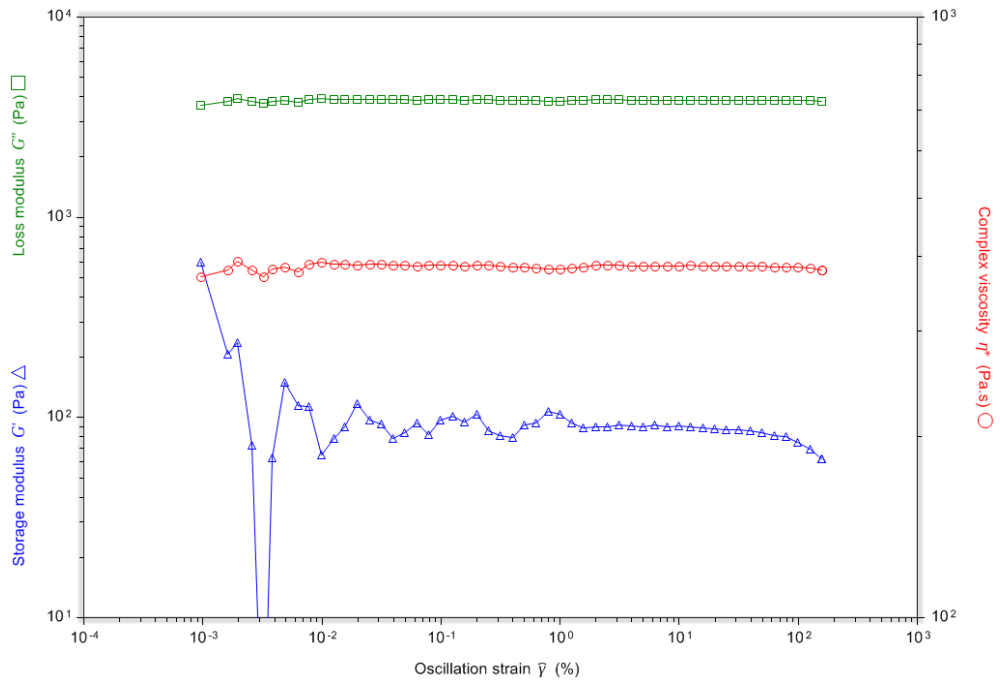


Figure A.2. Rheometer data for a strain sweep at 90°C. The storage modulus response became distinctly non-linear above 50% strain.

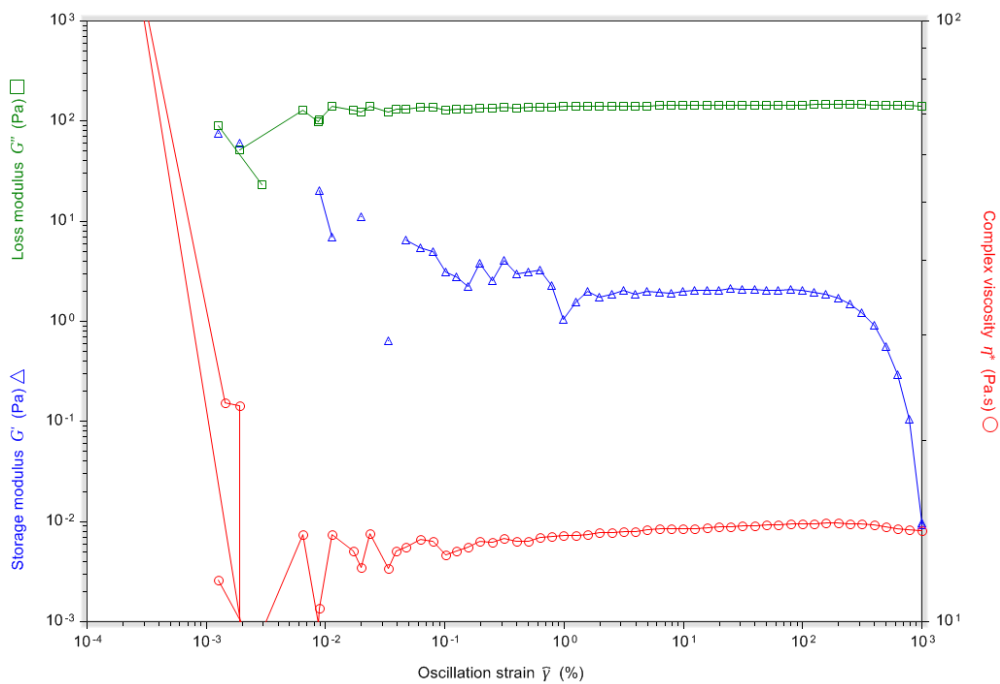


Figure A.3. Rheometer data for a strain sweep at 120°C. Although higher strains improved the resolution of the data, once again the storage modulus became non-linear at high strain.

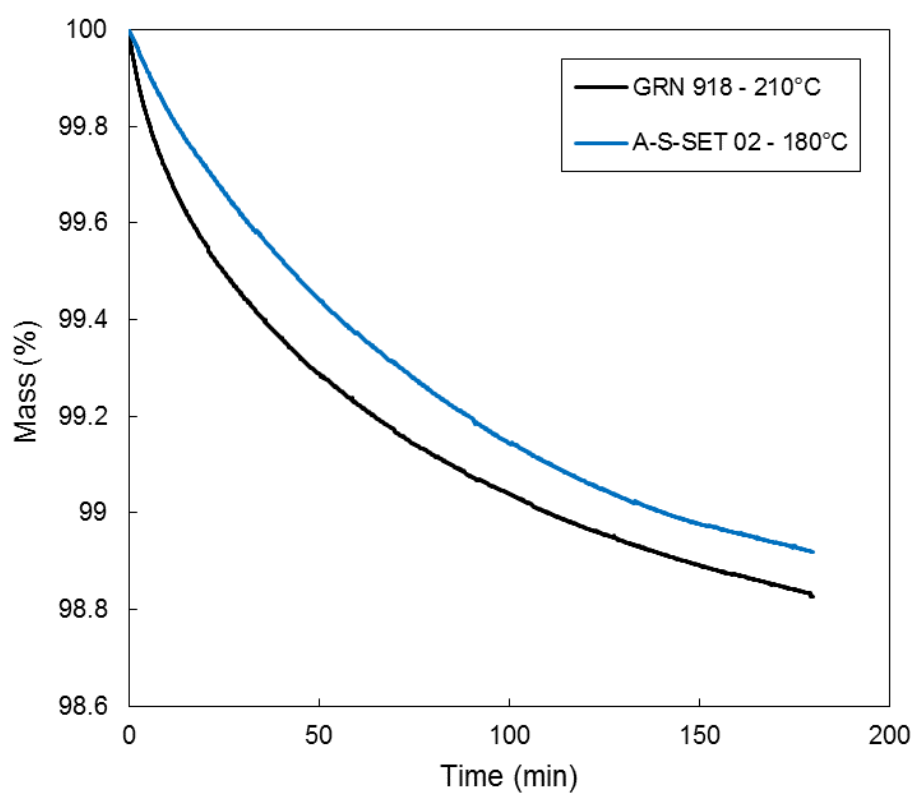


Figure A.4. Mass change for isothermal TGA tests of GRN 918 and A-S-SET 02 epoxy powders. Approx. 1% mass loss for both powders after 3 hr at elevated temperature.

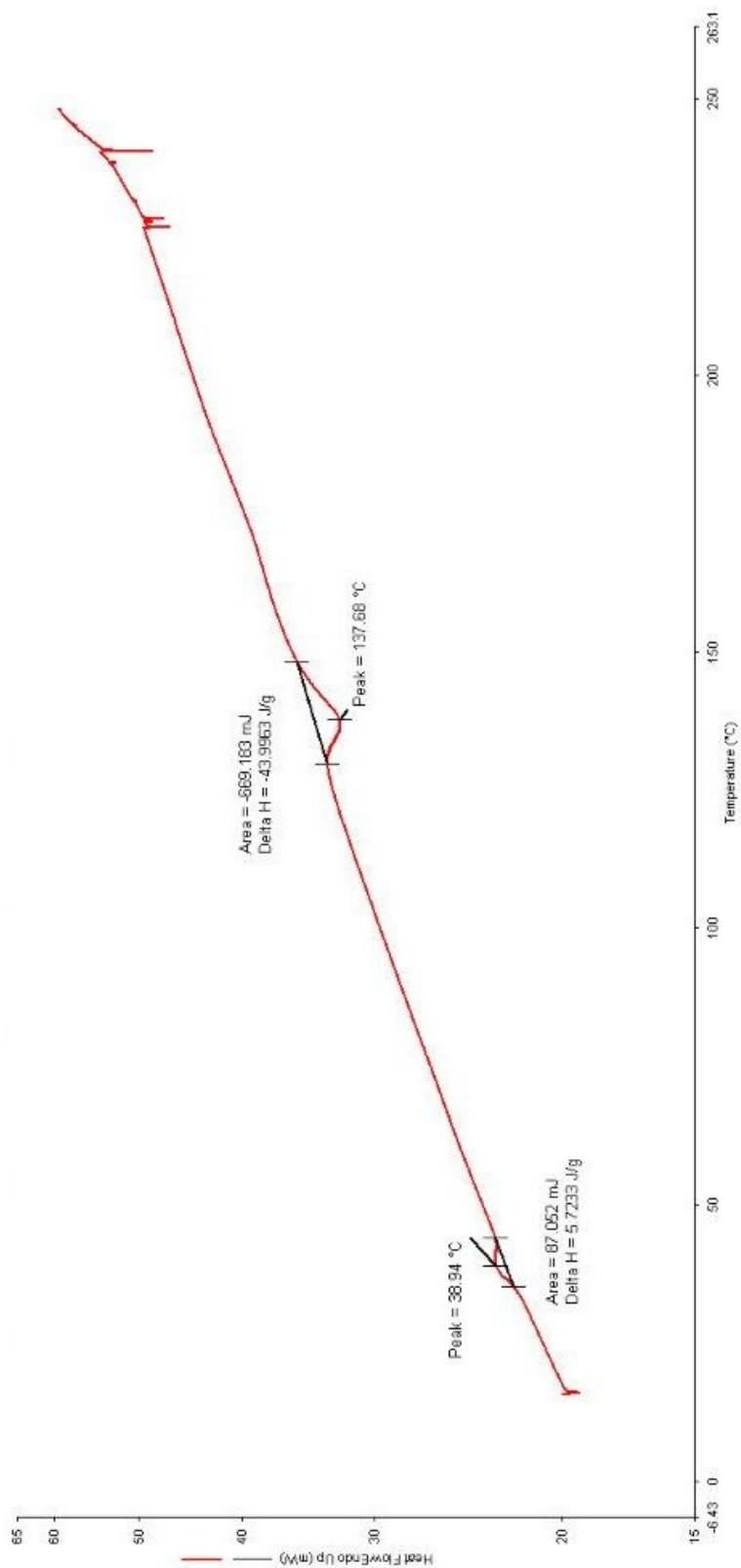


Figure A.5. DSC heat flow for A-S-SET 02 during a temperature scan at 1.5°C/min.

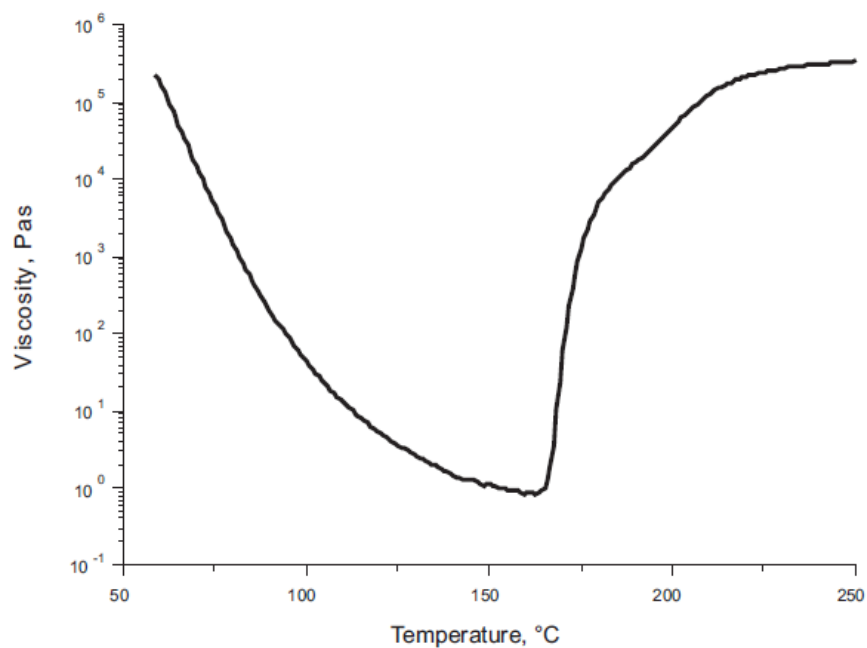


Figure A.6. Viscosity curve for a temperature scan of A-S-SET 02 epoxy powder (New Era Materials Sp. z o.o., 2014).

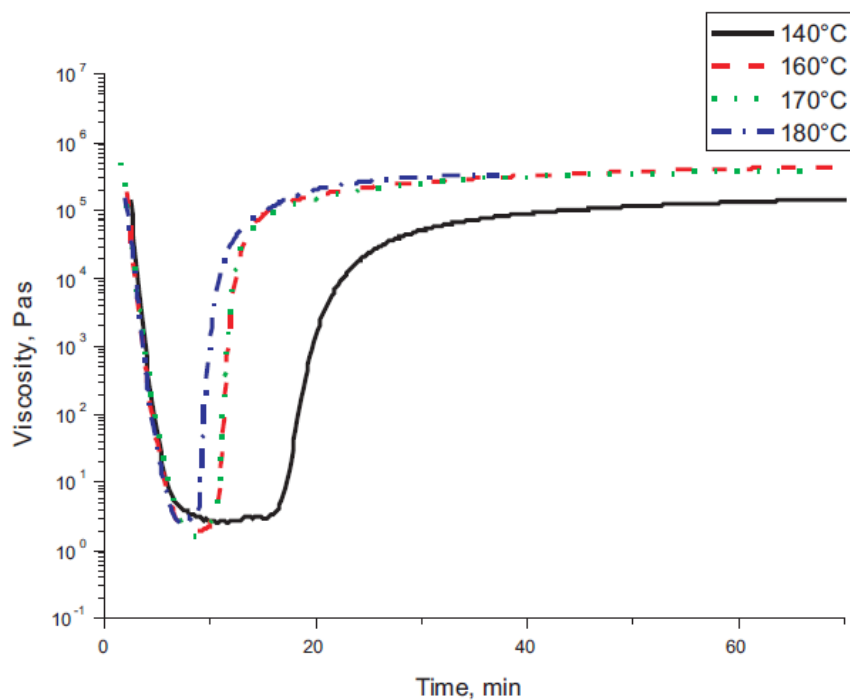


Figure A.7. Viscosity curves for isothermal tests of A-S-SET 02 epoxy powder (New Era Materials Sp. z o.o., 2014).



Figure A.8. Images of DMTA test specimens: (L) GRN 918 (yellow) and Ampreg 22 (green); (R) A-S-SET 02 suffered from severe porosity after being processed under vacuum.

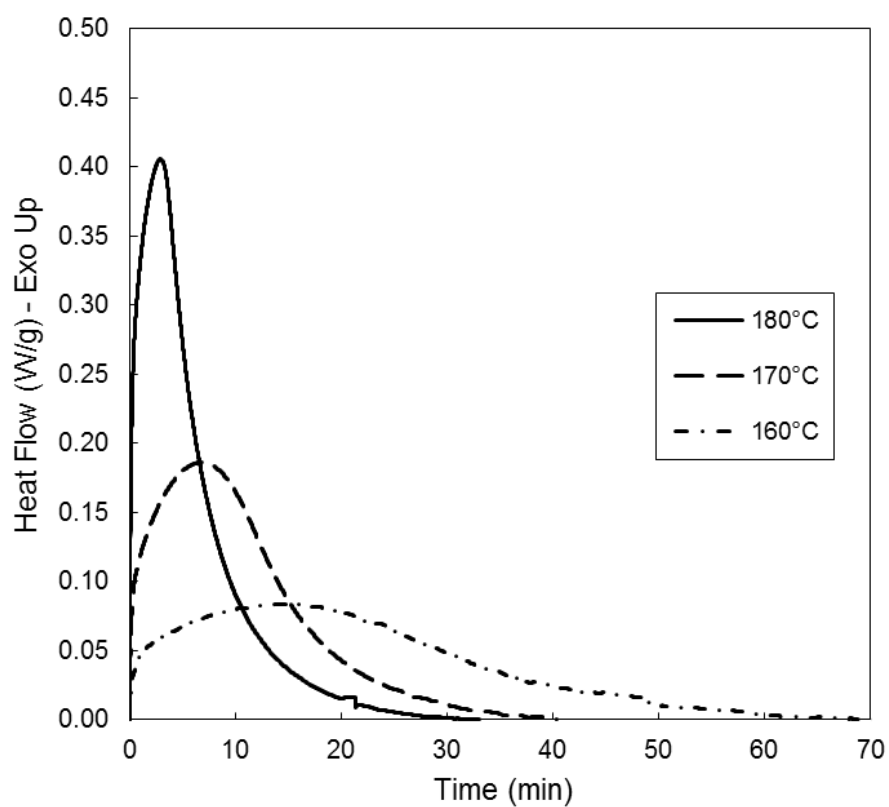


Figure A.9. Isothermal DSC heat flow data for GRN 918 at three test temperatures.

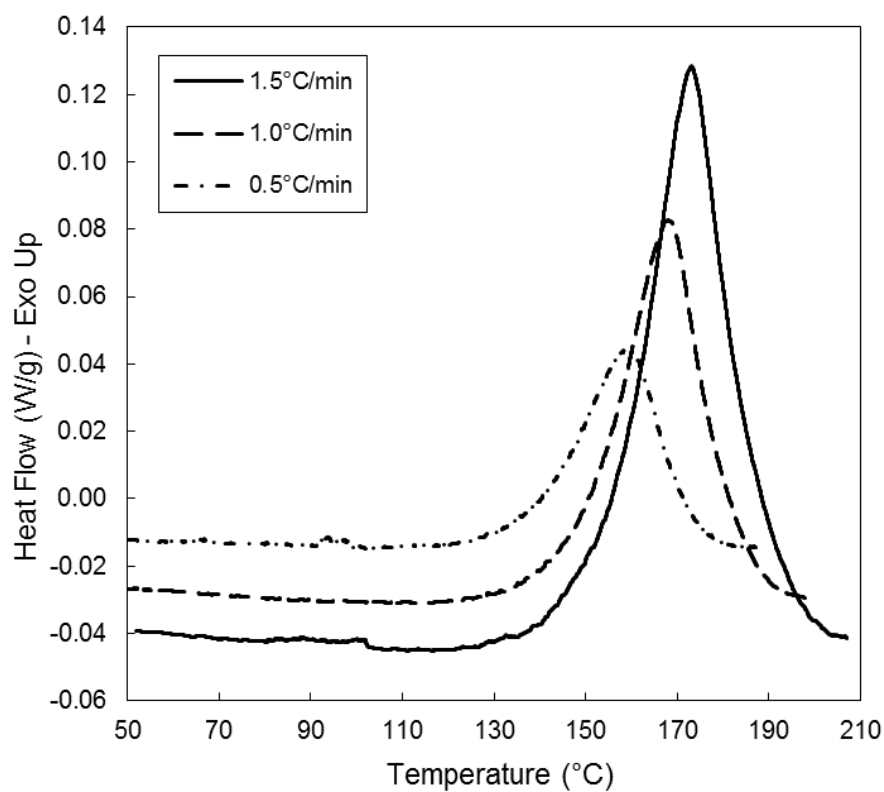


Figure A.10. DSC heat flow for temperature scans of GRN 918 epoxy powder at three temperature ramp rates.

Table A.1. Total enthalpy of reaction for each DSC used in the cure kinetics modelling.

Test	Total enthalpy of reaction [J/g]
160°C	163.5
170°C	170.5
180°C	181.0
0.5°C/min	184.0
1.0°C/min	172.5
1.5°C/min	178.5
10°C/min	178.0

B. Process Models

Derivation of analytical solutions for 1D isothermal dual-scale resin flow in VBO prepregs

The 1D flow velocity u can be written as the time derivative of the flow front position:

$$\frac{dl}{dt} = \frac{u}{\varphi} = -\frac{K}{\varphi\eta} \cdot \frac{dP}{dx} \quad (\text{B.1})$$

Integrating Equation B.1 for time and the pressure boundary conditions $P|_{x=0} = P_{app}$ and $P|_{x=l} = 0$,

$$\int_0^l \int_0^t \frac{dl}{dt} dt dx = \int_{P_{app}}^0 \int_0^t -\frac{K}{\varphi\eta} \cdot \frac{dP}{dx} dt dx \quad (\text{B.2})$$

$$\frac{l^2}{2} = \frac{-K_1}{\varphi_1\eta} [0 - P_{app}]t \quad (\text{B.3})$$

The solution for the flow front position in the inter-tow region is,

$$l = \sqrt{\frac{2K_1 P_{app}}{\varphi_1\eta} t} \quad , \quad l < L_1 \quad (\text{B.4})$$

For intra-tow flow, the pressure boundary condition at the interface of the two porous media P_{L1} must be derived. Assuming mass conservation for resin flow through the porous media,

$$\frac{du}{dx} = 0 \quad (\text{B.5})$$

Then,

$$\frac{-K_1(P_{app} - P_{L1})}{\eta L_1} = \frac{-K_2(P_{L1} - P_f)}{\eta(l - L_1)} \quad (\text{B.6})$$

Where P_f is the pressure at the flow front (assumed to be zero under vacuum conditions). As such, the equation reduces to:

$$P_{L1} = \frac{K_1 P_{app}(l - L_1)}{K_2 L_1 + K_1(l - L_1)} \quad (\text{B.7})$$

Integrating Equation B.2 again between time t and t_1 , and the pressure boundary conditions $P|_{x=0} = P_{L1}$ and $P|_{x=l} = 0$,

$$\int_{L_1}^l \int_{t_1}^t \frac{dl}{dt} dt dx = \int_{P_{L1}}^0 \int_{t_1}^t -\frac{K}{\varphi\eta} \cdot \frac{dP}{dx} dt \quad (\text{B.8})$$

$$\frac{(l - L_1)^2}{2} = -\frac{K_2}{\varphi_2\eta} \left[0 - \frac{K_1 P_{app}(l - L_1)}{K_2 L_1 + K_1(l - L_1)} \right] (t - t_1) \quad (\text{B.9})$$

$$K_2 L_1(l - L_1) + K_1(l - L_1)^2 = -\frac{2K_1 K_2 P_{app}}{\varphi_2\eta} (t - t_1) \quad (\text{B.10})$$

Solving the above quadratic equation, the solution for the flow front position in the intra-tow region is,

$$l = L_1 - \frac{K_2 L_1}{2K_1} + \sqrt{\left(\frac{K_2 L_1}{2K_1}\right)^2 + \frac{2K_2 P_{app}}{\varphi_2\eta} (t - t_1)} \quad , \quad l \geq L_1 \quad (\text{B.11})$$

Equations for heat transfer through the bagging or tooling

Heat transfer at the boundary of the laminate and bagging was written as,

$$\begin{aligned} \left(\Delta z \rho c_p \frac{dT}{dt} \right)_{i,B} &= \left(\frac{T_{j-1} - T_B}{R_{B,j-1}} + \frac{T_B - T_{B+1}}{R_{B+1,B}} \right)_i \\ &+ \left(z_r (1 - V_f) \rho_r \left(H_T \frac{d\alpha}{dt} - H_U \frac{d\chi}{dt} \right) \right)_{i,B} \end{aligned} \quad (\text{B.12})$$

Where subscript B represents the node at the boundary and is equivalent to node j in the laminate. Note that the above can be easily written for the boundary of the laminate and tooling by changing the subscripts appropriately.

The average spatial difference, Δz , was approximated by,

$$\Delta z_{(i,B)} = \frac{2h_{r(i,j)} + h_{fab} + 2z_{bt}}{2} \quad (\text{B.13})$$

Where z_{bt} is the spatial increment size for the bagging/tooling, represented by,

$$z_{bt} = \frac{h_{bt}}{N-1} \quad (B.14)$$

Where h_{bt} is the total thickness of the bagging/tooling, and N is the total number of nodes for the discretised bagging/tooling.

The combined density and specific heat capacity at the boundary node were approximated using a rule of mixtures approach,

$$\rho_{(i,B)} = \frac{\rho_{bt}z_{bt} + \rho_j(h_{r(i,j)} + h_{fab}/2)}{\Delta z_{(i,B)}} \quad (B.15)$$

$$c_{P,B} = \frac{c_{P,bt}\rho_{bt}z_{bt} + c_{P(i,j)}\rho_{(i,j)}(h_{r(i,j)} + h_{fab}/2)}{\rho_{bt}z_{bt} + \rho_{(i,j)}(h_{r(i,j)} + h_{fab}/2)} \quad (B.16)$$

The thermal resistance, $R_{B,j-1}$, was taken to be equivalent to $R_{j,j-1}$ (Equation 5.21). If the thermal conductivity and thickness of each bagging layer is known, a full thermal resistance term can be deduced. For this work, however, $R_{B+1,B}$ was simply written as,

$$R_{B+1,B} = \frac{z_{bt}}{\kappa_{bt}} \quad (B.17)$$

Where κ_{bt} was a lumped thermal conductivity for the whole bagging layer.

C. Numerical Codes

Main MATLAB code for 1D heat transfer and resin flow

```
% Set out global parameters to be read into function files
global A1 A2 A3 Ea1 Ea2 Ea3 R alp_c_sl alp_c_int m n C
% for "cure_kin" function
global Tg0 Tgf gam eta_g0 DOC_gel A C1 C2
% for "chemorheoDiBen" function
global K_perm phi_por P_grad Time_step pre_Flo Resin_store pre_DOI
phi_ply h_ply % for "DarcyFlow3" function

% Set out time step sizes
% max time step for thru-thickness HT of GF is about 1.8 secs
inter_step = 0.5;
intra_step = 0.5;
```

```

% Set oven temperature cycle
Start_temp = 18 + 273;
Ramp_rate = [10 1.5 1.5]/60;
Dwell_temp = [55 120 180] + 273;
Dwell_time = [900 360 180]*60;
Time_seg = [0 0 0 0 0 0];
Time_seg(1) = (Dwell_temp(1)-Start_temp)/Ramp_rate(1);
Time_seg(2) = Dwell_time(1) + Time_seg(1);
Time_seg(3) = (Dwell_temp(2)-Dwell_temp(1))/Ramp_rate(2) +
Time_seg(2);
Time_seg(4) = Dwell_time(2) + Time_seg(3);
Time_seg(5) = (Dwell_temp(3)-Dwell_temp(2))/Ramp_rate(3) +
Time_seg(4);
Time_seg(6) = Dwell_time(3) + Time_seg(5);

% Set the number of plies in the laminate and the number of
iterations to perform
plies = 48;
run_time = 190000;

%Set out material parameter values
P_vac = 85000; % Pressure value (P_b-P_a; units
of Pa)
h_tot = 0.001; % Cured ply thickness (the
thickness of the ply plus any extra resin needed to bring it to a
target FVF)
FVF_tar = 0.45; % Target FVF for the laminate
phi_tar = (1-FVF_tar); % Target porosity
phi_res = 1; % The porosity of neat resin -
for the extra resin layer
FVF_tow = 0.67; % 2004 paper by Amico and
Lekakou shows a method of calculating the tow porosity
experimentally - they give the tow porosity of GF as 0.33 i.e. FVF
of 67%
phi_intra = (1-FVF_tow); % Porosity of the intra-tow
space only
K_inter = 13.675e-10; % (In-plane) Inter-tow
permeability for stitched GF (average value from Kuentzer et al)
rho_fib = 2560;
rho_res_cured = 1220; % (density of epoxy)
kappa_pow = 0.075; % Value taken from Tian et al
(2018)
kappa_fib = 0.417; % Value for tranverse thermal
conductivity of E-glass fibre

% Gebart model for intra-tow permeability based on quadratic fibre
packing
fib_rad = 8e-6; % taken from Johns Manville datasheet for
StarRov 086 fibre (sized for epoxies, 1200/2400 tex for weaving)
K_intra = 16/(9*3.1416*sqrt(2))*((sqrt(3.1416/(4*FVF_tow))-
1)^(5/2))*fib_rad^2;

% Account for presence or absence of stitching
stit_vol = 0.00; % Set
percentage volume of stitching (e.g. set value to 0.05 for 5%
stitching w.r.t. total volume of fabric)

```

```

phi_inter = 0.2146;
phi_ply = phi_inter + phi_intra - phi_inter*phi_intra;           % Tahir,
Hallstrom, Akermo, 2014
h_ply = h_tot*(1-phi_tar)/(1-phi_ply);                           %
thickness of the ply (not including the extra resin to bring the ply
to the target FVF)
FVF_ply = 1 - phi_ply;

if stit_vol > 0                                                  %
Determine whether stitching is present and then account for it
    FVF_ply = FVF_ply/(1-stit_vol);                               %
recalculate FVF_ply, see 14/12/17 and 04/01/18 of notes for these
formula
    phi_ply = 1 - FVF_ply;
    h_ply = h_tot/(1+(phi_tar-phi_ply)/(phi_res-phi_tar));
    h_stit = h_ply*(FVF_ply*stit_vol);                           % where
FVF_ply*stit_vol is the FVF of the stitching
    phi_inter_0 = phi_inter;                                     % save
the original inter-tow porosity for use in calculating
phi_inter_flow
    phi_inter = phi_inter-(FVF_ply*stit_vol);
    phi_inter_flow = phi_inter/phi_inter_0;                       %
accounts for the reduced porosity due to the introduction of
stitching
else
    h_stit = 0;                                                 % needed
for later calculations
    phi_inter_flow = 1;                                         %
Porosity of the inter-tow space only - for the flow calculations
assume it is just empty space between tows and therefore equal to 1
end

% Calculate remaining components of the mesostructure of the model
h_extra = h_tot - h_ply;                                       %
thickness of extra resin layer
h_inter = h_ply*phi_inter;                                     %
representative thickness of the inter-tow region - upon complete
filling of this region, the flow calculations will switch to filling
the intra-tow region
h_intra = h_ply*phi_ply - h_inter;                             %
representative thickness of the intra-tow region
h_resin = h_ply*phi_ply + h_extra;                             % total
thickness of resin needed to reach target FVF
h_fib = h_ply*FVF_ply;                                         %
representative thickness of the fibres (not including any stitching)
- important to calculate this before altering FVF_ply to include
stitching as the representative thickness of the stitching is
calculated seperately
rho_comp = FVF_ply*rho_fib + (1-FVF_ply)*rho_res_cured;        %
ROM for the ply composite density - note it is based FVF_ply not
FVF_tar, so it is not the overall composite density

% Check that FVF of the bulk is not set as being greater than the
FVF of
% the tow, which is impossible and will give a negative volume for
the

```

```

% inter-tow volume
if FVF_tar > FVF_tow
    error('The bulk fibre volume fraction value, "FVF_tar", cannot
be larger that the fibre volume fraction of the tow, "FVF_tow".')
    exit
end

% Set out tool parameters

tool_type = 2; % Set value = 1 for mild steel, or = 2 for aluminium

if tool_type > 2 || tool_type < 1
    error('Please enter a suitable value for tool type')
    exit
end

if tool_type == 1
    % Tool steel - properties taken from
    k_tool = 53.35; % W/m.K
    rho_tool = 7822.8; % kg/m^3
    cp_tool = 485; % J/kg.K
    Tool_inc = 0.01; % m - to pass thermal stability criteria for
the above properties of stainless steel, the spatial increment must
be greater than approx. 0.0036 m
elseif tool_type == 2
    % Aluminium tool - properties taken fom Joshi et al (1999)
    k_tool = 216.3; % W/m.K
    rho_tool = 2692.1; % kg/m^3
    cp_tool = 916.9; % J/kg.K
    Tool_inc = 0.01; % m - to pass thermal stability criteria for
the above properties of aluminium, the spatial increment must be
greater than approx. 0.00935 m
end

Tool_thick = 0.01; % m
Nt_tool = Tool_thick/Tool_inc + 1; % Nt stands for node total
i.e. total number of nodes given to the tool - we add one because
for n spatial increments we will have n+1 nodes

% Set out bagging parameters - values from Joshi et al (1999)
k_bag = 0.069; % W/m.K
rho_bag = 355.6; % kg/m^3
cp_bag = 1256; % J/kg.K
Bag_thick = 0.0015; % m

% Set boundary conditions
BC_top_type = 2; % Set value = 1 for forced convection, or = 2
for specified temperature, or = 3 for natural convection
BC_bot_type = 2; % Set value = 1 for forced convection, or = 2
for specified temperature

if BC_top_type > 3 || BC_top_type < 1
    error('Please enter a suitable value for top boundary condition
type')

```



```

    exit
elseif BC_bot_type > 3 || BC_bot_type < 1
    error('Please enter a suitable value for bottom boundary
condition type')
    exit
end

if BC_top_type == 1
    h_conv_bag = 40;           % W/m^2.K
elseif BC_top_type == 2
    T_amb = 18 + 273;         % specify the temperature on the other
side of the insulating layer i.e. ambient temperature for glass
fibre slab
    Insul_thick = 0.2;        % Set the insulation thickness if any is
used, if none is used you can set it to the thickness of the heating
mat/tool - dimension in m
    % the properties below are given for a glass mineral wool from
http://www.greenspec.co.uk/building-design/insulation-materials-
thermal-properties/
    k_insul = 0.04;           % W/m.K           % for glass mineral wool
= 0.04
    rho_insul = 40;           % kg/m^3         % for glass mineral wool
= 40
    cp_insul = 1030;          % J/kg.K         % for glass mineral wool
= 1030
    Insul_inc = 0.01;         % m - to pass thermal stability criteria
for the above properties of glass mineral wool, the spatial
increment must be greater than approx. 0.0013 m
    Nt_insul = Insul_thick/Insul_inc + 1;      % Nt stands for node
total i.e. total number of nodes given to the insulation - we add
one because for n spatial increments we will have n+1 nodes -
however, note that the first node is the same as the node at the
bagging surface
elseif BC_top_type == 3
    % For insulated enclosure case, set box height in m - bear in
mind initial height of laminate
    Tot_box_height = 0.2;
end

if BC_bot_type == 1
    h_conv_tool = 40;         % W/m^2.K
elseif BC_bot_type == 2
    Mat_thick = 0.001;        % m
    k_mat = 0.53;             % W/m.K         % Value from Kratz et al
(2012)
    rho_mat = 1540;           % kg/m^3         % Value from Kratz et al
(2012)
    cp_mat = 1050;           % J/kg.K         % Value from Kratz et al
(2012)
end

% Preallocate arrays for variables
% NOTE: if you ever need to transfer array data into Excel, you can
transpose
% an array in the Command Window by opening the array variable in
the

```

```

% Workspace window and right clicking on the data and selecting
"Transpose
% variable"
Impreg_dep = zeros(plies+1,run_time);           % Preallocate an array
for the total impregnation depth
tspan = zeros(1,run_time);                     % Preallocate an array for
the timespan of the simulation
close_out = 0.997;                             % Set the limit for
saturation so that the simulation stops when all the resin has
entered the fibre bed
DOI = zeros(plies+1,run_time);
Fill_Time = zeros(plies,1);
Position = zeros(plies,1);
Resin_avail = zeros(plies+1,run_time);
Extra_resin = zeros(plies+1,run_time);
Inter_fill = zeros(plies+1,1);
Flo_bot = zeros(plies+1,run_time);
Flo_top = zeros(plies+1,run_time);
Final_sat = zeros(plies,1);
Thickness = zeros(1,run_time);
Node_temp = zeros(plies+1,run_time);
eta_epoxy = zeros(plies+1,run_time);
T_input = zeros(1,run_time);
kappa_liq = zeros(plies+1,run_time);
kappa_res = zeros(plies+1,run_time);
kappa_comp = zeros(plies+1,run_time);
rho = zeros(plies+1,run_time);
cp = zeros(plies+1,run_time);
cp_res = zeros(plies+1,run_time);
a = zeros(plies+1,run_time);
dadt = zeros(plies+1,run_time);
Tg = zeros(plies+1,run_time);
Count = zeros(1,run_time);
zpos = zeros(plies+1,run_time);
zpos_img = zeros(plies+1,1);
Tool_temp = zeros(Nt_tool,run_time);
Bag_temp1 = zeros(1,run_time);
Bag_temp2 = zeros(1,run_time);
Mat_temp1 = zeros(1,run_time);
Mat_temp2 = zeros(1,run_time);
if BC_top_type == 2
    Insul_temp = zeros(Nt_insul,run_time);      % Preallocate an
array for the insulation temperature
elseif BC_top_type == 3
    Ray_no = zeros(1,run_time);                % Preallocate an array
for the Rayleigh number
    Nu_corr = zeros(1,run_time);               % Preallocate an array
for the Nusselt number correlation
    Enclos_temp = zeros(1,run_time);           % Preallocate an
array for the temperature at the top of the enclosure
end
Temp_diff = zeros(1,run_time);
DOC_diff = zeros(1,run_time);
Inter_fill_top = zeros(plies+1,1);
Inter_fill_bot = zeros(plies+1,1);
Intra_fill_top = zeros(plies+1,1);

```

```

Intra_fill_bot = zeros(plies+1,1);
Vis_check_array = zeros(plies+1,run_time);
Resin_avail_thick = zeros(plies+1,run_time);
Extra_resin_thick = zeros(plies+1,run_time);
DOM = zeros(plies+1,run_time);
DOM_change = zeros(plies+1,run_time);
h_avg = zeros(plies+1,run_time);
Therm_Res = zeros(plies+1,run_time);
D_comp = zeros(plies+1,run_time);
Xt = zeros(plies+1,run_time);
dXtdt = zeros(plies+1,run_time);
dBdt = zeros(plies+1,run_time);
intra_switch = zeros(plies+1,1);

% Define cure kinetics model parameters
m = 1.24;
n = 1.8;
C = 50;
alp_c_sl = 0.006;
alp_c_int = -1.748;
A1 = 4.073e-4;
Ea1 = 12006;
A2 = 10.112e9;
Ea2 = 111792;
A3 = 1.636e13;
Ea3 = 131240;
R = 8.31446;
H_tot = 184*1000; % times 1000 to convert from J/g to J/kg

% Set out parameters for DiBenedetto equation (Tg - DOC
relationship)
Tg0 = 40;
Tgf = 106;
gam = 0.53;

% Set out parameters for chemorheological model
eta_g0 = 2e11;
C1 = 32.25;
C2 = 30;
DOC_gel = 0.56;
A = 1.6;

% Set the initial temperature conditions for the model in Kelvin
Node_temp(:,1) = Start_temp;
Tool_temp(:,1) = Start_temp;
Bag_temp1(1) = Start_temp;
Bag_temp2(1) = Start_temp;
T_input(1) = Start_temp;

if BC_top_type == 2
    Insul_temp(:,1) = Start_temp;
elseif BC_top_type == 3
    Enclos_temp(1) = Start_temp;
end

```

```

if BC_bot_type == 2
    Mat_temp1(1) = Start_temp;
    Mat_temp2(1) = Start_temp;
end

% Generate data for degree of cure using cure kinetics model (for
loop is
% from i=2)
a(:,1) = 0.2;          % Initial value for DOC

% Set initial resin quantity and resin flow - you want it set for
the first
% column because model starts from i = 2
init_DOI = 0.113;
phi_inter_frac = phi_inter/phi_ply;          % the
percentage fraction of inter-tow porosity in respect to the ply
porosity e.g. if phi_inter is 0.2146 and phi_ply is 0.4737, then the
inter-tow porosity accounts for 45.3% of the ply porosity
phi_intra_frac = (phi_ply-phi_inter)/phi_ply;
if init_DOI >= phi_inter_frac
    Impreg_dep(:,1) = (h_inter + h_stit) + (h_ply*phi_ply*init_DOI -
h_inter)/phi_intra;
else
    Impreg_dep(:,1) = phi_ply*h_ply*init_DOI;
end
Flo_bot(:,1) = Impreg_dep(:,1)/2;
% Assume the initial DOI is split evenly between top and bottom of
the ply
Flo_top(:,1) = Impreg_dep(:,1)/2;
Resin_avail(:,1) = h_resin - init_DOI*h_ply*phi_ply;
% Subtract the amount that has already flowed into the fabric from
the finite resin layers
Resin_avail(1,1) = 0;
% reset to zero because Extra_resin accounts for resin on the bottom
layer
Extra_resin(2,1) = (h_resin/2) - (init_DOI*h_ply*phi_ply)/2;
% assume only half the resin is required on bottom as there is no
fabric layer below to fill, otherwise there will be a resin rich
layer on the bottom - note, this is different to the extra resin in
each layer to reach a specific FVF
Resin_avail(plies+1,1) = Resin_avail(plies+1,1) +
(init_DOI*h_ply*phi_ply)/2;          % similarly, the top ply needs an
extra half a resin layer to achieve the target FVF
DOI(:,1) = init_DOI;
% DOI - degree of impregnation
DOI(1,1) = 0;
% reset to zero because it's just resin on the bottom layer

% Initialise powder melt model
k_m = 1.83;
d = 4.65;
T_melt = 313.483;
H_endo = 7.1*1000;          % Total enthalpy of the melting endotherm -
> to be included in the heat transfer equation (times 1000 to put it
in J/kg)
DOM(:,1) = 0.001;

```

```

% Initialise sintering model
DOS_inf = 0;
XA = 3e-5;
XC1 = 11.5;
XC2 = 24.5;
Xn = 0.5;
Xpow = 0.503; % Powder void fraction of raw powder
Xint = 0.503; % Initial powder void fraction
Xt(:,1) = Xint;
Resin_avail_thick(:,1) = Resin_avail(:,1)./(1-Xt(:,1));
Extra_resin_thick(:,1) = Extra_resin(:,1)./(1-Xt(:,1));
Thickness(1) = sum(Resin_avail_thick(:,1), 'omitnan') + plies*h_ply +
sum(Extra_resin_thick(:,1), 'omitnan');
rho_res(:,1) = rho_res_cured*(1-Xt(:,1));

% time_step_change tells the code when it is OK to increase the time
step without adversely affecting the resolution of the computation,
it is initially set to zero. Inter_fill is used to calculate the
pressure gradient if the intra-tow flow has begun
if init_DOI >= phi_inter_frac
    time_step_change = 1;
    Inter_fill(:) = h_inter + h_stit;
    Inter_fill_top(:) = (h_inter + h_stit)/2;
    Inter_fill_bot(:) = (h_inter + h_stit)/2;
    intra_switch(:) = 1;
else
    time_step_change = 0;
end

% Initialise count for image print - part of creating a simulation
video
Counter = 0;
ImgCount = 0;

% Create new folders for the video data based on the time and date
DateString = datestr(now, 'mmmm dd, yyyy HH-MM'); % creates the
folder name
mkdir('ImageFiles\Simulation Data', DateString) % Creates the
folder

%%%%%%%%%%%%%%%%%%%%%%%%%%%%%%%%%%%%%%%%%%%%%%%%%%%%%%%%%%%%%%%%%%%%%%%%
%%%%%%%%

for i = 1:run_time-1 % First loop progresses time

if time_step_change == 1
    Time_step = intra_step;
else
    Time_step = inter_step;
end

% Initialise tspan
if i == 1
    tspan(1) = Time_step;

```

```

end

tspan(i+1) = tspan(i) + Time_step;

% Set input temperatures for the process cycle
if tspan(i) < Time_seg(1)
    T_input(i+1) = T_input(i) + Ramp_rate(1)*Time_step;
elseif tspan(i) < Time_seg(2)
    T_input(i+1) = Dwell_temp(1);
elseif tspan(i) < Time_seg(3)
    T_input(i+1) = T_input(i) + Ramp_rate(2)*Time_step;
elseif tspan(i) < Time_seg(4)
    T_input(i+1) = Dwell_temp(2);
elseif tspan(i) < Time_seg(5)
    T_input(i+1) = T_input(i) + Ramp_rate(3)*Time_step;
else
    T_input(i+1) = Dwell_temp(3);
end

%%%%%%%%%%%%%%%%%%%%%%%%%%%%%%%%%%%%%%%%%%%%%%%%%%%%%%%%%%%%%%%%%%%%%%%%
%%%%%%%%%%%%%%%%%%%%%%%%%%%%%%%%%%%%%%%%%%%%%%%%%%%%%%%%%%%%%%%%%%%%%%%%
%%%%%%%%%%%%%%%%%%%%%%%%%%%%%%%%%%%%%%%%%%%%%%%%%%%%%%%%%%%%%%%%%%%%%%%%

    for j = 1:plies+1          % Second loop to move between plies -
for n plies there will be n+1 nodes, hence plies+1; however node 1
is only required for heat transfer and does not represent a volume
element for flow, so the loop begins from 2

% The resin flow section of this nested for-loop is split into a
series of conditional statements to determine whether the flow is
inter-tow, intra-tow, or in transition between the two. Then it
solves the respective set of equations. Otherwise, if no resin is
left, it fills the remaining space in the array with zeros until the
loop has finished

        % Code for flow

        % Determine whether inter-tow or intra-tow flow

        if (DOI(j,i) >= phi_inter_frac) && (intra_switch(j) == 0)
            Inter_fill(j) = Impreg_dep(j,i); %
Determine when the inter-tow region has been filled and store the
impregnation depth data so that it can be added to the flow front
position of the intra-tow flow
            Inter_fill_top(j) = Flo_top(j,i); %
Record how much Flo_top contributed to filling the inter-tow region
            Inter_fill_bot(j) = Flo_bot(j,i);
            intra_switch(j) = 1;
        end

        if DOI(j,i) < phi_inter_frac %
Check if the inter_tow space has yet to be filled

```

```

        P_grad_top = P_vac/Flo_top(j,i); %
Determine the pressure gradient from the previous time step so that
it may be used to approximate flow for the current step
        P_grad_bot = P_vac/Flo_bot(j,i);
        K_perm = K_inter;
        phi_por = phi_inter_flow;

    elseif (DOI(j,i) >= phi_inter_frac) || time_step_change == 1
        K_perm = K_intra;
        phi_por = phi_intra;
        Intra_fill_top(j) = 0.5*Inter_fill(j)+Flo_top(j,i)-
Inter_fill_top(j); % Accounting for when the top and bot flow
fronts meet and the pressure gradient becomes symmetrical
        Intra_fill_bot(j) = 0.5*Inter_fill(j)+Flo_bot(j,i)-
Inter_fill_bot(j);
        P_grad_top = (K_inter*P_vac)/((Intra_fill_top(j) -
0.499*Inter_fill(j))*K_inter + 0.5*Inter_fill(j)*K_intra); % In
this case the pressure gradient is the pressure at the interface
divided by (1-L1), note that L1 is multiplied by 0.499 because only
half the inter-fill value is used and the extra 0.001 stops it from
becoming a singularity
        P_grad_bot = (K_inter*P_vac)/((Intra_fill_bot(j) -
0.499*Inter_fill(j))*K_inter + 0.5*Inter_fill(j)*K_intra); % this
could be Flo_bot(j,i)-0.499*Inter_fill_bot(j)
    end

    % Solve cure kinetics and chemorheological models for time
    % and temperature

    if a(j,i) >= 0.559 && a(j,i) < 0.999 % accounting for
another singularity in the chemorheology model - for a(j,i-1)
approaching DOC_gel (i.e. 0.56) the viscosity will tend to infinity
        dadt(j,i) = cure_kin(a(j,i), Node_temp(j,i));
        a(j,i+1) = (dadt(j,i).*Time_step) + a(j,i);
        [Tg(j,i)] = chemorheoDiBenTg(a(j,i));
        eta_epoxy(j,i) = 10e10;
    elseif a(j,i) >= 0.999
        eta_epoxy(j,i) = 10e10;
        dadt(j,i) = 0;
        a(j,i+1) = 0.999;
        Tg(j,i) = Tg(j,i-1);
    else
        dadt(j,i) = cure_kin(a(j,i), Node_temp(j,i));
        a(j,i+1) = (dadt(j,i).*Time_step) + a(j,i);
        [Tg(j,i),eta_epoxy(j,i)] = chemorheoDiBen(a(j,i),
Node_temp(j,i));
    end

    % Solve resin flow

    if j > 1

```

```

        if j == 2
            if Extra_resin(j,i) == 0 %
Check if resin supply is finished
                Flo_bot(j,i+1) = Flo_bot(j,i);
                Extra_resin(j,i+1) = 0;
            elseif DOI(j,i) >= close_out %
Check if the fibre layer has been completely filled, if so, stop
allowing resin to flow in
                DOI(j,i+1) = DOI(j,i);
                Flo_bot(j,i+1) = Flo_bot(j,i);
                Extra_resin(j,i+1) = Extra_resin(j,i);
            else
                Resin_store = Extra_resin(j,i); %
Store the current resin supply info in the case that it is less than
what is required for the current flow step
                pre_DOI = DOI(j,i);
                pre_Flo = Flo_bot(j,i);
                P_grad = P_grad_bot;
                [DOI(j,i),Extra_resin(j,i+1),Flo_bot(j,i+1)] =
DarcyFlow3(eta_epoxy(j-1,i));
            end
        else
            if Resin_avail(j-1,i) == 0 %
Check if resin supply is finished
                Flo_bot(j,i+1) = Flo_bot(j,i);
                Resin_avail(j-1,i+1) = 0; % As
the flo_bot(j,i) is calculated after flo_top(j,i), Resin_avail(j-
1,i+1) must be set at this point
            elseif DOI(j,i) >= close_out %
Check if the fibre layer has been completely filled, if so, stop
allowing resin to flow in
                DOI(j,i+1) = DOI(j,i);
                Flo_bot(j,i+1) = Flo_bot(j,i);
                Resin_avail(j-1,i+1) = Resin_avail(j-1,i);
            else
                Resin_store = Resin_avail(j-1,i);
% Store the current resin supply info in the case that it is less
than what is required for the current flow step
                pre_DOI = DOI(j,i);
                pre_Flo = Flo_bot(j,i);
                P_grad = P_grad_bot;
                [DOI(j,i),Resin_avail(j-1,i+1),Flo_bot(j,i+1)] =
DarcyFlow3(eta_epoxy(j-1,i));
            end
        end

        if j == plies+1

            if Resin_avail(j,i) == 0 %
NOTE: we do not need to update DOI(j,i) in the first two cases of
this if statement because in all eventualities it will have been
updated for this time and spatial increment already by the previous
if statements and we do not need to repeat them by saying DOI(j,i) =
DOI(j,i)

                Flo_top(j,i+1) = Flo_top(j,i);
                DOI(j,i+1) = DOI(j,i);

```



```

        Resin_avail(j,i+1) = 0;
        elseif DOI(j,i) >= close_out
% Check if the fibre layer has been completely filled by the
previous if statements, if so, stop allowing resin to flow in
        Flo_top(j,i+1) = Flo_top(j,i);
        DOI(j,i+1) = DOI(j,i);
        Resin_avail(j,i+1) = Resin_avail(j,i);
    else
        Resin_store = Resin_avail(j,i);
        pre_DOI = DOI(j,i);
        pre_Flo = Flo_top(j,i);
        P_grad = P_grad_top;
        [DOI(j,i+1),Resin_avail(j,i+1),Flo_top(j,i+1)] =
DarcyFlow3(eta_epoxy(j,i));
    end

    else
        % w.r.t DOI, if there is resin available and the ply
is not full, then update DOI, if not then the DOI from the previous
if statement carries over
        if Resin_avail(j,i) == 0
            Flo_top(j,i+1) = Flo_top(j,i);
            DOI(j,i+1) = DOI(j,i);
        elseif DOI(j,i) >= close_out
% Check if the fibre layer has been completely filled by the
previous if statements, if so, stop allowing resin to flow in
            Flo_top(j,i+1) = Flo_top(j,i);
            DOI(j,i+1) = DOI(j,i);
        else
            Resin_store = Resin_avail(j,i);
            pre_DOI = DOI(j,i);
            pre_Flo = Flo_top(j,i);
            P_grad = P_grad_top;
            [DOI(j,i+1),Resin_avail(j,i),Flo_top(j,i+1)] =
DarcyFlow3(eta_epoxy(j,i));
        end

    end

    Impreg_dep(j,i+1) = Flo_bot(j,i+1) + Flo_top(j,i+1);
% Calculate for flow front progression for each iteration

% Determine the spatial position of the top of each ply
in the out-of-plane direction - this is to do with
creating a 2D contour plot for the simulation video

% Determine the degree of melt (DOM) of the powder

if DOM(j,i) >= 1
    DOM_change(j,i) = 0;
    DOM(j,i+1) = 1;
else
    DOM_change(j,i) = k_m.*(exp(-k_m.*(Node_temp(j,i)-
T_melt))).*(1+(d-1).*exp(-k_m.*(Node_temp(j,i)-T_melt))).^(d./(1-

```

```

d)); % Using the a cumulative distribution model (Greco and
Maffezzoli 2003)
    if i == 1
        DOM(j,i+1) = DOM(j,i);
    else
        DOM(j,i+1) = DOM(j,i) +
DOM_change(j,i)*(Node_temp(j,i)-Node_temp(j,i-1));
    end
end

    dBdt(j,i) = (DOM(j,i+1)-DOM(j,i))/Time_step; % the
rate of change for the degree of melting w.r.t. time

    if Xt(j,i) <= 0
        dXtdt(j,i) = 0;
        Xt(j,i+1) = 0;
    else
        X_check = Node_temp(j,i)-T_melt; % Must
account for the singularity in the sintering equation as the bottom
term can go to 0 where Node_temp(j,i) - T_melt = XC2 (similar to the
chemorheological model)
        if X_check < -22
            dXtdt(j,i) = 0;
        else
            dXtdt(j,i) = -XA.*exp(((XC1.*(Node_temp(j,i)-
T_melt)))/(XC2+Node_temp(j,i)-T_melt)).*(Xt(j,i)-DOS_inf).^Xn;
        end
        Xt(j,i+1) = Xt(j,i) + dXtdt(j,i)*Time_step;
    end

    % Determine the resin layer thickness based on the DOM
    if j == 2
        Resin_avail_thick(j,i) = Resin_avail(j,i)/(1-
Xt(j,i));
        Extra_resin_thick(j,i) = Extra_resin(j,i)/(1-
Xt(j,i));
    else
        Resin_avail_thick(j,i) = Resin_avail(j,i)/(1-
Xt(j,i));
    end

    if j == 2 % in this instance, for the bottom-most ply
we are combining the resin layers above and below, rather than
treating the extra resin layer below as a separate layer
        zpos(j,i) = Extra_resin_thick(j,i) +
Resin_avail_thick(j,i) + h_ply;
    else
        zpos(j,i) = Resin_avail_thick(j,i) + h_ply + zpos(j-
1,i);
    end
end
end

    % Determine the total laminate thickness for each time step

```

```

    Thickness(i) = sum(Resin_avail_thick(:,i), 'omitnan') +
plies*h_ply + sum(Extra_resin_thick(:,i), 'omitnan'); %the sum of
all the resin available (omitting any NaN values) + all the fibre
layers

%%%%%%%%%%%%%%%%%%%%%%%%%%%%%%%%%%%%%%%%%%%%%%%%%%%%%%%%%%%%%%%%%%%%%%%%
%

    if BC_bot_type == 1
        % Determine the heat transfer due to convection on the tool
        % underside

        Tool_Therm_Res = Tool_inc/k_tool;

        for jj = 1:Nt_tool-1

            if jj == 1
                Tool_temp(1,i+1) =
(2*Time_step/(rho_tool*cp_tool*Tool_inc)) *
(h_conv_tool*(T_input(i)-Tool_temp(1,i)) + k_tool*(Tool_temp(2,i)-
Tool_temp(1,i))/Tool_inc) + Tool_temp(1,i);
            else
                Tool_temp(jj,i+1) =
((Time_step*k_tool)/(rho_tool*cp_tool*Tool_inc^2))
*(Tool_temp(jj+1,i)-2*Tool_temp(jj,i)+Tool_temp(jj-1,i)) +
Tool_temp(jj,i);
            end

        end

    elseif BC_bot_type == 2
        % Determine the heat transfer due to conduction from
        specified temperature BC

        Mat_Therm_Res = Mat_thick/k_mat;
        Tool_Therm_Res = Tool_inc/k_tool;
        MTBound_avg = (Mat_thick+Tool_inc)/2;

        Mat_temp1(i) = T_input(i);

        for jj = 1:Nt_tool-1
            if jj == 1
                cp_tool_mat_avg = (cp_tool*rho_tool*Tool_inc +
cp_mat*rho_mat*Mat_thick)/(rho_mat*Mat_thick+rho_tool*Tool_inc);
                % a weighted average
                rho_tool_mat_avg = (rho_tool*Tool_inc +
rho_mat*Mat_thick)/(Mat_thick+Tool_inc); % a weighted average

                Mat_temp2(i+1) =
(Time_step/(rho_tool_mat_avg*cp_tool_mat_avg)) * ((Mat_temp1(i)-
Mat_temp2(i))/(MTBound_avg*Mat_Therm_Res) + (Tool_temp(jj+1,i)-
Mat_temp2(i))/(MTBound_avg*Tool_Therm_Res)) + Mat_temp2(i);
            end
        end
    end
end

```

```

        Tool_temp(jj,i+1) = Mat_temp2(i+1);
    else
        Tool_temp(jj,i+1) =
        ((Time_step*k_tool)/(rho_tool*cp_tool*Tool_inc^2)) * (Tool_temp(jj-
1,i)-2*Tool_temp(jj,i)+Tool_temp(jj+1,i)) + Tool_temp(jj,i);
    end
    % NOTE: calculation for Tool_temp(Nt_tool,i+1) is done
at a later stage
    end
end

if BC_top_type == 1

    % Determine the heat transfer due to convection at surface
of bagging

    Bag_Therm_Res = Bag_thick/k_bag;
    Bag_temp2(i+1) = (2*Time_step/(rho_bag*cp_bag*Bag_thick)) *
(h_conv_bag*(T_input(i)-Bag_temp2(i)) + k_bag*(Bag_temp1(i)-
Bag_temp2(i))/Bag_thick) + Bag_temp2(i);

    elseif BC_top_type == 2
        % Determine the heat transfer due to conduction from
specified temperature BC

        Bag_Therm_Res = Bag_thick/k_bag;
        Insul_Therm_Res = Insul_inc/k_insul;
        BIBound_avg = (Bag_thick+Insul_inc)/2;

        for jj = 1:Nt_insul
            if jj == Nt_insul
                Insul_temp(jj,i+1) = T_amb;
            elseif jj == 1
                cp_bag_insul_avg =
                ((cp_insul*rho_insul*Insul_inc)+(cp_bag*rho_bag*Bag_thick))/(rho_bag
*Bag_thick+Insul_inc*rho_insul); % a weighted average
                rho_bag_insul_avg =
                ((rho_insul*Insul_inc)+(rho_bag*Bag_thick))/(Bag_thick+Insul_inc);
                % a weighted average

                Bag_temp2(i+1) =
                (Time_step/(rho_bag_insul_avg*cp_bag_insul_avg)) * ((Bag_temp1(i)-
Bag_temp2(i))/(BIBound_avg*Bag_Therm_Res) + (Insul_temp(jj+1,i)-
Bag_temp2(i))/(BIBound_avg*Insul_Therm_Res)) + Bag_temp2(i);
                Insul_temp(jj,i+1) = Bag_temp2(i+1);
            else
                Insul_temp(jj,i+1) =
                ((Time_step*k_insul)/(rho_insul*cp_insul*Insul_inc^2)) *
                (Insul_temp(jj-1,i)-2*Insul_temp(jj,i)+Insul_temp(jj+1,i)) +
                Insul_temp(jj,i);
            end
        end
    elseif BC_top_type == 3
        % Determine the heat transfer due to natural convection at
surface of bagging

```

```

% Determine Rayleigh number for air in the enclosure
g = 9.81; % acceleration due to gravity
T_air_avg = (Bag_temp2(i)+Enclos_temp(i))/2;
beta = 0.99459*T_air_avg^-0.999; %
coefficient of volumetric expansion of air wrt temperature based on
power law fit to online data (engineeringtoolbox.com)
Lc = Tot_box_height - Thickness(i); % gap
between top laminate surface and the top of the interior of the
enclosure
kin_vis = 8e-10*T_air_avg^1.7431; %
kinematic viscosity of air wrt temperature based on power law fit to
online data (engineeringtoolbox.com)
Pr_no = -0.0002*T_air_avg + 0.7615; %
Prandtl No. of air wrt temperature based on linear fit to online
data (engineeringtoolbox.com)
k_air = 0.0014*T_air_avg +0.0242; %
Thermal conductivity of air wrt temperature based on linear fit to
online data (engineeringtoolbox.com)
rho_air = 363.05*T_air_avg^-1.005; %
Density of air wrt temperature based on power law fit to online data
(engineeringtoolbox.com)
cp_air = 1010; %
Specific heat of air (engineeringtoolbox.com)

Ray_no(i) = Pr_no*(g*beta*(Bag_temp2(i)-
Enclos_temp(i))*Lc^3)/kin_vis^2; % Calculation for Rayleigh
no.

% Determine the Nusselt number for the given Rayleigh number
using
% Hollands correlation

Nu_corr1 = 1-(1708/Ray_no(i));
Nu_corr2 = ((Ray_no(i)^(1/3))/18)-1;
if Nu_corr2 <= 0 || isnan(Nu_corr2) || Ray_no(i) < 0
    if Nu_corr1 <= 0 || isnan(Nu_corr1) || Ray_no(i) < 0
        Nu_corr(i) = 1;
    else
        Nu_corr(i) = 1 + 1.44*Nu_corr1;
    end
elseif Nu_corr1 <= 0 || isnan(Nu_corr1)
    Nu_corr(i) = 1 + Nu_corr2;
else
    Nu_corr(i) = 1 + 1.44*Nu_corr1 + Nu_corr2;
end

% Compute temperature change

Bag_temp2(i+1) = Bag_temp2(i) +
(2*Time_step/(rho_bag*cp_bag*Bag_thick))*(k_bag*(Bag_temp1(i)-
Bag_temp2(i))/Bag_thick - k_air*Nu_corr(i)*(Bag_temp2(i)-
Enclos_temp(i))/Lc);

```

```

        % Determine the temperature at the top of the enclosure
based on the it
        % being an insulated boundary condition

        Enclos_temp(i+1) = Enclos_temp(i) +
(Time_step/(rho_air*cp_air))*k_air*Nu_corr(i)*(Bag_temp2(i)-
Enclos_temp(i))/Lc;
        end

%%%%%%%%%%%%%%%%%%%%%%%%%%%%%%%%%%%%%%%%%%%%%%%%%%%%%%%%%%%%%%%%%%%%%%%%
%

        % Need to determine the thermal conductivity values for all the
nodes
        % before the finite difference approximation for HT can be
computed
        for j = 2:plies+1

            kappa_liq(j,i) = 0.04184*(3.85+(0.035*(Node_temp(j,i)-273)-
0.41)*a(j,i)); % See appendix of Shin and Hahn (2004) in Mendeley,
they cite Mijovic and Wang (1988)
            kappa_res(j,i) = kappa_pow*(Xt(j,i)/Xpow) +
kappa_liq(j,i)*(1-(Xt(j,i)/Xpow));
            kappa_dry = 0.2; % Based on thermal conductivity
data from Cormac Lee's thesis (2004)
            % Clayton model
            kappa_comp(j,i) = (kappa_res(j,i)/4)*(sqrt(((1-
FVF_ply)^2)*(((kappa_fib/kappa_res(j,i))-
1)^2)+(4*kappa_fib/kappa_res(j,i)))-(1-
FVF_ply)*((kappa_fib/kappa_res(j,i))-1))^2;

            rho_res(j,i) = rho_res_cured*(1-Xt(j,i));
            rho(j,i) = rho_comp*(h_tot/(h_ply+Resin_avail_thick(j,i)));
            cp_res(j,i) = 4184*(0.468+5.975e-4*(Node_temp(j,i)-273)-
0.141*a(j,i)); % relationship from Shin and Hahn 2004 -
"Compaction of thick composites..." - Note: the relationship has
been multiplied by 100 to put it in J/kg.K
            cp_fib = 810;
            % Shi (2016)
            cp(j,i) =
(phi_tar*rho_res_cured*cp_res(j,i)+FVF_tar*rho_fib*cp_fib)/(phi_tar*
rho_res_cured+FVF_tar*rho_fib); % ROM - see thesis -
rho_res_cured is used because the mass does not change, just the
volumes. Therefore, if you use rho_res(j,i), then you must also
change the FVF accordingly as the powder will take up a larger
volume. The results should be the same, however.
            RMF =
(phi_tar*rho_res_cured)/(phi_tar*rho_res_cured+FVF_tar*rho_fib);
            % Resin mass fraction
        end

        % Begin loop for heat transfer
        for j = 2:plies+1

```

```

if j == 2

    h_avg(j,i) = (Resin_avail_thick(j,i) + 2*h_ply +
Extra_resin_thick(j,i) + Resin_avail_thick(j+1,i)/2)/2;
    % Note: Both Therm_Res(j,i) and Therm_Res(j+1,i) are
both calculated here, therefore Therm_Res(j,i) doesn't need to be
re-calculated for the remaining nodes
    Therm_Res(j,i) =
Extra_resin_thick(j,i)/(2*kappa_res(j,i)) +
Impreg_dep(j,i)/kappa_comp(j,i) + (h_ply-Impreg_dep(j,i))/kappa_dry
+ Resin_avail_thick(j,i)/(2*kappa_res(j,i)); % kappa_res(j,i)
used for the extra resin layer as (j-1,i) doesn't exist
    Therm_Res(j+1,i) =
Resin_avail_thick(j,i)/(2*kappa_res(j,i)) +
Impreg_dep(j+1,i)/kappa_comp(j+1,i) + (h_ply-
Impreg_dep(j+1,i))/kappa_dry +
Resin_avail_thick(j+1,i)/(2*kappa_res(j+1,i));

    % Calculations for the tool surface
    cp_bot_avg = (cp_tool*Tool_inc +
cp(j,i)*h_avg(j,i))/(h_avg(j,i)+Tool_inc); % a weighted average
    rho_bot_avg = (rho_tool*Tool_inc +
rho(j,i)*h_avg(j,i))/(h_avg(j,i)+Tool_inc); % a weighted average
    h_bot_avg = (h_avg(j,i)+Tool_inc)/2;
    Tool_temp(Nt_tool,i+1) =
(Time_step/(rho_bot_avg*cp_bot_avg)) * ((Tool_temp(Nt_tool-1,i)-
Tool_temp(Nt_tool,i))/(h_bot_avg*Tool_Therm_Res) + (Node_temp(j,i)-
Tool_temp(Nt_tool,i))/(h_bot_avg*Therm_Res(j,i)) + rho_res(j,i)*(1-
FVF_tar)*(H_tot*dadt(j,i) - H_endo*dBdt(j,i))) +
Tool_temp(Nt_tool,i);
    Node_temp(j-1,i+1) = Tool_temp(Nt_tool,i+1);

    % Calculation for first ply
    Node_temp(j,i+1) = (Time_step/(rho(j,i)*cp(j,i))) *
((Tool_temp(Nt_tool,i)-Node_temp(j,i))/(h_avg(j,i)*Therm_Res(j,i)) +
(Node_temp(j+1,i)-Node_temp(j,i))/(h_avg(j,i)*Therm_Res(j+1,i)) +
rho_res(j,i)*(1-FVF_tar)*(H_tot*dadt(j,i) - H_endo*dBdt(j,i))) +
Node_temp(j,i);

elseif j > 2 && j < plies+1

    h_avg(j,i) = (Resin_avail_thick(j,i) + 2*h_ply +
Resin_avail_thick(j-1,i)/2 + Resin_avail_thick(j+1,i)/2)/2;
    Therm_Res(j+1,i) =
Resin_avail_thick(j,i)/(2*kappa_res(j,i)) +
Impreg_dep(j+1,i)/kappa_comp(j+1,i) + (h_ply-
Impreg_dep(j+1,i))/kappa_dry +
Resin_avail_thick(j+1,i)/(2*kappa_res(j+1,i));
    Node_temp(j,i+1) =
((Time_step/(h_avg(j,i)*rho(j,i)*cp(j,i))) * ((Node_temp(j-1,i)-
Node_temp(j,i))/Therm_Res(j,i) + (Node_temp(j+1,i)-
Node_temp(j,i))/Therm_Res(j+1,i))) +
((Time_step*RMF/cp(j,i))*(H_tot*dadt(j,i) - H_endo*dBdt(j,i))) +
Node_temp(j,i);

```

```

elseif j == plies+1

    h_avg(j,i) = Resin_avail_thick(j,i) + h_ply +
Resin_avail_thick(j-1,i)/2; % in this instance it is not an
average, merely the distance between the top surface node and the
previous node in the laminate
    cp_top_avg = (cp(j,i)*h_avg(j,i) +
cp_bag*Bag_thick)/(h_avg(j,i)+Bag_thick); % a weighted average
    rho_top_avg = (rho_bag*Bag_thick +
rho(j,i)*h_avg(j,i))/(h_avg(j,i)+Bag_thick); % a weighted average

    % No need to calculate Therm_Res(j,i) or Bag_Therm_Res
as they have already been done
    Node_temp(j,i+1) = (Time_step/(rho_top_avg*cp_top_avg))
* ((Node_temp(j-1,i)-Node_temp(j,i))/(h_avg(j,i)*Therm_Res(j,i)) +
(Bag_temp2(i)-Node_temp(j,i))/(Bag_thick*Bag_Therm_Res) +
rho_res(j,i)*(1-FVF_tar)*(H_tot*dadt(j,i) - H_endo*dBdt(j,i))) +
Node_temp(j,i);

    % the last node for Bag_temp is the same first node for
Node_temp, so set them to be equal
    Bag_temp1(i+1) = Node_temp(j,i+1);
end
end

%%%%%%%%%%%%%%%%%%%%%%%%%%%%%%%%%%%%%%%%%%%%%%%%%%%%%%%%%%%%%%%%%%%%%%%%
%

% Determine whether all plies have transitioned to intra-tow
flow, then
% change the time step
if nonzeros(DOI(:,i)) >= phi_inter_frac % Has to be i otherwise
bot_fill and top_fill don't get a value for the final ply
    time_step_change = 1;
end

% Determine max temperature difference and max DOC difference in
the laminate at each time step
Temp_diff(i) = max(Node_temp(:,i)) - min(Node_temp(:,i));
DOC_diff(i) = max(a(:,i)) - min(a(:,i));

% Set out a finite width for the laminate (just for illustrative
% purposes, in the actual model it is assumed that the width and
depth
% of the laminate is much greater than the thickness such that
there is
% no in-plane temperature gradient)
xpos = 0:1:1;

% Create a counter system that creates JPEG graphs of the data
being

```



```

% calculated wrt time and send them to a specific folder
time_limit = 600; % set the time intervals for creating the
graphs
if i == 1
    Count(i) = intra_step;
else
    Count(i) = Count(i-1) + intra_step;
end
if Count(i) >= time_limit
    Counter = 1;
end
if Counter == 1
    ImgCount = 1 + ImgCount; % Count the graphs so that they may
be given individual names
    tspan_hr_exact = tspan(i)/3600; % t_span_exact gives a
single time value for when the image is being taken, this is used if
you want to put the time into the title of the graph
    tspan_hr = tspan/3600; % this gives you an array of time
data, this is used for plotting the oven temp wrt time
    T_input_C = T_input(1:i) - 273; % Oven temperature in
Celsius

% Subplot for the Oven temperature
subplot(2,2,1);
plot(tspan_hr(1:i), T_input_C, '-r');
title('Input Temperature')
ylabel('Temperature (°C)')
xlabel('Time (hr)')
ylim([0,200]);
xlim([0,25]);

% Subplot for the cure through the thickness
subplot(2,2,2);
[X,Y] = meshgrid(xpos,zpos(:,i));
Z = zeros(length(zpos(:,i)),length(xpos));
Z(:,1) = a(:,i);
Z(:,2) = a(:,i);
contourf(X,Y,Z)
colormap jet
cb = colorbar('eastoutside');
cb.Label.String = 'Degree of cure';
caxis([0,1])
%title([num2str(tspan_hr_exact), ' hr(s) into process
cycle'])
title('Degree of cure Through Thickness')
ylabel('Thickness (m)')
ylim([0,0.1]);
xlim([0,1]);

% Subplot for the temperature through the thickness
subplot(2,2,[3,4]);
[X,Y] = meshgrid(xpos,zpos(:,i));
Z = zeros(length(zpos(:,i)),length(xpos));
Z(:,1) = Node_temp(:,i) - 273;
Z(:,2) = Node_temp(:,i) - 273;
contourf(X,Y,Z)

```



```

% Create an object to write videos to
Sim_Video = VideoWriter(fullfile('ImageFiles\Simulation
Data',DateString,'Sim_Video.avi'));
Sim_Video.FrameRate = 3; % set the frame rate i.e. the no. of images
per sec
open(Sim_Video)

% Write your images(graphs) into the video object you just created -
the
% for loop is based on the number of images
for ii = 1:length(Sim_images)
    img = imread(fullfile('ImageFiles\Simulation
Data',DateString,Sim_images{ii}));
    writeVideo(Sim_Video,img)
end

% Plot a graph with the impregnation depth curves for equally spaced
plies
% within the laminate
figure;
hLine1 = plot(tspan_hr(:), DOI(2,:), '-k');
hold all
hLine2 = plot(tspan_hr(:), DOI(13,:), '-r');
hLine3 = plot(tspan_hr(:), DOI(25,:), '-g');
hLine4 = plot(tspan_hr(:), DOI(37,:), '-b');
hLine5 = plot(tspan_hr(:), DOI(49,:), '--k');
hold off
hleg1 = legend([hLine1,hLine2,hLine3,hLine4,hLine5], 'Ply 1', 'Ply
12', 'Ply 24', 'Ply 36', 'Ply 48');
set(hleg1, 'Location', 'eastoutside', 'Orientation', 'vertical')
xlabel ('Time (hr)')
ylabel ('Degree-of-impregnation (l/h)')
ylim([0,1]);
xlim([0,25]);

% Plot the total thickness change wrt time
figure;
plot(tspan_hr(:), Thickness, 'color', 'r', 'linewidth', 2);
xlabel('Time (hr)')
ylabel('Laminate thickness (m)')
ylim([0.04,0.10]);
xlim([0,25]);

% Plot a graph with the temperature curves for equally spaced plies
% within the laminate
figure;
hLine1 = plot(tspan_hr(:), T_input_cel(:), '-m');
hold all
hLine2 = plot(tspan_hr(:), Temp_Cel(2,:), '-r');
hLine3 = plot(tspan_hr(:), Temp_Cel(13,:), '-g');
hLine4 = plot(tspan_hr(:), Temp_Cel(25,:), '-b');
hLine5 = plot(tspan_hr(:), Temp_Cel(37,:), '-k');
hLine6 = plot(tspan_hr(:), Temp_Cel(49,:), '--r');
hold off

```

```

hleg1 = legend([hLine1,hLine2,hLine3,hLine4,hLine5,hLine6], 'Input
Temperature', 'Ply 1', 'Ply 12', 'Ply 24', 'Ply 36', 'Ply 48'); %, 'Insul
40', 'Insul 100', 'Insul 190');
set(hleg1, 'Location', 'eastoutside', 'Orientation', 'vertical')
xlabel ('Time (hr)')
ylabel ('Temperature in Ply (°C)')
ylim([0,200]);
xlim([0,25]);

% Plot a graph of degree of cure through the thickness
figure;
hLine2 = plot(tspan_hr(:), a(2,:), '-k');
hold all
hLine3 = plot(tspan_hr(:), a(13,:), '-r');
hLine4 = plot(tspan_hr(:), a(25,:), '-g');
hLine5 = plot(tspan_hr(:), a(37,:), '-b');
hLine6 = plot(tspan_hr(:), a(49,:), '--k');
hold off
hleg1 = legend([hLine2,hLine3,hLine4,hLine5,hLine6], 'Ply 1', 'Ply
13', 'Ply 24', 'Ply 36', 'Ply 48');
set(hleg1, 'Location', 'eastoutside', 'Orientation', 'vertical')
xlabel ('Time (hr)')
ylabel ('Degree of cure')
ylim([0,1]);
xlim([0,25]);

% Plot a graph of degree of cure through the thickness
figure;
semilogy(tspan_hr(:), eta_epoxy(2,:), '-k');
hold all
semilogy(tspan_hr(:), eta_epoxy(13,:), '-r');
semilogy(tspan_hr(:), eta_epoxy(25,:), '-g');
semilogy(tspan_hr(:), eta_epoxy(37,:), '-b');
semilogy(tspan_hr(:), eta_epoxy(49,:), '--k');
hold off
hleg1 = legend('Ply 1', 'Ply 13', 'Ply 24', 'Ply 36', 'Ply 48');
set(hleg1, 'Location', 'eastoutside', 'Orientation', 'vertical')
xlabel ('Time (hr)')
ylabel ('Viscosity (Pa.s)')
ylim([1e2, 1e7])
xlim([15,23]);

% Plot the max temperature difference in the laminate wrt time
figure;
plot(tspan_hr(:), Temp_diff, 'color', 'r', 'linewidth', 2);
xlabel('Time (hr)')
ylabel('Max Temperature Difference (°C)')
ylim([0,80]);
xlim([0,25]);

% Plot the max DOC difference in the laminate wrt time
figure;
plot(tspan_hr(:), DOC_diff, 'color', 'r', 'linewidth', 2);
xlabel('Time (hr)')

```

```
ylabel('Max Degree of cure Difference')
ylim([0,1]);
xlim([0,25]);
```

Function file, “cure_kin”, for the cure kinetics model

```
function dadt = cure_kin(a,T)

global A1 A2 A3 Ea1 Ea2 Ea3 R alp_c_sl alp_c_int m n C

k1 = A1*exp(-Ea1./(R*T));
k2 = A2*exp(-Ea2./(R*T));
k3 = A3*exp(-Ea3./(R*T));

alp_c = alp_c_sl*T + alp_c_int;

dadt = ((k1+k2+k3*a^m)*((1-a)^n))/(1+exp(C*(a-alp_c)));

end
```

Function file, “chemorheoDiBen”, for the chemorheology model and DiBenedetto equation

```
function [Tg,eta_epoxy] = chemorheoDiBen(a,T)

global Tg0 Tgf gam eta_g0 DOC_gel A C1 C2

% Generate data for cure-dependent glass transition temperature
Tg_C = Tg0 + (gam*a*(Tgf-Tg0))/(1-(1-gam)*a);
Tg = Tg_C + 273;

Vis_check = T-Tg;
if Vis_check < -28 % Basically accounting for a singularity
in the Kenny-Opalicki model where the exponential term approaches
infinity as T-Tg approaches the value of C2
    eta_epoxy = eta_g0;
else
    eta_epoxy = eta_g0*exp((-C1*(T-Tg))/(C2+T-
Tg))*((DOC_gel/(DOC_gel-a))^(A)); % Kenny-Opalicki model
end

end
```

Function file, “DarcyFlow3”, for the resin flow model

```

function [DOI,Resin_avail,Flo] = DarcyFlow3(eta)

global K_perm phi_por P_grad Time_step pre_DOI phi_ply h_ply pre_Flo
Resin_store

dldt = (K_perm/(phi_por*eta))*P_grad;           % Finite version of
Darcy's law to solve the change in flow position for each time step
Resin_less = (dldt*Time_step)*(phi_por);       % The resin flow for
this increment is multiplied by the porosity so that it can be
determined how much resin this increment will take

DOI = pre_DOI + Resin_less/(phi_ply*h_ply);
Flo = pre_Flo + (dldt*Time_step);              % Add the above to
the previous step to find the overall flow front position...
Effectively, this is the Euler Method.
Resin_avail = Resin_store - Resin_less;        % determines the
current resin supply for the rest of the resin layers when the
bottom flow for this increment is taken away.

    if Resin_avail <= 0                          % check that
resin supply hasn't been fully depleted during this iteration
        DOI = pre_DOI + Resin_store/(phi_ply*h_ply);
        Flo = pre_Flo + Resin_store/(phi_por);   % if so,
redefine the flow amount as that of the previous iteration plus
whatever resin was left
        Resin_avail = 0;
    end

end

```

User-defined subroutine, UEXPAN and UMATHT, for Abaqus FEA

```

! First subroutine, UEXPAN, uses the resin flow calculations to update the
element thickness in the z direction
SUBROUTINE UEXPAN(EXPAN,DEXPANDT,TEMP,TIME,DTIME,PREDEF,
1 DPRED,STATEV,CMNAME,NSTATV,NOEL)
C
INCLUDE 'ABA_PARAM.INC'
C
CHARACTER*80 CMNAME
DIMENSION EXPAN(*),DEXPANDT(*),TEMP(2),TIME(2),PREDEF(*),
1 DPRED(*),STATEV(NSTATV)

! Call in relevant state variables
THICK = STATEV(11)
THICKDIFF = STATEV(12)

```

```

TimeCheck = TIME(2)-DTIME

EXPAN(1) = 0.0
EXPAN(2) = 0.0
if (TimeCheck .eq. ZERO) then
    EXPAN(3) = 0.0          ! Set initial value
else
    EXPAN(3) = -THICKDIFF/THICK          ! Use state variables to
update the element thickness in the z direction
end if

RETURN
END

! Second subroutine, UMATHT, calculates the incremental changes in resin
flow, cure, etc. and uses them to update the heat transfer calculations
SUBROUTINE UMATHT(U,DUDT,DUDG,FLUX,DFDT,DFDG,
1 STATEV,TEMP,DTEMP,DTEMDX,TIME,DTIME,PREDEF,DPRED,
2 CMNAME,NTGRD,NSTATV,PROPS,NPROPS,COORDS,PNEWDT,
3 NOEL,NPT,LAYER,KSPT,KSTEP,KINC)
C
INCLUDE 'ABA_PARAM.INC'
C
CHARACTER*80 CMNAME
DIMENSION DUDG(NTGRD),FLUX(NTGRD),DFDT(NTGRD),
1 DFDG(NTGRD,NTGRD),STATEV(NSTATV),DTEMDX(NTGRD),
2
TIME(2),PREDEF(1),DPRED(1),PROPS(NPROPS),COORDS(3),COND(3,3),ALPAUX(4),FLAUX(4
),XTAUX(4)

C
C
C    user coding to define U,DUDT,DUDG,FLUX,DFDT,DFDG,
C    and possibly update STATEV, PNEWDT
C
C-----
C    READ IN PROPERTIES
C-----
C    Heat Analysis (orthotropic)
C
C-----
C    Conductivity Parameters
C-----

cappa_dry = PROPS(1)          ! This is 0.2075 and 0.287 for GF and CF
respectively, based on thermal conductivity data from Cormac Lee's thesis
(2004)
cappa_fib_tran = PROPS(2)     ! For tranverse thermal conductivity of E-
glass fibre and carbon fibre, the value is 0.417 and 7.8 respectively, taken
from "Experimental investigation of heat dispersion due to impregnation..." by
Hsiao et al 2001... Cormac Lee has used 1 W/m.K and 17 W/m.K respectively
cappa_fib_long = PROPS(3)     ! Cormac Lee used 1 W/m.K and 17 W/m.K for
GF and CF respectively, Shi (2016) used 1.3 W/m.K, Oh and Lee (2002) used 1.04
for GF, Shin and Hahn (2004) used 26 for CF, while the Toray website gives
9.37 for T700

```

```

CP_fib = PROPS(4)          ! for GF, this is 810, Shi (2016)... for CF
it's 753 (Toray datasheet for T700)

C-----
C   Resin Flow PARAMETERS
C-----

h_tot = PROPS(5)
DOI_Init = PROPS(6)
perm1 = PROPS(7)          ! 13.675e-10 for stitched GF fabric,
Kuentzer (2006)... assuming values for woven CF are suitable as a first
approximation, 8.45e-10 was taken from the same publication
phi1 = PROPS(8)
phi2 = PROPS(9)          ! 0.33 for GF (Amico and Lekakou
2004) and 0.27 for CF (Centea and Hubert 2012)
P_vac = PROPS(10)

C-----
C   Additional PARAMETERS
C-----

phi_tar = PROPS(11)
rho_fib = PROPS(12)      ! 2560 for GF from Tan and Pillai (2012),
and 1800 for T700 from Toray
ALPInit = PROPS(13)
Xint = PROPS(14)
fib_rad = PROPS(15)     ! 8e-6 for GF - taken from Johns Manville
datasheet for StarRov 086 fibre (sized for epoxies, 1200/2400 tex for
weaving), 3.5e-6 for Toray T700

C-----
C   DEFINE STATE VARIABLES ! NOTE: The state variable names MUST be in
capital letters
C-----

ALP = STATEV(1)          ! Degree of cure
COND(1,1) = STATEV(2)   ! conductivity
COND(2,2) = STATEV(3)
COND(3,3) = STATEV(4)
CP = STATEV(5)          ! specific heat
V = STATEV(6)
FLO = STATEV(7)
RES = STATEV(8)
DOI = STATEV(9)
TRAN = STATEV(10)
THICK = STATEV(11)
THICKDIFF = STATEV(12)
HFLO = STATEV(13)
XT = STATEV(14)

C-----
C   CURE KINETICS, CHEMORHEOLOGICAL AND RESIN FLOW MODELS
C-----
! Initialising the model at t = 0
! Cure kinetics parameters
A1 = 4.073e-4
A2 = 10.112e9

```



```

A3 = 1.636e13
Ea1 = 12006.0
Ea2 = 111792.0
Ea3 = 131240.0
paraM = 1.24
paraN = 1.8
HR = 184000.0
C = 50.0
ALCT = 0.006
ALC0 = -1.748
R = 8.31446
! Chemorheological parameters
eta_g0 = 2e11
aGel = 0.56
A = 1.6
C1 = 32.25
C2 = 30.0
! Parameters for DiBenedetto
Tg0 = 40.0
Tgf = 106.0
gam = 0.53
! Sintering parameters
T_melt = 40.483 + 273.0
DOS_inf = 0.0
XA = 3e-5
XC1 = 11.5
XC2 = 24.5
Xn = 0.5
Xpow = 0.503

! Gebart model for intra-tow permeability based on quadratic fibre packing
perm2 = (16.0/(9.0*3.1416*(2.0**0.5)))*(((3.1416/(4.0*(1.0-phi2)))**0.5)-
1.0)**(2.5))*(fib_rad)**2.0

! Ply Microstructure
phi_inter = 0.2146 ! Approached
differently from phi1 for the flow equations, in this instance it is based on
ratio of the inter-tow region to the total rectangular region with height and
width equal to the dimensions of the elliptical tow - see 12/12/17 in notes
phi_ply = phi_inter + phi2 - phi_inter*phi2 ! Tahir,
Hallstrom, Akermo, 2014 - proof on 12/12/17 of notes)
h_ply = h_tot*(1.0-phi_tar)/(1.0-phi_ply) ! thickness
of the ply (not including the extra resin to bring the ply to the target FVF)
h_extra = h_tot - h_ply ! thickness of
extra resin layer
h_inter = h_ply*phi_inter !
representative thickness of the inter-tow region - upon complete filling of
this region, the flow calculations will switch to filling the intra-tow region
h_resin = h_ply*phi_ply + h_extra ! total
thickness of resin needed to reach target FVF
phi_inter_frac = phi_inter/phi_ply ! the percentage
fraction of inter-tow porosity in respect to the ply porosity e.g. if
phi_inter is 0.2146 and phi_ply is 0.4737, then the inter-tow porosity
accounts for 45.3% of the ply porosity
phi_intra_frac = (phi_ply-phi_inter)/phi_ply

! Initial conditions

```

```

if (TIME(2) .eq. ZERO) then
  ALP = ALPInit
  DOI = DOI_Init
  RES_fill = h_ply*phi_ply*DOI_Init
  if (DOI_Init >= phi_inter_frac) then           ! Check if the
inter-tow region has been filled
    FLO = h_inter + (RES_fill - h_inter)/phi2    ! FLO is
equivalent to the impregnation depth
    TRAN = 1
  else
    FLO = RES_fill
    TRAN = 0
  end if
  RES = h_resin - RES_fill
  XT = Xint
  RES_thick = RES/(1.0-XT)
  RES_fill_thick = RES_fill/(1.0-XT)
  Fib_thick = h_ply - RES_fill
  THICK = RES_thick + RES_fill_thick + Fib_thick
  V = eta_g0
end if

order = 4           ! Number of iterations for the 4th order Runge-Kutta
method
TK = TEMP+273.0
THICK_init = THICK           ! Determine the thickness at the start of
the increment so that the change can be calculated at the end and sent to
UEXPAN

if (RES <= 0 .or. DOI >= 1.0 .or. ALP >= 0.53) then           ! Note, if large
time step sizes are used, the limit for ALP may need to be reduced so that the
viscosity model (V_nex) does not create a singularity when ALP_nex = ALP +
ALPAUX(3) becomes greater than aGel i.e 0.56
  FLO = FLO
  DOI = DOI
  RES_LS = 0
  XT = 0
  if (RES <= 0) then
    RES = 0
  else
    RES = RES
  end if
  if (ALP >= 0.99) then
    ALP = 1
    V = eta_g0
  else
    ! Use 4th order Runge-Kutta for cure
kinetics model
    DO I=1, order
      if (I .eq. 1) then
        TK_nex = TK
        ALP_nex = ALP           ! Don't get ALP_nex and
ALPAUX(I) mixed up; ALP_nex is the DoC at time step i+1, while ALPAUX is the
auxiliary value for the rate of change for DoC
      else if (I .eq. 2) then
        TK_nex = TK + 0.5*DTEMP
        ALP_nex = ALP + 0.5*ALPAUX(1)
      else if (I .eq. 3) then

```

```

        TK_nex = TK + 0.5*DTEMP
        ALP_nex = ALP + 0.5*ALPAUX(2)
    else
        TK_nex = TK + DTEMP
        ALP_nex = ALP + ALPAUX(3)
    end if
    Denom = 1.0+Exp(C*(ALP_nex-ALC0-ALCT*TK_nex))
    rate1 = A1*Exp(-Ea1/(R*TK_nex))
    rate2 = A2*Exp(-Ea2/(R*TK_nex))
    rate3 = A3*Exp(-Ea3/(R*TK_nex))
    ALPAUX(I) = DTIME*((rate1+rate2+rate3*ALP_nex**paraM)*(1.0-
ALP_nex)**paraN)/Denom
                                ! Cure kinetics model
    END DO
    DALP = (ALPAUX(1)+2.0*ALPAUX(2)+2.0*ALPAUX(3)+ALPAUX(4))/6.0
    ! Sum the auxiliary values to determine the rate of change
    ALP = ALP + DALP
    if (ALP < 0.55) then
        TgC = Tg0 + (gam*ALP*(Tgf-Tg0))/(1.0-(1.0-gam)*ALP)
        Tg = TgC + 273.0
        Vis_check = (TK+DTEMP)-Tg
        if (Vis_check < -28.0) then
            ! Basically accounting
            for a singularity in the Kenny-Opalicki model where the exponential term
            approaches infinity as T-Tg approaches the value of C2
            V = eta_g0
        else
            V = eta_g0*((aGel/(aGel-ALP))**(A))*Exp(-C1*((TK+DTEMP)-
Tg)/(C2+(TK+DTEMP)-Tg))
        end if
    else
        V = eta_g0
    end if
end if
else
    DO J=1, order
                                ! in this case the ODE
                                for resin flow is also solved using the 4th order Runge-Kutta
        if (J .eq. 1) then
            TK_nex = TK
            ALP_nex = ALP
            fl_nex = FLO
            XT_nex = XT
        else if (J .eq. 2) then
            TK_nex = TK + 0.5*DTEMP
            ALP_nex = ALP + 0.5*ALPAUX(1)
            fl_nex = FLO + 0.5*FLAUX(1)
            XT_nex = XT + 0.5*XTAUX(1)
        else if (J .eq. 3) then
            TK_nex = TK + 0.5*DTEMP
            ALP_nex = ALP + 0.5*ALPAUX(2)
            fl_nex = FLO + 0.5*FLAUX(2)
            XT_nex = XT + 0.5*XTAUX(2)
        else
            TK_nex = TK + DTEMP
            ALP_nex = ALP + ALPAUX(3)
            fl_nex = FLO + FLAUX(3)
            XT_nex = XT + XTAUX(3)
        end if
        ! Resin material models

```

```

Denom = 1.0+Exp(C*(ALP_nex-ALC0-ALCT*TK_nex))
rate1 = A1*Exp(-Ea1/(R*TK_nex))
rate2 = A2*Exp(-Ea2/(R*TK_nex))
rate3 = A3*Exp(-Ea3/(R*TK_nex))
ALPAUX(J) = DTIME*((rate1+rate2+rate3*ALP_nex**paraM)*(1.0-
ALP_nex)**paraN)/Denom
! Cure kinetics model
TgC_nex = Tg0 + (gam*ALP_nex*(Tgf-Tg0))/(1.0-(1.0-gam)*ALP_nex)
! DiBenedetto model

Tg_nex = TgC_nex + 273.0
Vis_check = TK_nex-Tg_nex
if (Vis_check < -28.0) then
! Basically accounting for a
singularity in the Kenny-Opalicki model where the exponential term approaches
infinity as T-Tg approaches the value of C2
V_nex = eta_g0
else
V_nex = eta_g0*((aGel/(aGel-ALP_nex))**(A))*Exp(-C1*(TK_nex-
Tg_nex))/(C2+TK_nex-Tg_nex) ! Chemorheological model
end if
X_check = TK_nex-T_melt
if (X_check < -22.0) then
XTAUX(J) = 0.0
else
XTAUX(J) = DTIME*(-XA*Exp(((XC1*(TK_nex-T_melt)))/(XC2+TK_nex-
T_melt))*(XT_nex-DOS_inf)**Xn)
X_check2 = XT + XTAUX(J)
if (X_check2 <= 0.0) then
XT = 0.0
XTAUX(J) = 0.0
end if
end if
! Resin flow models
if (TRAN == 0) then
FLAUX(J) = DTIME*2.0*(perm1/(phi1*V_nex))*(P_vac/(f1_nex/2.0))
! Resin flow model for inter-tow flow
else if (TRAN == 1) then
P_grad = (perm1*P_vac)/((0.5*f1_nex - 0.49*h_inter)*perm1 +
0.5*h_inter*perm2) ! Note that the negative term in the denominator should
never be large enough to produce an infinitely high pressure gradient, or a
negative pressure gradient.
FLAUX(J) = DTIME*2.0*(perm2/(phi2*V_nex))*P_grad
! Resin flow model for intra-tow flow
end if
END DO
DALP = (ALPAUX(1)+2.0*ALPAUX(2)+2.0*ALPAUX(3)+ALPAUX(4))/6.0
ALP = ALP + DALP
if (XT <= 0.0) then
XT = 0.0
else
DXT = (XTAUX(1)+2.0*XTAUX(2)+2.0*XTAUX(3)+XTAUX(4))/6.0
XT = XT + DXT
end if
DFL = (FLAUX(1)+2.0*FLAUX(2)+2.0*FLAUX(3)+FLAUX(4))/6.0
TgC = Tg0 + (gam*ALP*(Tgf-Tg0))/(1.0-(1.0-gam)*ALP)
Tg = TgC + 273.0
Vis_check = (TK+DTEMP)-Tg

```

```

        if (Vis_check < -28.0) then          ! Basically accounting for a
singularity in the Kenny-Opalicki model where the exponential term approaches
infinity as T-Tg approaches the value of C2
            V = eta_g0
        else
            V = eta_g0*((aGel/(aGel-ALP))**(A))*Exp(-C1*((TK+DTEMP)-
Tg)/(C2+(TK+DTEMP)-Tg))
        end if
        if (TRAN == 0) then
            fl_check3 = FLO + DFL
            if (fl_check3 >= h_inter) then    ! check if flow is just after
transitioning (i.e. TRAN = 0, but fl_check3 >= vol_inter)
                res_ter = h_inter - FLO      ! gives you the amount of
resin that was needed to fill the last bit of the inter-tow region
                res_tra = fl_check3 - h_inter ! the additional resin
that was taken due to intra-tow flow
                RES_LS = res_ter*phi1 + res_tra*phi2 ! still need to get the
resin flow in terms of the unfilled volume
                TRAN = 1
            else
                RES_LS = DFL*phi1           ! resin reduction for inter-tow flow
                TRAN = 0
            end if
        else
            RES_LS = DFL*phi2               ! resin reduction for intra-
tow flow
            TRAN = 1
        end if
        DOInew = DOI + RES_LS/(phi_ply*h_ply)
        if (DOInew >= 1) then
            RES_LS = (1-DOI)*(phi_ply*h_ply)
            DFL = RES_LS/phi2
            DOI = 1.0
        else
            DOI = DOInew
        end if
        if (RES_LS >= RES) then            ! check if the resin has run
out
            RES_LS = RES
            FLO = FLO + RES_LS/phi2
        else
            FLO = FLO + DFL
        end if
        RES = RES - RES_LS
    end if

    RES_thick = RES/(1.0-XT)
    RES_fill = h_ply*phi_ply*DOI
    RES_fill_thick = RES_fill/(1.0-XT)
    Fib_thick = h_ply - RES_fill
    THICK = RES_thick + RES_fill_thick + Fib_thick
    THICKDIFF = THICK_init - THICK

C-----
C   DEFINE HEAT ANALYSIS PART
C-----
! Density

```

```

rho_res = 1220.0/(1.0-XT)           ! 1220 kg/m^2 is the density of cure
epoxy powder
rho_comp = (1.0-phi_tar)*rho_fib + phi_tar*rho_res           ! ROM

! Specific heat capacity
CP_res = 4184.0*(0.468+(5.975E-4)*(TEMP+DTEMP)-0.141*ALP) ! model for
specific heat capacity of resin (see Shin and Hahn 2004)
CP = (phi_tar*rho_res*CP_res + (1.0-
phi_tar)*rho_fib*CP_fib)/(phi_tar*rho_res + (1.0-phi_tar)*rho_fib) ! ROM
based on mass fraction

! Thermal conductivity models
cappa_liq = 0.04184*(3.85+(0.035*(TEMP+DTEMP)-0.41)*ALP) ! See appendix of
Shin and Hahn (2004) in Mendeleev, they cite Mijovic and Wang (1988)
cappa_pow = 0.075
cappa_res = cappa_pow*(XT/Xpow) + cappa_liq*(1-(XT/Xpow))
cappa_comp = (cappa_res/4.0)*(((1.0-
phi_ply)**2.0)*((cappa_fib_tran/cappa_res)-
1.0)**2.0)+(4.0*cappa_fib_tran/cappa_res)**0.5-(1.0-
phi_ply)*((cappa_fib_tran/cappa_res)-1.0)**2.0
Therm_Res = RES_thick/cappa_res + FLO/cappa_comp + (h_ply-FLO)/cappa_dry
cappa_eff = (Therm_Res**-1.0)*THICK
COND(1,1) = phi_tar*cappa_res + (1.0-phi_tar)*cappa_fib_long
COND(2,2) = cappa_eff
COND(3,3) = COND(2,2)

DUDT = CP*(h_tot/(THICK))
DU = DUDT*DTEMP
HFLO = h_resin*rho_res*HR*(DALP/DTIME)
U = U+DU - (phi_tar*rho_res*HR/(rho_comp*(h_tot/(THICK))))*DALP  !--
In order to properly represent the thickness of the ply, we need to read in
inputs for targeted FVF (1-phi_tar), fabric ply thickness (h_ply) and the
actual max ply FVF (for nested tows this will tend toward the tow FVF, which
we assume to be 0.67 for GF)
C
C   Heat fluxes
C
C
C   Input orthotropic conductivity
C
DO K=1, NTGRD
    FLUX(K) = -COND(K,K)*DTEMPDX(K)
    DFDG(K,K) = -COND(K,K)
END DO
C   Activation
C

STATEV(1) = ALP
STATEV(2) = COND(1,1)
STATEV(3) = COND(2,2)
STATEV(4) = COND(3,3)
STATEV(5) = CP
STATEV(6) = V
STATEV(7) = FLO
STATEV(8) = RES
STATEV(9) = DOI
STATEV(10) = TRAN

```

```
STATEV(11) = THICK  
STATEV(12) = THICKDIFF  
STATEV(13) = HFLO  
STATEV(14) = XT
```

```
RETURN  
END
```

D. Simulation Results

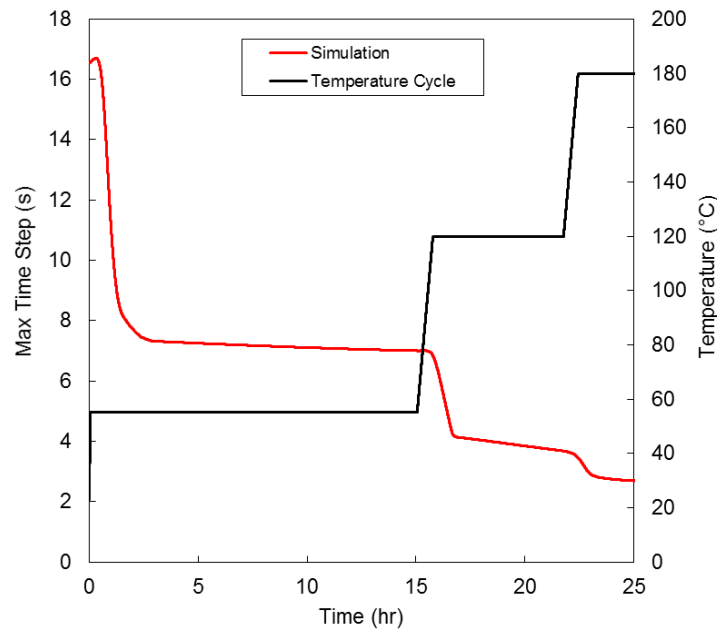


Figure D.1. The maximum allowable time step to achieve a stable solution for a GF/Epoxy-powder ply. The curing and compaction during the cycle caused the thermal diffusivity, γ , and the spatial increment, Δz , to change. This resulted in the max time step being reduced.

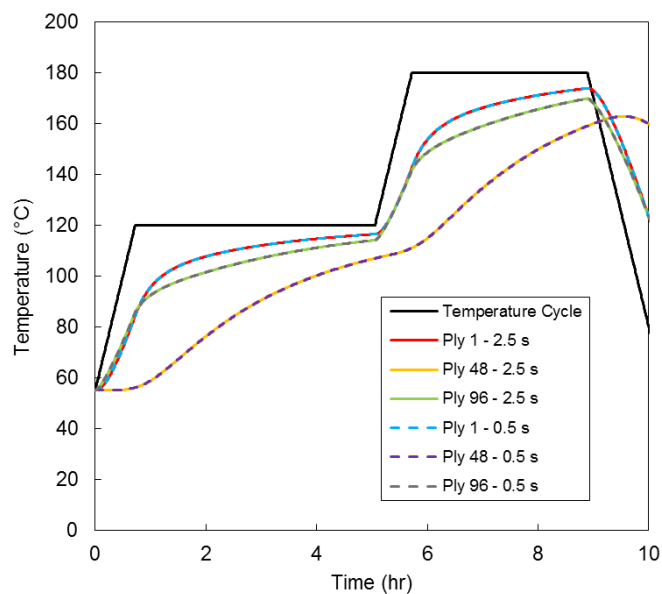


Figure D.2. Test of simulation accuracy for two time step sizes: 0.5 s, and 2.5 s. Heat transfer through a 96-ply GF/Epoxy-powder laminate was simulated with a 10 mm steel tool.

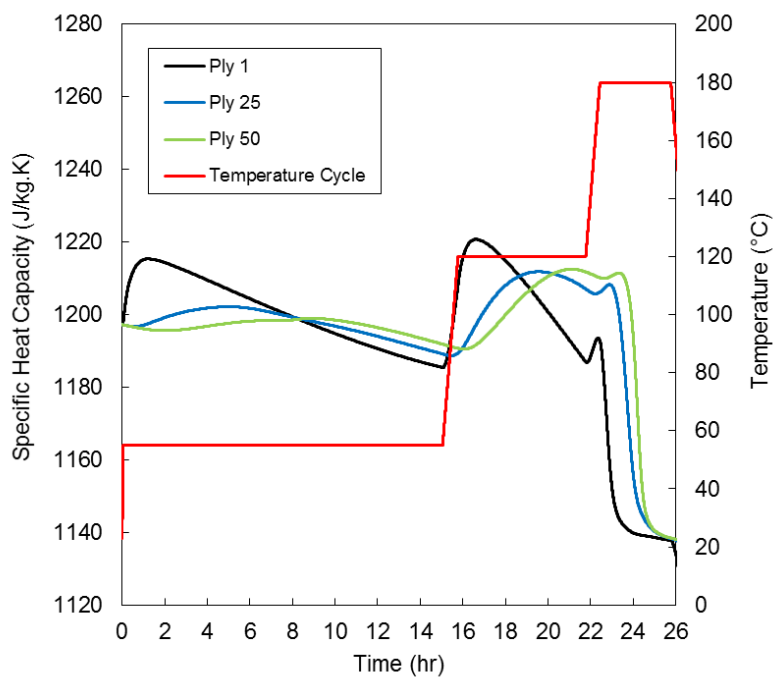


Figure D.3. Plot of the specific heat capacity variation during the temperature cycle. It increased with temperature, and it decreased with the advancement of cure.

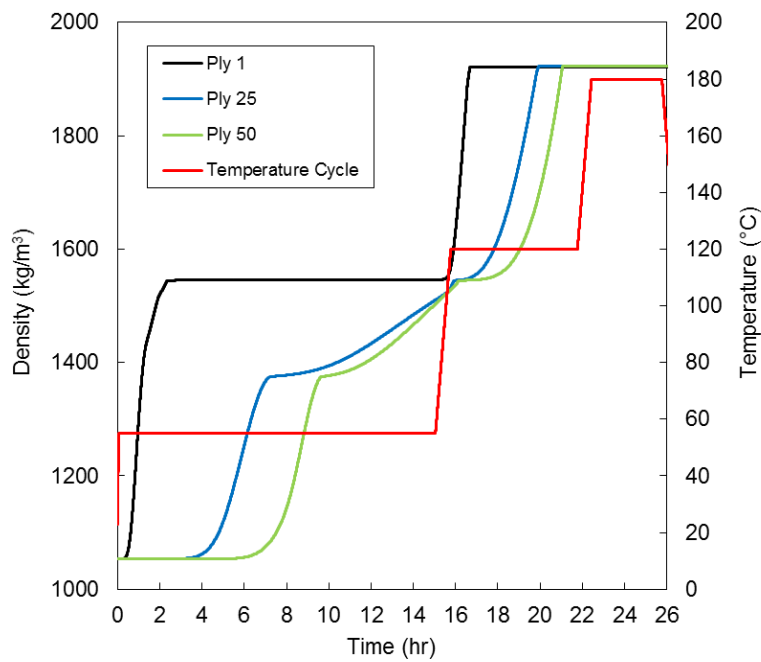


Figure D.4. Plot of the density variation of the plies during the temperature cycle. The ply density increased as the epoxy powder sintered and infused into the fibre-bed.

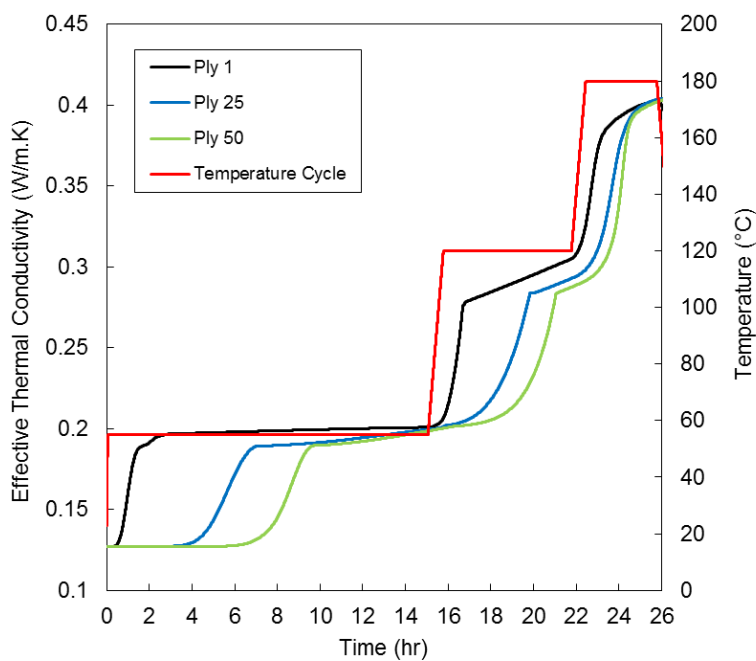


Figure D.5. Plot of the effective thermal conductivity variation during the temperature cycle. It increased with temperature, and was also affected by sintering of the powder and impregnation of the fibre-bed. The values were back-calculated from the thermal resistances of each ply.

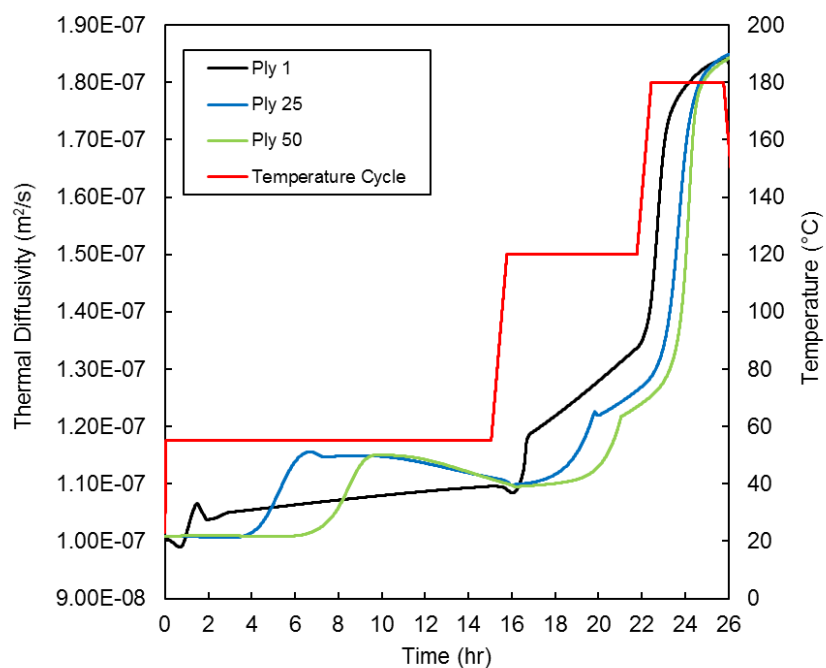


Figure D.6. Plot of the effective thermal diffusivity variation during the temperature cycle. The thermal diffusivity was most greatly affected by curing of the epoxy when the thermal conductivity increased and the specific heat capacity decreased.

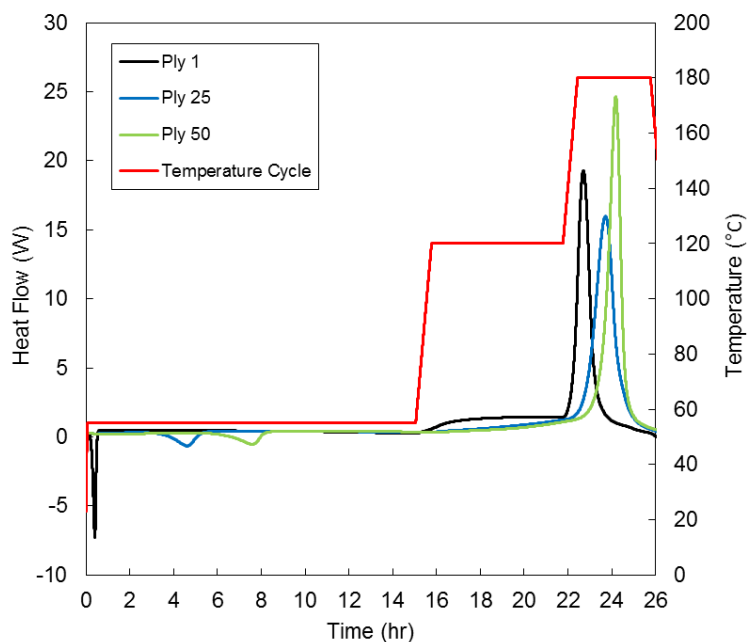


Figure D.7. Plot of the heat flow to/from the resin during the temperature cycle. Melting resulted in small endothermic peaks, while curing resulted in large exothermic peaks.

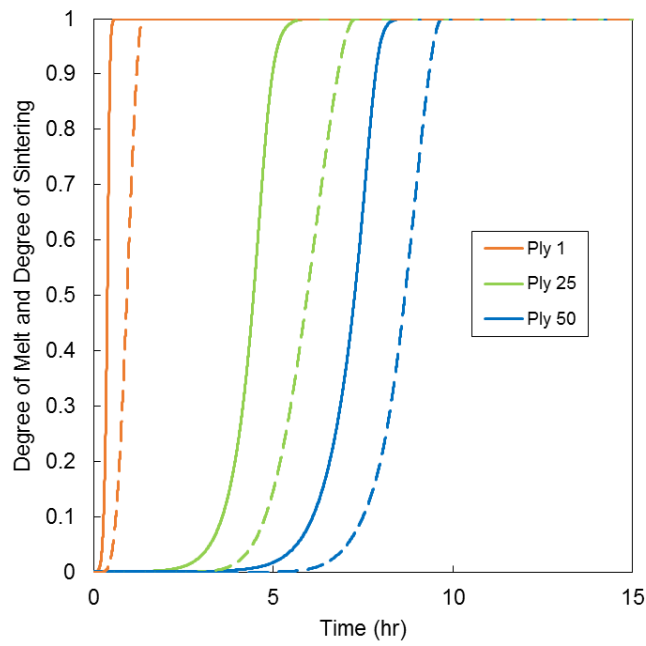


Figure D.8. Powder melting and sintering during the drying stage. The sintering (dashed line) lags the melting (solid line) due to the high viscosity of the epoxy at low temperatures. A thermal lag between the melting and sintering was observed by Greco and Maffezzoli (2003) also.

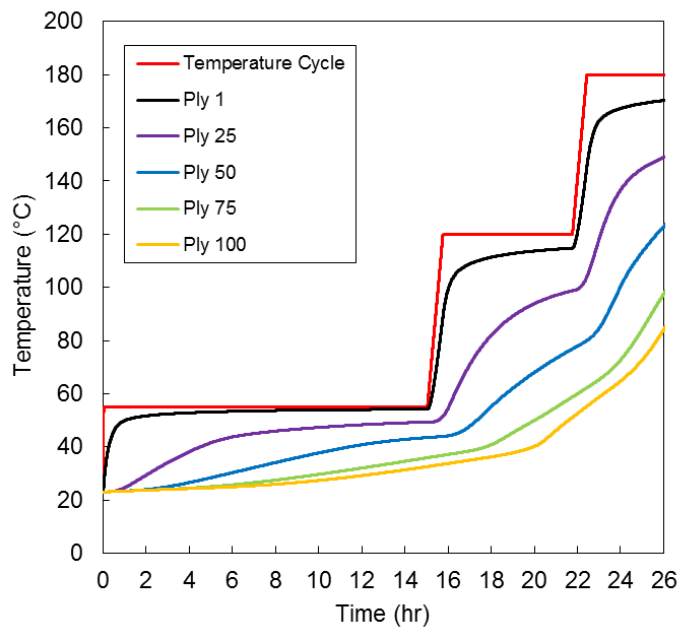


Figure D.9. Simulated temperatures in a 100-ply laminate manufactured using a heated steel tool, and 200 mm insulation at the top boundary. The laminate was made with UD GF and epoxy powder (GRN 918).

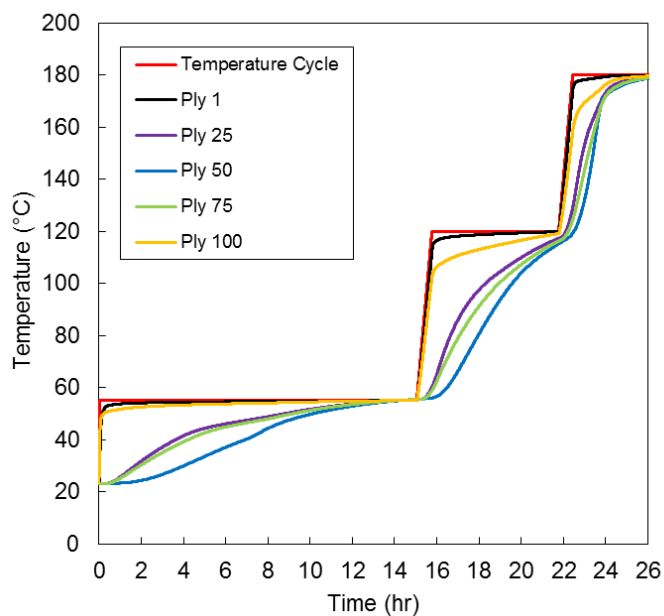


Figure D.10. Simulated temperatures in a 100-ply laminate manufactured using a heated steel tool, and a silicone rubber heating mat at the top boundary. The laminate was made with UD GF and epoxy powder (GRN 918).

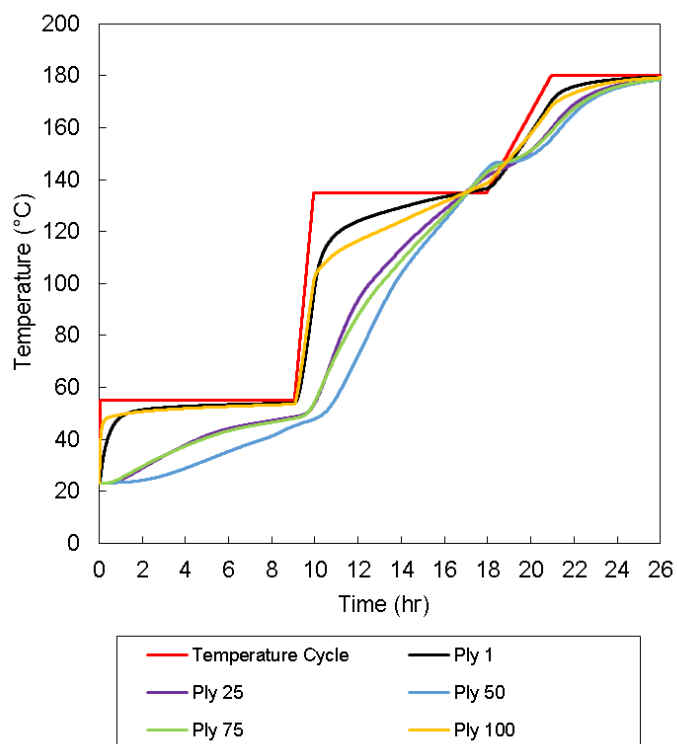


Figure D.11. Simulated temperatures for a 100-ply laminate processed using a modified cycle.

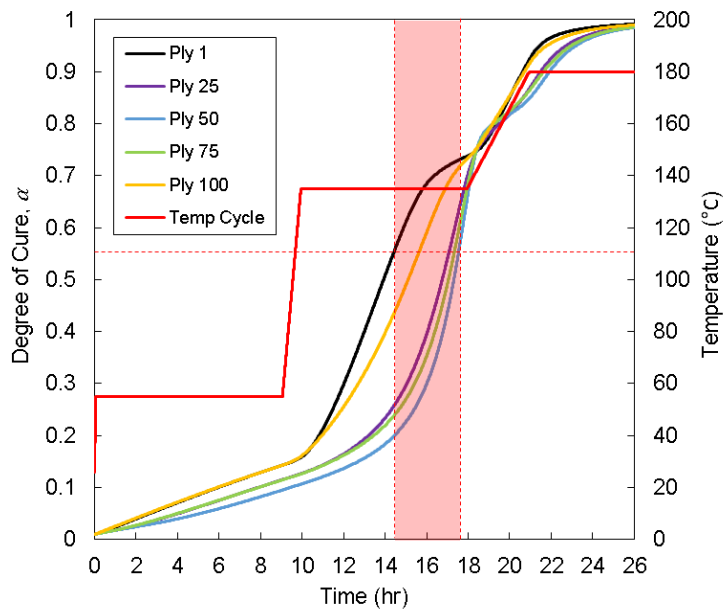


Figure D.12. Simulated DoC evolution for the modified temperature cycle. The horizontal dashed red line represents the gel point and the shaded red area highlights the duration of gelation in the laminate.

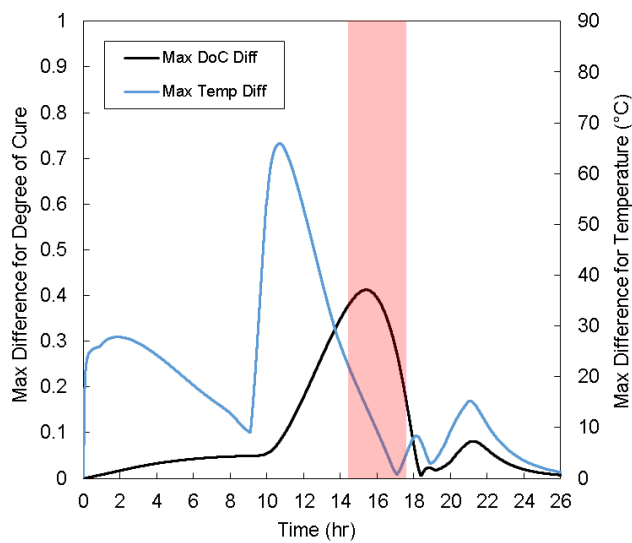


Figure D.13. Maximum temperature difference and maximum DoC difference for the modified temperature cycle. The temperature difference was significantly reduced during gelation, while the peak in DoC difference was reduced by approx. 0.1.

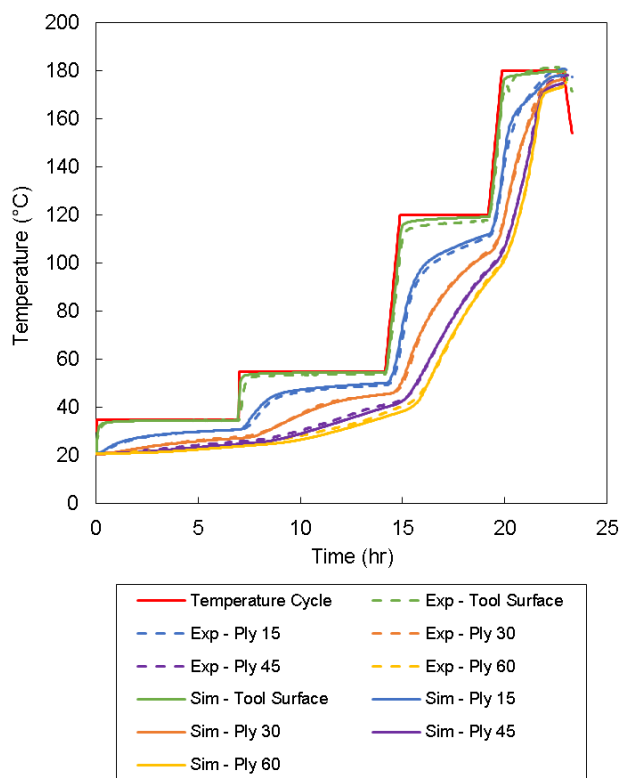


Figure D.14. Comparison of the simulated temperature distribution from Abaqus FEA and the thermocouple data for Test Laminate 1.

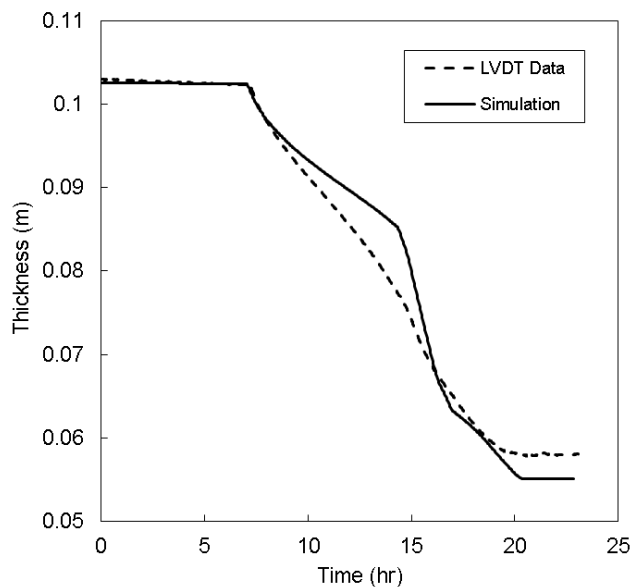


Figure D.15. Comparison of the simulated laminate thickness change from Abaqus FEA and the LVDT data for Test Laminate 1.

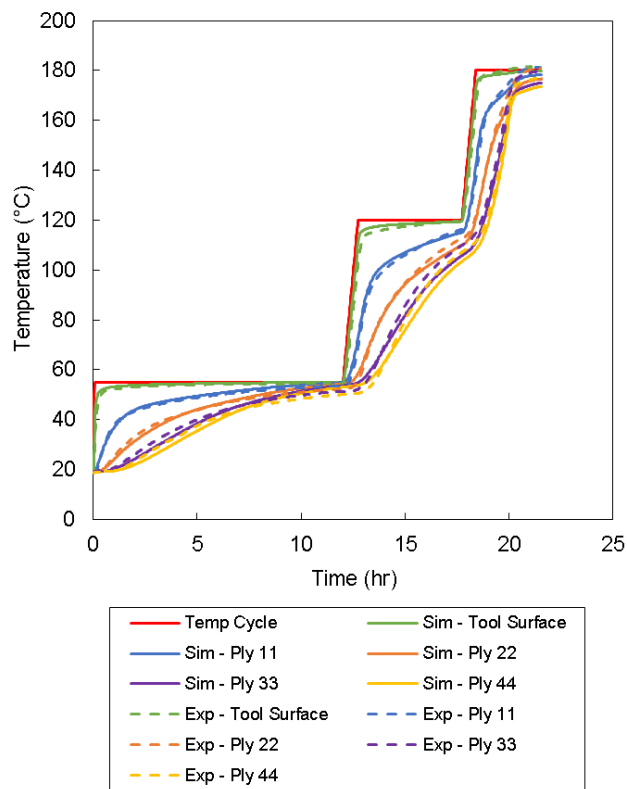


Figure D.16. Comparison of the simulated temperature distribution from Abaqus FEA and the thermocouple data for Test Laminate 2.

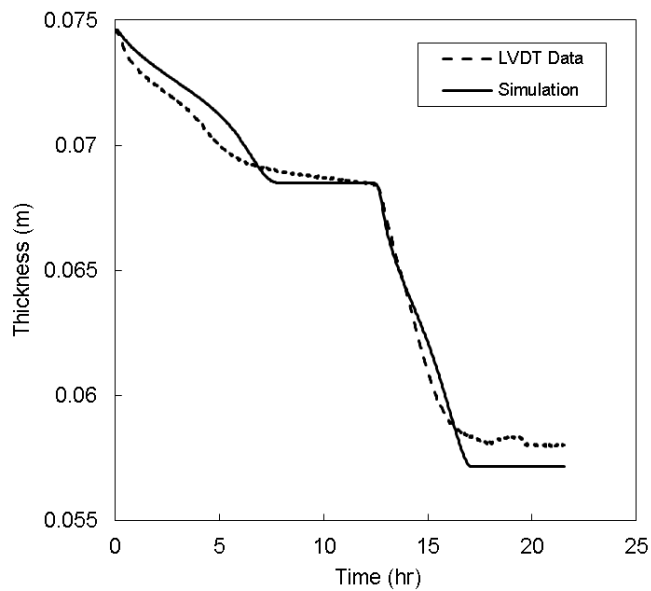


Figure D.17. Comparison of the simulated laminate thickness change from Abaqus FEA and the LVDT data for Test Laminate 2.

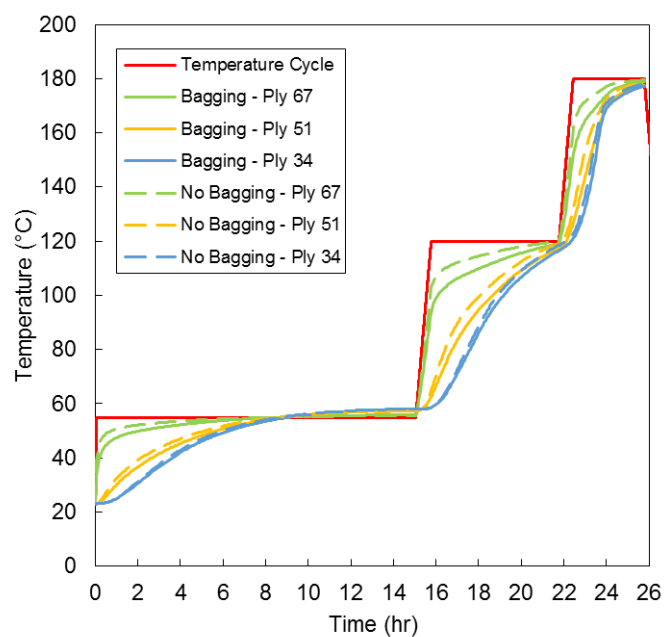


Figure D.18. 1D simulation results for the tapered root section, taken at the thickest point in the section i.e. 67 plies thick. One simulation was performed with bagging included, and the other without. There was a noticeable difference in the temperature predictions, especially on the bagging side of the laminate.

Bibliography

- Abou Msallem, Y., Jacquemin, F., Boyard, N., Poitou, A., Delaunay, D. and Chatel, S. (2010) 'Material characterization and residual stresses simulation during the manufacturing process of epoxy matrix composites', *Composites Part A: Applied Science and Manufacturing*, 41(1), pp. 108–115. doi: <https://doi.org/10.1016/j.compositesa.2009.09.025>.
- Advani, S. G. and Hsiao, K.-T. (2012) '1 – Introduction to composites and manufacturing processes', in *Manufacturing Techniques for Polymer Matrix Composites (PMCs)*. Woodhead Publishing Limited, pp. 1–12. doi: <https://doi.org/10.1533/9780857096258.1.1>.
- Akzo Nobel Powder Coatings GmbH (2016) *HZH01R Product Datasheet*.
- Allada, R., Maruthapillai, A., Palanisamy, K. and Chappa, P. (2016) 'Hygroscopicity Categorization of Pharmaceutical Solids by Gravimetric Sorption Analysis: A Systematic Approach', *Asian Journal of Pharmaceutics*, 10(4), pp. 279–286.
- Allred, R. E., Wesson, S. P. and Babow, D. A. (2004) 'Powder Impregnation Studies for High Temperature Towpregs', *SAMPE Journal*, 40(6), pp. 40–48.
- Amico, S. and Lekakou, C. (2004) 'Flow through a Two-Scale Porosity, Oriented Fibre Porous Medium', *Transport in Porous Media*, 54(1), pp. 35–53. doi: <https://doi.org/10.1023/A:1025799404038>.
- Antonucci, V., Giordano, M., Hsiao, K.-T. and Advani, S. G. (2002) 'A methodology to reduce thermal gradients due to the exothermic reactions in composites processing', *International Journal of Heat and Mass Transfer*, 45(8), pp. 1675–1684. doi: [https://doi.org/10.1016/S0017-9310\(01\)00266-6](https://doi.org/10.1016/S0017-9310(01)00266-6).
- Arafath, A. R. A., Fernlund, G. and Poursartip, A. (2009) 'Gas transport in prepregs: model and permeability experiments', in *Proceedings of the 17th International Conference on Composite Materials*. Available at: <http://www.iccm-central.org/Proceedings/ICCM17proceedings/Themes/Manufacturing/RESIDUAL STRESS & PROCE/C4.9 Fernlund.pdf>.

- Aref-Azar, A., Arnoux, F., Biddlestone, F. and Hay, J. N. (1996) 'Physical ageing in amorphous and crystalline polymers. Part 2. Polyethylene terephthalate', *Thermochimica Acta*, 273, pp. 217–229. doi: [https://doi.org/10.1016/0040-6031\(95\)02434-4](https://doi.org/10.1016/0040-6031(95)02434-4).
- Barletta, M., Lusvardi, L., Pighetti Mantini, F. and Rubino, G. (2007) 'Epoxy-based thermosetting powder coatings: Surface appearance, scratch adhesion and wear resistance', *Surface and Coatings Technology*, 201, pp. 7479–7504. doi: <https://doi.org/10.1016/j.surfcoat.2007.02.017>.
- Baucom, R. M. and Marchello, J. M. (1990) 'Powder towpreg process development', in *Proceedings of NASA Advanced Composite Technology Conference*, pp. 443–454.
- Bayha, T. D., Osborne, P. P., Thrasher, T. P., Hartness, J. T., Johnston, N. J., Marchello, J. M. and Hugh, M. K. (1993) 'Processing, Properties and Applications of Composites Using Powder-Coated Epoxy Towpreg Technology', in *Proceedings of NASA's 4th Advanced Composite Technology Conference*. Salt Lake City, Utah.
- Belder, E. ., Rutten, H. J. . and Perera, D. . (2001) 'Cure characterization of powder coatings', *Progress in Organic Coatings*, 42(3–4), pp. 142–149. doi: [https://doi.org/10.1016/S0300-9440\(01\)00149-7](https://doi.org/10.1016/S0300-9440(01)00149-7).
- Bogetti, T. A. and Gillespie, J. W. (1991) 'Two-Dimensional Cure Simulation of Thick Thermosetting Composites', *Journal of Composite Materials*, 25(3), pp. 239–273. doi: <https://doi.org/10.1177/002199839102500302>.
- Bogetti, T. A. and Gillespie, J. W. (1992) 'Process-Induced Stress and Deformation in Thick-Section Thermoset Composite Laminates', *Journal of Composite Materials*, 26(5), pp. 626–660. doi: <https://doi.org/10.1177/002199839202600502>.
- Brody, J. C. and Gillespie, J. W. (2005a) 'Reactive and non-reactive binders in glass/vinyl ester composites', *Polymer Composites*, 26(3), pp. 377–387. doi: <https://doi.org/10.1002/pc.20068>.
- Brody, J. C. and Gillespie, J. W. (2005b) 'The Effects of a Thermoplastic Polyester Preform Binder on Vinyl Ester Resin', *Journal of Thermoplastic Composite Materials*, 18(3), pp. 157–179. doi: <https://doi.org/10.1177/0892705705043535>.

- Calabrese, L., Di Bella, G. and Fiore, V. (2016) '3 – Manufacture of marine composite sandwich structures', in *Marine Applications of Advanced Fibre-Reinforced Composites*. Woodhead Publishing, pp. 57–78. doi: <https://doi.org/10.1016/B978-1-78242-250-1.00003-X>.
- Castro, J. M. and Macosko, C. W. (1980) 'Kinetics and Rheology of Typical Polyurethane Reaction Injection Molding Systems', in *Proceedings of Society of Plastics Engineers (Technical Papers) 38th Annual Technical Conference*. New York, USA, pp. 434–438.
- Cender, T. A., Simacek, P. and Advani, S. G. (2013) 'Resin film impregnation in fabric prepregs with dual length scale permeability', *Composites Part A: Applied Science and Manufacturing*, 53, pp. 118–128. doi: <https://doi.org/10.1016/j.compositesa.2013.05.013>.
- Cender, T. A., Simacek, P., Davis, S. and Advani, S. G. (2016) 'Gas Evacuation from Partially Saturated Woven Fiber Laminates', *Transport in Porous Media*, 115(3), pp. 541–562. doi: <https://doi.org/10.1007/s11242-016-0784-x>.
- Çengel, Y. A. (2003) *Heat Transfer – A Practical Approach*. 2nd edn. New York, USA: McGraw-Hill.
- Centea, T., Grunenfelder, L. K. and Nutt, S. R. (2015) 'A review of out-of-autoclave prepregs – Material properties, process phenomena, and manufacturing considerations', *Composites Part A: Applied Science and Manufacturing*, 70, pp. 132–154. doi: <https://doi.org/10.1016/j.compositesa.2014.09.029>.
- Centea, T. and Hubert, P. (2011) 'Measuring the impregnation of an out-of-autoclave prepreg by micro-CT', *Composites Science and Technology*, 71(5), pp. 593–599. doi: [10.1016/j.compscitech.2010.12.009](https://doi.org/10.1016/j.compscitech.2010.12.009).
- Centea, T. and Hubert, P. (2012) 'Modelling the effect of material properties and process parameters on tow impregnation in out-of-autoclave prepregs', *Composites Part A: Applied Science and Manufacturing*, 43(9), pp. 1505–1513. doi: <https://doi.org/10.1016/j.compositesa.2012.03.028>.
- Centea, T. and Hubert, P. (2013) 'Out-of-autoclave prepreg consolidation under

deficient pressure conditions’, *Journal of Composite Materials*, 48(16), pp. 2033–2045. doi: <https://doi.org/10.1177/0021998313494101>.

Centea, T., Peters, G., Hendrie, K. and Nutt, S. (2017) ‘Effects of thermal gradients on defect formation during the consolidation of partially impregnated prepregs’, *Journal of Composite Materials*, 51(28), pp. 3987–4003. doi: <https://doi.org/10.1177/0021998317733317>.

Chatterjee, A. (2009) ‘Thermal degradation analysis of thermoset resins’, *Journal of Applied Polymer Science*, 114(3), pp. 1417–1425. doi: <https://doi.org/10.1002/app.30664>.

Chern, C.-S. and Poehlein, G. W. (1987) ‘A kinetic model for curing reactions of epoxides with amines’, *Polymer Engineering & Science*, 27(11), pp. 788–795. doi: <https://doi.org/10.1002/pen.760271104>.

Clayton, W. A. (1971) ‘Constituent and composite thermal conductivities of phenolic-carbon and phenolic-graphite ablators’, in *Proceedings of 12th Structures, Structural Dynamics and Materials Conference*. Anaheim, CA, USA, pp. 19–21.

Cole, C., Hechler, J. J. and Noel, D. (1991) ‘A New Approach to Modeling the Cure Kinetics of Epoxy Amine Thermosetting Resins. 2. Application to a Typical System Based on Bis[4-(diglycidylamino)phenyl]methane and Bis(4-aminophenyl) Sulfone’, *Macromolecules*, 24, pp. 3098–3110. doi: <https://doi.org/10.1021/ma00011a012>.

Conesa, C., Saleh, K., Thomas, A., Guigon, P. and Guillot, N. (2004) ‘Characterization of Flow Properties of Powder Coatings Used in the Automotive Industry’, *KONA Powder and Particle Journal*, 22, pp. 94–106. doi: <https://doi.org/10.14356/kona.2004013>.

Costa, V. A. F. and Sousa, A. C. M. (2003) ‘Modeling of flow and thermo-kinetics during the cure of thick laminated composites’, *International Journal of Thermal Sciences*, 42, pp. 15–22. doi: [https://doi.org/10.1016/S1290-0729\(02\)00003-0](https://doi.org/10.1016/S1290-0729(02)00003-0).

Daelemans, L., van der Heijden, S., De Baere, I., Muhammad, I., Van Paepegem, W., Rahier, H. and De Clerck, K. (2015) ‘Bisphenol A based polyester binder as an effective interlaminar toughener’, *Composites Part B*, 80, pp. 145–153. doi:

<https://doi.org/10.1016/j.compositesb.2015.05.044>.

Darcy, H. (1856) *Les fontaines publiques de la ville de Dijon*. Edited by V. Dalmont. Paris, France.

Dave, R., Kardos, J. L. and Duduković, M. P. (1987) 'A Model for Resin Flow During Composite Processing, Part 1: General Mathematical Development', *Polymer Composites*, 8(1), pp. 29–38. doi: <https://doi.org/10.1002/pc.750080106>.

Davies, P. and Rajapakse, Y. D. S. (2014) *Durability of Composites in a Marine Environment*. 1st edn. Springer Netherlands. doi: <https://doi.org/10.1007/978-94-007-7417-9>.

DiBenedetto, A. T. (1987) 'Prediction of the glass transition temperature of polymers: A model based on the principle of corresponding states', *Journal of Polymer Science Part B: Polymer Physics*, 25(9), pp. 1949–1969. doi: <https://doi.org/10.1002/polb.1987.090250914>.

Eddie, D. ., Lickfield, G. C., Allen, L. E. and McCollum, J. R. (1989) *Thermoplastic Coating of Carbon Fibres*. Hampton, VA, USA. Available at: <https://ntrs.nasa.gov/archive/nasa/casi.ntrs.nasa.gov/19890015117.pdf>.

ÉireComposites Teo. (2013) *GRN 918 Datasheet*.

El-Hage, Y., Hind, S. and Robitaille, F. (2018) 'Thermal conductivity of textile reinforcements for composites', *Journal of Textiles and Fibrous Materials*, 1, pp. 1–12. doi: <https://doi.org/10.1177/2515221117751154>.

Equinor (2018) *Hywind: The Supplier Puzzle*. Available at: <https://www.equinor.com/no/what-we-do/hywind-where-the-wind-takes-us/hywind-the-bits-and-pieces.html> (Accessed: 28 August 2018).

Fiore, V. and Valenza, A. (2013) '5 – Epoxy resins as a matrix material in advanced fiber-reinforced polymer (FRP) composites', in *Advanced Fibre-Reinforced Polymer (FRP) Composites for Structural Applications*. Woodhead Publishing Limited, pp. 88–121. doi: <https://doi.org/10.1533/9780857098641.1.88>.

Flaig, J. (2017) *Tidal energy giant Atlantis reports £7.3m pre-tax loss in 'very*

- challenging year*, *Institution of Mechanical Engineers*. Available at: <https://www.imeche.org/news/news-article/tidal-energy-giant-atlantis-reports-7.3m-pre-tax-loss-in-'very-challenging-year'> (Accessed: 28 August 2018).
- Flanagan, T., Maguire, J., O'Bradaigh, C. M., Mayorga, P. and Doyle, A. (2015) 'Smart Affordable Composite Blades for Tidal Energy', in *Proceedings of the 11th European Wave and Tidal Energy Conference (EWTEC)*. Nantes, France, p. 08A2-3-1-08A2-3-8.
- Frenkel, J. (1945) 'Viscous Flow of Crystalline Bodies under the Action of Surface Tension', *J. Phys. (U. S. S. R)*, 9(5), pp. 385–391.
- Gardiner, G. (2012) 'Big parts? Big tooling breakthrough', *Composites World*. Available at: <https://www.compositesworld.com/articles/big-parts-big-tooling-breakthrough>.
- Garschke, C., Parlevliet, P. P., Weimer, C. and Fox, B. L. (2013) 'Cure kinetics and viscosity modelling of a high-performance epoxy resin film', *Polymer Testing*, 32(1), pp. 150–157. doi: <https://doi.org/10.1016/j.polymertesting.2012.09.011>.
- Garschke, C., Weimer, C., Parlevliet, P. P. and Fox, B. L. (2012) 'Out-of-autoclave cure cycle study of a resin film infusion process using in situ process monitoring', *Composites Part A: Applied Science and Manufacturing*, 43(6), pp. 935–944. doi: <https://doi.org/10.1016/j.compositesa.2012.01.003>.
- Gebart, B. R. (1992) 'Permeability of Unidirectional Reinforcements for RTM', *Journal of Composite Materials*, 26(8), pp. 1100–1133. doi: <https://doi.org/10.1177/002199839202600802>.
- Gherlone, L., Rossini, T. and Stula, V. (1998) 'Powder coatings and differential scanning calorimetry: the perfect fit', *Progress in Organic Coatings*, 34(1–4), pp. 57–63. doi: [https://doi.org/10.1016/S0300-9440\(98\)00039-3](https://doi.org/10.1016/S0300-9440(98)00039-3).
- Goldsworthy, M. J. (2014) 'Measurements of water vapour sorption isotherms for RD silica gel, AQSOA-Z01, AQSOA-Z02, AQSOA-Z05 and CECA zeolite 3A', *Microporous and Mesoporous Materials*, 196, pp. 59–67. doi: <https://doi.org/10.1016/j.micromeso.2014.04.046>.

- Greco, A. and Maffezzoli, A. (2003) 'Polymer Melting and Polymer Powder Sintering by Thermal Analysis', *Journal of Thermal Analysis and Calorimetry*, 72, pp. 1167–1174. doi: <https://doi.org/10.1023/A:1025096432699>.
- Greenspec (2018) *Insulation materials and their thermal properties*. Available at: <http://www.greenspec.co.uk/building-design/insulation-materials-thermal-properties/>.
- Grogan, D., Flanagan, M., Walls, M., Leen, S., Doyle, A., Harrison, N., Mamalis, D. and Goggins, J. (2018) 'Influence of microstructural defects and hydrostatic pressure on water absorption in composite materials for tidal energy', *Journal of Composite Materials*, 52(21), pp. 2899–2917. doi: <https://doi.org/10.1177/0021998318755428>.
- Grunenfelder, L. K., Centea, T., Hubert, P. and Nutt, S. R. (2013) 'Effect of room-temperature out-time on tow impregnation in an out-of-autoclave prepreg', *Composites Part A: Applied Science and Manufacturing*, 45, pp. 119–126. doi: <https://doi.org/10.1016/J.COMPOSITESA.2012.10.001>.
- Grunenfelder, L. K. and Nutt, S. R. (2010) 'Void formation in composite prepreps – Effect of dissolved moisture', *Composites Science and Technology*, 70(16), pp. 2304–2309. doi: <https://doi.org/10.1016/j.compscitech.2010.09.009>.
- Grunenfelder, L. K. and Nutt, S. R. (2012) 'Prepreg age monitoring via differential scanning calorimetry', *Journal of Reinforced Plastics and Composites*, 31(5), pp. 295–302. doi: <https://doi.org/10.1177/0731684411431020>.
- Gurit Holding AG (2015) *Ampreg 22 - Epoxy Laminating System - Version 19*. Wattwil, Switzerland.
- Gutowski, T. G., Cai, Z., Bauer, S., Boucher, D., Kingery, J. and Wineman, S. (1987) 'Consolidation Experiments for Laminate Composites', *Journal of Composite Materials*, 21(7), pp. 650–669. doi: <https://doi.org/10.1177/002199838702100705>.
- Halley, P. J. and Mackay, M. E. (1996) 'Chemorheology of thermosets - an overview', *Polymer Engineering & Science*, 36(5), pp. 593–609. doi: <https://doi.org/10.1002/pen.10447>.

- Hardis, R., Jessop, J. L. P., Peters, F. E. and Kessler, M. R. (2013) 'Cure kinetics characterization and monitoring of an epoxy resin using DSC, Raman spectroscopy, and DEA', *Composites Part A: Applied Science and Manufacturing*, 49, pp. 100–108. doi: <https://doi.org/10.1016/j.compositesa.2013.01.021>.
- Harper, P., Hallett, S., Fleming, A. and Dawson, M. (2016) '9 – Advanced fibre-reinforced composites for marine renewable energy devices', in *Marine Applications of Advanced Fibre-Reinforced Composites*. Woodhead Publishing, pp. 217–232. doi: <https://doi.org/10.1016/B978-1-78242-250-1.00009-0>.
- Helmus, R., Centea, T., Hubert, P. and Hinterhölzl, R. (2016) 'Out-of-autoclave prepreg consolidation: Coupled air evacuation and prepreg impregnation modeling', *Journal of Composite Materials*, 50(10), pp. 1403–1413. doi: <https://doi.org/10.1177/0021998315592005>.
- Hill, L. W. (1997) 'Calculation of crosslink density in short chain networks', *Progress in Organic Coatings*, 31(3), pp. 235–243. doi: [https://doi.org/10.1016/S0300-9440\(97\)00081-7](https://doi.org/10.1016/S0300-9440(97)00081-7).
- Hollaway, L. C. (2013a) '19 – Sustainable energy production: key material requirements', in *Advanced Fibre-Reinforced Polymer (FRP) Composites for Structural Applications*. Woodhead Publishing Limited, pp. 705–736. doi: <https://doi.org/10.1533/9780857098641.4.705>.
- Hollaway, L. C. (2013b) '20 – Advanced fibre-reinforced polymer (FRP) composite materials for sustainable energy technologies', in *Advanced Fibre-Reinforced Polymer (FRP) Composites for Structural Applications*. Woodhead Publishing Limited, pp. 737–779. doi: <https://doi.org/10.1533/9780857098641.4.737>.
- Hollaway, L. C. (2014) '10 – High performance fibre-reinforced composites for sustainable energy applications', in *High Performance Textiles and their Applications*. Woodhead Publishing, pp. 366–417. doi: <https://doi.org/10.1533/9780857099075.366>.
- Hsiao, K.-T. and Heider, D. (2012) '10 – Vacuum assisted resin transfer molding (VARTM) in polymer matrix composites', in *Manufacturing Techniques for Polymer*

- Matrix Composites (PMCs)*. Woodhead Publishing Limited, pp. 310–347. doi:
<https://doi.org/10.1533/9780857096258.3.310>.
- Hsiao, K.-T., Laudorn, H. and Advani, S. G. (2001) ‘Experimental Investigation of Heat Dispersion Due to Impregnation of Viscous Fluids in Heated Fibrous Porous During Composites Processing’, *Journal of Heat Transfer*, 123(1), pp. 178–187. doi:
<https://doi.org/10.1115/1.1338131>.
- Hubert, P. (1996) *Aspects of flow and compaction of laminated composite shapes during cure*. PhD Thesis, University of British Columbia.
- ISO 11357-1 (2009) *Plastics - Differential scanning calorimetry (DSC) - Part 1: General principles*.
- ISO 11357-5 (2013) *Plastics - Differential scanning calorimetry (DSC) - Part 5: Determination of characteristic reaction-curve temperatures and times, enthalpy of reaction and degree of conversion*.
- ISO 11358-1 (2014) *Plastics - Thermogravimetry (TG) of polymers - Part 1: General principles*.
- ISO 6721-10 (1999) *Plastics - Determination of dynamic mechanical properties - Part 10: Complex shear viscosity using a parallel-plate oscillatory rheometer*.
- ISO 6721-5 (1996) *Plastics — Determination of dynamic mechanical properties — Part 5: Flexural vibration - Non-resonance method*.
- Jacob, G. C., Hoevel, B., Pham, H. Q., Dettloff, M. L., Verghese, N. E., Turakhia, R. H., Hunter, G., Mandell, J. F. and Samborsky, D. D. (2009) ‘Technical advances in epoxy technology for wind turbine blade composite fabrication’, in *Proceedings of 2009 SAMPE Fall Technical Conference and Exhibition*.
- Johns Manville (2018) *Single-end Roving Selector Guide*. Available at:
<https://www.jm.com/content/dam/jm/global/en/engineered-products/EP-documents/product-selector-guide/Direct Roving or Single End Roving Product Selector Guide 2018.pdf>.
- Joshi, S. C., Liu, X. L. and Lam, Y. C. (1999) ‘A numerical approach to the

modeling of polymer curing in fibre-reinforced composites', *Composites Science and Technology*, 59(7), pp. 1003–1013. doi: [https://doi.org/10.1016/S0266-3538\(98\)00138-9](https://doi.org/10.1016/S0266-3538(98)00138-9).

Juska, T. D., Musser, B. S., Jordan, B. P. and Hall, J. C. (2009) 'The new infusion: Oven vacuum bag prepreg fabrication', in *Proceedings of SAMPE '09 Spring Symposium*. Baltimore, MD, USA.

Kalkuhl, M., Edenhofer, O. and Lessmann, K. (2013) 'Renewable energy subsidies: Second-best policy or fatal aberration for mitigation?', *Resource and Energy Economics*, 35(3), pp. 217–234. doi: <https://doi.org/10.1016/J.RESENEECO.2013.01.002>.

Kamal, M. R. (1974) 'Thermoset characterization for moldability analysis', *Polymer Engineering & Science*, 14(3), pp. 231–239. doi: <https://doi.org/10.1002/pen.760140312>.

Kamal, M. R. and Sourour, S. (1973) 'Kinetics and Thermal Characterization of Thermoset Cure', *Polymer Engineering & Science*, 13(1), pp. 59–64. doi: <https://doi.org/10.1002/pen.760130110>.

Kandis, M. and Bergman, T. L. (1997) 'Observation, Prediction, and Correlation of Geometric Shape Evolution Induced by Non-Isothermal Sintering of Polymer Powder', *Journal of Heat Transfer*, 119(4), pp. 824–831. doi: <https://doi.org/10.1115/1.2824189>.

Kennedy, C. R. (2013) *Fatigue of Glass Fibre Composites in Marine Renewable Energy*. PhD Thesis, National University of Ireland, Galway.

Kenny, J. M. and Opalicki, M. (1993) 'Influence of the chemorheology of toughened epoxy matrices on the processing behavior of high performance composites', *Makromolekulare Chemie. Macromolecular Symposia*, 68(1), pp. 41–56. doi: <https://doi.org/10.1002/masy.19930680106>.

Khoun, L., Centea, T. and Hubert, P. (2009) 'Characterization Methodology of Thermoset Resins for the Processing of Composite Materials -- Case Study: CYCOM 890RTM Epoxy Resin', *Journal of Composite Materials*, 44(11), pp. 1397–1415.

doi: <https://doi.org/10.1177/0021998309353960>.

Khoun, L. and Hubert, P. (2010) 'Cure shrinkage characterization of an epoxy resin system by two in situ measurement methods', *Polymer Composites*, 31(9), pp. 1603–1610. doi: <https://doi.org/10.1002/pc.20949>.

Kim, D., Centea, T. and Nutt, S. R. (2014) 'Out-time effects on cure kinetics and viscosity for an out-of-autoclave (OOA) prepreg: Modelling and monitoring', *Composites Science and Technology*, 100, pp. 63–69. doi: <https://doi.org/10.1016/j.compscitech.2014.05.027>.

Kim, D., Centea, T. and Nutt, S. R. (2017) 'Modelling and monitoring of out-time and moisture absorption effects on cure kinetics and viscosity for an out-of-autoclave (OoA) prepreg', *Composites Science and Technology*, 138, pp. 201–208. doi: <https://doi.org/10.1016/J.COMPSCITECH.2016.11.023>.

Kluge, N. E. J., Lundström, T. S., Ljung, A.-L., Westerberg, L. G. and Nyman, T. (2016) 'An experimental study of temperature distribution in an autoclave', *Journal of Reinforced Plastics and Composites*, 35(7), pp. 566–578. doi: <https://doi.org/10.1177/0731684415624768>.

Kontopoulou, M. and Vlachopoulos, J. (2001) 'Melting and densification of thermoplastic powders', *Polymer Engineering & Science*, 41(2), pp. 155–169. doi: <https://doi.org/10.1002/pen.10718>.

Kratz, J., Hsiao, K., Fernlund, G. and Hubert, P. (2012) 'Thermal models for MTM45-1 and Cycom 5320 out-of-autoclave prepreg resins', *Journal of Composite Materials*, 47(3), pp. 341–352. doi: <https://doi.org/10.1177/0021998312440131>.

Kratz, J. and Hubert, P. (2013) 'Anisotropic air permeability in out-of-autoclave prepregs: Effect on honeycomb panel evacuation prior to cure', *Composites Part A: Applied Science and Manufacturing*, 49, pp. 179–191. doi: <https://doi.org/10.1016/J.COMPOSITESA.2013.02.013>.

Kravchenko, O. G., Kravchenko, S. G. and Pipes, R. B. (2016) 'Chemical and thermal shrinkage in thermosetting prepreg', *Composites Part A: Applied Science and Manufacturing*, 80. doi: <https://doi.org/10.1016/j.compositesa.2015.10.001>.

- Kreyszig, E., Kreyszig, H. and Norminton, E. J. (2011) *Advanced Engineering Mathematics*. 10th edn. John Wiley & Sons, Ltd.
- Kuentzer, N., Simacek, P., Advani, S. G. and Walsh, S. (2006) 'Permeability characterization of dual scale fibrous porous media', *Composites Part A: Applied Science and Manufacturing*, 37(11), pp. 2057–2068. doi: <https://doi.org/10.1016/j.compositesa.2005.12.005>.
- Lee, C. (2004) *An Investigation into the Transverse Thermal Conductivity of Fibre Beds*. MEng Thesis, University of Limerick.
- Lee, S.-Y. and Springer, G. S. (1990) 'Filament Winding Cylinders I. Process Model', *Journal of Composite Materials*, 24(12), pp. 1270–1298. doi: <https://doi.org/10.1177/002199839002401202>.
- Lionetto, F., Moscatello, A. and Maffezzoli, A. (2016) 'Effect of binder powders added to carbon fiber reinforcements on the chemoreology of an epoxy resin for composites', *Composites Part B*, 112, pp. 243–250. doi: <https://doi.org/10.1016/j.compositesb.2016.12.031>.
- Liu, J. (D.), Sue, H.-J., Thompson, Z. J., Bates, F. S., Dettloff, M., Jacob, G., Verghese, N. and Pham, H. (2009) 'Effect of crosslink density on fracture behavior of model epoxies containing block copolymer nanoparticles', *Polymer*, 50(19), pp. 4683–4689. doi: <https://doi.org/10.1016/J.POLYMER.2009.05.006>.
- Loos, A. C. and MacRae, J. D. (1996) 'A process simulation model for the manufacture of a blade-stiffened panel by the resin film infusion process', *Composites Science and Technology*, 56(3), pp. 273–289. doi: [https://doi.org/10.1016/0266-3538\(96\)80008-X](https://doi.org/10.1016/0266-3538(96)80008-X).
- Loos, A. C. and Springer, G. S. (1983) 'Curing of Epoxy Matrix Composites', *Journal of Composite Materials*, 17(2), pp. 135–169. doi: <https://doi.org/10.1177/002199838301700204>.
- Luchoo, R., Harper, L. T., Bond, M. D., Warrior, N. A. and Dodworth, A. (2010) 'Net shape spray deposition for compression moulding of discontinuous fibre composites for high performance applications', *Plastics, Rubber and Composites*,

- 39(3–5), pp. 216–231. doi: <https://doi.org/10.1179/174328910X12647080902493>.
- Maguire, J. M., Roy, A. S., Doyle, D. A., Logan, M. G. and Brádaigh, C. Ó. (2015) ‘Resin characterisation for numerical modelling of through-thickness resin flow during OOA processing of thick-section wind or tidal turbine blades’, in *Proceedings of 20th International Conference on Composite Materials*. Copenhagen, Denmark.
- Mamalis, D., Flanagan, T. and Ó Brádaigh, C. M. (2018) ‘Effect of fibre straightness and sizing in carbon fibre reinforced powder epoxy composites’, *Composites Part A: Applied Science and Manufacturing*, 110, pp. 93–105. doi: <https://doi.org/10.1016/j.compositesa.2018.04.013>.
- Martinez, G. M. (1990) ‘FAST CURES FOR THICK LAMINATED ORGANIC MATRIX COMPOSITES’, *Chemical Engineering Science*, 46(2), pp. 439–450. doi: [https://doi.org/10.1016/0009-2509\(91\)80005-J](https://doi.org/10.1016/0009-2509(91)80005-J).
- Michaud, V. and Manson, J.-A. E. (2001) ‘Impregnation of Compressible Fiber Mats with a Thermoplastic Resin. Part I: Theory’, *Journal of Composite Materials*, 35(13), pp. 1150–1173. doi: <https://doi.org/10.1177/002199801772662271>.
- Miller, A., Wei, C. and Gibson, A. G. (1996) ‘Manufacture of polyphenylene sulfide (PPS) matrix composites via the powder impregnation route’, *Composites Part A*, 27(1), pp. 49–56. doi: [https://doi.org/10.1016/1359-835X\(95\)00010-Y](https://doi.org/10.1016/1359-835X(95)00010-Y).
- Misev, T. A. and van der Linde, R. (1998) ‘Powder coatings technology: new developments at the turn of the century’, *Progress in Organic Coatings*, 34(1–4), pp. 160–168. doi: [https://doi.org/10.1016/S0300-9440\(98\)00029-0](https://doi.org/10.1016/S0300-9440(98)00029-0).
- Mohan, J., Ivanković, A. and Murphy, N. (2013) ‘Effect of prepreg storage humidity on the mixed-mode fracture toughness of a co-cured composite joint’, *Composites Part A: Applied Science and Manufacturing*, 45, pp. 23–34. doi: <https://doi.org/10.1016/j.compositesa.2012.09.010>.
- Monaghan, P. F., Brogan, M. T. and Oosthuizen, P. H. (1991) ‘Heat transfer in an autoclave for processing thermoplastic composites’, *Composites Manufacturing*. Elsevier, 2(3–4), pp. 233–242. doi: [https://doi.org/10.1016/0956-7143\(91\)90145-7](https://doi.org/10.1016/0956-7143(91)90145-7).

- Murray, J. J., Pappa, E. J., Mamalis, D., Breathnach, G., Doyle, A., Flanagan, T., Di Noi, S. and Ó Brádaigh, C. M. (2018) 'Characterisation of carbon fibre reinforced powder epoxy composites for wind energy blades', in *Proceedings of 18th European Conference on Composite Materials*. Athens, Greece.
- National Instruments (2018) *Measuring Position and Displacement with LVDTs*. Available at: <http://www.ni.com/white-paper/3638/en/>.
- New Era Materials Sp. z o.o. (2014) *A-S-SET 02 Product Datasheet*.
- Nicolini, M. and Tavoni, M. (2017) 'Are renewable energy subsidies effective? Evidence from Europe', *Renewable and Sustainable Energy Reviews*, 74, pp. 412–423. doi: <https://doi.org/10.1016/J.RSER.2016.12.032>.
- Nijssen, R. and de Winkel, G. D. (2016) '5 - Developments in materials for offshore wind turbine blades', in *Offshore Wind Farms*. Woodhead Publishing, pp. 85–104. doi: <https://doi.org/10.1016/B978-0-08-100779-2.00005-2>.
- Novo, P. J., Silva, J. F., Nunes, J. P. and Marques, A. T. (2016) 'Pultrusion of fibre reinforced thermoplastic pre-impregnated materials', *Composites Part B*, 89, pp. 328–339. doi: <https://doi.org/10.1016/j.compositesb.2015.12.026>.
- O&M Heater Co. Ltd. (2018) *Products - Silicone Rubber Heater - Stretch Type*. Available at: http://om-heater.jp/english/products/srh_strc.html (Accessed: 6 December 2018).
- Ó Brádaigh, C. M., Doyle, A., Doyle, D. and Feerick, P. J. (2011) 'Electrically-Heated Ceramic Composite Tooling for Out-of-Autoclave Manufacturing of Large Composite Structures', *SAMPE Journal*, 47(4).
- Oh, J. H. (2007) 'Prediction of Temperature Distribution During Curing Thick Thermoset Composite Laminates', *Materials Science Forum*, 545, pp. 427–430. doi: <https://doi.org/10.4028/www.scientific.net/MSF.544-545.427>.
- Oh, J. H. and Lee, D. G. (2002) 'Cure Cycle for Thick Glass/Epoxy Composite Laminates', *Journal of Composite Materials*, 36(1), pp. 19–45. doi: <https://doi.org/10.1177/0021998302036001300>.

- Osterhold, M. and Niggemann, F. (1998) 'Viscosity–temperature behaviour of powder coatings', *Progress in Organic Coatings*. Elsevier, 33(1), pp. 55–60. doi: [https://doi.org/10.1016/S0300-9440\(98\)00008-3](https://doi.org/10.1016/S0300-9440(98)00008-3).
- Padaki, S. and Drzal, L. T. (1999) 'A simulation study on the effects of particle size on the consolidation of polymer powder impregnated tapes', *Composites Part A: Applied Science and Manufacturing*, 30(3), pp. 325–337. doi: [https://doi.org/10.1016/S1359-835X\(98\)00115-8](https://doi.org/10.1016/S1359-835X(98)00115-8).
- Park, H. C., Goo, N. S., Min, K. J. and Yoon, K. J. (2003) 'Three-dimensional cure simulation of composite structures by the finite element method', *Composite Structures*, 62(1), pp. 51–57. doi: [https://doi.org/10.1016/S0263-8223\(03\)00083-7](https://doi.org/10.1016/S0263-8223(03)00083-7).
- Parra, D. F., Mercuri, L. P., Matos, J. R., Brito, H. F. and Romano, R. R. (2002) 'Thermal behavior of the epoxy and polyester powder coatings using thermogravimetry/differential thermal analysis coupled gas chromatography/mass spectrometry (TG/DTA–GC/MS) technique: identification of the degradation products', *Thermochimica Acta*, 386, pp. 143–151. doi: [https://doi.org/10.1016/S0040-6031\(01\)00809-7](https://doi.org/10.1016/S0040-6031(01)00809-7).
- Pascault, J.-P., Sautereau, H., Verdu, J. and Williams, R. J. J. (2002) *Thermosetting polymers*. 1st edn. CRC Press.
- Pillai, V., Beris, A. N. and Dhurjati, P. (1997) 'Intelligent Curing of Thick Composites Using a Knowledge-Based System', *Journal of Composite Materials*, 31(1), pp. 22–51. doi: <https://doi.org/10.1177/002199839703100103>.
- Price, R. V. (1973) 'Production of Impregnated Rovings'. United States Patent.
- Pusatcioglu, S. Y., Hassler, J. C., Fricke, A. L. and McGee, H. A. (1980) 'Effect of temperature gradients on cure and stress gradients in thick thermoset castings', *Journal of Applied Polymer Science*, 25(3), pp. 381–393. doi: <https://doi.org/10.1002/app.1980.070250305>.
- Radanitsch, J. (2014) 'Multi-layered Carbon Stacks for Large Wind Turbine Blades', in *Proceedings of CAMX 2014*. Orlando, FL, USA.

- Ramasamy, A., Wang, Y. and Muzzy, J. (1996) 'Braided thermoplastic composites from powder-coated towpregs. Part I: Towpreg characterization', *Polymer Composites*, 17(3), pp. 497–504. doi: <https://doi.org/10.1002/pc.10639>.
- Ramis, X., Cadenato, A., Morancho, J. M. and Salla, J. M. (2003) 'Curing of a thermosetting powder coating by means of DMTA, TMA and DSC', *Polymer*, 44(7), pp. 2067–2079. doi: [https://doi.org/10.1016/S0032-3861\(03\)00059-4](https://doi.org/10.1016/S0032-3861(03)00059-4).
- Recktenwald, G. W. (2011) *Finite-Difference Approximations to the Heat Equation*. Available at: <http://math5022spring2010.weebly.com/uploads/3/6/3/0/3630523/fdheat.pdf>.
- Renewable Energy World (2016) *World's Longest Wind Turbine Blade Unveiled in Denmark*, *Renewable Energy World*. Available at: <http://www.renewableenergyworld.com/articles/2016/06/world-s-longest-wind-turbine-blade-unveiled-in-denmark.html> (Accessed: 19 March 2018).
- Robert, C., Mamalis, D., Alam, P., Lafferty, A. D., Ó Cadhain, C., Breathnach, G., McCarthy, E. D. and Ó Brádaigh, C. M. (2018) 'Powder Epoxy Based UD-CFRP Manufacturing Routes For Turbine Blade Application', in *Proceedings of SAMPE Europe Conference '18*. Southampton, UK.
- Rouw, A. C. (1998) 'Model epoxy powder coatings and their adhesion to steel', *Progress in Organic Coatings*, 34(1–4), pp. 181–192. doi: [https://doi.org/10.1016/S0300-9440\(98\)00018-6](https://doi.org/10.1016/S0300-9440(98)00018-6).
- Ruiz, E. and Trochu, F. (2005) 'Numerical analysis of cure temperature and internal stresses in thin and thick RTM parts', *Composites Part A: Applied Science and Manufacturing*, 36(6), pp. 806–826. doi: <https://doi.org/10.1016/j.compositesa.2004.10.021>.
- Ruiz, E. and Trochu, F. (2006) 'Multi-criteria thermal optimization in liquid composite molding to reduce processing stresses and cycle time', *Composites Part A: Applied Science and Manufacturing*, 37(6), pp. 913–924. doi: <https://doi.org/10.1016/j.compositesa.2005.06.010>.
- Saad, G. R. and Serag Eldin, A. F. (2012) 'Isothermal cure kinetics of uncatalyzed

and catalyzed diglycidyl ether of bisphenol-A/carboxylated polyester hybrid powder coating', *Journal of Thermal Analysis and Calorimetry*, 110(3), pp. 1425–1430. doi: <https://doi.org/10.1007/s10973-011-2074-8>.

Saliba, P. A., Mansur, A. A., Santos, D. B. and Mansur, H. S. (2015) 'Fusion-bonded epoxy composite coatings on chemically functionalized API steel surfaces for potential deep-water petroleum exploration', *Applied Adhesion Science*, 3(1), pp. 1–22. doi: <https://doi.org/10.1186/s40563-015-0052-2>.

Schlimbach, J. and Ogale, A. (2012) '14 – Out-of-autoclave curing process in polymer matrix composites', in *Manufacturing Techniques for Polymer Matrix Composites (PMCs)*. Woodhead Publishing Limited, pp. 435–480. doi: <https://doi.org/10.1533/9780857096258.3.435>.

Schramm, G. (1994) *A Practical Approach to Rheology and Rheometry*. 2nd edn. Gebrueder HAAKE GmbH.

Sharma, S. and Luzinov, I. (2011) 'Ultrasonic curing of one-part epoxy system', *Journal of Composite Materials*, 45(21), pp. 2217–2224. doi: <https://doi.org/10.1177/0021998311401075>.

Sharp, N., Li, C., Strachan, A., Adams, D. and Pipes, R. B. (2017) 'Effects of Water on Epoxy Cure Kinetics and Glass Transition Temperature Utilizing Molecular Dynamics Simulations', *Journal of Polymer Science, Part B: Polymer Physics*, 55, pp. 1150–1159. doi: <https://doi.org/10.1002/polb.24357>.

Shi, L. (2016) *Heat Transfer in the Thick Thermoset Composites*. PhD Thesis, Technische Univeristeit Delft.

Shin, D. D. and Hahn, H. T. (2004) 'Compaction of Thick Composites: Simulation and Experiment', *Polymer Composites*, 25(1), pp. 49–59. doi: <https://doi.org/10.1002/pc.20004>.

Siemens (2012) *Siemens strengthens its position in future-oriented market for marine current power plants – Acquisition of Marine Current Turbines*. Available at: [https://www.siemens.com/press/en/presspicture/?press=/en/presspicture/pictures-photonews/2012/pn201201.php&content\[\]=EX&content\[\]=CC&content\[\]=CT&cont](https://www.siemens.com/press/en/presspicture/?press=/en/presspicture/pictures-photonews/2012/pn201201.php&content[]=EX&content[]=CC&content[]=CT&cont)

ent[]=EH&content[]=E&content[]=Corp&content[]=WP (Accessed: 28 August 2018).

Sloan, J. (2012) ‘Tidal turbine blade toughened for turbulent salt sea’, *Composites World*. Available at: <https://www.compositesworld.com/articles/tidal-turbine-blade-toughened-for-turbulent-salt-sea>.

Sorrentino, L. and Bellini, C. (2015) ‘Validation of a Methodology for Cure Process Optimization of Thick Composite Laminates’, *Polymer-Plastics Technology and Engineering*, 54, pp. 1803–1811. doi: <https://doi.org/10.1080/03602559.2015.1050513>.

Sorrentino, L., Polini, W. and Bellini, C. (2014) ‘To design the cure process of thick composite parts: experimental and numerical results’, *Advanced Composite Materials*, 23(3), pp. 225–238. doi: <https://doi.org/10.1080/09243046.2013.847780>.

Sozer, E. M., Simacek, P. and Advani, S. G. (2012) ‘9 – Resin transfer molding (RTM) in polymer matrix composites’, in *Manufacturing Techniques for Polymer Matrix Composites (PMCs)*. Woodhead Publishing Limited, pp. 245–309. doi: <https://doi.org/10.1533/9780857096258.3.243>.

Springer, G. S. and Tsai, S. W. (1967) ‘Thermal Conductivities of Unidirectional Materials’, *Journal of Composite Materials*, 1(2), pp. 166–173. doi: <https://doi.org/10.1177/002199836700100206>.

Stone, K. R. and Springer, J. J. (1995) *Advanced Composites Technology Case Study at NASA Langley Research Center*.

Struzziero, G. and Skordos, A. A. (2017) ‘Multi-objective optimisation of the cure of thick components’, *Composites Part A: Applied Science and Manufacturing*, 93, pp. 126–136. doi: <https://doi.org/10.1016/J.COMPOSITESA.2016.11.014>.

Summerscales, J. (2016) ‘2 – Composites manufacturing for marine structures’, in *Marine Applications of Advanced Fibre-Reinforced Composites*. Woodhead Publishing, pp. 19–55. doi: <https://doi.org/10.1016/B978-1-78242-250-1.00002-8>.

Surface Measurement Systems (2018) *DVS Adventure*. Available at:

<https://www.surfacemeasurementsystems.com/products/dynamic-vapor-sorption-instruments/vapor-sorption-analyzer/dvs-adventure/> (Accessed: 16 September 2018).

Tahir, M. W., Hallström, S. and Åkermo, M. (2014) 'Effect of dual scale porosity on the overall permeability of fibrous structures', *Composites Science and Technology*, 103, pp. 56–62. doi: <https://doi.org/10.1016/J.COMPSCITECH.2014.08.008>.

Tan, H. and Pillai, K. M. (2012) 'Multiscale modeling of unsaturated flow of dual-scale fiber preform in liquid composite molding II: Non-isothermal flows', *Composites Part A: Applied Science and Manufacturing*, 43(1), pp. 14–28. doi: <https://doi.org/10.1016/j.compositesa.2011.06.012>.

Tanoglu, M. and Tugrul Seyhan, A. (2003) 'Investigating the effects of a polyester preforming binder on the mechanical and ballistic performance of E-glass fiber reinforced polyester composites', *International Journal of Adhesion & Adhesives*, 23, pp. 1–8. doi: [https://doi.org/10.1016/S0143-7496\(02\)00061-1](https://doi.org/10.1016/S0143-7496(02)00061-1).

The European Technology and Innovation Platform for Ocean Energy (2016) *Strategic Research Agenda for Ocean Energy European Technology and Innovation Platform for Ocean Energy*. Available at: https://www.oceanenergy-europe.eu/wp-content/uploads/2017/03/TPOcean-Strategic_Research_Agenda_Nov2016.pdf (Accessed: 28 August 2018).

Thomas, A., Saleh, K., Guigon, P. and Czechowski, C. (2008) 'Characterisation of electrostatic properties of powder coatings in relation with their industrial application', *Powder Technology*, 190(1–2), pp. 230–235. doi: <https://doi.org/10.1016/j.powtec.2008.04.072>.

Tian, X., Peng, G., Yan, M., He, S. and Yao, R. (2018) 'Process prediction of selective laser sintering based on heat transfer analysis for polyamide composite powders', *International Journal of Heat and Mass Transfer*, 120, pp. 379–386. doi: <https://doi.org/10.1016/J.IJHEATMASSTRANSFER.2017.12.045>.

Toray Carbon Fibers America (2019) *T700S Data Sheet*. Available at: https://www.toraycma.com/file_viewer.php?id=4459.

Toribio, F., Bellat, J. P., Nguyen, P. H. and Dupont, M. (2004) 'Adsorption of water

vapor by poly(styrenesulfonic acid), sodium salt: isothermal and isobaric adsorption equilibria', *Journal of Colloid and Interface Science*, 280(2), pp. 315–321. doi: <https://doi.org/10.1016/J.JCIS.2004.08.009>.

Twardowski, T. E., Lin, S. E. and Geil, P. H. (1993) 'Curing in Thick Composite Laminates: Experiment and Simulation', *Journal of Composite Materials*, 27(3), pp. 216–250. doi: <https://doi.org/10.1177/002199839302700301>.

Vernet, N., Ruiz, E., Advani, S., Alms, J. B., Aubert, M., Barburski, M., Barari, B., Beraud, J. M., Berg, D. C., Correia, N., Danzi, M., Delavrière, T., Dickert, M., Di Fratta, C., Endruweit, A., Ermanni, P., Francucci, G., Garcia, J. A., George, A., Hahn, C., Klunker, F., Lomov, S. V, Long, A., Louis, B., Maldonado, J., Meier, R., Michaud, V., Perrin, H., Pillai, K., Rodriguez, E., Trochu, F., Verheyden, S., Wietgreffe, M., Xiong, W., Zaremba, S. and Ziegmann, G. (2014) 'Experimental determination of the permeability of engineering textiles: Benchmark II', *COMPOSITES PART A*, 61, pp. 172–184. doi: <https://doi.org/10.1016/j.compositesa.2014.02.010>.

White, S. R. and Kim, Y. K. (1996) 'Staged curing of composite materials', *Composites Part A: Applied Science and Manufacturing*, 27(3), pp. 219–227. doi: [https://doi.org/10.1016/1359-835X\(95\)00023-U](https://doi.org/10.1016/1359-835X(95)00023-U).

Wieland, B. and Ropte, S. (2017) 'Process Modeling of Composite Materials for Wind-Turbine Rotor Blades: Experiments and Numerical Modeling', *Materials*, 10(10), pp. 1157–1169. doi: <https://doi.org/10.3390/ma10101157>.

Winter, H. H. (1987) 'Can the gel point of a cross-linking polymer be detected by the $G' - G''$ crossover?', *Polymer Engineering and Science*, 27(22), pp. 1698–1702. doi: <https://doi.org/10.1002/pen.760272209>.

Witzeman, J. S. (1996) 'Studies on low temperature curable powder coatings', *Progress in Organic Coatings*, 27(1–4), pp. 269–276. doi: [https://doi.org/10.1016/0300-9440\(95\)00543-9](https://doi.org/10.1016/0300-9440(95)00543-9).

Woolard, D. E. and Ramani, K. (1995) 'Electric field modeling for electrostatic powder coating of a continuous fiber bundle', *Journal of Electrostatics*, 35(4), pp.

373–387. doi: [https://doi.org/10.1016/0304-3886\(95\)00029-A](https://doi.org/10.1016/0304-3886(95)00029-A).

Wu, W., Klunker, F., Xie, L., Jiang, B. and Ziegmann, G. (2013) ‘Simultaneous binding and ex situ toughening concept for textile reinforced pCBT composites: Influence of preforming binders on interlaminar fracture properties’, *Composites Part A*, 53, pp. 190–203. doi: <https://doi.org/10.1016/j.compositesa.2013.06.013>.

Wu, W., Xie, L., Jiang, B. and Ziegmann, G. (2013) ‘Influence of textile preforming binder on the thermal and rheological properties of the catalyzed cyclic butylene terephthalate oligomers’, *Composites Part B*, 55, pp. 453–462. doi: <https://doi.org/10.1016/j.compositesb.2013.07.005>.

Wuzella, G., Kandelbauer, A., Mahendran, A. R., Müller, U. and Teischinger, A. (2014) ‘Influence of thermo-analytical and rheological properties of an epoxy powder coating resin on the quality of coatings on medium density fibreboards (MDF) using in-mould technology’, *Progress in Organic Coatings*, 77(10), pp. 1539–1546. doi: <https://doi.org/10.1016/j.porgcoat.2013.10.016>.

Xue, S. and Barlow, J. W. (1990) ‘Thermal Properties of Powders’, in *Proceedings of 1990 International Solid Freeform Fabrication Symposium*, pp. 179–185.

Yan, X. (2008) ‘Finite Element Simulation of Cure of Thick Composite: Formulations and Validation Verification’, *Journal of Reinforced Plastics and Composites*, 27(4), pp. 339–355. doi: <https://doi.org/10.1177/0731684407083007>.

Yang, P., Varughese, B. and Muzzy, J. D. (1991) ‘Flexible thermoset towpregs by electrostatic powder fusion coating’, in *Proceedings of 36th International SAMPE Symposium and Exhibition*. San Diego, USA.

Yi, S., Hilton, H. H. and Ahmad, M. F. (1997) ‘A Finite Element Approach for Cure Simulation of Thermosetting Matrix Composites’, *Computers & Structures*, 64(1–4), pp. 383–388. doi: [https://doi.org/10.1016/S0045-7949\(96\)00156-3](https://doi.org/10.1016/S0045-7949(96)00156-3).

Young, W.-B. (1994) ‘Three-dimensional nonisothermal mold filling simulations in resin transfer molding’, *Polymer Composites*, 15(2), pp. 118–127. doi: <https://doi.org/10.1002/pc.750150205>.

- Young, W.-B. (1995) 'Compacting Pressure and Cure Cycle for Processing of Thick Composite Laminates', *Composites Science and Technology*, 54(3), pp. 299–306. doi: [https://doi.org/10.1016/0266-3538\(95\)00067-4](https://doi.org/10.1016/0266-3538(95)00067-4).
- Yousefi, A., Lafleur, P. G. and Gauvin, R. (1997) 'Kinetic studies of thermoset cure reactions: A review', *Polymer Composites*, 18(2), pp. 157–168. doi: <https://doi.org/10.1002/pc.10270>.
- Yuan, X., Carter, B. P. and Schmidt, S. J. (2011) 'Determining the Critical Relative Humidity at which the Glassy to Rubbery Transition Occurs in Polydextrose Using an Automatic Water Vapor Sorption Instrument', *Journal of Food Science*, 76(1), pp. E78–E89. doi: <https://doi.org/10.1111/j.1750-3841.2010.01884.x>.
- Zhou, F., Kuentzer, N., Simacek, P., Advani, S. G. and Walsh, S. (2006) 'Analytic characterization of the permeability of dual-scale fibrous porous media', *Composites Science and Technology*, 66(15), pp. 2795–2803. doi: <https://doi.org/10.1016/j.compscitech.2006.02.025>.
- Zimmermann, K. and Van Den Broucke, B. (2012) 'Assessment of process-induced deformations and stresses in ultra thick laminates using isoparametric 3D elements', *Journal of Reinforced Plastics and Composites*, 31(3), pp. 163–178. doi: <https://doi.org/10.1177/0731684411433315>.

